Istituto Nazionale di Fisica Nucleare
LABORATORI NAZIONALI DI FRASCATI
SIS – Pubblicazioni

LNF–09/ 5 (P)
April 16, 2009

Papers presented at EPAC 2008

Accelerator Division

Contributions to the
11th European Particle Accelerator Conference (EPAC 2008)
Genoa, Italy, June 23-27, 2008

CONTENTS

SPARC

Invited Oral

Contributed Posters

CNAO
Contributed Posters

CTF3
Contributed Posters

CRAB WAIST COLLISIONS IN DAΦNE AND SUPER-B DESIGN

P. Raimondi, INFN Laboratori Nazionali Frascati, Frascati, Italy

Abstract

The new idea of increasing the luminosity of a collider with crab waist collisions and first experimental results from the DAΦNE Φ-Factory at LNF, Frascati, using this concept are presented. Consequences for the design of future factories will be discussed. An outlook to the performance reach with crab waist collisions is given, with emphasis on future B Factories.

INTRODUCTION

A novel collision scheme, the "large Piwinski angle and crab waist" [1,2] has been studied, which will allow to reach unprecedented luminosity with low beam currents and reduced background at affordable operating costs. The principle of operation of this scheme is under test at the DAΦNE Frascati Φ-Factory [3].

The scheme finds its natural application to the SuperB project [4] aims at the construction of a very high luminosity (10^{36} cm^{-2} s^{-1}) asymmetric (4 on 7 GeV) e^+e^- Flavour Factory with possible location at the campus of the University of Rome Tor Vergata near the INFN Frascati National Laboratory. A Super-B Conceptual Design Report (CDR) [5] was issued in May 2007.

LARGE PIWINSKI ANGLE AND CRAB WAIST CONCEPT

The Crab Waist scheme of beam-beam collisions can substantially increase collider luminosity since it combines several potentially advantageous ideas.

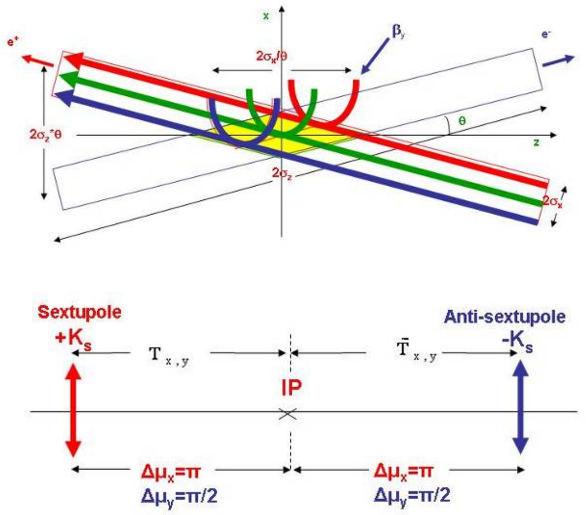

Figure 1: Collision scheme with large Piwinski angle and crabbing sextupoles.

The first one is large Piwinski angle. For collisions under a crossing angle θ the luminosity L and the horizontal ξ_x and vertical ξ_y tune shifts scale as (see, for example, [6]):

$$L \propto \frac{N\xi_y}{\beta_y} \propto \frac{1}{\sqrt{\beta_y}}; \quad \xi_y \propto \frac{N\sqrt{\beta_y}}{\sigma_z\theta}; \quad \xi_x \propto \frac{N}{(\sigma_z\theta)^2}$$

Here the Piwinski angle is defined as:

$$\phi = \frac{\sigma_z}{\sigma_x} tg\left(\frac{\theta}{2}\right) \approx \frac{\sigma_z}{\sigma_x}\frac{\theta}{2}$$

with N being the number of particles per bunch. Here we consider the case of flat beams, small horizontal crossing angle $\theta << 1$ and large Piwinski angle $\phi >>1$.

In the CW scheme described here, the Piwinski angle is increased by decreasing the horizontal beam size and increasing the crossing angle. In such a case, if it were possible to increase N proportionally to $\sigma_z\theta$, the vertical tune shift ξ_y would remain constant, while the luminosity would grow proportionally to $\sigma_z\theta$.. Moreover, the horizontal tune shift ξ_x drops like $1/\sigma_z\theta$.. However, the most important effect is that the overlap area of the colliding bunches is reduced, as it is proportional to σ_x/θ (see Fig. 1). Then, the vertical beta function β_y can be made comparable to the overlap area size (i.e. much smaller than the bunch length):

$$\beta_y \approx \frac{\sigma_x}{\theta} << \sigma_z$$

We get several advantages in this case:

- Small spot size at the IP, i.e. higher luminosity L.
- Reduction of the vertical tune shift ξ_y.
- Suppression of synchrobetatron resonances [7].

Besides, there are additional advantages in such a collision scheme: there is no need to decrease the bunch length to increase the luminosity as proposed in standard upgrade plans for B- and Φ-factories [8, 9, and 10]. This will certainly helps solving the problems of HOM heating, coherent synchrotron radiation of short bunches, excessive power consumption etc. Moreover, parasitic collisions (PC) become negligible since with higher crossing angle and smaller horizontal beam size the beam separation at the PC is large in terms of σ_x.

However, large Piwinski angle itself introduces new beam-beam resonances which may strongly limit the maximum achievable tune shifts (see [11], for example). At this point the crab waist transformation enters the game boosting the luminosity. This takes place mainly due to suppression of betatron (and synchrobetatron) resonances arising (in collisions without CW) through the vertical motion modulation by the horizontal oscillations [12]. The CW vertical beta function rotation is provided by sextupole magnets placed on both sides of the IP in phase with the IP in the horizontal plane and at $\pi/2$ in the vertical one (see Fig. 1). A numerical example of the resonance suppression is shown in Fig. 2.

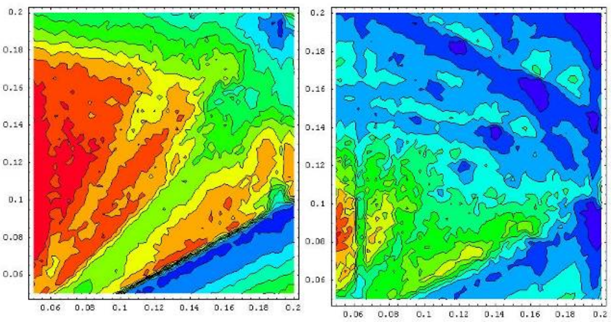

Figure 2: Luminosity tune scan (ν_x and ν_y from 0.05 to 0.20). CW sextupoles on (left), CW sextupoles off (right).

DAΦNE UPGRADE

During a six months shut-down in 2007, DAΦNE has been modified to implement the large piwinsky angle configuration. The collider has been turned on again in Dec-2007 and the machine has been running until May-2008. A new experiment called Siddharta has been installed at the IP and has been taking data since March-2008. The new beam parameters are summarized in Table 1. For comparison, the parameters used during the last DAΦNE run with the KLOE detector (2005-2006) are also shown.

Table 1. Comparison of beam parameters for KLOE run (2006) and for DAΦNE upgrade for SIDDHARTA run

Parameters	KLOE	Siddharta Design	Siddharta Achieved
L (cm^{-2} s^{-1})	$1.5x10^{32}$	$>5.0x10^{32}$	$>2.2x10^{32}$
N_{bunch}	110	110	95
N_{part}/bunch	$2.65*10^{10}$	$2.65*10^{10}$	$2.65*10^{10}$
I_{bunch} (mA)	13.	13.	11.
ε_x (nm)	300.	200.	260.
ε_y (nm)	1.5	1.	1.25
Coupling (%)	0.5	0.5	0.5
σ_x (μm)	700.	200.	260.
σ_y (μm)	15 (blow up)	2.4	4.0
σ_z (mm)	25.	20	20
β_x (m)	1.5	0.2	0.26
β_y (mm)	18.	6.	10.5
θ (mrad)	2x16	2x25	2x25

LUMINOSITY RESULTS

The most relevant results of the commissioning concern the luminosity. So far the maximum measured peak luminosity is in excess of $L_{peak} = 2.2\ 10^{32}$ $cm^{-2}s^{-1}$, the best daily integrated luminosity is $L_{\int day} \sim 8$ pb^{-1} and the highest integrated luminosity in one hour is $L_{\int 1hour}$ ~0.5 pb^{-1} averaged over a two hours run (see Fig. 3).

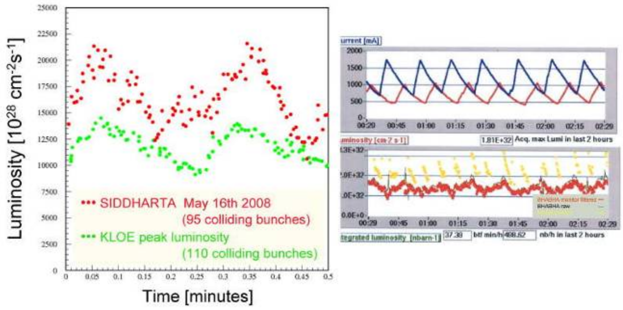

Figure 3: Peak luminosity (left) and integrated luminosity (right) over 2 hours.

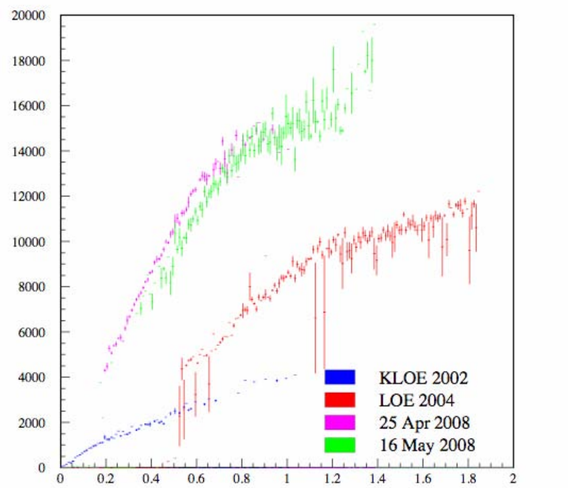

Figure 4: Peak luminosity (*1e28$cm^{-2}s^{-1}$) vs currents product ($Amps^2$)for the KLOE run and for the Siddharta run.

These results have been obtained without reaching the low beta parameters and the CW sextupole strength to their nominal values (now running at about 50% of the theoretical geometric value). The present vertical size increase w.r.t. the low current one is about 60%; 30% is due to single beam effects, ion trapping electron cloud and HOM instabilities, 30% is due to beam-beam. In order to reduce the beam-beam blowup, we plan further squeeze in β^*_y and a 30% increase in the CW sextupoles strength in the near future. Moreover the number of colliding bunches will gradually increase from 95 to 110 as the vacuum conditioning proceeds, this should also mitigate the ion-trapping and electron cloud blowup. The peak luminosity is foreseen to reach 4.0 10^{32} $cm^{-2}s^{-1}$ and the monthly integrated luminosity ~ 0.5 fb^{-1} by the end of the Siddharta run.

SUPER-B DESIGN

The construction and operation of modern multi-bunch e^+e^- colliders [1,2,3] have brought about many advances in accelerator physics in the area of high currents, complex interaction regions, high beam-beam tune shifts, high power RF systems, controlled beam instabilities, rapid injection rates, and reliable uptimes (~90%):

A Conceptual Design Report (CDR) [5] was issued in May 2007, with about 200 pages dedicated to the accelerator design. This report discusses site requirements, crab waist compensation, parameters optimization in order to save power, IP quadrupole design, Touschek backgrounds, spin rotator scheme, and project costs. A possible layout at Tor Vergata University near Rome is shown in Fig. 5. The ring lattices have been modified to produce very small horizontal (a few nm-rad) and vertical emittances (a few pm-rad).

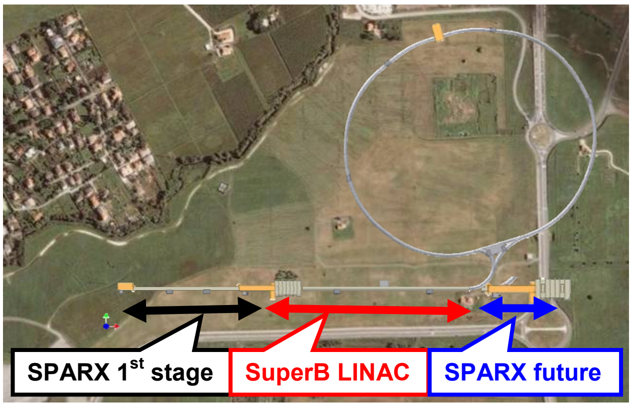

Figure 5: Possible SuperB location at Tor Vergata University with a ring circumference of 1800 m and an injector located adjacent to the future SPARX FEL.

SUPER-B PARAMETERS

The Super-B accelerator consists of two asymmetric energy rings, colliding in one Interaction Region (IR) at a large horizontal angle, with a spin rotator section in the HER to provide longitudinal polarization of the electron beam at the IP. In order to have equal tune shifts for the two beams, asymmetric B-Factories operate at unbalanced beam currents, with a current ratio inverse to the energy ratio. For SuperB, with an energy ratio of 7/4 and a large crossing angle, new conditions for having equal tune shifts are possible. LER (+) and HER (-) beams can have different emittances and β* but equal currents:

$$\xi^+ = \xi^- \Leftrightarrow \frac{\beta_y^+}{\beta_y^-} = \frac{E^+}{E^-} \qquad (1)$$

Then, in order to have equal vertical beam sizes at IP, the LER and HER vertical and horizontal emittances must be:

$$\varepsilon_y^+ = \frac{E^-}{E^+}\varepsilon_y^-, \quad \varepsilon_x^+ = \frac{E^-}{E^+}\varepsilon_x^- \qquad (2)$$

with the horizontal beam sizes in the inverse ratio with the beam energies. Thus, the LER beam sees a shorter interaction region, in a ratio 4/7, with respect to the HER beam. This allows for further β_y* reduction, a larger emittance, increased the Touschek lifetime, and reduced the injection rates. Table 2 summarizes Super-B beam parameters for the three operational scenarios. Fig. 2 shows the left-right crab waist compensation at the IP. Fig. 6 shows the beam cross sections at the IP with unequal emittances but equal beam-beam tune shifts.

Table 2: SuperB main parameters

Parameter (LER/HER)	Nominal	Upgrade	Ultimate
Energy (GeV)	4/7	4/7	4/7
Luminosity ($cm^{-2}s^{-1}$)	1×10^{36}	2×10^{36}	4×10^{36}
C (m)	1800	1800	1800
N. of bunches	1251	1251	2502
F_{RF} (MHz)	476	476	476
N. part/bunch	5.5×10^{10}	5.5×10^{10}	6.8×10^{10}
I_{beam} (A)	1.85/1.85	1.85/1.85	3.7/3.7
β_x* (mm)	35/20	35/20	35/20
β_y* (mm)	0.22/0.39	0.16/0.27	0.16/0.27
ε_x* (nm rad)	2.8/1.6	1.4/0.8	1.4/0.8
ε_y* (pm rad)	7/4	3.5/2	3.5/2
σ_x* (μm)	10/5.7	7/4	7/4
σ_y* (μm)	0.039	0.023	0.023
σ_z (mm)	6.	6.	6.
θ_{cross}(mr)	48	48	48
α_c ($\times10^{-4}$)	3.2/3.8	3.2/3.8	3.2/3.8
$\tau_{x,y}/\tau_s$ (ms)	40/20	28/14	28/14
x-tune shift	0.004/0.003	0.006/0.003	0.006/0.003
y-tune shift	0.15	0.20	0.20
RF power (MW)	26	54	64

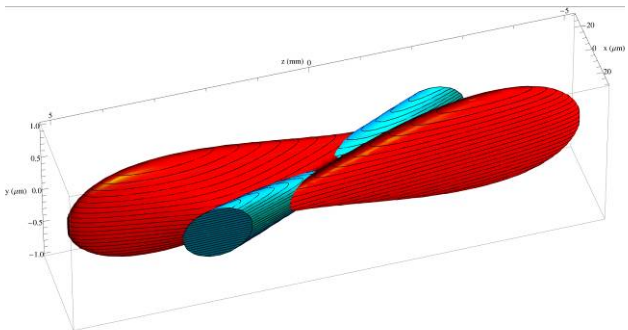

Figure 6: Beam cross sections at the IP with parameters from Table 1 and crab waists.

SUPER-B FACTORY LAYOUT

The two rings each have four arcs, one long straight section for diagnostics, RF and injection, two short straight sections for damping wigglers (optional) and a Final Focus section that also provides about 35degrees of toal beand angle. The Crab Sextupoles are located just at the end of the Final Focus section. Good dynamic apertures have been found with the crab waist sextupoles [6] as shown in Fig. 7.

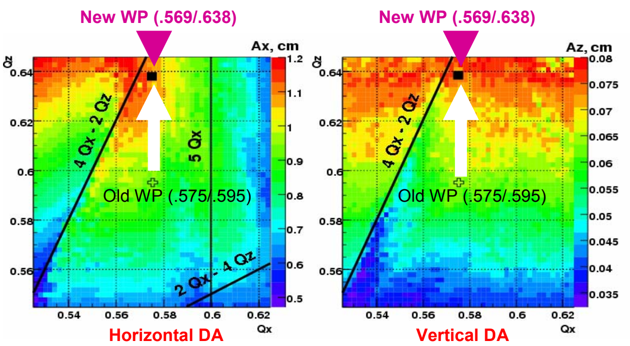

Figure 7: Dynamic aperture with crab waist versus horizontal and vertical tune used to find the optimum tune plane locations. Red is better and blue is worse.

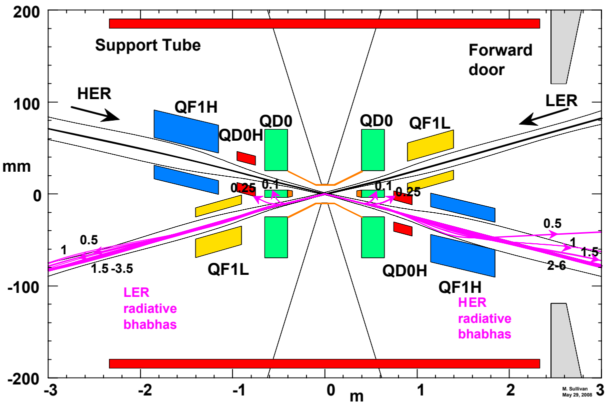

Figure 8: Interaction region for two asymmetric beams.

INTERACTION REGION PARAMETERS

The interaction region (Fig. 8) is designed to be similar to that of the ILC and to leave about the same longitudinal free space for the detector as that presently used by BABAR or BELLE, but with superconducting quadrupole doublets QD0/QF1 as close to the interaction region as possible [13,14]. The total FF length is about 160 m and the final doublet is at 0.5m from the IP. A plot of the optical functions in the incoming half of the FF region is presented in Fig. 9. The choice for a finite crossing angle at the IP greatly simplifies the IR design, naturally separating the beams at the parasitic collisions. The resulting vertical beta is about 0.2-0.3 mm and the horizontal 35 mm. These beta values are much closer to a linear collider design than a traditional circular collider. The beams enter the interaction point nearly straight to minimize synchrotron radiation and lost particle backgrounds. The beams are bent more while exiting the IR to avoid parasitic collisions and the resulting beam-beam effects.

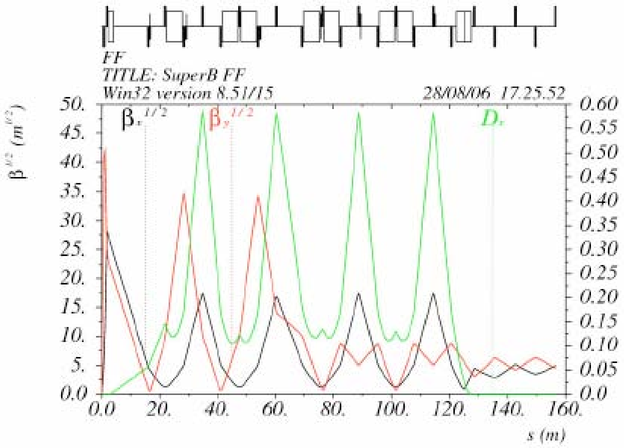

Figure 9: IR optical parameters for a Super-B-Factory.

POWER REQUIREMENTS

The power required for this collider is the sum of power for the magnets, RF system, cooling water, controls, and the accelerator operation. The present estimates indicate about 25 MW is needed for the nominal case. These values do not include the campus power requirements or that of the particle physics detector. There are upgrade possibilities for this collider to 2 to 4 times the design luminosity that will require more power [15]. Due to the advantages of the very low emittances and the crab waist with this design, the power requirements are significantly lower than those of the present B-Factory colliders.

INJECTION REQUIREMENTS

The injection system needed for the Super-B is similar to that for PEP-II, shown in Fig. 10. Table 3 shows the basic injector parameters. Since the beam lifetimes are of the order of 10 minutes, continuous injection is needed. The injector will operate at 100 Hz and inject about 2 bunches per pulse. The values shown here are for the upgraded collider at higher luminosity.

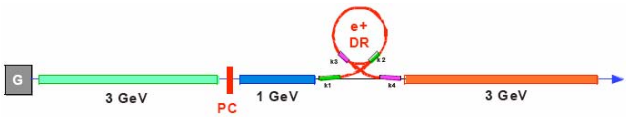

Figure 10: Schematic of the Super-B injector.

Table 3 Super-B Injection Parameters

Parameter	Unit	e+	e-
Linac energy	GeV	4	7
Damping ring energy	GeV	1	1
Linac frequency	MHz	2856	2856
Bunches per pulse		2	2
Injection efficiency	%	67	85
Pulse rate per beam	Hz	75	25
Injected particles/pulse	10^{10}	4	5.1
Injection rate total	10^{12}/sec	2.0	2.6

SUPERB BEAM-BEAM SIMULATIONS

Beam-beam studies for SuperB started with a beam parameters set similar to that of the ILC damping ring Numerical simulations with LIFETRAC have shown that the design luminosity of 10^{36} $cm^{-2}s^{-1}$ is achieved already with 2-2.5x10^{10} particles per bunch. According to the simulations, for this bunch population the beam-beam tune shift is well below the maximum achievable value. Indeed, as one can see in Fig. 11, the luminosity grows quadratically with the bunch intensity till about 7.5x10^{10} particles per bunch. We have used this safety margin to significantly relax and optimize many critical parameters, including damping time, crossing angle, number of bunches, bunch length, bunch currents, emittances, beta functions and coupling, while maintaining the design luminosity of 10^{36} $cm^{-2}s^{-1}$.

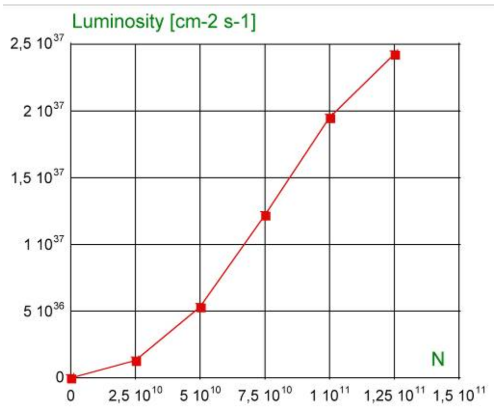

Figure 11: SuperB luminosity versus bunch intensity.

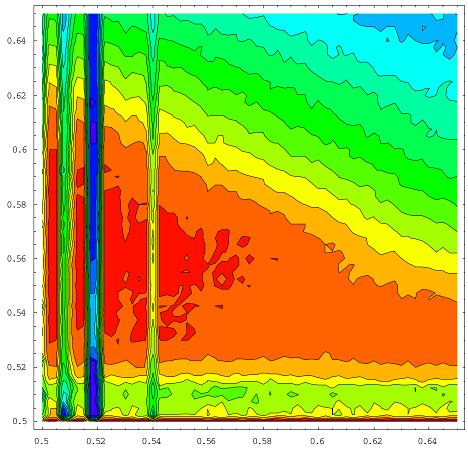

Figure 12: SuperB luminosity tune scan (horizontal axis - ν_x from 0.5 to 0.65; vertical axis – ν_y from 0.5 to 0.65).

In order to define how large is the “safe” area with the design luminosity, a luminosity tune scan has been performed for tunes above the half integers, which is typical for the operating B-factories. The resulting 2D contour plot is shown in Fig. 12. Individual contours differ by 10% in luminosity. The maximum luminosity found inside the scanned area is 1.21x10^{36} $cm^{-2}s^{-1}$, while the minimum one is as low as 2.25x10^{34} $cm^{-2}s^{-1}$. We can conclude that the design luminosity can be obtained over a wide tune area. It has also been found numerically that for the best working points the distribution tails growth is negligible.

CONCLUSIONS

The DAΦNE collider has been successfully commissioned in the new “Crab-Waist” mode and is presently delivering luminosity to the SIDDHARTA prototype detector. The final detector will be installed next August. Peak and average luminosity are already sufficient to perform the experiment in few months.

Further improvements of machine operation are likely to fulfill the requirements for a future roll-in of the KLOE detector.

The numerical simulations indicate that by exploiting the crab waist scheme the luminosity of the low emittance Super B-factory can be as high as 10^{36} $cm^{-2}s^{-1}$.

REFERENCES

[1] P. Raimondi, 2nd SuperB Workshop, Frascati, 2006.
[2] D. Alesini et al., LNF-06/33 (IR), 2006.
[3] C. Milardi et al., TUPAN033, this conference.
[4] M. Biagini et al., MOOBKI02, this conference.
[5] SuperB CDR, INFN/AE-07/2, SLAC-R-856, 2007.
[6] D. Shatilov and M. Zobov, ICFA BDN 37, 99 (2005).
[7] D. Pestrikov, Nucl.Instrum.Meth. A336, 427 (1993).
[8] J. Seeman, PAC05, p. 2333.
[9] H. Koiso, PAC05, p. 64.
[10] DANAE Letter of Intent, see http://www.lnf.infn.it.
[11] K. Ohmi et al., PRSTAB 7, 104401 (2004).
[12] P. Raimondi et al., e-Print:physics/0702033, 2007.
[13] M. Sullivan et al, “Super-B interaction region design,” EPAC 2008.
[14] E. Paoloni et al, “IR SC quadrupole design for Super-B,” EPAC 2008.
[15] U. Wienands, S. Nikitin et al, Super-B Elba meeting, https://agenda.infn.it/conferenceDisplay.py?confId=347.

BEAM DIAGNOSTICS WITH IR LIGHT EMITTED BY POSITRON AT DAΦNE

A. Bocci, A. Clozza, A. Drago, A. Grilli, A. Marcelli, M. Piccinini, A. Raco, R. Sorchetti, INFN/LNF, Frascati, Italy
L. Gambicorti, INOA, Firenze, Italy
A. De Sio, E. Pace, Università degli Studi di Firenze, Firenze, Italy
J. Piotrowski, Vigo System Sa, Warsaw, Poland

Abstract

Real-time beam diagnostics is a key issue of accelerator operations and is certainly one of the most demanding aspects of modern storage rings and 4th generation radiation sources such as FEL's. Compact and vacuum compatible mid-IR fast uncooled photo-detectors have been tested at DAΦNE to monitor single e^- bunches with a FWHM of 150-300 ps separated by 2.7 ns. These detectors appear suitable to set up a compact and low cost bunch-by-bunch longitudinal diagnostic device useful to improve the DAΦNE diagnostic. To this purpose a bending magnet synchrotron radiation (SR) front end on the e^+ ring has been set-up with a HV chamber, a gold-coated plane mirror and an IR window. The system will allow collection of the SR light for tests of IR detectors and diagnostic of e^+ bunches using a compact optical system installed in air after the IR window. Here we will present the DAΦNE source characteristics, the optical setup and the detector acquisition system that may allow to monitor, identify and characterize bunch instabilities and/or increase the DAΦNE current in the e^+ ring.

INTRODUCTION

Beam diagnostics is a fundamental aspect of any collider dedicated to high-energy physics experiments but also of storage rings optimized as synchrotron light sources. Indeed, particle accelerators emit synchrotron radiation in a wide energy range that spans from IR to X-ray energies with a time structure that depends by the temporal characteristic of the stored beam. Actually, the analysis of the radiation characteristics, e.g., intensity, spatial distribution, spectral emission, polarization, etc., can be used to observe the beam instability and to measure the characteristic of the light source, i.e., the spatial and temporal distribution of the accumulated particles. As consequence, in storage rings the synchrotron radiation can be really used for beam diagnostics and the principal advantage of photon diagnostic is that it is a direct and non-destructive probe. Typical diagnostic based on synchrotron radiation is based on expensive imaging techniques that allow measurements of the beam transverse dimensions as well as the longitudinal structure such as the bunch length of stored particles. The bunch length is an important parameter of accelerators that is directly correlated with beam dynamics. However, due to the short pulse length fast detectors are required to perform diagnostics with synchrotron light.

Diagnostics at third generation synchrotron radiation sources needs devices with response times from the sub-ns to the ps range. Future FEL sources will require faster detectors with a response time in the fs domain.

An almost standard beam diagnostic device is a streak camera. With such a device images of the temporal structure of particle beams can be obtained with a time of ~1 ps or below. The principal drawback of streak cameras is the cost. Moreover streak cameras are delicate and complex devices to manage. Fast, compact and cheaper photon devices such as photodiodes, much easier to manage with respect to a streak camera may represent an effective and reliable alternative for photon beam diagnostics. Indeed, the principal requirements of future beam diagnostic devices are: temporal resolution at least in the sub-ns regime to guarantee the installation in all accelerators, compactness and robustness. Moreover, they could be also easy to manage, possibly vacuum compatible and of low cost.

The accessibility of room temperature infrared devices based on HgCdTe alloy semiconductors already now allow obtaining sub-ns response times [1]. These detectors optimized for the mid-IR range can be used for fast detection of the brilliant synchrotron radiation IR sources and afterwards for beam diagnostics. Recently at DAΦNE, the e^+-e^- collider of the LNF laboratory of the Istituto Nazionale di Fisica Nucleare (INFN) measurements of the pulsed synchrotron light emission have been performed with uncooled IR photo-conductive detectors achieving a resolution time of about few hundred of picoseconds [2,3]. Experiments have been performed at SINBAD (Synchrotron Infrared Beamline At DAΦNE), the IR beamline operational at Frascati since 2001 [4]. To improve DAΦNE diagnostics a new experiment, 3+L (*Time Resolved Positron Light Emission*), funded by the Vth INFN Committee, started the installation at the front end of one of the bending magnet of the DAΦNE positron ring. The experiment will allow monitoring the positron bunch lengths at DAΦNE with the principal aim to study and characterize the instabilities of the positron beam and in order to possibly increase the positron current and the collider luminosity.

In the next a short description of the 3+L experiment, of the optical simulations and of the actual status of the experiment will be given. We will present also preliminary measurements of electron bunches collected at the SINBAD beamline and performed with photo-voltaic IR detectors working at room temperature. These photo-voltaic detectors are based on HgCdTe multilayer heterostructures grown by MOCVD on (211) and (111) GaAs substrates. Their response time is of the order of 100 ps or lower if cooled at 205 K [5,6]. A preliminary characterization of these photo-voltaic devices has been performed and the analysis is in progress. Additional tests on these photodiodes will be performed on the electron beam in order to understand how to improve the resolution time with respect to the response time characteristic of photo-conductive devices. After the characterization on the SINBAD beamline devices will be used for the beam diagnostics in the 3+L experimental set up. Finally we will show how to perform transverse diagnostics with new fast IR array detectors working at room temperature.

3+L EXPERIMENT: POSITRON BEAM DIAGNOSTICS

To improve storage ring diagnostics and to perform bunch by bunch beam diagnostics on the positron ring, a compact experimental installation has been recently set up inside the DAΦNE hall in the framework of the 3+L experiment. DAΦNE is the Frascati e^+/e^- collider, with a center of mass energy of 1.02 GeV, designed to operate at high current (~2 A), up to 120 bunches [7] and with different bunch patterns. The minimum bunch gap is 2.7 ns with a maximum achieved single-bunch current of ~20 mA. Bunches have a quasi-Gaussian shape with a FWHM length ranging from 100 to 300 ps and will be monitored with fast IR photo-conductive and photo-voltaic detectors whose preliminary tests have been recently performed at SINBAD. In Fig. 1 a characteristic measurement of the IR emission of the first bunch of the electron structure is showed.

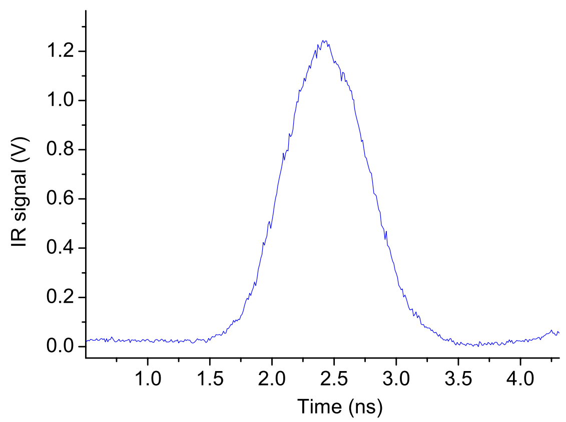

Figure 1 : The first bunch of the electron structure measured with a fast photovoltaic IR detector.

The rise time and the fall time of the IR signal showed in Fig. 1 are about of 550 ps and 630 ps, respectively with a FWHM of about 750 ps. The current of the measured bunch was about of 14 mA. The signal of the IR photodiode has been amplified by a voltage amplifier with a bandwidth of 2.5 GHz and a gain of ~40 db and stored with a 6 GHz Tektronix TDS 820 scope. Measurements were performed at room temperature although using a three stage Peltier cooler such detectors cooled at lower temperature (~ 205 K) may achieve a response time of the order of 100 ps or lower. Further characterization of these detectors will be then performed at lower temperature before they will be used for the diagnostics of the positron beam.

The layout of the 3+L exit port installed in the DAΦNE hall is outlined in Fig. 2. The IR light will be extracted by a bending magnet having a critical energy of 273 eV positioned after one of the two interaction regions of DAΦNE. Actually, this exit-port is the only available in the positron ring. The experiment, in the final installation phase, consists in a simple front-end with an HV chamber that hosts a gold-coated plane mirror. This mirror collects and deflects the IR radiation through a ZnSe window. The IR window allows transmission of radiation in the range 0.6 to 12 μm (800-17000 cm^{-1}). Finally, as illustrated in Fig. 2, a simple optical layout composed by 5 mirrors in air, set after the window, will allow focusing radiation on a small spot.

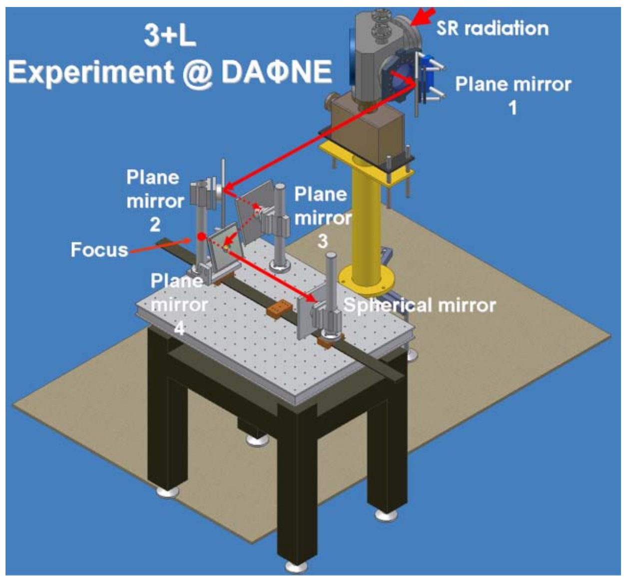

Figure 2 : The optical layout of the 3+L experiment. The path of the light is outlined by red lines. The 4th (plane) mirror has a center hole because the radiation is focalized by the 5rd (spherical) mirror behind this mirror.

The mirrors of the optical system are mounted on an optical table as showed by the photo in Fig. 3. The optical layout is based on four plane mirrors that collect the emitted radiation towards a spherical mirror that will focus 10 x 10 $mrad^2$ of the radiation on the detector position (see Fig. 2). Ray tracing simulations have been carried out to design and optimize the optical system.

Different fast IR detectors could be aligned on the focus spot of the optical system through a motorized and remotely controlled xyz stages. A remotely controlled scope connected to a PC by a GPIB I/O controller will be used to collect data with a dedicated software package developed for acquisition under the Labview platform.

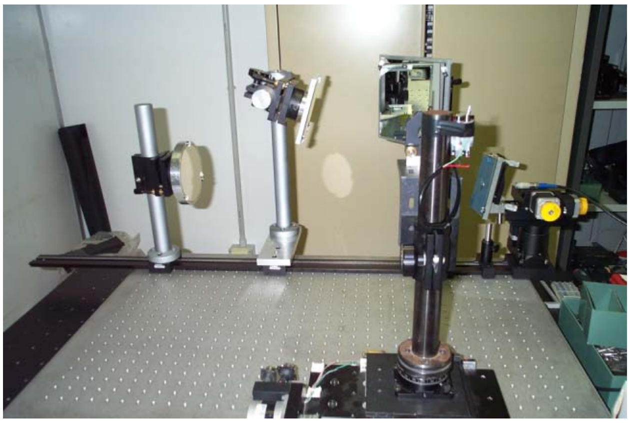

Figure 3: Photo of three plane mirrors and of the spherical mirror (on the left) of the 3+L optical system under alignment on an optical table.

To design and optimize the optical system and to compare the measured intensity of the IR source we performed wavefront propagation simulations at the wavelength of 10 μm with the SRW software package [8]. To calculate the flux of the source at the focus of the optical system different simulations have been performed. To characterize the power of the source we have also performed preliminary measurements at the exit of the window with a calibrated NIST power meter. Data have been collected with the Melles Griot 13 PEM 001/J power meter and different filters in the range 5-20 μm. The source power measured after the first mirror of the 3+L optical system is ~0.08 mW. A careful comparison between measurements, simulations and calculations is in progress although from the first evaluations we estimated that in the energy range 0.6-10 μm, more than 50 % of the energy of the source at the exit port is focused in a 400 x 400 micron^2 spot at the end of the optical system. When the optical system will be aligned a direct measurement of the power concentrated in the focus spot will allow an effective evaluation of the transmission of the optical system.

CONCLUSIONS

To improve beam diagnostics of the DAΦNE accelerator complex, in addition to test of fast IR detectors, the set up of the 3+L experiment is in progress at the exit port of one of the bending magnet of the positron ring. Using this optical layout, IR photo-conductive and photo-voltaic will characterize the bunch by bunch emission of the beam. These devices made by MCT semiconductors working at room temperature or cooled down to 205 K are: fast, robust, vacuum compatible, easy to manage and in particular are available at much lower cost if compared with existing diagnostic systems. Measurements performed at DAΦNE at the SINBAD beamline, with uncooled photo-conductive detectors, looking at the time structure of the electron bunches showed a sub-ns response time. Preliminary measurements with faster IR photodiodes (~100 ps response time) are also in progress.

The 3+L experiment has been also designed to monitor the bunch profiles of the stored positrons and to identify and characterize beam instabilities. Data could be used to increase the current on the e^+ ring and the collider luminosity. Indeed, positron bunch instabilities already observed at DAΦNE and associated to the occurrence of e^- cloud effect inside the pipe [9,10], actually limit the maximum available positron current to ~1.3 A.

Detailed and simultaneous measurements and comparison of bunch lengths in both electron and positron rings by fast photon detectors could be very helpful to investigate and characterize instabilities phenomena and possibly to understand the role of e^- cloud effects and how they limit the maximum stored current in the DAΦNE positron ring.

Future foreseen applications of the uncooled IR technology are small array detectors to perform bunch by bunch imaging of the source and to investigate simultaneously transverse bunches instabilities on the DAΦNE rings. First prototypes made by 32x2 pixels each 50x50 μm^2 are under test at the SINBAD beamline.

REFERENCES

[1] J. Piotrowski and A. Rogalski, Inf. Phys. & Tech. 46 (2004) 115–131.

[2] A. Bocci et al., Nucl. Instr. Meth. Phys. Res. A., 580, 1 (2007) 190-193.

[3] A. Bocci et al., Beam diagnostics at DAΦNE with fast uncooled IR detectors, BIW08, Lake Tahoe, 2008, arXiv:0806.1958v1.

[4] M. Cestelli Guidi et al., J. Opt. Soc. Amer. A22, (2005) 2810.

[5] http://www.vigo.com.pl/.

[6] A. Piotrowski et al., Proceedings of the SPIE, Volume 6542, (2007) 65421B.

[7] A. Drago et al., Proc. PAC2003, Portland, Oregon, (2003).

[8] O. Chubar and P. Elleaume, Proceedings EPAC98 (1998) 1177-1179.

[9] A. Drago and M. Zobov, Particle Accelerator Conference (PAC2005) Knoxville, Tennessee, USA - May 16-20, 2005.

[10] A. Drago, C. Vaccarezza and M. Zobov, Analysis of Mechanisms Driving the Horizontal Instability in the DAΦNE Positron Ring, DAΦNE TECHNICAL NOTES, G-67, 2006.

A RETARDING FIELD DETECTOR TO MEASURE THE ACTUAL ENERGY OF ELECTRONS PARTECIPATING IN E-CLOUD FORMATION IN ACCELERATORS.

M. Commisso*, T. Demma, S. Guiducci, L.Ping, A. Raco, V. Tullio,
G.Viviani and R. Cimino LNF- INFN, Frascati , Italy
P. Vilmercati, University of Trieste , and SincrotroneTrieste, ITALY

Abstract

Electron cloud related phenomena can cause potentially detrimental effects on beam stability in many planned and under construction accelerators. The possibility to reduce such unwanted phenomena lies on the observation that, machine commissioning does reduce Secondary Electron Yield (SEY). Such SEY reduction (“scrubbing”) is due to the fact that electrons produced during e-cloud formation hit the accelerator walls, modifying their surface properties. ‘Scrubbing” has been studied only as a function of impinging electron dose but never as a function of the e-cloud electron energy. Simulations predict that the e-cloud is formed by electrons with very low energies (<50 eV)[1]. Given the potentially lower scrubbing efficiency for equal dose of very low energy electrons compared to medium energy one, it would be important to measure the actual energy of the electrons forming the cloud in real accelerators. For this reason we decided to construct an optimized Retarding Field Energy Electrometer to be installed in accelerators. Here we will describe what solutions has been adopted during the design phase of such “home made” detector and some laboratory test that will be performed.

INTRODUCTION

For a number of reasons it could be extremely interesting to actually measure not only the number of electrons involved in electron cloud formation in accelerators, but also their energy distribution curves (EDC). Such EDC’s can be directly compared with simulations to verify the validity of the calculation assumptions, and of the algoritms used to simulate e-cloud formation and build-up. The avaible simulation codes first compute the actual acceleration of the existing electrons as due to their interaction with the beam, than use the calculated EDC’s to simulate the resulting multipacting build-up [2,3]. A direct comparison between directly measured EDC’s and calculated ones could than be very useful. Also, recently [4] the scrubbing efficiency of the electrons hitting the accelerator walls has been suggested to depend on their actual kinetic energy, being lower than expected at low energy (< 50 eV). This strengthen the usefulness of measuring EDC’s.

Measuring EDC’s of the electrons hitting the real internal walls of particle accelerators, with emphasis on the low energy region (0 to 50 eV) is by no means a trivial issue. One should design a detector which can be used in an accelerator environment and should fulfil several constrain. It should be compact, non-perturbing the accelerator inpedence, easy to operate, economic, and robust. Pick ups, strip detectors and RFA has been used [5,6], but their energy resolution, their efficiency at low energy and their transmission were hard to define. Moreover the number of total electron current induced by the e-cloud is measurable with a simple biased anode, while if grids are set to select energies, the number of energy dependent electrons will give a too small current to be easily and accurately measured by standard picoammeters expecially for low energy electrons. Surface science community has a longstanding tradition in measuring EDC with very constant, stable and high resolution electron analysers. Their costs and handling in an accelerator environments did not suggest to use such cylindrical or spherical analysers. One more option, used in Surface Science is to use the 4 curved grid optics for LEED to perform Auger studies, hence energy resolved spectra. This is done by using a LEED-AUGER optic in connection with an etherodine technique to clean up the small signal by locking it to a oscillating band pass filter.

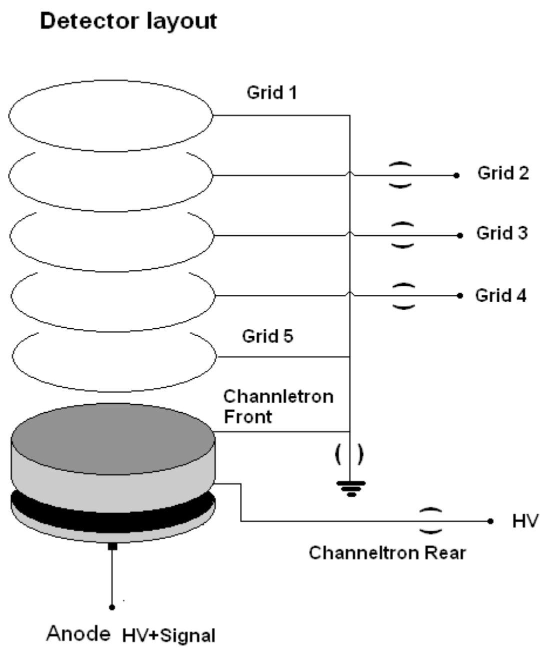

Figure 1: View of the LNF-Retarding Field Detector.

*Mario.commisso@lnf.infn.it

It is by looking at those working analysers we planned to construct a small, robust and compatible to accelerator environment detector using already existing electronic control units and new acquisition programs.

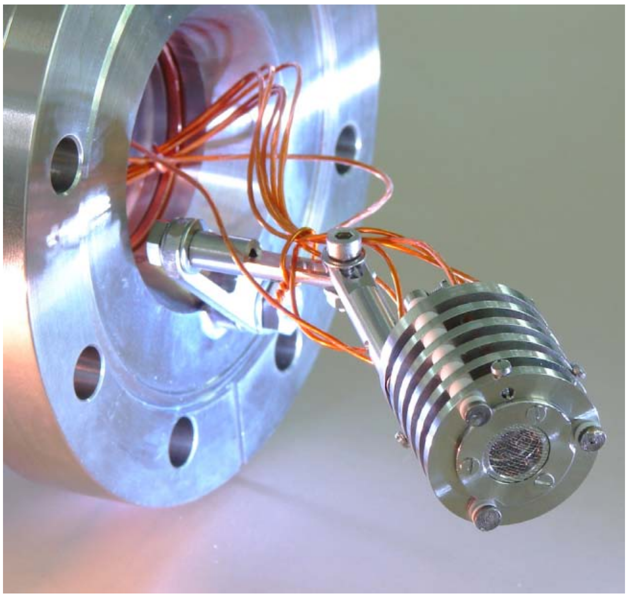

Figure 2: Photograph of the LNF-Retarding Field Detector built at LNF mounted on a CF 63 Conflat flange.

EXPERIMENTAL

We designed a small home made 5 flat grid band pass analyser ready to be connected with a slightly LEED-Auger electronic of OMICRON. In fig. 1 the schematic view of the analyser is shown, while in fig.2 and fig.3 some photos of the real object are shown. The first grid is held at ground so that the beam passing in the accelerator ring will not be disturbed by "seeing" any applied voltage, and, like all the other four grids, has in its centre a 5mm in diameter 90% metallic mesh. The second grid was inserted to measure the total current of electrons entering in the detector by applying on it a positive bias like a simple Faraday cup. In usual LEED Auger system this grid is absent, but one of the problem we faced by the choice of using a channelplate to multiply our signal, was that all the data than collected are in arbitrary units, since the multiplication factor of a channelplate depends not only on its voltage, but also on its history. For this reason, this grid, will give the integral values in number of electrons of the EDC measured. During EDC acquisition this grid will be at ground. The third and fourth grids are used as a band pass filter to obtain electron energy selection and their voltage oscillate to reduce noise, as normally done when acquiring data with an etherodine technique. Their voltage, and the modulation intensity are directly controlled by the OMICRON control unit. The fifth grid is held at ground, to isolate the counting system from the grid voltage. Then the electrons will be energy selected by passing through the grids and will be multiplied by a quantum sub-miniature advanced performance Detector from BURLE. This channelplate is constitued of a grounded front end and a rear which is biased positively with a voltage varying from 0 to 1000 V from a computer controlled HV Spellman Power supply. Such channelplate has a collection diameter of 3.9 mm and, if biased at 1000V, can multiply the signal up to 10^3. We estimate such multiplication to be necessary and sufficient to measure EDC from E-cloud induced electron fluxes. The anode voltage is given by an home made floating battery box, to cancel eventual noise to the signal as due to HV commercial power supplies. The standard OMICRON LEED–Auger plug has been modified to accept current signal from our anode placed at 1050 V rather than the 300 V usually given at wich the LEED screen is normally biased to be used as the collector in standard Omicron LEED Auger.

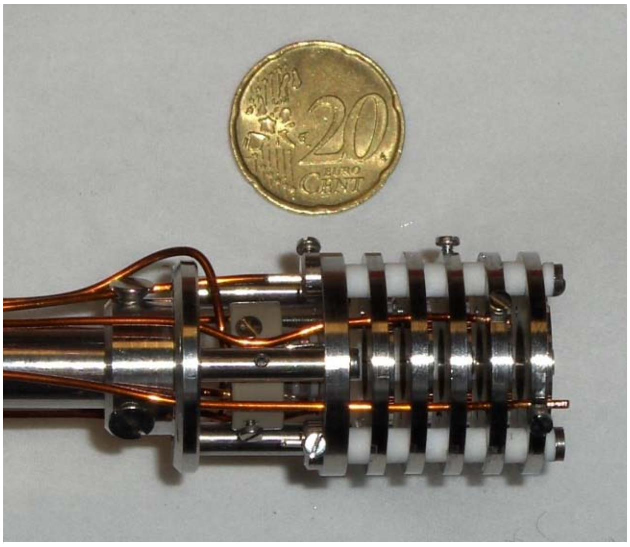

Figure 3: Photograph of the LNF-Retarding Field Detector compared to a 20 Cent Euro coin.

Fig 4 shows a block diagram of the electric lay-out of the Detector control system. The core of it is the standard OMICRON SpectaLEED control unit [7] which has been slightly modified to acquire EDC's from a channelplate. The control of the detector is than performed through an interface "Prototype Box". Such box allows to transmit lock-in oscillations to grid 3 and 4, drive the Spellman power supply for biasing the channelplate, and read on the second grid the total current of the electrons entering in detectors. The standard Omicron unit controls also the lock-in amplifier and define the frequency and the amplitude for the grid modulation signal via a Data Auger software acquisition system. It is not scope of this note to describe the LEED-Auger functioning principle, which can be found in textbook and literature [8,9]. This system will allow us to acquire EDC curves varying incident electron energies and to measure the actual energy of the electrons forming the cloud in real accelerator.

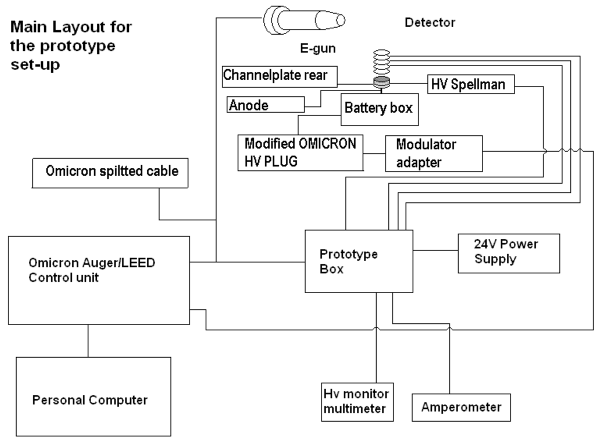

Figure 4: Electric lay-out of the Detector control system.

Such detector has been produced as a prototype to be tested by irradiating it with electrons at different intensities and energies from a Omicron e-gun. We are ready to test it, measuring its efficiency, its transmission curve (i.e. the efficiency of detecting equal intensity electron beams at different energies) with special attention to linearity at low electron energies. We plan to insert 2 of such detectors in the DAFNE storage ring [10] to measure in equivalent places in the positron and the electron ring EDC's, observing their intensities and studying in details the differences expected from the two rings [11]. The detectors in the ring are planned to be mounted as shown in fig 5, and will "look" at the beam, trough the vacuum slots of similarly placed interconnects. The electronic to be used will be only one since we developed a "distribution" board, in order to measure EDC's from different detectors by choosing which one is measuring by remote control, i.e. without need to enter into the accelerator hall.

After final testing we could mount this detector also at ANKA in connection with the COLDIAG diagnostic set up described in this proceedings [12].

CONCLUSION

We described the adopted solutions used for the construction of an optimized Retarding Field Energy Electrometer to be installed in accelerators. Such "home made" detectors use existing LEED–Auger technology developed for Surface science experiments. Its aim is to acquire EDC's and to measure the actual energy of the electron forming the cloud in accelerators during operation.

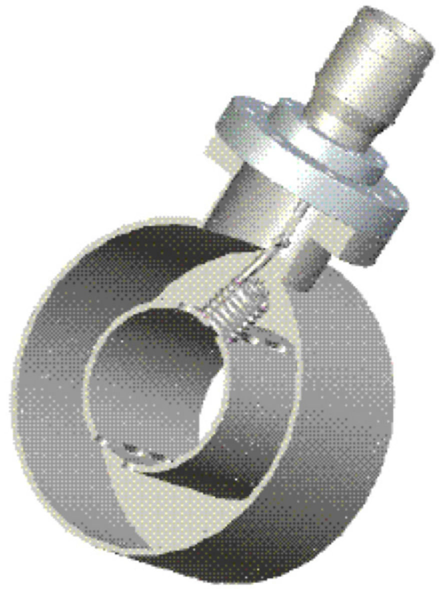

Figure 5: View of the LNF-Retarding Field Detector mounted in DAFNE ring

REFERENCES

[1] F. Zimmermann, in Proceedings of Chamonix XI (CERN Report No . CERN-SL-2001-003 DI, 2001).
[2] F. Zimmermann, in Proceedings of the ECLOUD'2, CERN, Geneva, April 15-18, CERN –2002-001, 2002.
[3] M. Furman, V. H. Chaplin, Phys. Rev. ST Accel. Beams 9, (2006) 034403.
[4] R. Cimino et al. these proceedings (EPAC 08).
[5] R. J. Macek et al., in Proceedings of the 2003 Particle Accelerator Conference, 508.
[6] J. M. Jimenez, B. Henrist, J-M. Laurent, K. Weiss, LHC Project Report 677, CERN, 2003.
[7] Omicron manuals and technical notes, avaible at http://www.omicron-instruments.com.
[8] H. Lüth, "Surfaces and Interfaces of Solids, Springer-Verlag Berlin Heidelberg 1993.
[9] G. Ertl, J. Küppers, "Low Energy Electrons and Surface Chemistry", Deerfield Beach, F1, USA edit VCH (1985).
[10] G. Vignola et al., PAC91, San Francisco.
[11] C.Vaccarezza et al., Proceedings of PAC05, 779.
[12] S. Casalbuoni et al., these proceedings (EPAC 08).

LUMINOSITY MEASUREMENT AT DAFNE FOR CRAB WAIST SCHEME

M. Boscolo, F. Bossi, B. Buonomo, G. Mazzitelli, F. Murtas, P. Raimondi, G. Sensolini
(INFN/LNF, Via E. Fermi 40 - 00044, Frascati, RM, Italy)
M. Schioppa
(Gruppo Collegato INFN, Via P. Bucci - 87036, Rende, CS, Italy)
F. Iacoangeli, P. Valente
(INFN-Roma, P.le Aldo Moro 5, Roma, Italy)
N. Arnaud, D. Breton, A. Stocchi, A. Variola, B. Viaud
(LAL, Univ Paris-Sud, CNRS/IN2P3, Orsay, France)
Paolo Branchini
(INFN Roma3, Via della Vasca Navale, 84 - 00146, Roma, Italy)

Abstract

Since the beginning of 2008 the DAFNE complex started to test the "crabbed scheme" to improve the luminosity performance of the accelerator. In order to ensure a fast, accurate and absolute measurement of the luminosity and to fully understand the background conditions, the new interaction region has been equipped with three different luminosity monitors: a Bhabha calorimeter, a Bhabha GEM tracker and a gamma bremsstrahlung proportional counter. The detectors design, construction, and performance, as well as the first measurements performed at DAFNE during the crab waist commissioning are here presented. Data are also compared with the Monte Carlo simulations of the full setup. First results acquired during the SIDDHARTA run are supposed to be presented.

INTRODUCTION

The promising idea to enhance the luminosity with the introduction of a large Piwinski angle and low vertical beta function compensated by crab waist [1], will be a crucial point in the design of future factory collider [2], where the luminosity is the fundamental parameter. The DAFNE accelerator, located in the National Laboratory of Frascati (INFN), optimized for the high production of Φ mesons ($\sqrt{s}$=1020 MeV), has been modified during last year to test the crab waist sextupoles compensation scheme. Since fall of 2007 the machine has restarted operations, and at the beginning of February various luminosity detectors have been put in operation in order to guarantee an accurate measurement of the luminosity and of backgrounds, as well as to provide powerful and fast diagnostics tools for the luminosity improvement.

Three different processes are used to measure the luminosity at DAFNE:

- The Bhabha elastic scattering $e^+e^- \rightarrow e^+e^-$; it has a very clean signature (two back-to-back tracks); the available angle is limited due to the presence of the low-β quadrupoles, however, in the actual polar angle range covered by our calorimeters, 18^0-27^0, the expected rate (~440 Hz at a luminosity of 10^{32} cm^{-2} s^{-1}) is high enough and the backgrounds low enough to allow an online clean measurement.
- The very high rate $e^+e^- \rightarrow e^+e^-\gamma$ (radiative Bhabha process); it has the advantage that 95% of the signal in contained in a cone of 1.7 mrad aperture, but it suffers heavily from beam losses due to: interactions with the residual gas in the beam-pipe, Touschek effect, and particles at low angles generated close to interaction region (IR).
- The resonant decay $e^+e^- \rightarrow \Phi \rightarrow K^+K^-$; a rate of about 25 Hz at 10^{32} is expected in the SIDDHARTA experiment monitor at ~90^o [3].

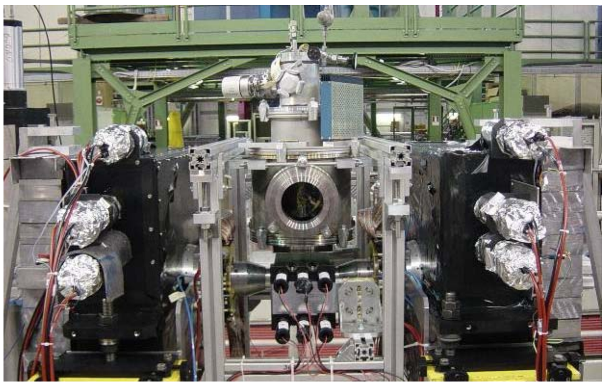

Figure 1: the SIDDHARTA preliminary setup installed at DAFNE. The Bhabhas calorimeters (black boxes) are visible on the left and right of the interaction region.

BHABHA MONITOR

The Bhabha monitors consist of two different detectors, a 4-module sandwich calorimeter, made of lead and scintillator, and two triple GEM annular trackers.

Calorimeters

Four modules of calorimeters surround the final permanent quadrupole magnets, located at a distance of 32.5 cm on both sides of the interaction region (IR), as shown in Fig. 1. They cover an acceptance of 18^o -27^o in polar angle, and are segmented in azimuthal angle in five sectors, 30^o wide. The choice of not instrumenting 1/6 of the acceptance, i.e. the ±15° region, was dictated by the consideration that most of the machine backgrounds are expected on the machine plane. Each sector is a sandwich of 12 trapezoidal tiles of 1cm thick scintillator, wrapped with Tyvek* paper, alternated with lead plates: eight 5 mm thick plates towards the interaction point and three 1cm thick plates in the back part, lead plates for a total thickness of 19 cm. This choice was driven by the compromise between the need of having a good longitudinal containment of 510 MeV electron showers (the total depth corresponds to about 12.5 X_0), and the necessity of having a detector not exceeding the permanent quadrupole length.

The 240 scintillator tiles have been produced with injection-molded technique in IHEP, Protvino. Each tile has three radial grooves on one face, 2 mm deep (one in the middle and two 1 cm from the edge of the tile) inside which wavelength shifting (WLS) fibers of 1 mm diameter are placed; the 36 WLS fibers, are collected to an optical adapter to fit the photocathode of 20 Photonis-Philips XP 2262B photomultipliers, read by a prototype data acquisition system of the KLOE2 experiment: the analog signals are actively splitted to be digitized by a constant fraction discriminator for time measurement (using the KLOE TDC, 1.04 ns resolution), and for the pulse height measurement by the KLOE charge ADC, with a 0.25 pC resolution.

All modules has been tested at the DAFNE Beam Test Facility [8] where an energy resolution of 14%√E(GeV) has been measured.

The triple GEM tracker

In front of each calorimeter, at a distance of 18.5cm from the IR, a ring of triple-GEM detectors [4] is installed around the beam pipe. The two GEM trackers are divided in two units, with an half-moon shape; the top (bottom) half covers azimuthal angles between 14° and 166° (194° and 346°) respectively. Each of the four GEM units is segmented into 32 pads: eight cells in azimuth (covering 19° each) are arranged in four rings of equal radial extension. When a charged particle crosses the 3 mm drift gap, it generates electrons that will be multiplied by the three GEM foils separated by 2/1/2 mm. Each of the GEM planes is made of a thin (50μm) kapton foil sandwiched between two copper clads and perforated by a dense set of holes (70μm diameter, 140 μm pitch).

As a high potential difference (about 400 kV) is applied between the copper sides, the holes act as multiplicating channels and the gain of each layer is about 20 (and hence roughly 8,000 in total).

The GEM trackers, as well as the gamma monitors, have been included into the main DAQ system.

* Tyvek™ is a trademark of DuPont company.

GAMMA MONITOR

Two gamma monitor detectors are located 170 cm away from the IR, collecting the photons radiated by electron or positron beam.

The detectors replace the gamma monitors previously installed in DAFNE [5] and are now made of four $PbW0_4$ crystals (squared section of 30×30mm^2 and 110mm high) assembled together along z, in order to have a 30 mm face towards the photon beam, and a total depth of 120 mm corresponding to about $13X_0$. Each crystal is readout by a Hamamatsu R7600 compact photomultiplier. Each of the crystal signals is splitted: one half is sent to the charge ADC of the KLOE2 data acquisition system, while the other is sent to an analog mixer. The analog sum of the four crystals is then discriminated and the counts are read by the DAFNE Control system, providing a prompt estimate of the luminosity for machine optimization.

Because of the boost introduced by the beam crossing angle, the trajectories of the photons are shifted towards the inner side (along x coordinate) of the machine; the gamma monitors and GEM trackers are then placed along the beam pipe at x=–5cm and rotated by 4° in the horizontal plane with respect to the beam axis.

Thanks to the high rate, those detectors are mainly used as a fast feedback for the optimization of machine luminosity versus background, more than providing a measurement of the luminosity, since the relative contribution of background is changing with the machine conditions. However, on the short time scale and as relative luminosity monitors, those counters have demonstrated to be extremely useful.

SIMULATION

In order to correct the Bhabha event rate measured using the calorimeters and the GEM trackers for the detectors' acceptance and selection efficiency, we developed a full simulation of the whole experimental set-up, based on the GEANT3 package. This includes all the materials and fields present in the interaction region as well as a simulation of the detectors response.

The BHWIDE package is used to generate Bhabha events with a full treatment of the radiation [6].

The contamination due to the Touschek background is investigated by interfacing an ad hoc generator [7] with the simulation.

Particular care was given to the implementation in the simulation of the materials and fields distribution all along the interaction region, since this impacts directly on the background level in the calorimeters as well as on the signal detection efficiency of the gamma monitors.

The simulation predicts a measured Bhabha event rate of ~440 Hz when the luminosity equals 10^{32} cm^{-2} s^{1}. The rate actually measured at the IP is compared with this number to derive the actual luminosity. The simulation is also used to evaluate the systematic uncertainties affecting this measurement. It's dominated by the alignment of the calorimeter and of the conical shielding in front of it ("Soyuz"), as well as by the definition of the energy threshold. Also the presence of the SIDDHARTA detector is taken into account. For a preliminary measurement involving only the calorimeters, an 11% uncertainty should be quoted. It drops to 7% when the GEMs are also in operation.

We also used the simulation to determine the optimal location for the GEMs. They're shifted in the horizontal plane by 5 mm in the direction of the boost to compensate for the loss of back-to-back-ness caused by this boost.

Finally, we based on the simulation to design the part of the beam-tests devoted to the measurement of the attenuation length of the scintillating tiles. This constant has to be precisely known for the simulation to describe accurately the energy reconstruction, thus the signal efficiency.

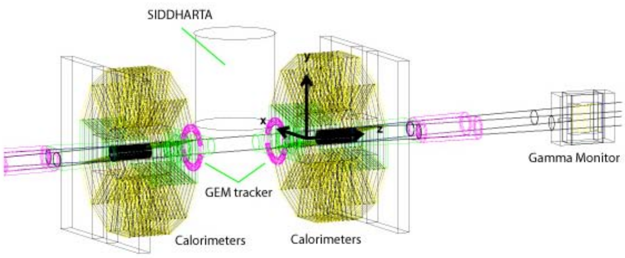

Figure 2: GEANT simulated setup

RESULTS

The four calorimeters, the GEM trackers and the crystal gamma detectors are acquired by KLOE2 farm data acquisition prototype. The trigger condition (T1FREE) consists of the coincidence of two opposite, upside down modules when the energy released in the modules is above 200MeV. Data can be acquired for offline analysis when particular studies have to been performed. All single and coincidence rate are acquired by the DAFNE control system, in order to provide a fast reading of luminosity and background condition very useful for machine parameters optimization.

Various analyses of trigger condition, luminosity and background have been performed in order to check the trigger efficiency and background contamination in the luminosity evaluation. For this reason an online filtering process has been implemented on the DAQ farm, providing an offline estimate of the rate (T2FARM), corrected by the percentage of background contamination in the coincidence. This correction is estimated analyzing blocks of 1000 events, and by looking at the time distribution of the time of the two triggering modules. The difference of the arrival time of a Bhabha candidate for the couple of triggering modules, as selected by the T1FREE hardware trigger. As expected, a Gaussian distribution peaked at $\Delta t=0$ is clearly visible. Superimposed on this narrow Gaussian ($\sigma\cong2$ counts), a flat distribution due to background is also present. Indeed, the narrow peak completely disappears when the beams are longitudinally separated. The width of the background flat distribution is determined by the duration of the digital signals building the coincidence (≈25 ns).

In order to isolate genuine Bhabha's, the online filter selects events in a $\Delta t=\pm3\ \sigma$ window (±6 counts). In order to estimate the amount of background beneath the peak, events in the sideband (12 counts wide) are counted and subtracted.

CONCLUSIONS

The diagnostics installed on the new DAFNE IR in order to measure luminosity for the test of the new crab waist scheme, started to operate at the beginning of February 2008 and is collecting the first encouraging results from the machine.

All systems showed very good performance and fully achieved the design parameters. A total systematic uncertainty on the luminosity measurement of 11% can be estimated.

Detectors have been fully implemented in the machine controls, and data are available for the community on word wide web DAFNE accelerator page.

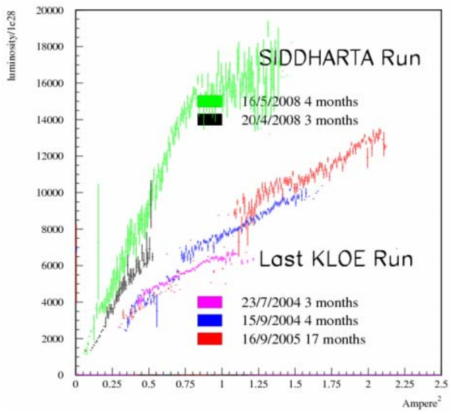

Figure 3: DAFNE performance (luminosity vs current product) during the tree major optics steps.

ACKNOWLEDGEMENTS

We would like to thank L. Iannotti, V. Romano and the LNF SSCR service for the mechanical works, and all the electronic staff of the Accelerator Division; G Corradi, M. Pistilli, D. Tagnani for the GEM electronics and detector construction. We also would like to thank W. Placzek for the support on BHWIDE code.

REFERENCES

[1] D. Alesini et al, LNF-06/033 (IR), 2006.
[2] M. Bona et al, INFN/AE-07-2, SLAC-R-856, LAL 07-15, 2007
[3] Marton et all, Proceedings to the XLV International Winter Meeting on Nuclear Physics, Bormio, Italy, 2007
[4] M.Alfonsi, et al. IEEE 53(1): 322-325 2006
[5] G. Mazzitelli et al, NIM.A486:568-589,2002.
[6] S. Jadach et al, Phys.Lett. B390 (1997) 298-308
[7] M. Boscolo et al, PAC2007, Albuquerque, New Mexico, USA, 2007.
[8] A. Ghigo, et al, NIM A 515 (2003) 524-542

ELECTRON ENERGY DEPENDENCE OF SCRUBBING EFFICIENCY TO MITIGATE E-CLOUD FORMATION IN ACCELERATORS

R. Cimino*, M. Commisso, T. Demma, A. Grilli, M. Pietropaoli, L.Ping, V. Sciarra,
LNF- INFN, Frascati , Italy
V. Baglin, CERN, Geneva, Switzerland
P. Barone, A. Bonnanno Dep. of Phys. University of Calabria, and INFN-Cosenza

Abstract

Recently built and planned accelerators, base their ability to reach design parameters, on the capability to reduce Secondary Electron Yield (SEY) during commissioning, hence mitigating the potentially detrimental effects of e-cloud driven machine limitations. This SEY reduction (called “scrubbing”) is due to the fact that the electrons of the cloud, hit the vacuum chamber wall, modifying its surface properties and reducing its SEY. This may minimize any disturbing effects of the c-cloud to the beam. “Scrubbing” has been studied in laboratory experiments as a function of impinging electron dose only by bombarding surfaces with 300-500 eV electrons, but no scrubbing dependence on the bombarding electron energy has ever been discussed. The actual energy of electrons of the cloud hitting the wall in real accelerators has never been measured accurately, while simulations predict very low electron energies (<50 eV). For this reason and given the peculiar behaviour observed for low energy electrons [1] we decided to study this dependence accurately. Here we present some preliminary results calling for a more intense experimental effort to clarify the role of electron energy and scrubbing efficiency and their eventual implications to machine commissioning procedures.

INTRODUCTION

During operation, the internal walls of modern particle accelerators are subjected to Syncrotron radiation irradiation and/or electrons bombardment [2]. Such phenomena do affect the surface properties such as the secondary electron yield, SEY, i.e. the number of emitted electrons per incident electron. The reduction of the SEY is advantageous for the operation of particle accelerators and it is called surface conditioning or beam scrubbing [3,4]. In fact the design luminosity of present and future particle accelerators such as the Large Hadron Collider (LHC), can only be achieved if the SEY of the beam vacuum walls is strongly reduced by surface conditioning during its initial operations or commissioning, hence mitigating the potentially detrimental effects of e-cloud instabilities. The understanding of the conditioning process may therefore help to optimise the conditioning required to reach the LHC design parameters.

Surface scrubbing can be studied in various ways [5,6], for instance by measuring the electron dose dependence of SEY yield. All the available experiments found in literature have been performed by bombarding technological metal surfaces with electron beams of fixed energy as 300-500 eV[1,7-9] and 2.5 keV[10,11]. These experiments showed that even after a low electron exposure of about 10^{-6} C·mm^{-2} the SEY of technological surfaces starts to decrease significantly, reaching its lowest value after about 10^{-2} C·mm^{-2}. By measuring the amount of molecules desorbed from bombarded surfaces [8] and by monitoring the variation of Carbon Auger peak intensity as function of electron dose with Auger Spectroscopy, the origin of SEY reduction versus dose is explained as a two steps process, involving a surface cleaning caused by primary beams and an accumulation of carbonaceous species coming probably from the material itself [10,11].

Despite these investigations are useful to elucidate the origin of conditioning in accelerators, they are not complete and other studies are required to clarify the scrubbing dependence on the bombarding electron energy since this parameter is missing. Furthermore the actual energy of the electron of the cloud (EC) hitting the walls in real accelerators has never been measured accurately, while simulations, which study EC formation and evolution, predict very low electron energies (<50 eV)[12]. For this reason and given the peculiar behaviour observed for low energy electrons [1], we decided to study this dependence accurately. In this contribution we present some preliminary results obtained bombarding surfaces of the actual Cu sample used in the LHC beam screen with electron beam in the range of primary energies 20-500 eV. Our measurements seem to show that scrubbing efficiency depends on the impinging energy of the electron beams. Such results, if confirmed by further experiments performed by bombarding with electrons of energy even lower than 20eV, could have significant implications to machine commissioning procedures.

EXPERIMENTAL

The experiments were performed in a UHV μ-metal chamber with less than 5mGauss residual magnetic field at the sample position, pumped by a CTI8 cryo-pump to ensure a vacuum better than 10^{-10} Torr after bake-out. Ion pumps are not used due to their detrimental stray magnetic field, which can be a serious problem when dealing with very low energy electrons.

The sample is mounted on a close cycle Sumitomo cold finger manipulator specially designed to obtain a stable temperature on the sample between 8 and 400 K. The data here shown were performed at room temperature. The samples studied were all part of the final production of co-laminated Cu for LHC beam screen, hence are representative for the real surface “seen” by the proton

*roberto.cimino@lnf.infn.it

beam in the machine. The electron beam was set to be smaller than 0.25 mm^2 in transverse cross-sectional area and stable in current for energies between 10 and 500 eV, as confirmed by a line profile and by stability tests done using a homemade 1 mm slot Faraday cup. Unfortunately it has been observed that the beam move slightly in position during energy scans, forcing us to manually irradiate with the same doses the neighbouring areas of the sample around the measuring spot. Such rastering procedure, although time consuming, ensure that the SEY measurements were done on a uniformly irradiated area for every bombarding electron energy. To measure low-energy impinging primary electrons, a negative bias voltage was applied on the sample. Such bias allows us to work at very low primary energy (close to zero eV) while keeping the gun in a region where it is stable and focused. Our set-up has been chosen among different bias and geometrical conditions to guarantee the absence of any spurious effects on the measured data caused by the possible presence of electric field lines induced by the sample bias.
The SEY (δ) is determined from: $\delta=I_e/I_0 = (I_0-I_S)/I_0$ where I_e is the current due to electrons emitted by the sample; I_0 is the impinging electron current as measured by a positively biased Farday cup (75V). I_s is the drain current measured from sample to ground (applying on it a negative bias voltage –75V) with a Keithley picoammeter. I_0 was set to be as low as possible (about few nA at 500eV) to avoid giving any significant scrubbing dose during SEY measurements. Electron dose is determined from: $D=Q/A=I_0t/A$, where Q is the total charge incident per unit area on sample surface, I_0 is the imping beam current (generally of few μA while dosing the sample) and t is time period for which the sample was exposed to the beam. The area is determined assuming that the electron beam hits the surface sample with a circular spot. Unit chosen here for dose are Cmm^{-2}. All SEY and doses have been performed at normal incidence. Given some uncertainty on the irradiated spot and on the adopted rastering procedure doses have to be considered within 20% of their quoted values. The data acquisition system is a customized LABVIEW program which allows to scan beam energy from lowest to highest value and to acquire beam and sample current in order to calculate SEY.

RESULTS AND DISCUSSION

In fig. 1(a) and (b) we present the variation of SEY curves versus incident beam energy for a LHC sample type as a function of the electron dose. These curves are obtained bombarding the sample with an incident energy of 500 (a) and 50 eV (b) at normal incidence. The curves are consistent with those found in literature [1,9], showing respectively a maximum and a minimum value, which depend on the actual sample and on its conditions (temperature, scrubbing...).
In these curves it is clear that that secondary electron yield decreases with the increase of the electron dose for every primary impinging energy. After the impact of an electron dose equivalent to some 10-6 C.mm-2, δmax (the maximum value of the SEY) decreases until it stabilizes at a value close to 1.15 for doses greater than 1x10-3 C.mm-2, as indicated by the reference doted line.

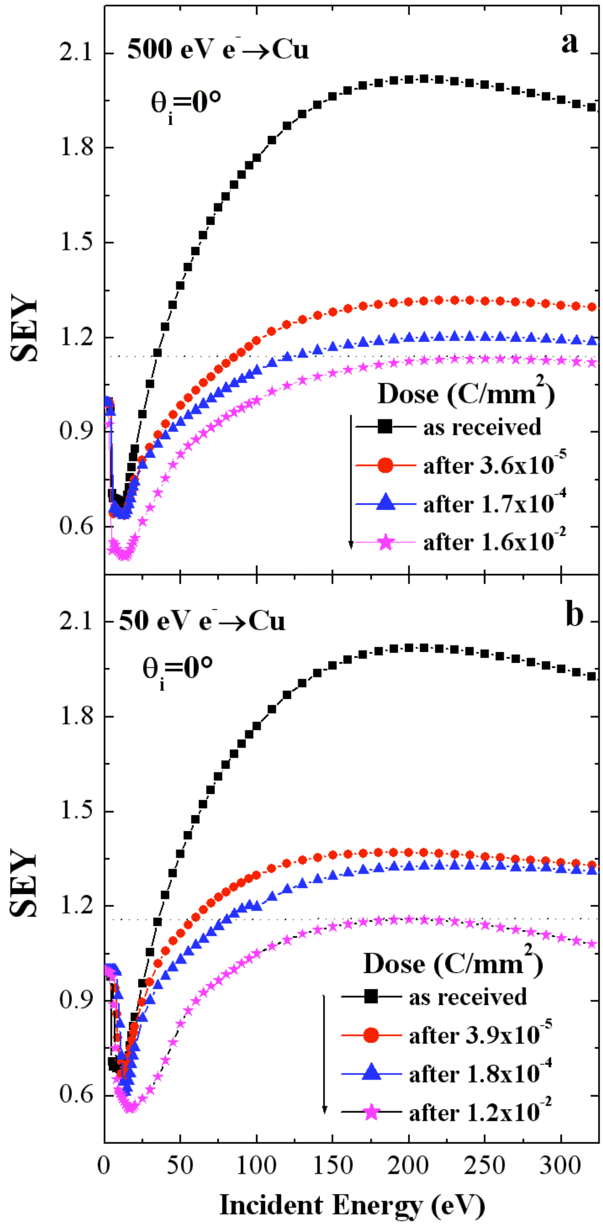

Figure 1: SEY measurements for 500 eV a), and 50 eV b) impinging electron energy at normal incidence

Furthermore the corresponding energy, E_{max}, shifts versus lower values with doses.
The behaviour of the SEY curves at low primary energy (<30 eV) is largely independent of δ_{max} and of the degree of scrubbing, showing a SEY value close to unity in all cases, which is consistent with previous experimental studies [1].
Fig 2 shows the behaviour of δ_{max} as a function of the electron dose for various measurements performed using different primary electron energies. The curve obtained while conditioning the sample with 500 eV has been

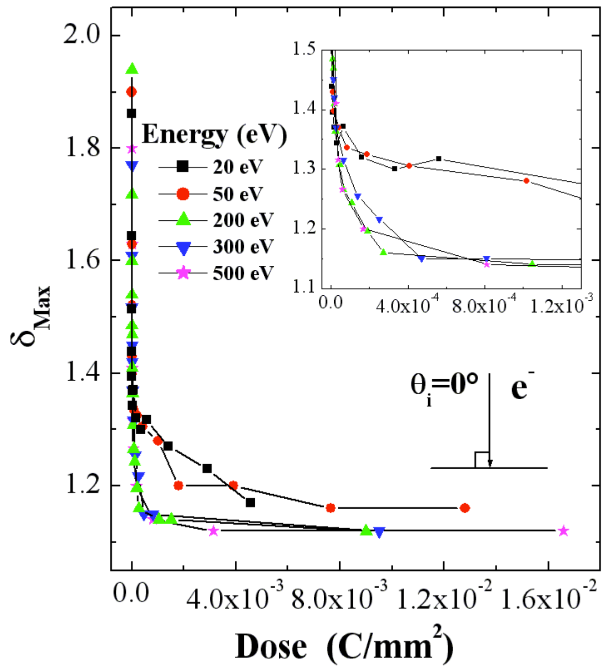

Figure 2: δ_{max} versus dose for different impinging electron energies at normal incidence.

performed for reference to various works reported in literature [8].

Our measures show that an electron dose, between $8x10^{-4}$ and $2x10^{-3}$ Cmm^{-2} is required to reach a SEY lower than 1.3, while the minimum of the SEY (close to 1.15) is obtained for an electron dose close to 10^{-2} $C{\cdot}mm^{-2}$ (fully conditioned sample). These measures agree well with available results from the literature [1,8,11]. We notice also that when sample is conditioned with an incident energy of 200 eV and 300 eV, the reduction of δ_{max} versus electron dose is similar to 500 eV electron bombardment. As shown in the inset of fig.2, the situation is different for samples conditioned with primary electron energies of 50 and 20 eV. In those cases one can observe that the δ_{max} reduction versus incident dose proceeds with a much slower rate with respect to 200-500 eV. In addition the final value of δ_{max} obtained at the dose of 10^{-2} Cmm^{-2} is different. These measurements have been reproduced on different Cu beam screen samples showing that the conditioning behaviour does not depend on the slightly different initial condition of the sample (i.e. δ_{max} on "as received" samples). This difference in efficiency with respect to electron energy is consistent with experiments performed in EPA at CERN while conditioning a copper sample with photoelectrons with energies between 100 and 820 eV [5,13].

Our measure seems to indicate that the efficiency of scrubbing depend on the energy of the irradiating beams. Therefore the time required to obtain a fully scrubbed surface is consequently different especially when low energy electron beams are considered. These new information need further investigation especially at very low impinging electron energies, and might be useful in evaluating the impact of electron cloud in large accelerators in order to improve both the commissioning procedures and the input parameters of simulations.

CONCLUSION

We reported new experimental results obtained by bombarding a LHC type samples with primary electron beams of different energies. Our data show that scrubbing efficiency depends on the energy of irradiating beams. Further studies, exploring in details the peculiar behaviour of impinging electrons of very low energy (<20 eV) could have significant implications to machine commissioning procedures.

REFERENCES

[1] R. Cimino, I. R. Collins, M. A. Furman, M. Pivi, F. Ruggiero, G. Rumolo, F. Zimmermann, Phys. Rev. Lett. 93 (2004) 014801.

[2] J.M. Jimenez, G. Arduini, P. Collier, G. Ferioli, B. Henrist, N. Hilleret, J-M. Laurent, K. Weiss, F. Zimmermann, LHC Project Report 634, CERN, 2003.

[3] Proceedings of ECLOUD'02, CERN, Geneva, April 15-18, CERN-2002-001, 2002, and references therein.

[4] B. Henrist, N. Hilleret, C. Scheuerlein, M. Taborelli, G. Vorlaufer, LHC P.R. 583 and Proceedings of EPAC 2002.

[5] V. Baglin, J. Bojko, O. Gröbner, B. Henrist, N. Hilleret, C. Scheuerlein, M. Taborelli, in Proceedings of EPAC 2000, Vienna, Austria.

[6] F. Le Pimpec, R.E. Kirby, F. K. King, M. Pivi, Nucl. Instr. And Meth. A 564 (2006) 44-50.

[7] R.E. Kirby, F. K. King, Nucl. Instr. And Meth. A 469(2001) 1-12.

[8] V. Baglin, I. Collins, B. Henrist, N. Hilleret, G. Vorlaufer, LHC Project Report 472, CERN, 2001.

[9] R. Cimino, I. R. Collins, Appl. Surf. Sci. 235 (2004) 231-235.

[10] C. Scheuerlein, M. Taborelli, J. Vac. Sci. Technol. A 20 (1) (2002) 93-101.

[11] C. Scheuerlein, M. Taborelli, N. Hilleret, A. Brown, M. A. Baker, Appl. Surf. Sci. 202 (2002) 57-67.

[12] F. Zimmermann, in Proceedings of Chamonix XI (CERN Report No . CERN-SL-2001-003 DI, 2001).

[13] V. Baglin, I. R. Collins, O. Gröbner, C. Grünhagel, B. Henrist, N. Hilleret, B. Jenninger, Proceedings of the XI workshop on LEP-SPS performance Chamonix, 141, 2001.

A FORMULA FOR THE ELECTRON CLOUD MAP COEFFICIENT IN THE PRESENCE OF A MAGNETIC FIELD

T. Demma, INFN-LNF, Frascati (Italy),
S. Petracca, University of Sannio, Benevento (Italy).

Abstract

The bunch-to-bunch evolution of the electron cloud density can be modeled using a cubic map. The map approach has been proved reliable for RHIC [1] and LHC [2]. The coefficients that parameterize the map may be obtained by fitting from time consuming numerical simulations. In this communication we derive a simple approximate formula for the linear coefficient in the electron cloud density map, along the lines laid in [3], in the presence of a dipole magnetic field, and compare the result to numerical simulations, for the LHC.

INTRODUCTION

The build-up of a quasi-stationary electron cloud through beam induced multipacting processes can be accurately modeled using sophisticated computer simulation codes like PEI , POSINST, and ECLOUD.

In [1] it was shown that the evolution of the electron cloud density from one bunch passage to the next can be described using a cubic map of the form:

$$\rho_{m+1} = a\rho_m + b\rho_m + c\rho_m \tag{1}$$

where ρ is the average electron cloud density between successive bunches, and the coefficients a, b and c can be extrapolated from simulations, and are functions of the beam parameters and of the beam pipe features. Simulations based on the above map are orders of magnitude faster than those based on particle-tracking codes. An analytic expression for the linear coefficient a in (1), valid for weak clouds, has been derived from first principles in [3], for the straight sections of RHIC. In this paper we obtain an analytic expression for a in the presence of a dipole magnetic field, with specific reference to a toy model of LHC.

We assume N_m electrons in the cloud, uniformly distributed across the (transverse) section of the beam pipe, sketched in Fig. 1, at the arrival of bunch m. We compute the average energy gain $\bar{E}_g$ of these electrons assumed initially at rest due to the passage of bunch-m, and the (average) energy-dependent wall-to-wall flight times in the strong magnetic field limit.

Next, following [3], we compute the total number N_{m+1} of electrons in the cloud at the arrival of bunch-$(m+1)$, by tracing appropriately the build up of the high-energy (backscattering) and low-energy (secondary emission) electrons produced by successive collisions at the beam pipe wall. The ratio N_{m+1}/N_m gives the linear coefficient a, and the result is compared to numerical simulations obtained using ECLOUD[4], for the case of an LHC-like dipole.

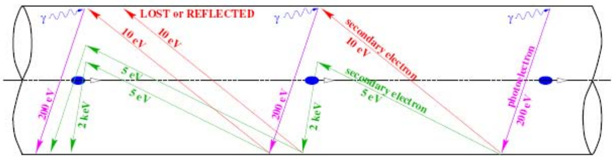

Figure 1: Schematic view of the evolution of an electron cloud between successive bunch passages. Courtesy F. Ruggiero

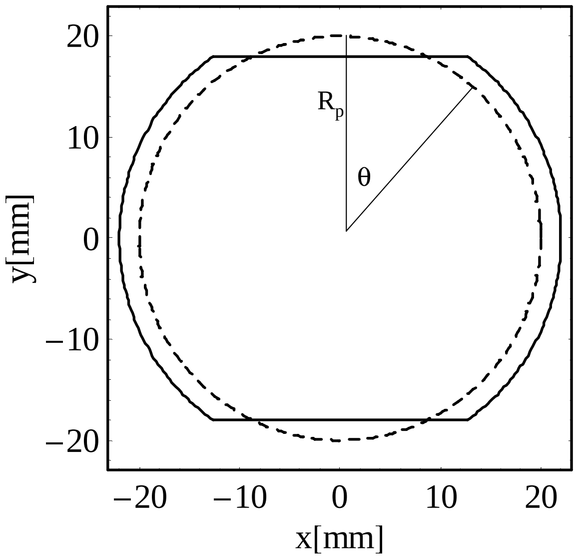

Figure 2: LHC beam pipe cross-section geometry, actual (solid line) and approximate (dashed line).

ELECTRON DYNAMICS

The actual cross section of the LHC beam-screen, is shown in Fig. 2, together with the (approximate) circular one used here. In the limit of a large y-directed magnetic field we may consider only the (transverse) vertical motion of the electrons (the cyclotron radius of the particle elical trajectories is very small compared to the transverse beam-pipe radius R_p). The same approximation is also allowed in electron-cloud simulation codes. The wall-to-wall flight-time for an electron with energy E originating at (R_p, θ) is accordingly

$$t_f(E,\theta) = \frac{2R_p \cos\theta}{\sqrt{2E/m_e}} \tag{2}$$

where m_e is the electron mass, and θ is the polar angle defined in Fig.2.

The energy gained by an electron at (r,θ) after the passage of a bunch can be computed under the kick-approximation [5] as follows:

$$\Delta E(r,\theta) = 2m_e c^2 \frac{N_b^2 r_e^2 \cos^2\theta}{r^2}, \tag{3}$$

where N_b is the number of electrons in each bunch, and r_e is the electron classical radius.

The average energy in a population of electrons uniformly distributed across the (transverse) section of the beam pipe, can be written as:

$$\bar{E}_g = \frac{1}{\pi R_p^2}\int_0^{2\pi}\int_{\sigma_r}^{R_p} \Delta E(r,\theta) r dr d\theta, \tag{4}$$

where we neglect the contribution from electrons trapped inside the beam core, by setting the lower radial integration limit at the effective (transverse) beam radius σ_r.

The secondary emission yield (SEY) includes the contribution of both the *true secondary* electrons, and the *reflected* ones, denoted as $\delta_t(E)$ and $\delta_r(E)$ respectively; *rediffused* electrons are usually neglected.

We shall assume that the *reflected* electrons have exactly the same average energy $\bar{E}_g$ as the incident ones, whereas the true secondary electrons are emitted with an energy $E_s \ll \bar{E}_g$ (typically, $E_s \approx 5eV$ [6]).

The total secondary emission yield and its partial contributions from reflection and true secondary emission [6], [7] are shown in Fig.3.

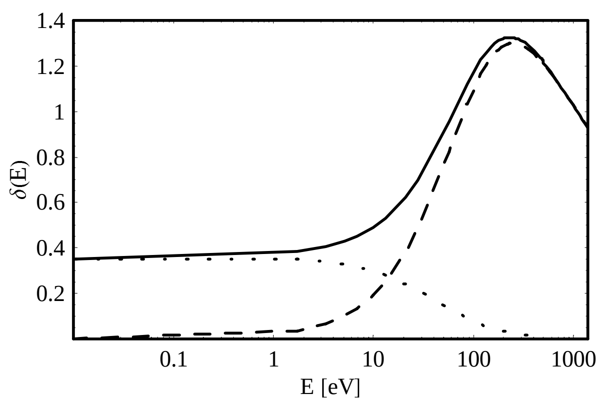

Figure 3: Secondary electron yield as a function of electron energy. The contributions of the secondary (dashed line), and backscattered electrons (dotted line) is also shown.

LINEAR MAP COEFFICIENT

To compute the linear term in (1) we follow Iriso and Peggs [3]. We denote by N_m the number of electrons uniformly distributed across the (transverse) section of the beam pipe just before bunch-m passes. After the passage of bunch-m, these electrons acquire an average energy $\bar{E}_g$. When these electrons hit the chamber wall, $N_m\delta_r$ *reflected* electrons with energy $\bar{E}_g$ emerge, and $N_m\delta_t$ *secondary* electrons, with energy $E_s \ll \bar{E}_g$ are created. Before the arrival of bunch-$(m+1)$, the reflected electrons travel across the beam pipe and undergo an average number n of collisions with the chamber wall given by:

$$n = \left\lfloor \frac{t_{bb}}{\bar{t}_f} \right\rfloor - 1, \tag{5}$$

where t_{bb} is the time interval between successive bunches, and

$$\bar{t}_f(E) = \frac{4R_p}{\pi\sqrt{2E/m_e}} \tag{6}$$

is the angular average of $t_f(E,\theta)$.

The total number of reflected electrons with energy $\bar{E}_g$ at the passage of bunch-$(m+1)$ will be accordingly:

$$N_{m+1}^{(ref)} = N_m \delta_r^n(\bar{E}_g). \tag{7}$$

The secondary electrons originated upon each collision at the chamber wall, on the other hand, upon further collisions with the chamber wall, will produce *secondary* as well as *reflected* electrons all having the *same* low energy E_s.

The total number of secondary (low-energy) electrons at the passage of bunch-$(m+1)$ will be accordingly given by

$$N_{m+1}^{(sec)} = N_m \delta_t(\bar{E}_g) \sum_{p=1}^{n} \delta_r^{p-1}(\bar{E}_g)\delta_s^{k_p}(E_s), \tag{8}$$

where $\delta_s = \delta_r + \delta_t$ and

$$k_p = \left\lfloor \frac{t_{bb} - p\bar{t}_f(\bar{E}_g)}{\bar{t}_f(E_s)} \right\rfloor, \tag{9}$$

is the number of collisions undergone by the low-energy electrons originated after p wall-collisions of the high-energy population.

The *total* number of electrons at the passage of bunch-$(m+1)$ will be the sum of (7) and (8), viz.:

$$N_{m+1} = N_m \left(\delta_r^n(\bar{E}_g) + \delta_t(\bar{E}_g) \sum_{p=1}^{n} \delta_r^{p-1}(\bar{E}_g)\delta_s^{k_p}(E_s) \right), \tag{10}$$

whereby the coefficient of the linear term in the map (1) can be written in closed form as follows:

$$a = \frac{N_{m+1}}{N_m} = \delta_r^n(\bar{E}_g) + \delta_t(\bar{E}_g)\delta_s^{\eta}(E_s) \cdot \\ \cdot \frac{\delta_s^{n\eta}(E_s) - \delta_r^n(\bar{E}_g)}{\delta_s^{\eta}(E_s) - \delta_r(\bar{E}_g)}, \tag{11}$$

where $\eta = \bar{t}_f(\bar{E}_g)/\bar{t}_f(E_s) = (E_s/E_g)^{1/2} \ll 1$. In fig. 4 the coefficient a is displayed as a function of the bunch spacing t_{bb} for different values of the maximum total SEY δ_{max}, using the machine parameters listed in Table I. For this same set of parameters, equation (11) is compared to ECLOUD based simulations in fig. 5.

Table 1: Parameters used for ECLOUD simulations.

parameter	units	value
beam particle energy	GeV	7000
bunch spacing	m	7.48
bunch length	m	0.075
number of bunches N_b	-	72
no. of particles per bunch	$N/10^{10}$	8 to 14
bending field B	T	8.4
length of bending magnet	m	1
vacuum screen half height	m	0.018
vacuum screen half width	m	0.022
circumference	m	27000
primary photo-emission yield	-	$7.98 \cdot 10^{-4}$
maximum SEY δ_{max}	-	1.3 to 1.7
energy for max. SEY E_{max}	eV	237.125
energy width for secondary e^-	eV	1.8
energy of secondary e^- E_s	eV	5

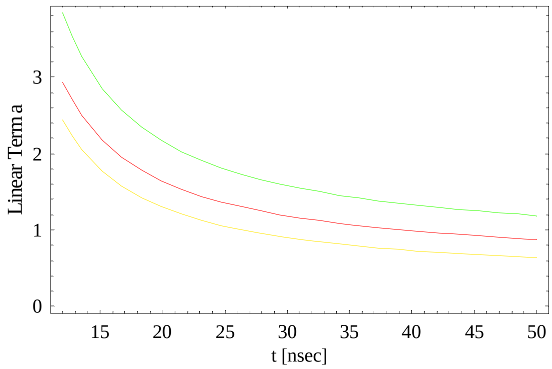

Figure 4: Approximate linear map coefficient a as a function of bunch spacing, for $\delta_{max} = 1.3$ (yellow), $\delta_{max} = 1.5$, (red) $\delta_{max} = 1.7$ (green).

CONCLUSIONS

An approximate formula has been derived for the linear coefficient in the map (1) describing the bunch-to-bunch evolution of the electron cloud density with a dipole magnetic field. The results are in acceptable agreement with numerical simulations obtained from ECLOUD, for an LHC-like dipole. Quick and dirty estimates of the safe regions in the machine parameter space where electron cloud. A more complicated (and more accurate) result is obtained by tracing separately electrons originating at different θ's, and averaging the final θ-dependent linear coefficient. This more general case will be discussed elsewhere.

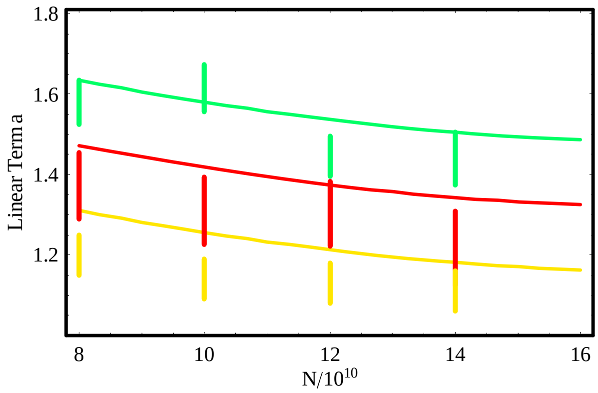

Figure 5: Comparison of the linear map coefficient a derived using ECLOUD simulations (bars) and using the analytic calculation (lines with the same color), as a function of the bunch population N for $\delta_{max} = 1.3$ (yellow), $\delta_{max} = 1.5$, (red) $\delta_{max} = 1.7$ (green).

REFERENCES

[1] U.Iriso and S.Peggs, "Maps for Electron Clouds", Phys. Rev. ST-AB 8, 024403, 2005.

[2] T.Demma et al., "Maps for Electron Clouds: Application To LHC", Phys. Rev. ST-AB 10, 114401 (2007).

[3] U. Iriso and S. Pegg. Proc. of EPAC06, pp. 357-359.

[4] http://wwwslap.cern.ch/electron-cloud/Programs/Ecloud/ecloud.html.

[5] J. Scott Berg, "Energy gain in an electron cloud during the passage of a bunch", LHC Project Note 97, CERN, Geneva (CH), 1997.

[6] D. Schulte et al., "Electron cloud measurements in the SPS in 2004", PAC-2005-FPAP014, 2005.

[7] R. Cimino et al., "Can low energy electrons affect high energy physics accelerators?", Phys. Rev. Lett. 93, 014801, 2004.

ELECTRON CLOUD SIMULATIONS FOR DAΦNE*

T. Demma, R. Cimino, S. Guiducci, C. Vaccarezza, and M. Zobov
INFN-LNF, Frascati, Italy

Abstract

After the first experimental observations compatible with the presence of the electron cloud effect in the DAΦNE positron ring, a systematic study has been performed regarding the electron cloud build-up. To assess the effects of the electron cloud, simulations of the cloud build up were carried out using ECLOUD [1]. The obtained numerical results are compared with experimental observations.

INTRODUCTION

After the 2003 shutdown for the FINUDA detector installation, and some optics and hardware modifications, the appearance of a strong horizontal instability for the positron beam at a current $I \approx 500mA$, triggered the study of the e-cloud effect in the DAΦNE collider. Experimental observation that seems to provide an evidence that the electron cloud effects are present in the DAΦNE positron ring can be summarized as follow: a larger positive tune shift is induced by the positron beam current [2]; the horizontal instability rise time cannot be explained only by the beam interaction with parasitic HOM or resistive walls and increase with bunch current [3]; the anomalous vacuum pressure rise with beam current in positron ring [4], bunch-by-bunch tune shifts measured along the DAΦNE bunch train present the characteristic shape of the electron cloud build-up [5]. There are also indications that wigglers play an important role in the instability, since the main changes after the 2003 shutdown were the modification of the wiggler poles, and lattice variation which gave rise to an increase of the horizontal beta functions in wigglers [6]. To better understand the electron cloud effects and possibly to find a remedy, a detailed simulation study is undergoing. In this communication we present recent simulation results relative to the build up of the electron cloud in the DAΦNE wiggler and in straight sections in presence of a solenoid magnetic field. When possible simulation results are compared to experimental observation. Conlusions follow in the last section.

BUILD UP IN THE WIGGLER

The wiggler magnetic field characterization was performed measuring the vertical magnetic field component B_y, over a rectangular point matrix on the x-z plane [7].

* This work is partly supported by the Commission of the European Communities under the 6^{th} Framework Programme "Structuring the European Research Area", contract number RIDS-011899.

Table 1: DAΦNE beam and pipe parameters used as input for ECLOUD simulations.

parameter	unit	value
bunch population N_b	10^{10}	2.1
number of bunches N	–	100
missing bunches N_{gap}	–	20
bunch spacing L_{sep}	m	0.8
bunch length σ_z	mm	18
bunch horiz. size σ_x	mm	1.4
bunch vert. size σ_y	mm	0.05
wiggler chamber horiz. aperture $2h_x$	mm	120
wiggler chamber vert. aperture $2h_y$	mm	20
straight sections radius	mm	44
primary photo-emission yield $d\lambda/ds$	–	0.0088
photon reflectivity	–	50%
maximum SEY δ_{max}	–	1.9
energy for max. SEY E_{max}	eV	250

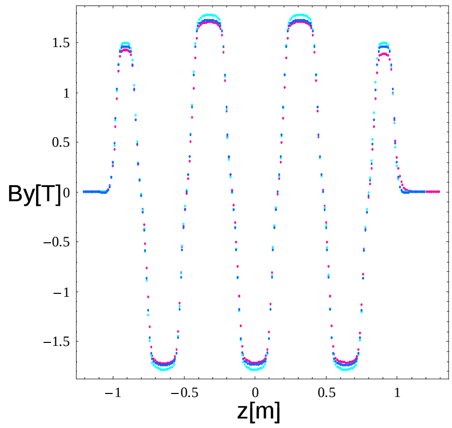

Figure 1: Vertical component of the magnetic field along the longitudinal axis for the old (blue), current (red), and recently proposed (cyan) wiggler.

Starting form these values a spline fit was performed, and the obtained coefficients were used for the field reconstruction as showed in [4]. This method has been applied to build three models of the wiggler field, the first corresponding to the wiggler before the pole modification in 2003, the second corresponding to the field after the pole modification (currently installed at DAΦNE), and the third corresponding to a further modification of the wiggler recently proposed to improve field quality and reduce nonlinearities [8]. In Figure 1 the field reconstruction results are reported

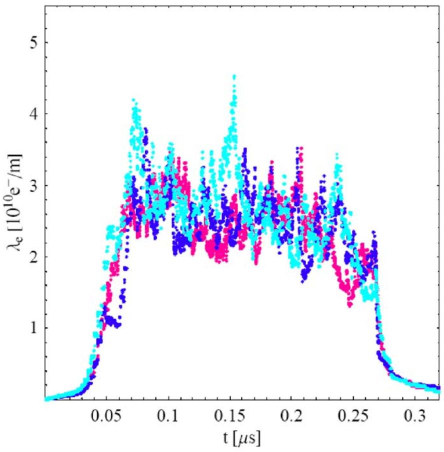

Figure 2: Electron cloud build up along a DAΦNE bunch train for the old (blue), current (red), and recently proposed (cyan) wiggler.

for the three different models. Using these models of the DAΦNE wiggler field, the electron build-up was simulated. The input parameters for ECLOUD are collected in Table 1. The reflectivity and photo-emission yield values have been obtained by measurements performed on Al samples with the same finishing of the actual vacuum chamber [9]. The secondary emission yield (SEY) curve model used is the one described in [10] scaled to an elastic reflection probability at zero electron energy of 0.5 [11], and with a maximum value $\delta_{max} = 1.9$ as were found for technical Al surfaces after electron conditioning [12]. It has to be noted that the presence of the slots has been taken into account considering only the photon flux that is not intercepted by the antechamber ($\approx 5\%$). With this prescription part of the electrons are emitted at the position of the antechamber slots. However, since in a dipole magnetic field these electrons contribute little to the multipacting and the electron build up, this approximation does not introduce any noticeable error. In Figure 2 the electron cloud linear density evolution is reported for the three wiggler magnetic field models discussed above, showing a negligible dependence of the build up on the magnetic field model. A very preliminary comparison with observations has been performed considering the horizontal instability growth rate dependence on the bunch spacing obtained by grow-damp measurement [3]. In particular, the values of bunch spacing L_{sep} and bunch population N_b corresponding to a growth rate $1/\tau \approx 8ms^{-1}$ has been extrapolated from recorded data, shown in Figure 3, and used as input for the simulation code. The resulting build up evolutions are shown in figure 4. The electron line densities corresponding to spacing by L_{sep} , $2L_{sep}$, and $3L_{sep}$ are comparable at the end of the train, while density corresponding to $4L_{sep}$ is about 3 times lower. This behaviour is in qualitative agreement with observations [3]. However, a deeper understanding of the instability mechanism would be gained comparing simulated single and multi-bunch growth rate with experimental data. Work in this direction is in progress.

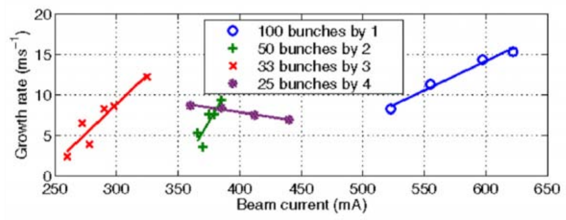

Figure 3: Horizontal growth rate for different bunch spacing and beam current recorded at DAΦNE on July 22, 2004 [3] (courtesy A.Drago).

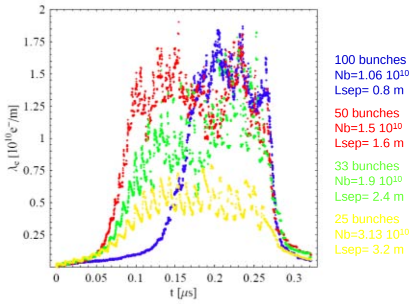

Figure 4: Electron cloud evolution along a bunch train for the measured values of L_{sep} and N_b corresponding to $1/\tau \approx 8ms^{-1}$.

BUILD UP IN SOLENOIDAL FIELD

At the startup after the recent shutdown for the setup of the crab waist collision scheme [13] the instability threshold dropped to $I \approx 270mA$ for the positron current, with the vertical feedback switched off. In the attempt to find a remedy solenoids were installed in the field free regions of DAΦNE, leading to an increase of the threshold to $I \approx 400mA$. Simulations followed to better understand this mechanism. Here we focus our attention on the electrons accumulated through the secondary emission from the beam pipe in the straight sections. In the simulation, we generate a large number of electrons only at the first bunch passage and let electron cloud develops by the secondary emission process. The electron cloud density build up along the train is shown in Figure 5, for different values of the solenoidal field B_z. Without solenoids (black curve in Figure 5) the average density grows along the train and saturates due to the balance between the space charge and secondary yield. For $Bs > 20G$ electron density decrease very quickly after the passage of the first bunch. A resonance is expected when the time between two consecutive collisions of the electrons in the cloud with the beam pipe surface, that is about half of the electrons cyclotron period T_c, is equal to the time interval between two bunch passage. For the DAΦNE parameters, this condition reads to

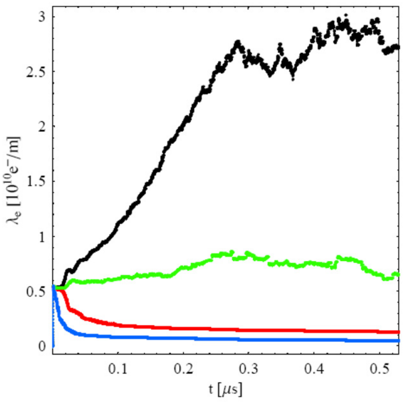

Figure 5: Density of electron cloud as a function of time for different solenoid settings: $B_z = 0G$ (black), $B_z = 20G$ (green), $B_z = 40G$ (red), $B_z = 60G$ (blue).

the following resonance condition for the magnetic field:

$$B_z^c = \frac{\pi m_e c^2}{eL_{sep}} \approx 66G. \qquad (1)$$

However there is a threshold value of bunch population, related to the energy gain of the electrons in the cloud during the passage of a bunch and independent of the bunch spacing [14], above which the resonance takes place. As shown in Figure 6, simulations for DAΦNE exhibit a threshold $N_b^c \approx 5 \cdot 10^{10}$ for both single and double bunch spacing that is above the currently operated current. The effectiveness

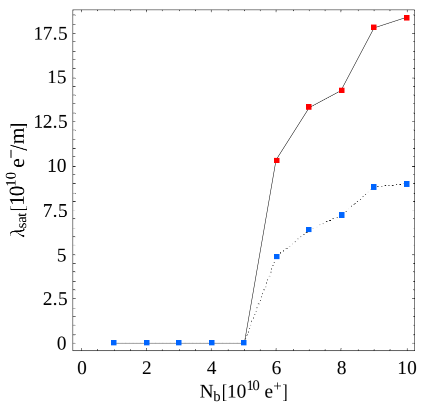

Figure 6: Saturated density as a function of the bunch population. Red dots represent the case of L_{sep} spacing and 66G field. Blue dots represent $2L_{sep}$ spacing and 33G field.

of solenoids in reducing the electron cloud density has also been checked by monitoring the vacuum behaviour for the positron beam. The vacuum pressure read-out is reported in Figure 7 for the solenoid ON-OFF cases as recorded by a vacuum gauge located in a region of the positron ring where solenois are installed. The pressure reduction in the region with solenoids is clear.

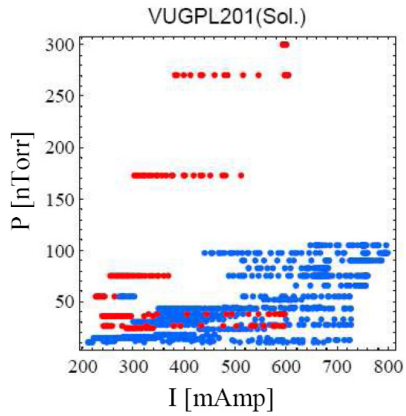

Figure 7: vacuum pressure read-out vs. total current as recorded in a straight section of the positron ring where a 40 G solenoidal field was turned on (blue dots) and off (red dots).

CONCLUSIONS

Simulations for the DAΦNE wiggler show a negligible dependence of the build up on the magnetic field model, and a build-up variation with bunch filling pattern that is compatible with experimental observations. Simulations for the build up in solenoidal field show that a small field is effective in reducing the electron cloud density in straight section, and that the threshold for the cyclotron resonance is above the bunch population currently available in DAΦNE. Also in this case there is a qualitative agreement with observations.

REFERENCES

[1] http://wwwslap.cern.ch/electron-cloud/Programs/ECLOUD /ecloud.html.

[2] C. Vaccarezza, et al, ECLOUD04, Napa Valley proc.

[3] A.Drago et al., Proceedings of PAC05, p.1841.

[4] C.Vaccerezza et al., Proceedings of PAC05, p.779.

[5] A.Drago, proc. of the 40th ICFA Beam Dynamics Workshop on High Luminosity e+e- Factories.

[6] A.Drago et al., DAΦNE Tech. Notes, G-67.

[7] M. Preger, DAΦNE Tech. Notes, L-34.

[8] S.Bettoni et al., Proceedings of PAC07, p. 1463.

[9] N.Mahne et al., Proceedings of PAC05, p.817.

[10] R. Cimino et al., PRL93, 014801, 2004;

[11] D.Schulte et al., PAC-2005-FPAP014, 2005.

[12] F. Le Pimpec et al., SLAC-PUB-10894 (2004).

[13] C.Milardi et al.,WEPP036, these proceedings.

[14] Y.Cai et al., Phys. Rev. ST-AB 7, 024402 (2004).

COUPLING IMPEDANCE OF DAΦNE UPGRADED VACUUM CHAMBER

F. Marcellini, D. Alesini, P. Raimondi, G. Sensolini, B. Spataro, A. Stella, S. Tomassini and M. Zobov,
INFN Laboratori Nazionali di Frascati, Frascati, Italy

Abstract

The DAΦNE Φ-factory at INFN LNF has been upgraded in the second half of 2007 with a scope to test a recently proposed scheme of crab waist collisions. The vacuum chamber of the collider has been substantially modified: two new low impedance interaction regions have been designed and installed, the new stripline injection kickers have been implemented, the old bellows have been substituted by the new ones and almost all ion clearing electrodes removed. In the paper we discuss the low impedance design of these new vacuum chamber components and compare bunch lengthening measurements in the modified DAΦNE with simulation results.

INTRODUCTION

DAΦNE is an electron-positron collider working at the c.m. energy of the Φ resonance (1.02 GeV) to produce a high rate of K mesons [1]. The collider complex consists of two independent rings having two common Interaction Regions (IR) and an injection system composed of a full energy linear accelerator, a damping/accumulator ring and transfer lines. Fig. 1 shows a view of the DAΦNE accelerator complex while some of the main collider parameters are listed in Table 1.

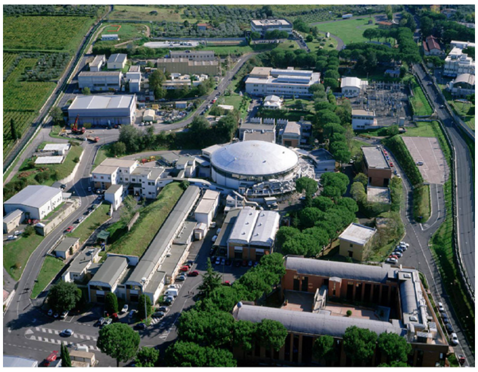

Figure 1: View of DAΦNE accelerator complex.

Since 2000 DAΦNE has been delivering luminosity to three experiments, KLOE [2], FINUDA [3] and DEAR [4]. The KLOE experimental detector surrounded by a superconducting solenoid has been used for a wide variety of physics measurements with emphasis on the kaon decays, and most notably on the issue of CP violation. The second magnetic detector FINUDA is devoted to the study of hypernuclei physics. The small non-magnetic experiment DEAR has been used for the study of the properties of kaonic atoms.

In 2007 DAΦNE was shut down for the SIDDHARTA experiment installation [5] and for relevant collider modifications aimed at testing the novel idea of crab waist collisions [6, 7, 8]. DAΦNE operations with the crab waist scheme started in the very end of 2007 and the first results of the new scheme implementation are reported in [9] at this Conference.

The DAΦNE upgrade required a new magnetic and mechanical layout [10] [11] to exploit “Large Piwinski Angle” and “Crab Waist” concepts. As a result, the collider vacuum chamber has been substantially modified. Relying on our long-term experience in coupling impedance calculations and measurements, all the new vacuum chamber components have been carefully designed and optimized in order to reduce both the broad band and narrow band impedances.

In the first part of this paper we overview designs of the principal new vacuum chamber elements and describe the design solutions aimed at the coupling impedance minimization. In the second part we report the results of bunch lengthening measurements in the DAΦNE upgraded rings that clearly prove the vacuum chamber beam impedance reduction.

Table 1: DAΦNE main parameters (KLOE run)

Energy [GeV]	0.51
Trajectory length [m]	97.69
RF frequency [MHz]	368.26
Harmonic number	120
Damping time, τ_E/τ_x [ms]	17.8/36.0

NEW VACUUM CHAMBER COMPONENTS

The New Interaction Region

The beam pipe is composed essentially by straight tubes without sharp discontinuities, except for the Y-shape section, where the common IR chamber is split in the two separate rings (see Fig.2).

Figure 2: The new IR vacuum chamber layout (half).

HOMs could be trapped in the Y-section and, if the beam interacts with them, problems related to power losses may arise, as confirmed by HFSS simulations. The diameter and the shape of the single pieces of pipes have been designed in order to reduce as much as possible the total number of HOMs, and to keep the frequencies of the residual ones far enough from the beam power spectrum lines. From simulation results [12], this distance is always more than 200 MHz and even if full coupling should occur, the power losses would be less than 200W. Despite such a power seems to be manageable, two cooling channels have been placed at each Y-chamber junction.

The New Injection Kicker

New injection kicker has been realized to have the possibility of using fast high voltage pulsers which minimize the perturbation of the stored bunches. The design of the new kicker [13] is based on a couple of tapered strips in a vacuum chamber with rectangular cross section (see Fig. 3).

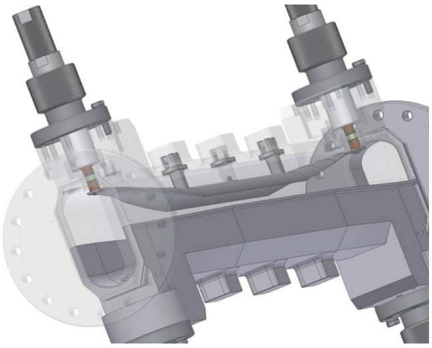

Figure 3: Drawing of the new injection kicker

The stripline tapering allows to reduce the broadband beam impedance of the device and to obtain a better matching of the transition to the external coaxial lines, hence a better damping of possible HOMs. Moreover the cross section of the kicker chamber is now the same of the adjacent beam pipe in the dipole regions and this also contributes to reduce the total beam coupling impedance of the machine. In Fig.4, the longitudinal coupling impedance of the structure has been evaluated with HFSS applying the principle of the wire method.

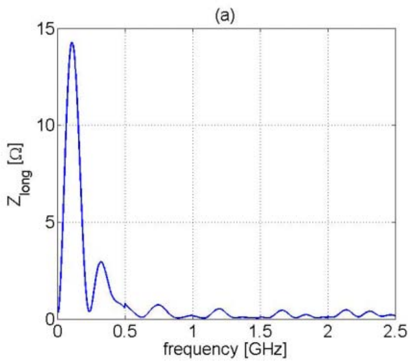

Figure 4: Kicker coupling impedance calculated by HFSS.

The New Shielded Bellows

The new bellows [14] connect pipes having circular cross section with 88mm diameter. The inner radius of bellows convolutions is about 65mm, the outer one 80mm and the length about 50mm. Then a RF shield is necessary to hidden the chamber discontinuity to the beam. The shield has been designed as shown in Fig. 5. Two cylindrical shells made of aluminium are fixed at the bellows ends and assure continuity to the beam pipes except for the gap between them. But even this gap is shielded by a number of adjacent Be-Cu strips placed all around the Al shells. The shape of the strips is preformed as a Ω that gives elasticity to the system.

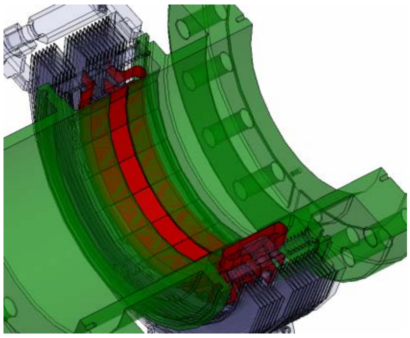

Figure 5: Drawing of the shielded bellows.

The structure has been simulated with HFSS in a frequency range from DC to 6 GHz and no HOMs have been found. The beam coupling impedance has been calculated as well and the result is plotted in Fig.6.

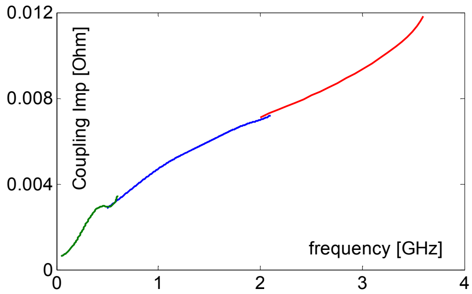

Figure 6: Beam coupling impedance obtained by HFSS.

BUNCH LENGTHENING

The broad-band coupling impedance of the DAΦNE original vacuum chamber is well-known for both the positron [15] and electron rings [16]. Numerical simulations based on the numerically computed wake fields reproduce well the measured bunch length and charge distribution in lattices with negative and positive momentum compaction factors.

In Fig.7 one can see the bunch length as a function of bunch currents and bunch charge distribution measured by Hamamatsu C5680 streak camera in the DAΦNE electron ring.

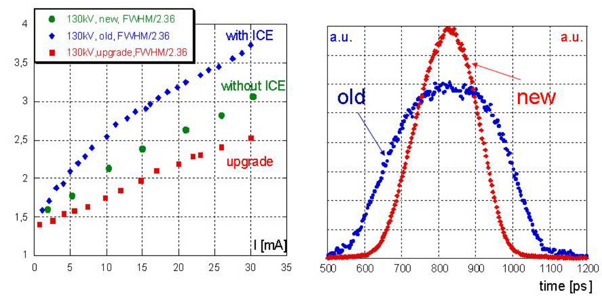

Figure 7: Bunch length as a function of bunch current (left) and bunch charge distribution (right) in the electron ring.

The blue curve corresponds to the bunch length measured in the DAΦNE original vacuum chamber. The first notable impedance reduction of the electron ring has been already obtained after the long ion clearing electrode removal from the collider wiggler sections [17]. Besides the evident bunch lengthening reduction (see the green curve in Fig.7), it has helped to eliminate other two harmful impedance related effects: the single bunch quadrupole instability and single bunch vertical size blow up. This has resulted in about 50% specific luminosity increase during the last run for the FINUDA experiments [18].

The vacuum chamber modifications for the crab waist experiment have brought another big factor in the coupling impedance reduction. As one can see in Fig. 7 by comparing the green and red curves, now bunches in the electron ring are by about 20% shorter with respect to the previous FINUDA run. As it is also shown in Fig. 7 the bunch charge distribution has cardinally changed. In the original vacuum chamber the longitudinal bunch profile had the typical parabolic shape due to bunch interaction with the inductive chamber impedance (the blue curve on the right plot taken at 30 mA per bunch). After the modifications, the distribution is close to a gaussian one with some small asymmetry due to the resistive part of the coupling impedance (the red curve on the right plot).

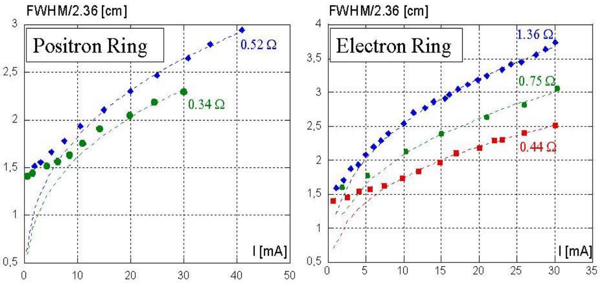

Figure 8. Bunch lengthening positron (left) and electron rings (right)

Looking at the left plot of Fig. 8 we see that also positron bunches are shorter after the vacuum chamber upgrade even though the effect of the bunch length reduction is slightly smaller than that in the electron ring. This is due to the fact that in addition to the similar vacuum chamber modifications made in both rings also the most part of ion clearing electrodes have been removed from the electron ring. At present bunch lengths in both rings are very similar. Some very small observable difference is explained by the presence of few ion clearing electrodes still remaining in the e^- ring.

In order to obtain a quick but rather rough estimate of the impedance improvements after the modifications we can use the following scaling property above the microwave instability threshold valid in the assumption of the purely inductive impedance [19]:

$$\left(\frac{\sigma_z}{R}\right) \approx \left(\frac{2}{\pi}\right)^{1/6} \xi^{1/3} \left(\frac{Z}{n}\right)^{1/3} \quad with \quad \xi = \frac{2\pi I}{h e V_{RF} \cos\varphi_S} \quad (*)$$

with R the ring radius, I the bunch current; h the harmonic number; V_{RF} the RF voltage; Z/n the normalized longitudinal impedance, ϕ_S the synchronous phase.

Assuming that bunches have a gaussian shape, i.e. rms bunch length σ_z is equal FWHM/2.355, we have fit the measured bunch length data (see Fig. 8) with the expression (*). According to this rough estimate the longitudinal coupling impedance of the positron ring has been decreased by about 50% while the reduction of the electron ring impedance is as high as 70%.

Fortunately, the semi-qualitative estimate is confirmed by numerical simulations of the bunch lengthening. By simply scaling the known wake potential used for bunch lenghtening simulations in the original DAΦNE vacuum chamber [15] and performing numerical tracking have given a satisfactory agreement between the measurement data and simulation results, as seen in Fig.9.

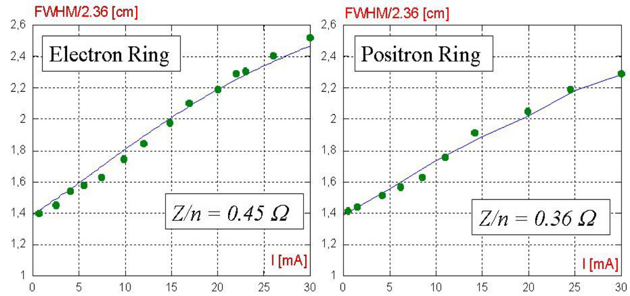

Figure 9. Bunch length in electron and positron rings (dots – measurement data, solid line – tracking results)

CONCLUSIONS

Careful designing of the new vacuum chamber components, required for DAΦNE modifications aimed at testing the crab waist collision scheme, has allowed reducing the coupling impedance of the positron ring by about 50% and that of the electron ring by approximately 70%.

REFERENCES

[1] G.Vignola et al., Frascati Phys.Ser.4:19-30,1996; C.Milardi et al., Frascati Phys.Ser.16:75-84,1999; M.Zobov et al., arXiv:0709.3696.
[2] KLOE Coll., Nucl.Instrum.Meth. A482:363-385,2002.
[3] FINUDA Coll., Proc. HYP2000 (Torino, 2000).
[4] DEAR Coll., Phys.Lett. B535:52-58,2002.
[5] SIDDHARTA Coll., Eur.Phys.J. A31:537-539,2007.
[6] P.Raimondi, 2nd SuperB Workshop, Frascati, 2006.
[7] P.Raimondi, D.Shatilov, M.Zobov, physics/0702033.
[8] M.Zobov et al., arXiv:0802.2667.
[9] C.Milardi et al., this Conference.
[10] S.Tomassini et al., PAC07, pp. 1466-1468.
[11] C.Milardi et al., arXiv:0803.1450.
[12] F.Marcellini, PAC07, pp. 3988-3990, 2007.
[13] D.Alesini et al., DAΦNE Note I-17, 2006.
[14] S.Tomassini et al., TUPP074, this conference.
[15] M.Zobov et al., physics/0312072.
[16] B.Spataro, M.Zobov, DAΦNE Note G-64, 2005.
[17] M.Zobov et al., JINST 2:08002, 2007.
[18] C.Milardi et al., PAC07, pp.1457-1459, 2007.
[19] A.W.Chao, J.Gareyte, Part.Accel.25:229, 1990.

A NEW RF SHIELDED BELLOWS FOR DAΦNE UPGRADE

S. Tomassini#, F. Marcellini, P. Raimondi, G. Sensolini, INFN-LNF, Frascati, Italy.

Abstract

A new Radio Frequency (RF) shielded bellows, using the technology of omega shaped strip of beryllium copper material, has been developed and tested on DAΦNE UPGRADE [1] [6] [7]. The RF omega shield is composed of many Be-Cu strips held by an external floating ring. Thermal power loss on strips can be easily extracted and dissipated allowing high beam current operation. Leakage of beam induced electromagnetic fields through the RF shield is almost suppressed. Twenty omega bellows were manufactured and installed in the DAΦNE storage rings and showed good performances up to 1.9A stored current.

MECHANICAL STRUCTURE

The new shielded bellows designed for the DAΦNE upgrade [2] has a circular cross section with a bore of 88 mm. The inner diameter of bellows convolutions is about 130 mm, the outer one is 160 mm while the length is about 50 mm. An RF shielding has been used to avoid the chamber discontinuity seen by the beam as shown in Fig. 1.

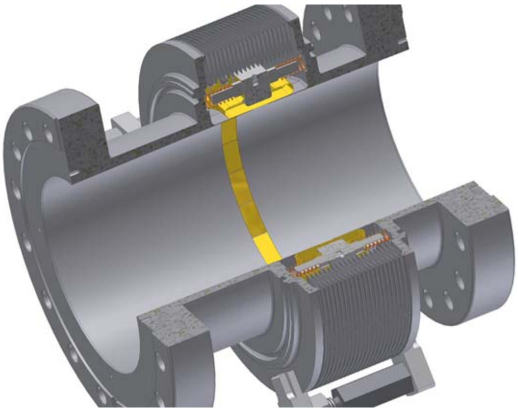

Figure 1: Section view of the RF shielded bellows (not cooled).

The shield is composed of 20 omega shaped Be-Cu alloy 25 strips of 0.15 mm thickness. The 20 formed strips are gold-coated with a thickness of 10μm and bolted on a thick aluminium annular ring. Two cylindrical AISI304 pipes are welded at the bellows ends and give continuity to the beam pipes except for the gap between them. The shape of the strips is preformed like an **Ω**. The aluminium ring supporting all the 20 omega strips is floating and centered on the gap by eight Be-Cu springs. The advantages of the RF-shield are the following:

(1) The RF shield has a high thermal strength due to the high thermal capacity of the annular supporting ring and cooling possibility shown in the next paragraph.

(2) There is a very small radial step (0.5 mm) on the inner surface of the beam duct.

(3) The RF shield can fit beam ducts with various cross sections.

(4) The axial stroke of the RF shield is structurally limited at ±7 mm.

(5) The maximum offset of the bellows is ±3 mm limited by strip detachment and bending angle is more than 50 mrad.

Table 1 summarizes the main parameters of the RF shielded bellows with shielding strips made of Be-Cu [3]. Fig. 1 shows an overall assembly view of the no cooled bellows. There are no specific devices to dissipate thermal power loss. In Fig. 2 there is a detailed view of the shielding and the centering system that pushes the sliding shielding always on the middle of the gap independently from the position or angle or radial offset of the external flanges.

Table 1: RF shielded bellows main parameters

	Be-Cu Strip
Axial Stroke	±7 mm
Radial Offset	±3 mm
Bend angle	50 mrad
Be-Cu strip thickness	0.15 mm
Minimum strip contact pressure	0.1 MPa

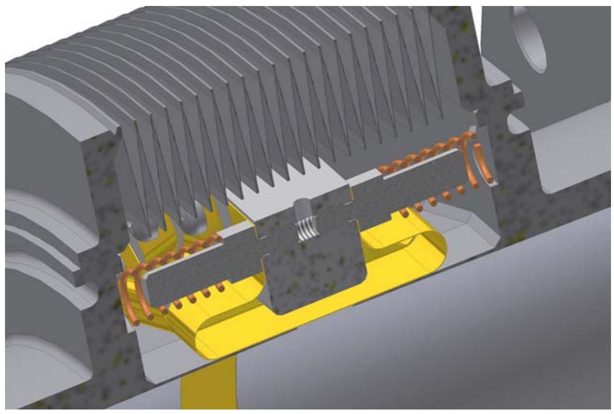

Figure 2: Detailed view of the RF shielding and centering system.

#Sandro.Tomassini@lnf.infn.it

Ω Strip Design

In order to obtain the maximum axial stroke and radial offset listed in table 1, a detailed study of the strips shape has been done. By means of finite element analysis the contact problem between the strip and the beam pipe was investigated. The optimization of the unloaded shape of the strip was performed in order to have the maximum contact pressure at the maximum radial offset and bending angle. After forming, the strip side facing the beam is planar and straight (see Fig. 3 (a)). Once the strip is bolted on the supporting annular ring it gets the required Ω shape like represented in Fig. 3 (b). In Fig. 3 (c) shows the assembling stage before bellows welding.

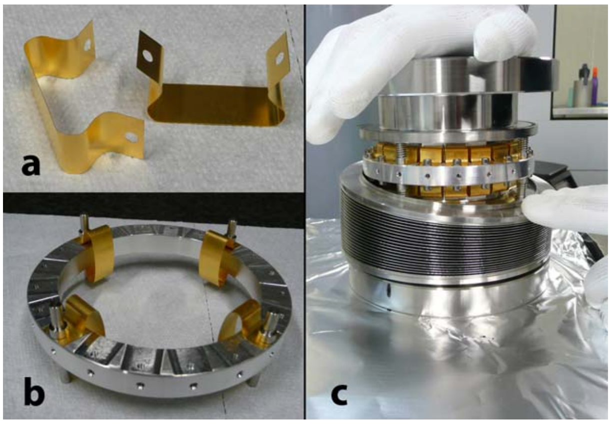

Figure 3: View of gold coated strip (a), supporting annular ring (b), RF shielded bellows assembly (c).

Ω Cooled Strips Shield

As shown in the next paragraph, the power dissipated on each strip is negligible in the case of DAΦNE and so no cooling is required. However for high energy accelerators, where the power loss on the strips is higher, a cooling system on the supporting annular ring is foreseen. The uncooled shielded bellows was modified as shown in Fig. 4. The bellows convolutions were split in two halves and an external cooling serpentine was set around the annular supporting ring. The mechanical performances are the same of the uncooled one while the thermal behaviour was improved.

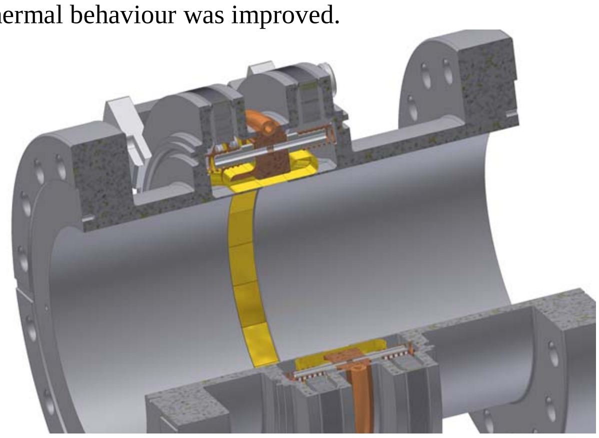

Figure 4: Pictorial view of the RF shielded cooled bellows.

A detailed view of the cooled shielding is shown in Fig. 5. The external serpentine is brazed on the outer skin of the supporting annular ring and it is TIG welded to the two lateral AISI304 flanges.

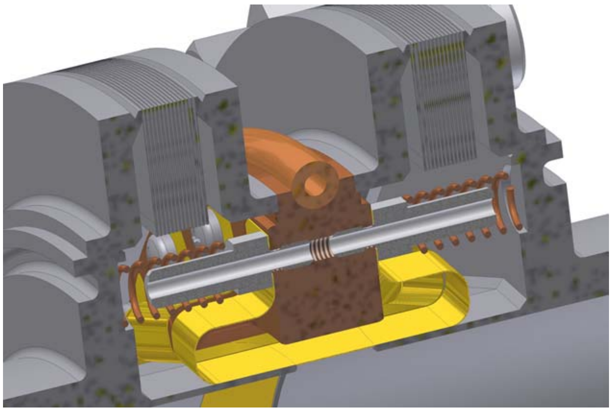

Figure 5: Detailed view of the RF cooled shielding.

BEAM IMPEDANCE AND POWER LOSS

The effects of the electromagnetic interaction between the bellows and the beam have been studied with the HFSS code [4] [5]. The geometry used in the simulations is a thin slice of the bellows (9 degrees since the shield is composed of 20 strips) with a conductor placed along the axis of the structure. Adopting the same principle of the wire method for impedance measurements, the current flowing through the central conductor simulates the beam current. The distribution of the fields generated at 1 GHz by the beam in the bellows is shown in Fig. 6. The scale of the representation is logarithmic and the plot shows that the intensity of the fields in the volume outside the shielding is very weak .The simulations have covered the frequency range from DC to 6 GHz: no HOMs have been found and even at the highest frequency the shields come out to work properly reducing the field intensity by several orders of magnitude.

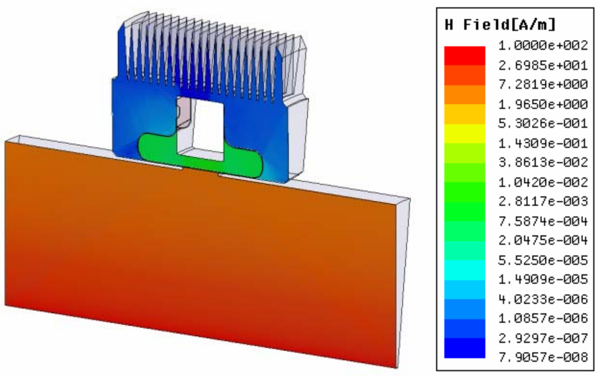

Figure 6: H field excited by the beam in the shielded bellows.

been obtained (see Fig. 2) consistent with the value measured at the Synchrotron Light Monitor.

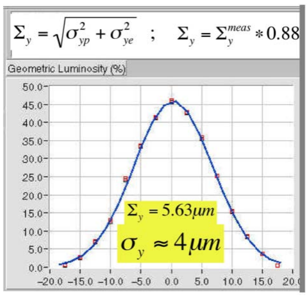

Figure 2: Vertical beam-beam luminosity scan.

A simple test of the new collision scheme consists in switching off the Crab-Waist sextupoles of one beam in collision. As a consequence the growth of both horizontal and vertical transverse sizes can be observed together with a luminosity reduction recorded by all the monitors. Such a behaviour is compatible with the appearance of beam-beam resonances when the CW sextupoles are off.

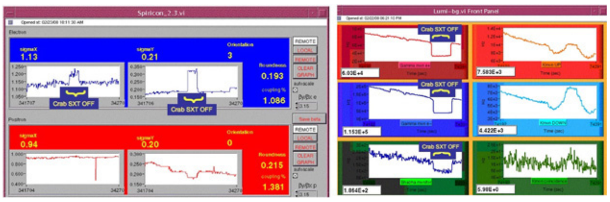

Figure 3: Transverse size (left) and luminosity dependence (right) on the CW sextupole excitation in the e^- ring.

The geometric luminosity, defined as the luminosity divided by the product of the total currents in the two beams (taking into account also the number of colliding bunches), exceeds by 3÷4 times the best value measured during the past DAΦNE runs, and the beam-beam tune shift exhibits a fairly linear behaviour as a function of current per bunch in the opposite colliding beam.

Collisions involving 10 bunches per beam have been studied both in the low and high current regimes. Such a situation avoids the effects due to the multi-bunch longitudinal beam dynamics. The maximum measured luminosity is consistent with the numerical simulations of the Crab-Waist collision scheme with the present low-β parameters.

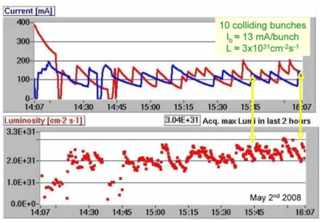

Figure 4: 10 bunches luminosity run.

LUMINOSITY RESULTS

The most relevant results of the commissioning concern the luminosity. So far the maximum measured peak luminosity is in excess of $L_{peak} = 2.2\ 10^{32}\ cm^{-2}s^{-1}$, the best daily integrated luminosity is $L_{\int day} \sim 8\ pb^{-1}$ and the highest integrated luminosity in one hour is $L_{\int 1hour}$ ~0.5 pb^{-1} averaged over a two hours run (see Fig. 5).

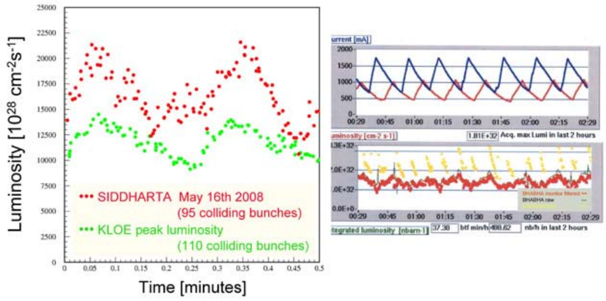

Figure 5: Peak luminosity (left) and integrated luminosity (right) over 2 hours.

However these results have been obtained without reaching the low beta parameters and the CW sextupole strength to their nominal values. As a matter of fact it is reasonable to foresee a 10% reduction in β^*_y and a 20% increase in the CW sextupoles strength in the near future. Moreover the number of colliding bunches, due to the recovered vacuum conditions and to the recent developments on the transverse and longitudinal feedback systems, can be raised from 95 to 110, as during the past DAΦNE runs. The average luminosity can also profit from speeding up the switch electron and positron injection. With all these improvements the peak luminosity is expected to reach 4.0 $10^{32}\ cm^{-2}s^{-1}$ and the monthly integrated luminosity ~ 0.5 fb^{-1}.

CONCLUSIONS

The DAΦNE collider has been successfully commissioned in the new configuration. The CW sextupoles proved to be effective in controlling transverse beam blowup and increasing luminosity.

DAΦNE is presently delivering luminosity to the SIDDHARTA prototype detector to establish the best background rejection configuration. Peak and average luminosity are already sufficient to perform the experiment in few months.

Further improvements of machine operation are likely to fulfill the requirements for a future physics experiments at DAΦNE.

REFERENCES

[1] G. Vignola et al., Frascati Phys.Ser.4:19-30,1996;
C. Milardi et al., Frascati Phys.Ser.16:75-84,1999.
[2] C. Milardi et al., e-print: physics/0408073.
[3] A. Gallo et al., Edimburgh 2006, EPAC p. 604-606.
[4] C. Milardi et al., PAC07, p. 1457.
[5] C. Milardi et alt., arXiv:physics/0607129v1.
[6] P. Raimondi et al., physics/0702033.
[7] P. Raimondi et al., this conference, WEPP045.
[8] M. Zobov et al., arXiv:0802.2667v1.
[9] C. Milardi et al., arXiv:0803.1450v1.
[10] F. Marcellini et al., this conference, TUPP051.
[11] A. Drago et al., this conference, THPC116.
[12] B. Buonomo et al., this conference, TUPC065

MAGNETIC DESIGN STUDIES FOR THE FINAL FOCUS QUADRUPOLES OF THE SUPERB LARGE CROSSING ANGLE COLLISION SCHEME

E. Paoloni, University of Pisa and INFN, Pisa, Italy
S. Bettoni, CERN, Geneva, Switzerland
M. E. Biagini, P. Raimondi, INFN/LNF, Frascati, Italy

Abstract

The final doublets of the Super*B* factory project [1], based on the large crossing angle collision scheme, must provide a pure quadrupolar field on each of the two beams to avoid the high background rates in the detector. Because of the small separation of the low energy (LER) and the high energy (HER) beams the influence of each winding on the other one is not negligible and, for the same space limitation, a multi-layer configuration is not suitable to compensate the high order multipoles. A novel helical-type design has been studied to compensate the fringe field of the quadrupole of one line onto the other one. The 2D algorithm and the 3D finite elements models of this design are presented.

INTRODUCTION

Most of the present, KEK B [2] and DAΦNE [3], and future, Super*B*, colliders exploit the crossing angle scheme to quickly separate the two beams and reach high collision frequency. The magnetic element closest to the Interaction Point (IP) in these machines is usually a horizontal defocusing quadrupole (QD0) common to the two beams. The off-axis particles see a dipolar component which is critical in Super*B* more than in the other machines because of the high strength of the QD0, so that most of the off energy particles produced by bremsstrahlung at the IP hit the beam pipe, producing high multiplicity electromagnetic showers whose cascade enters into the detector. To mitigate their effect massive tungsten shielding should be provided to keep the detector occupancies and radiation damages at a reasonable level [4].

A definitive solution to this problem is to replace the common QD0 with a special quadrupole whose magnetic center lies on the beam reference trajectory for each beam line. In the Super*B* the horizontal separation of the beam lines at the QD0 entrance ($2\,\mathrm{cm} \sim 180\ \sigma_x$) is enough to accommodate only four millimeters of superconducting windings and two cold beam pipe walls, still leaving a reasonable aperture as showned in Fig. 1. Themechanical constraints are too tight for a conventional septum magnet and to compensate the cross-talk among the quadrupoles of the two lines, therefore a novel design has been studied.

CROSS TALK COMPENSATION

Let consider a current density $\mathbf{j}$ concentrated in a unit radius cylinder with axis z. Let $\mathbf{j} = \hat{z} j_z(\varphi)\delta(r-1)$ be

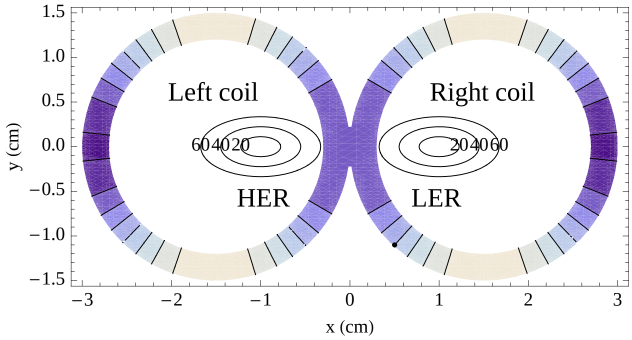

Figure 1: Schematic $x-y$ cross section of the double quadrupole. $20, 40, 60\ \sigma_x$ beam envelopes at the QD0 entrance are sketched. Gray-tones represents the intensity of j_z.

invariant under z translation and let φ be the angle in polar coordinates with respect to the cylinder axis. The magnetic field B is independent from the z coordinate and can be expressed at point $\zeta \equiv x + iy$ as:

$$B(\zeta) \equiv B_y(\zeta) + iB_x(\zeta) = k \int_0^{2\pi} d\varphi\, \frac{j_z(\varphi)}{\zeta - e^{i\varphi}}$$

where x and y are the transverse coordinates. Using the algebraic relation:

$$\frac{1}{\zeta - e^{i\varphi}} = \frac{1}{\zeta} - \frac{1}{\zeta^2} \frac{1}{\frac{1}{\zeta} - e^{-i\varphi}}$$

it can be derived that:

$$B(\zeta) = -\frac{1}{\zeta^2}\overline{B}\left(\frac{1}{\overline{\zeta}}\right) + \frac{k}{\zeta}\int_0^{2\pi} d\varphi\, j_z(\varphi) \qquad (1)$$

where $\overline{\zeta}$ is the ζ complex conjugate. If ζ is outside the cylinder then $1/\overline{\zeta}$ in inside and vice-versa, therefore eq. 1 relates the far and near field generated by $\mathbf{j}$, so that the set of functional equations can be written:

$$\begin{cases} B_{\mathrm{L}}(\zeta) + B_{\mathrm{R}}(\zeta - \Delta) &= B_{\mathrm{L}}(\zeta) - \frac{1}{(\zeta-\Delta)^2}\overline{B_{\mathrm{R}}}\left(\frac{1}{\overline{\zeta}-\Delta}\right) \\ &= B_{\mathrm{L}}^{\mathrm{tot}}(\zeta) \\ B_{\mathrm{R}}(\zeta) + B_{\mathrm{L}}(\zeta + \Delta) &= B_{\mathrm{R}}(\zeta) - \frac{1}{(\zeta+\Delta)^2}\overline{B_{\mathrm{L}}}\left(\frac{1}{\overline{\zeta}+\Delta}\right) \\ &= B_{\mathrm{R}}^{\mathrm{tot}}(\zeta) \end{cases}$$

where Δ is the distance among the cylinder centers, B_{L} (B_{R}) represents the field generated by the left (right) coil and $B_{\rm L}^{\rm tot}$ ($B_{\rm R}^{\rm tot}$) is the total, assigned, field present inside the left (right) coil. The succession of functions:

$$
\begin{aligned}
B_{{\rm L}n}(\zeta) &= \tfrac{1}{(\zeta-\Delta)^2}\overline{B_{{\rm R}n}}(\tfrac{1}{\bar\zeta-\Delta}) + B_{\rm L}^{\rm tot}(\zeta) \\
B_{{\rm R}n}(\zeta) &= \tfrac{1}{(\zeta+\Delta)^2}\overline{B_{{\rm L}n-1}}(\tfrac{1}{\bar\zeta+\Delta}) + B_{\rm L}^{\rm tot}(\zeta) \\
B_{\rm L0}(\zeta) &= 0
\end{aligned}
$$

converges quite fast to the solution of eq.(1). For typical values of Δ and target fields $n = 20$ gives solutions with 10^{-8} accuracy. The left field sources $j_{{\rm L}z}$ is then determined according to the Ampère law:

$$
\begin{aligned}
j_{{\rm L}z}(\varphi) &= \lim_{\delta\to 0}\left[B_{\rm L}(e^{i\varphi}(1+\delta)) - B_{\rm L}(e^{i\varphi}(1-\delta))\right]\, e^{i\varphi} \\
&= \left[B_{\rm L}(e^{i\varphi}) + \frac{1}{e^{2i\varphi}}\overline{B}_{\rm L}(\frac{1}{e^{-i\varphi}})\right]\, e^{i\varphi}
\end{aligned}
$$

The winding shape to obtain such a current distribution is obtained using the AML-like technique [5], which consists in superimposing to this current density distribution a solenoidal one:

$$\mathbf{j} = \left[\hat z\; j_{{\rm L}z}(\varphi) + \hat z\frac{\Delta z}{2\pi} + \hat\varphi\right]\, \delta(r-1)$$

The winding shape $\mathbf{x}(\lambda)$ is then readily obtained solving the differential equation:

$$\mathbf{x}'(\lambda) = \mathbf{j}(\mathbf{x})$$

To cancel-out the inner solenoidal field and the outer $1/\zeta$ field a second layer is wound reversing the solenoidal superimposed current:

$$\mathbf{j} = \left[\hat z\; j_{{\rm L}z}(\varphi) - \hat z\frac{\Delta z}{2\pi} - \hat\varphi\right]\, \delta(r-1)$$

Finally the right field sources is obtained with the same technique starting from $B_{\rm R}$.

3D SIMULATIONS

Magnetic models of the windings obtained applying the algorithm described in the previous section have been simulated in 3D [6]. The windings shape has been optimized to improve as much as possible the field quality in 3D in the central part of the magnet and to minimize the end-effect at the extremities of the coils. Assuming a NbTi strand the margin to quench of the best configuration has therefore been determined using as parameters the strand properties and the radius of the windings both at 4.2 K and 1.9 K. These parameterizations will be used to adapt the design to the Super*B* final focus requests.

Field Quality

The windings shape in 3D has been optimized varying the minimum angle of the wire with respect to the z axis from 84 ° to 45 °. In Fig. 2 some of the simulated configurations are shown. For each model at several $\overline{z}$ the vertical component of the magnetic field around the center of the coils on the mid-plane, (x_C,0,$\overline{z}$) has been computed and fitted according to:

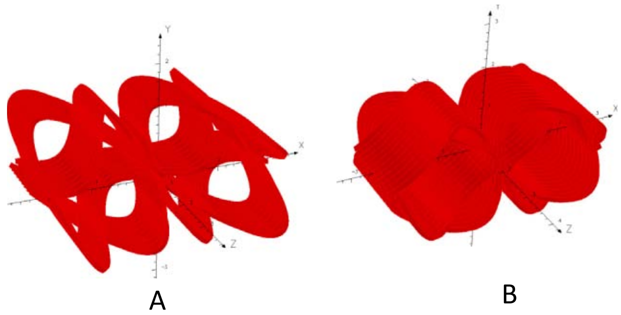

Figure 2: Some of the simulated configurations. A and B correspond to an increasing scan number.

$$B_y(x - x_C, 0, \overline{z}) = \sum_{i=0}^{N} b_i (x - x_C)^i \tag{2}$$

The higher order terms normalized to the quadrupole B_i/B_1 have therefore been calculated as:

$$\frac{B_i}{B_1} \equiv \frac{b_i(x - x_C)^{i-1}}{b_1}, i = 2, 3, \ldots \tag{3}$$

The third order polynomial allowed to obtain norm of residuals normalized to the quadrupolar field of the order of 10^{-6}. The second and the third order coefficients of the most promising configurations are shown in Fig. 3. The configurations 4 and 7 allow for having a field quality better than 10 parts over a million. For J equal to 500 A/mm^2 they have a similar gradient (b_1 = 31.46 T/m for 4 and 31.44

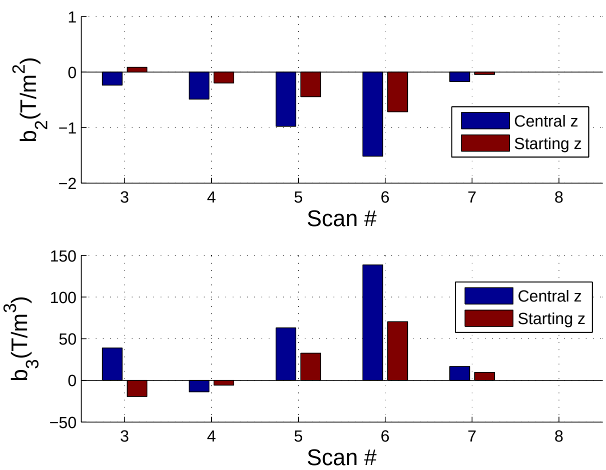

Figure 3: b_2 and b_3 of the best configurations of the scan at half of the length of the coil (Central z) and at the extremities of the windings (Starting z).

T/m for 7), maximum field in the conductor (0.50 T for 4 and 0.52 T for 7) and field quality in the central part of the windings, but configuration 7 has been preferred because of the better end-effect and the higher radius of curvature, both advantageous for the mechanics and the degradation. In Table 1 the second and third term of the field expansion of this configuration are shown. This configuration

Table 1: Higher order terms normalized to the quadrupole of the best configuration of the scan.

	z center	**z start**
B_2/B_1	$-2.72 \cdot 10^{-5}$	$-1.36 \cdot 10^{-5}$
B_3/B_1	$+1.33 \cdot 10^{-5}$	$+1.52 \cdot 10^{-5}$

has therefore been used to study the margin to quench of coils built according to this kind of design.

Margin to Quench

At a fixed geometry (1 cm internal radius, 2 mm conductor thickness) and NbTi strand properties (1 mm x 1 mm wire, Cu/SC equal to 0) the gradient and the maximum field in the conductor have been determined as a function of J. Imposing a target gradient, the necessary current density is determined from the first function and, known J, the maximum field in the conductor is calculated from the second one. This pair (J,$|B|_{MAX}$) defines the working point of the coils, which is compared to the NbTi [7] critical curve at a fixed temperature as a function of Cu/SC both at 4.2 K and 1.9 K. The dependence of the margin to quench on Cu/SC is shown in Fig. 4. Assuming a Cu/SC between 1.0 and 1.5

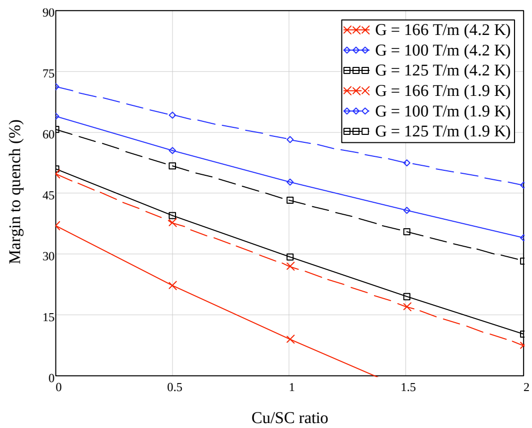

Figure 4: Margin to quench as a function of Cu/SC for several gradients (internal radius of the coils equal to 1 cm) at 4.2 K and 1.9 K.

a gradient of 125 T/m at 4.2 K and of 166 T/m at 1.9 K are feasible with a margin between 20% and 30%.

The dependence of the margin to quench on the coils geometry (variable internal radius) at a fixed Cu/SC has been also studied. The result is shown in Fig. 5. In the Super*B* final focus this layout would allow to produce gradient equal to 100 T/m at 4.2 K and 125 T/m at 1.9 K.

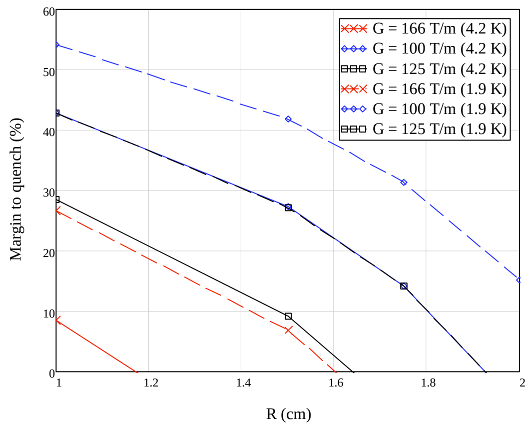

Figure 5: Margin to quench as a function of the internal radius of the coils (Cu/SC assumed equal to 1) at 4.2 K and 1.9 K.

CONCLUSIONS

A new configuration based on one quadrupole for each beam line of the Super*B* final focus has been recently proposed to eliminate the high background due to off energy particles. Due to the very tigh requests of this design (no more than 3 mm for the conductors for each quadrupole and distance between the axes of the magnets of only 1 cm), the cross talk between the quadrupoles is not negligible and, for the same reason, a multi-layer design is not feasible. In this paper an algorithm to compensate this effect has been presented. 3D simulations showed that with this technique an excellent field quality (better than 10 part per million) can be achieved. Also the margin to quench has been studied using as parameters the aperture radius and the copper over superconductor ratio both at 4.2 K and at 1.9 K. This will allow to adapt the design to the Super*B* final focus design requests. The authors wish to thank Luca Argenti for the many insightful conversations and advices.

REFERENCES

[1] J. Seeman *et al.*, “Design of a 1036cm-2s-1 Super*B* factory” WEPP039 this conference.

[2] Y. Funakoshi, “Performance of KEKB with crab cavities” WEXG01 this conference.

[3] C. Milardi *et al.*, “DAFNE Setup and Operation with the Crab Waist Collision Scheme” WEPP036 this conference.

[4] M. Bona *et al.*, “Super*B*: A High-Luminosity Asymmetric e^+e^- Super Flavor Factory. Conceptual Design Report,” arXiv:0709.0451 [hep-ex].

[5] Advanced Magnet Lab, AML, internet site `http://magnetlab.com/technology`.

[6] Opera Vector Fields analysis (Tosca), software for electromagnetic design, version 11.0, Vector Fields Ltd., Oxford, England, Vector Fields Inc., Illinois, USA.

[7] L. Bottura, “A practical fit for the critical surface of NbTi,” IEEE Transactions on Applied Superconductivity, Vol. 10, no. 1, March 2000.

DAΦNE SETUP AND OPERATION WITH THE CRAB-WAIST COLLISION SCHEME

C. Milardi for the DAΦNE Commissioning Team*

Abstract

In the second half of 2007 a major upgrade has been implemented on the Frascati DAΦNE collider in order to test the novel idea of *Crab-Waist* collisions. New vacuum chambers and permanent quadrupole magnets have been designed, built and installed to realize the new configuration. At the same time the performances of relevant hardware components, such as fast injection kickers and shielded bellows have been improved relying on new design concepts.

The collider has been successfully commissioned in this new configuration. The paper describes several experimental results about linear and non-linear optics setup and optimization, damping of beam-beam instabilities and discusses the obtained luminosity performances.

INTRODUCTION

DAΦNE [1] is the Frascati lepton collider working at the c.m. energy of the Φ meson resonance (1020). It came in operation in 2001 and till summer 2007 provided luminosity, in sequence, to three different experiments which logged a total integrated luminosity of ~ 4.4 fb^{-1}.

During these years the collider reached its best performances in terms of luminosity and background (L_{peak}=1.6x 10^{32} $cm^{-2}s^{-1}$ $L_{\int day}$~10 pb^{-1}) by means of several successive upgrades, relying on the experience gathered during the collider operations and implemented exploiting the shutdowns required for the experiment change over [2, 3, 4].

PHYSICAL BASIS FOR THE UPGRADE

Pushing the peak luminosity beyond the achieved limit of 1.6 10^{32} $cm^{-2}s^{-1}$ required a drastic change of the collision scheme. In fact the value of the betatron function at the Interaction Point (IP) was comparable with the longitudinal bunch length and the maximum storable current in collision was affected by the non-linear effects induced by the 24 parasitic crossing [5] occurring in each one of the two Interaction Regions (IRs).

A new collision scheme with a large Piwinski angle, obtained by increasing the horizontal crossing angle and reducing the transverse horizontal beam size at the IP, has been proposed and implemented at DAΦNE [6]. The large Piwinski angle provides several advantages: it reduces the beam-beam tune shift in both planes, shrinks the longitudinal size of the overlap between the colliding bunches, thus allowing for a lower β_y at the IP, and cancels almost all the parasitic crossings: in fact it becomes possible to completely separate the vacuum chambers of the two beams just after the first low-beta quadrupole in the IR. Moreover a couple of *Crab-Waist* (CW) sextupoles, installed in symmetric position with a proper phase advance with respect to the IP, suppresses the betatron and sinchrobetatron resonances coming from the vertical motion modulation due to the horizontal oscillation [7].

The second unused IR has been eliminated by separating vertically the two vacuum chambers. Some devices, such as bellows and injection kickers have been redesigned in order to improve their performances and to reduce their contribution to the total coupling impedance of the rings.

The new *Crab-Waist* collision scheme [8] and the collider mechanical and magnetic layout evolution [9] have been already extensively described in many papers.

DAΦNE UPGRADE COMMISSIONING

DAΦNE operation restarted at the end of November 2007 with the aim to optimize the collider performance, test the new devices, verify the *Crab-Waist* collision scheme and provide luminosity to the SIDDHARTA experiment preliminary setup.

Main Ring Optics

In the early stage of the commissioning a detuned optics, with ν_x slightly above 5, ν_y above 4, and without *Crab-Waist* sextupoles has been applied to both rings in order to speed up beam injection, put the diagnostics in operation and perform a satisfactory machine modeling. Beam closed orbit has been minimized together with the steering magnet strengths relying also on beam based procedure to point out and fix misalignment errors. Vertical dispersion has been minimized by global vertical orbit correction and by centering the beam vertical position in the arc sextupoles.

Once a reliable machine model has been defined, the ring optics has been moved progressively towards the nominal one with both tunes above 5. The β functions are now $\beta^*_{y/x}$ ~ 0.01/0.25 m at the IP, slightly larger than the *Crab-Waist* design values ($\beta^*_{y/x}$ ~ 0.0065/.20 m). The present main ring optics is shown in Fig. 1. Finally the

* D.Alesini, M.E.Biagini, C.Biscari, R.Boni, M.Boscolo, F.Bossi, B.Buonomo, A.Clozza, G.Delle Monache, T.Demma, E.Di Pasquale, G.Di Pirro, A.Drago, A.Gallo, A.Ghigo, S.Guiducci, C.Ligi, F.Marcellini, G.Mazzitelli, C.Milardi, F.Murtas, L.Pellegrino, M.Preger, L.Quintieri, P.Raimondi, R.Ricci, U.Rotundo, C.Sanelli, M.Serio, F.Sgamma, B.Spataro, A.Stecchi, A.Stella, S.Tomassini, C.Vaccarezza, M.Zobov INFN-LNF, Frascati, Roma; I.Koop, E.Levichev, P.Piminov, D.Shatilov, BINP SB RAS, Novosibirsk; V.Smaluk BINP, Novosibirsk; S.Bettoni, CERN, Geneva; M.Schioppa INFN- Cosenza, Cosenza; P.Valente, INFN-Roma1, Roma; K.Ohmi, KEK, Ibaraki; N.Arnaud, D.Breton, P.Roudeau, A.Stocchi, A.Variola, B.F.Viaud, LAL, Orsay; M.Esposito, University La Sapienza, Roma; E.Paoloni, University of Pisa and INFN, Pisa; P.Branchini, INFN-Roma3, Rome; D.Teytelman SLAC, Menlo Park, California.

Crab-Waist sestupoles have been switched on, at half their nominal strength, however five times higher than the strength of the ordinary sextupoles used for chromaticity correction. Beam orbit deviations in the CW sextupoles have been carefully corrected to avoid tune changes.

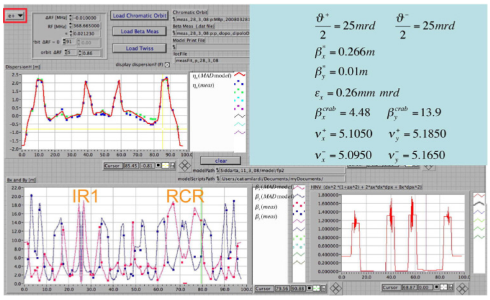

Figure 1: DAΦNE model compared with beam measurements – up left: dispersion function; down left: betatron functions; down right: betatron invariant.

In January two electromagnetic quadrupoles have been added symmetrically with respect to IP1 on each ring, in order to finely tune the phase advance between the CW sestupoles and the IP.

The transverse betatron coupling has been corrected mainly by correcting rotation errors in the low-β focusing quadrupoles, now independent for the two rings. The best value obtained so far is $\kappa \sim 0.4\%$ for both beams measured at the synchrotron light monitor after a careful calibration.

The nonlinear optics has been optimized by finely tuning the sextupole configuraton to minimize the dependence of the betatron functions on energy and to improve the dynamic aperture and, therefore, the beam lifetime.

Coupling Impedance

The ring coupling impedance is responsible for several harmful effects to the beam dynamics, and to the luminosity as well, as it has been pointed out during the last FINUDA run [4]. Coupling impedance affects bunch length and has to be kept as low as possible to avoid geometric luminosity reduction due to the hourglass effect.

The coupling impedance in the two rings has been reduced [10] by adopting new injection kickers and new shielded bellows and, on the e^- ring, by removing some broken ion clearing electrodes. A bunch length of 1.7 mm has been measured for both beams at 10 mA/bunch, which, for the e^- beam, is consistent with a 20% bunch length reduction.

High Currents Issues

Machine operation at high current strongly depends on vacuum conditions. The new vacuum chambers installed on the IR and in the opposite ring crossing region (RCR), as well as the new bellows and injection kickers required a careful and time consuming beam conditioning.

After three months of operation a reasonable vacuum condition has been obtained. However no more than 95 e^- bunches can be stored, so far, in collision instead of the 110 used during the past DAΦNE runs.

In turn the e^+ beam is affected by fast transverse instability leading to partial or total beam loss. Such instabilities have been cured by tuning the transverse and longitudinal feedback systems. The four e^- e^+ transverse feedbacks have been upgraded by adopting the new iGP (Integrated Gigasample Processor) feedback unit [11]. Beyond its ordinary stabilization function, this system allows to build a variety of diagnostic tools ranging from the single bunch tune to the single turn beam position measurement, a feature which has been extensively used in the injection induced transient analysis aimed at reducing the impact of the injection kickers on the maximum storable current, especially for the e^+ beam.

A further e^+ current improvement has been obtained installing solenoid windings (Bsol ~ 45 Gauss) in long section of the IR and of the RCR in the e^+ ring. Solenoids have been effective especially in the first commissioning phase, in fact they reduce the transverse instability rise-time boosting the action of the transverse feedbacks.

High current operations also profited from the lower coupling impedance introduced by the new bellows and injection kickers. A more relevant contribution is expected when the fast high voltage pulsers (5 ns, 40kV), perturbing only one bunch during injection, will replace the old ones (200 ns, 25kV) presently feeding the new stripline kickers.

As an overall result the highest currents stored by now are in single beam: $I^- = 1.8$ A (95 bunches), $I^+ = 1.15$ A (120 bunches) and in 95 colliding bunches: $I^- = 1.2$ A, $I^+ = 1.1$ A.

Luminosity Measurement

Three different monitors are used to evaluate the luminosity. The γ monitor measures the photons emitted at small angle (≈1 mrad) in the e^+ e^- inelastic scattering by means of two detectors aligned along the direction of each beam at the IP. It is used essentially for relative measurements aimed at optimizing the luminosity since its acceptance cannot be easily defined. An absolute luminosity measurements is provided by a Bhabha calorimeter [12] with a large acceptance (17÷27 degrees). The kaon counting rate is yielded by the SIDDHARTA experiment trigger system.

The Bhabha and Kaon monitors are in agreement within 15%.

NEW COLLISION SCHEME TESTS

Several measurements and qualitative observations of the beam-beam behaviour have confirmed the effectiveness of the new collision scheme.

The convoluted vertical size Σ_y of the interaction region can be measured by scanning a beam through the other one at low current looking at the luminosity; the vertical bunch size at the IP σ_y can be obtained by taking into account the hourglass effect. At DAΦNE $\sigma_y \sim 4$ μm has been obtained (see Fig. 2) consistent with the value measured at the Synchrotron Light Monitor.

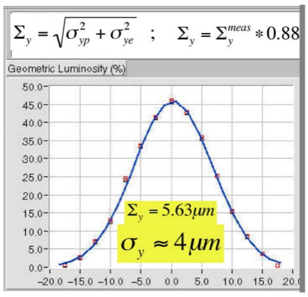

Figure 2: Vertical beam-beam luminosity scan.

A simple test of the new collision scheme consists in switching off the Crab-Waist sextupoles of one beam in collision. As a consequence the growth of both horizontal and vertical transverse sizes can be observed together with a luminosity reduction recorded by all the monitors. Such a behaviour is compatible with the appearance of beam-beam resonances when the CW sextupoles are off.

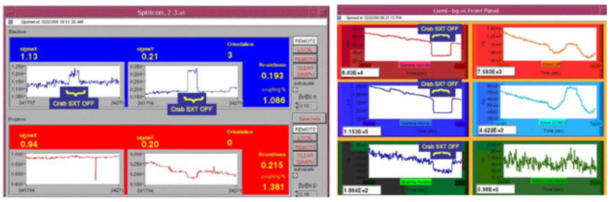

Figure 3: Transverse size (left) and luminosity dependence (right) on the CW sextupole excitation in the e^- ring.

The geometric luminosity, defined as the luminosity divided by the product of the total currents in the two beams (taking into account also the number of colliding bunches), exceeds by 3÷4 times the best value measured during the past DAΦNE runs, and the beam-beam tune shift exhibits a fairly linear behaviour as a function of current per bunch in the opposite colliding beam.

Collisions involving 10 bunches per beam have been studied both in the low and high current regimes. Such a situation avoids the effects due to the multi-bunch longitudinal beam dynamics. The maximum measured luminosity is consistent with the numerical simulations of the Crab-Waist collision scheme with the present low-β parameters.

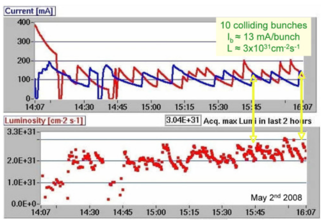

Figure 4: 10 bunches luminosity run.

LUMINOSITY RESULTS

The most relevant results of the commissioning concern the luminosity. So far the maximum measured peak luminosity is in excess of $L_{peak} = 2.2\ 10^{32}\ cm^{-2}s^{-1}$, the best daily integrated luminosity is $L_{\int day} \sim 8\ pb^{-1}$ and the highest integrated luminosity in one hour is $L_{\int 1hour} \sim 0.5\ pb^{-1}$ averaged over a two hours run (see Fig. 5).

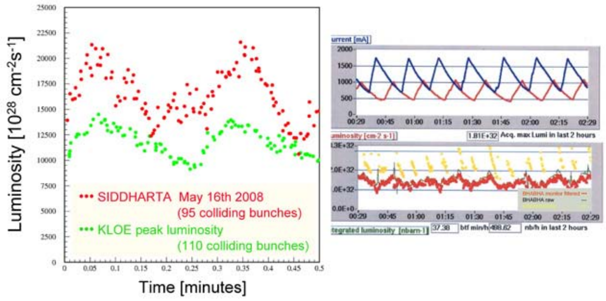

Figure 5: Peak luminosity (left) and integrated luminosity (right) over 2 hours.

However these results have been obtained without reaching the low beta parameters and the CW sextupole strength to their nominal values. As a matter of fact it is reasonable to foresee a 10% reduction in β^*_y and a 20% increase in the CW sextupoles strength in the near future. Moreover the number of colliding bunches, due to the recovered vacuum conditions and to the recent developments on the transverse and longitudinal feedback systems, can be raised from 95 to 110, as during the past DAΦNE runs. The average luminosity can also profit from speeding up the switch electron and positron injection. With all these improvements the peak luminosity is expected to reach $4.0\ 10^{32}\ cm^{-2}s^{-1}$ and the monthly integrated luminosity ~ $0.5\ fb^{-1}$.

CONCLUSIONS

The DAΦNE collider has been successfully commissioned in the new configuration. The CW sextupoles proved to be effective in controlling transverse beam blowup and increasing luminosity.

DAΦNE is presently delivering luminosity to the SIDDHARTA prototype detector to establish the best background rejection configuration. Peak and average luminosity are already sufficient to perform the experiment in few months.

Further improvements of machine operation are likely to fulfill the requirements for a future physics experiments at DAΦNE.

REFERENCES

[1] G. Vignola et al., Frascati Phys.Ser.4:19-30,1996; C. Milardi et al., Frascati Phys.Ser.16:75-84,1999.
[2] C. Milardi et al., e-print: physics/0408073.
[3] A. Gallo et al., Edimburgh 2006, EPAC p. 604-606.
[4] C. Milardi et al., PAC07, p. 1457.
[5] C. Milardi et alt., arXiv:physics/0607129v1.
[6] P. Raimondi et al., physics/0702033.
[7] P. Raimondi et al., this conference, WEPP045.
[8] M. Zobov et al., arXiv:0802.2667v1.
[9] C. Milardi et al., arXiv:0803.1450v1.
[10] F. Marcellini et al., this conference, TUPP051.
[11] A. Drago et al., this conference, THPC116.
[12] B. Buonomo et al., this conference, TUPC065

DESIGN OF A 10^{36}CM^{-2}S^{-1} SUPER-B FACTORY *

M. E. Biagini, R. Boni, M. Boscolo, T. Demma, A. Drago, S. Guiducci, P. Raimondi, S. Tomassini, M. Zobov, INFN Laboratori Nazionali Frascati, Frascati, Italy, K. Bertsche, A. Novokhatski, J. Seeman, M. Sullivan, U. Wienands, W. Wittmer, SLAC, Menlo Park, CA, USA, S. Bettoni, CERN, Geneva, Switzerland, E. Paoloni, G. Marchiori, Pisa University, Pisa, Italy, A. Bogomyagkov, I. Koop, E. Levichev, S. Nikitin, P. Piminov, D. Shatilov, BINP, Russia

Abstract

Parameters have been studied for a high luminosity e+e- collider operating at the Upsilon 4S that would deliver a luminosity of 1 to 4 x 10^{36}/cm^2/s. This collider, called a Super-B Factory, would use a combination of linear collider and storage ring techniques. In this scheme an electron beam and a positron beam are stored in low-emittance damping rings similar to those designed for a Linear Collider (LC) or the next generation light source. A LC style interaction region is included in the ring to produce sub-millimeter vertical beta functions at the collision point. A large crossing angle (+/- 24 mrad) is used at the collision point to allow beam separation. A crab-waist scheme is used to reduce the hourglass effect and restore peak luminosity. Beam currents of 1.8 A at 4 x 7 GeV in 1251 bunches can produce a luminosity of 10^{36}/cm^2/s with upgrade possibilities. Such a collider would produce an integrated luminosity of about 10,000 fb^{-1} (10 ab^{-1}) in a running year (10^7 sec) at the Υ(4S) resonance. Further possibilities include having longitudinally polarized e- at the IR and operating at the J/Psi and Psi' beam energies.

DESIGN STRATEGY

The construction and operation of modern multi-bunch e^+e^- colliders [1,2,3] have brought about many advances in accelerator physics in the area of high currents, complex interaction regions, high beam-beam tune shifts, high power RF systems, controlled beam instabilities, rapid injection rates, and reliable uptimes (~90%). A Conceptual Design Report (CDR) [4] was issued in May 2007, with about 200 pages dedicated to the accelerator design. This report discusses site requirements, crab waist compensation, parameters optimization in order to save power, IP quadrupole design, Touschek backgrounds, spin rotator scheme, and project costs. A possible layout at Tor Vergata University near Rome is shown in Figure 1. The ring lattices have been modified to produce very small horizontal (a few nm-rad) and vertical emittances (a few pm-rad). Crab waist sextupoles near the interaction region introduce a left-right longitudinal waist position variation in each beam allowing a vertical beta function which is much smaller than the bunch lengths.

*Supported by US DOE contract DE-AC02-76SF00515.
†seeman@slac.stanford.edu

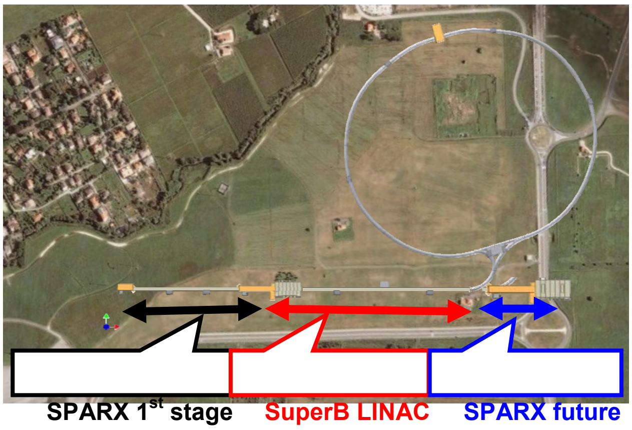

Figure 1: Possible SuperB location at Tor Vergata University with a ring circumference of 1800 m and an injector located adjacent to the future SPARX FEL.

LUMINOSITY AND CROSSING ANGLE

The luminosity L and beam-beam parameters, ξ_y, ξ_x, in an e^+e^- collider with a horizontal crossing angle are given by the expressions:

$$\mathcal{L} = \frac{\gamma^+ \xi_y N^+ f_c}{2 r_e \beta_y}\left(1+\frac{\sigma_y}{\sigma_x}\right) \propto \frac{N^+ \xi_y}{\beta_y}$$

$$\xi_y = \frac{r_e N^-}{2\pi\gamma^+}\frac{\beta_y}{\sigma_y\left(\sigma_x\sqrt{1+\varphi^2}+\sigma_y\right)} \propto \frac{N^-\sqrt{\beta_y}}{\sigma_y \sigma_z \theta}$$

$$\xi_x = \frac{r_e N^-}{2\pi\gamma^+}\frac{\beta_x}{\sigma_x^2\left[(1+\varphi^2)+\frac{\sigma_y}{\sigma_x}\sqrt{1+\varphi^2}\right]} \propto \frac{N^-\beta_x}{(\sigma_z\theta)^2}$$

where f_c is the frequency of collision of each bunch, N is the number of particles in the positron (+) and electron (-) bunches, σ is the beam size in the horizontal (x) and vertical (y) directions, γ is the normalized beam energy, ε is the beam emittance, β is the beta function (cm) at the collision point for each plane and θ is the crossing angle. The Piwinski angle is $\phi = \theta\sigma_z/\sigma_x$.

The Super-B accelerator consists of two asymmetric energy rings, colliding in one Interaction Region (IR) at a large horizontal angle, with a spin rotator section in the HER to provide longitudinal polarization of the electron beam at the IP. In order to have equal tune shifts for the two beams, asymmetric B-Factories operate at unbalanced beam currents, with a current ratio inverse to the energy ratio. For SuperB, with an energy ratio of 7/4 and a large crossing angle, new conditions for having equal tune shifts are possible. LER (+) and HER (-) beams can have different emittances and β* but equal currents:

$$\xi^{+} = \xi^{-} \Leftrightarrow \frac{\beta_y^{+}}{\beta_y^{-}} = \frac{E^{+}}{E^{-}} \qquad (1)$$

Then, in order to have equal vertical beam sizes at IP, the LER and HER vertical and horizontal emittances must be:

$$\varepsilon_y^{+} = \frac{E^{-}}{E^{+}}\varepsilon_y^{-}, \quad \varepsilon_x^{+} = \frac{E^{-}}{E^{+}}\varepsilon_x^{-} \qquad (2)$$

with the horizontal beam sizes in the inverse ratio with the beam energies. Thus, the LER beam sees a shorter interaction region, in a ratio 4/7, with respect to the HER beam. This allows for further β_y* reduction, a larger emittance, increased Touschek lifetime, and reduced injection rates. Table 1 summarizes Super-B beam parameters for three operational scenarios. Figure 2 shows the left-right crab waist compensation at the IP. Figure 3 shows the beam cross sections at the IP with unequal emittances but equal beam-beam tune shifts.

Table 1: SuperB main parameters

Parameter (LER/HER)	Nominal	Upgrade	Ultimate
Energy (GeV)	4/7	4/7	4/7
Luminosity ($cm^{-2}s^{-1}$)	$1x10^{36}$	$2x10^{36}$	$4x10^{36}$
C (m)	1800	1800	1800
N. of bunches	1251	1251	2502
F_{RF} (MHz)	476	476	476
N. part/bunch	$5.5x10^{10}$	$5.5x10^{10}$	$5.5x10^{10}$
I_{beam} (A)	1.85/1.85	1.85/1.85	3.7/3.7
β_x* (mm)	35/20	35/20	35/20
β_y* (mm)	0.22/0.39	0.16/0.27	0.16/0.27
ε_x* (nm rad)	2.8/1.6	1.4/0.8	1.4/0.8
ε_y* (pm rad)	7/4	3.5/2	3.5/2
σ_x* (μm)	10/5.7	7/4	7/4
σ_y* (μm)	0.039	0.023	0.023
σ_z (mm)	6.	6.	6.
θ_{cross}(mr)	48	48	48
α_c ($x10^{-4}$)	3.2/3.8	3.2/3.8	3.2/3.8
$\tau_{x,y}/\tau_s$ (ms)	40/20	28/14	28/14
x-tune shift	0.004/0.003	0.006/0.003	0.006/0.003
y-tune shift	0.15	0.20	0.20
RF AC power (MW)	26	54	64

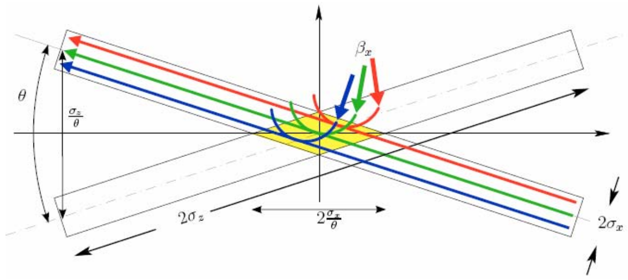

Figure 2: Interaction region showing two beams crossing at a large angle with the crab waist to improve the beam-beam interaction.

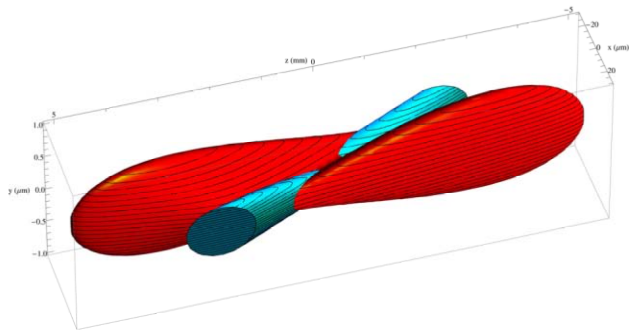

Figure 3: Beam cross sections at the IP with parameters from Table 1 and crab waists.

SUPER-B FACTORY LAYOUT

The two rings each have two arcs and two long straight sections. One straight is for the interaction region. The other is for diagnostics, RF, damping wigglers and injection. Sextupoles near the interaction region in a dispersive section are used to create a longitudinal waist shift over the width of the beam. The crab waist concept is being tested at the DAFNE collider at INFN, Frascati, Italy, with good results [5,6]. Dynamic apertures have been studied with the crab waist sextupoles [6], shown in Figure 4, with more work continuing.

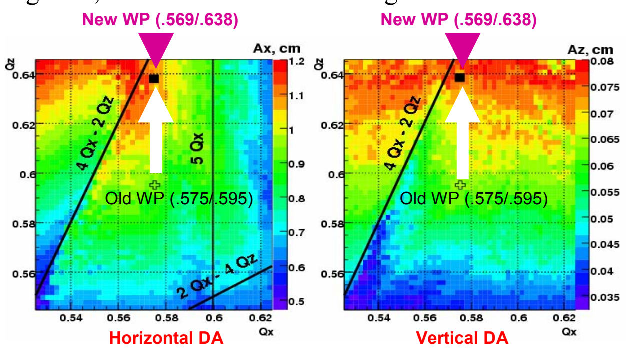

Figure 4: Dynamic aperture with crab waist for the HER versus horizontal and vertical tune used to find the optimum tune plane locations. Red is better and blue is worse.

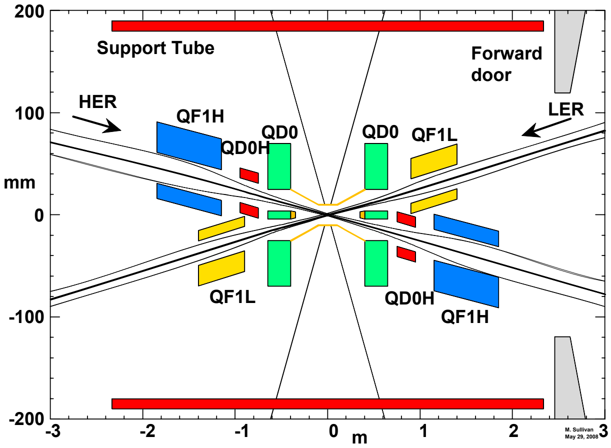

Figure 5: Interaction region for two asymmetric beams.

INTERACTION REGION PARAMETERS

The interaction region (Figure 5) is designed to be similar to that of the ILC and to leave about the same longitudinal free space for the detector as that presently used by BABAR or BELLE, but with superconducting quadrupole doublets QD0/QF1 as close to the interaction region as possible [7,8]. The total FF length is about 160 m and the final doublet is at 0.5m from the IP. A plot of the optical functions in the incoming half of the FF region is presented in Figure 6. The choice for a finite crossing angle at the IP greatly simplifies the IR design, naturally separating the beams at the parasitic collisions. The resulting vertical beta is about 0.2-0.3 mm and the horizontal 35 mm. These beta values are much closer to a linear collider design than a traditional circular collider. The beams enter the interaction point nearly straight to minimize synchrotron radiation and lost particle backgrounds. The beams are bent more while exiting the IR to avoid parasitic collisions and the resulting beam-beam effects.

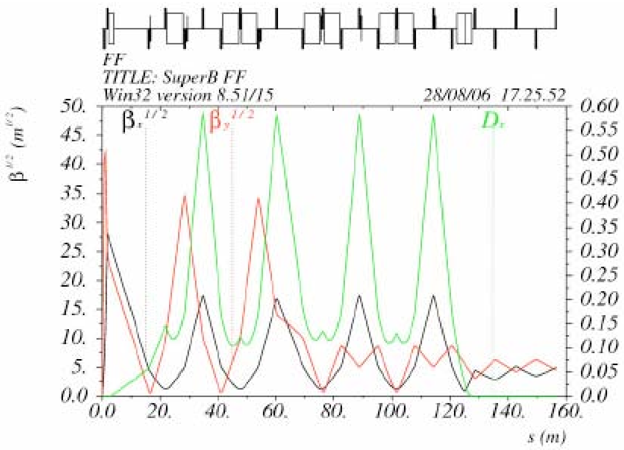

Figure 6: IR optical parameters for a Super-B-Factory.

POWER REQUIREMENTS

The power required for this collider is the sum of power for the magnets, RF system, cooling water, controls, and the accelerator operation. The present estimates indicate about 26 MW is needed for the nominal case. These values do not include the campus power requirements or that of the particle physics detector. There are upgrade possibilities for this collider to 2 to 4 times the design luminosity that will require more power [9]. Due to the advantages of the very low emittances and the crab waist with this design, the power requirements are significantly lower than those of the present B-Factory colliders.

INJECTION REQUIREMENTS

The injection system needed for the Super-B is similar to that for PEP-II, shown in Figure 7. Table 2 shows the basic injector parameters. Since the beam lifetimes are of the order of 10-30 minutes, continuous injection is needed. The injector will operate at 100 Hz and inject about 2 bunches per pulse. The values shown here are for the upgraded collider at higher luminosity.

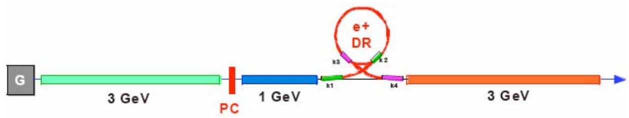

Figure 7: Schematic of the Super-B injector.

Table 2: Super-B Injection Parameters

Parameter	Unit	e+	e-
Linac energy	GeV	4	7
Damping ring energy	GeV	1	1
Linac frequency	MHz	2856	2856
Bunches per pulse		2	2
Injection efficiency	%	67	85
Pulse rate per beam	Hz	75	25
Injected particles/pulse	10^{10}	4	5.1
Injection rate total	10^{12}/sec	2.0	2.6
Polarization	%	0	89

REFERENCES

[1] P. Raimondi, “Super-B design directions,” PAC 2007.

[2] J. Seeman et al, “Last year of the PEP-II collider,” EPAC 2008.

[3] D. Shatilov, M. Zobov, “Tune shift in beam-beam collisions with an arbitrary crossing angle”, DAΦNE Tech. Note G-59, May 1003.

[4] Super-B Factory CDR, March 2007 SLAC-R-856, arXiv:0709.0451 (2007) 480 pp.

[5] P. Raimondi et al, “DAFNE crab waist beam tests”, EPAC 2008.

[6] M. Zobov et al, “Suppression of beam-beam resonances with a crab waist,” EPAC 2008.

[7] M. Sullivan et al, “Super-B interaction region design,” EPAC 2008.

[8] E. Paoloni et al, “IR SC quadrupole design for Super-B,” EPAC 2008.

[9] U. Wienands, S. Nikitin et al, Super-B Elba meeting, https://agenda.infn.it/conferenceDisplay.py?confId=347.

NEW LOW EMITTANCE LATTICE FOR THE SUPER-B ACCELERATOR

M. E. Biagini, M. Boscolo, P. Raimondi, S. Tomassini, M. Zobov, INFN-LNF, Frascati, Italy
J.Seeman, M. Sullivan, U. Wienands, W. Wittmer, SLAC, Menlo Park, CA, USA
S. Bettoni, CERN, Geneva, Switzerland
E. Paoloni, Pisa University and INFN, Pisa, Italy
A.Bogomyagkov, I.Koop, E.Levichev, S.Nikitin,P.Piminov, D.Shatilov, BINP, Novosibirsk, Russia

Abstract

New low emittance lattices have been designed for the asymmetric SuperB accelerator, aiming at a luminosity of 10^{36} cm^{-2} s^{-1}. Main optics features are two alternating arc cells with different horizontal phase advance, decreasing beam emittance and allowing at the same time for easy chromaticity correction in the arcs. Emittance can be further reduced by a factor of two for luminosity upgrade. Spin rotation schemes for the e^- beam have been studied to provide longitudinal polarization at the IP, and implementation into the lattice is in progress.

INTRODUCTION

The SuperB project [1] aims at the construction of a very high luminosity (10^{36} cm^{-2} s^{-1}) asymmetric (4 on 7 GeV) e^+e^- Flavour Factory with possible location at the campus of the University of Rome Tor Vergata near the INFN Frascati National Laboratory.

The design is based on a novel collision scheme, the “large Piwinski angle and crab waist” [2, 3], which will allow to reach unprecedented luminosity with low beam currents and reduced background at affordable operating costs. A polarized electron beam will allow for producing polarized τ leptons, opening an entirely new realm of exploration in lepton flavor physics. The principle of operation of this scheme is under test at the DAΦNE Frascati Φ-Factory [2,4].

A Conceptual Design Report (CDR) [5] was issued in May 2007, with about 200 pages dedicated to the accelerator design.

Several accelerator issues such as site requirements, crab waist compensation, parameter optimization in order to save power consumption and costs, first IP quadrupole design, Touschek backgrounds and spin rotators have been addressed after completion of CDR, and the rings lattice has been modified accordingly.

BEAM PARAMETERS

The SuperB accelerator consists of two rings of different energy colliding in one Interaction Region (IR) at a large horizontal angle. The crab waist scheme, with a couple of sextupoles per ring at appropriate phase with respect to the IP, will provide suppression of betatron and synchrobetatron resonances arising from the crossing angle geometry. Spin rotator sections in the HER will provide helicity of a polarized electron beam.

The three operation scenarios (Nominal, upgrade and ultimate) have different peak luminosity goals: the upgrade one will use emittances 50% smaller than the nominal, while the ultimate will push up the beam currents and number of bunches.

SuperB beam parameters are summarized in Table 1.

Table 1: SuperB main parameters

Parameter (LER/HER)	Nominal	Upgrade	Ultimate
Energy (GeV)	4/7	4/7	4/7
Luminosity ($cm^{-2}s^{-1}$)	$1x10^{36}$	$2x10^{36}$	$4x10^{36}$
C (m)	1800	1800	1800
N. of bunches	1251	1251	2502
F_{RF} (MHz)	476	476	476
N. part/bunch	$5.5x10^{10}$	$5.5x10^{10}$	$5.5x10^{10}$
I_{beam} (A)	1.85/1.85	1.85/1.85	3.7/3.7
β_x* (mm)	35/20	35/20	35/20
β_y* (mm)	0.22/0.39	0.16/0.27	0.16/0.27
ε_x* (nm rad)	2.8/1.6	1.4/0.8	1.4/0.8
ε_y* (pm rad)	7/4	3.5/2	3.5/2
σ_x* (μm)	10/5.7	7/4	7/4
σ_y* (μm)	0.039	0.023	0.023
σ_z (mm)	5.	4.3	4.3
α_c ($x10^{-4}$)	3.2/3.8	3.2/3.8	3.2/3.8
θ_{cross}(mr)	48	48	48
$\tau_{x,y}/\tau_s$ (ms)	40/20	28/14	28/14

RINGS LATTICE

The optimization of the ring lattices, performed after the CDR completion, aimed to minimize the intrinsic emittance so that nominal values can be obtained even without wigglers and the ring circumference is shortened, better fitting the proposed construction site.

When increasing the horizontal phase advance μ_x in the SuperB arc cell, the intrinsic emittance naturally decreases. The damping time increases by 30% but the RF power decreases, with a net operational costs saving. Beam-beam simulations (see for example in [5], page 211) have studied the degree to which an increase in the damping time affects the luminosity and beam-beam induced tails: an increase by a factor of 2.5 does not lead to any substantial luminosity degradation. In the new lattice the longitudinal damping times are of the order of 20 msec in both rings, about 1.3 times larger than the CDR values and still below the threshold of beam tail growth.

LER and HER lattices are very similar, and based on the reuse of most PEP-II (SLAC) hardware. The arcs have an alternating sequence of two different cells: a $\mu_x = \pi$ cell, that provides the best dynamic aperture, and a $\mu_x = 0.72$ cell that has a much smaller intrinsic emittance and provides a phase slippage for the sextupoles pairs, in such a way that one arc corrects all the phases of the chromaticity. As a consequence, the chromatic functions W_x and W_y are lower than 20 and the second order dispersion is almost zero everywhere except in the Interaction Region (IR). With this arrangement, the number of arcs can be reduced to 4, with two 40 m long "empty" wiggler sections for the upgrade scenario. The increase of the phase advance, together with future wigglers installation, will provide the required emittance and damping time for the upgrade parameters. With 14 cells in each arc a horizontal emittance of 1.6 nm in HER and 2.8 nm in LER are obtained, the LER lattice having still room for further reduction. The LER optical functions are shown in Fig. 1 (HER's are very similar), while the 2 different phase arc cells for HER (top) and LER (bottom) are shown in Fig. 2.

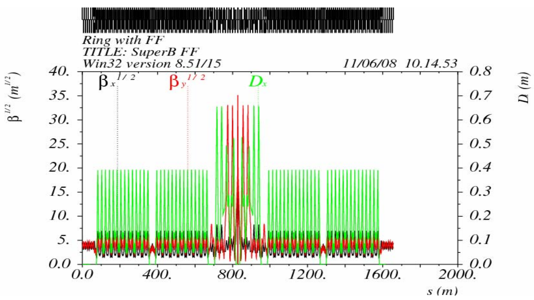

Figure 1: LER optical functions.

INTERACTION REGION

The design of the IR [6] has also been optimized. The new design provides better bandwidth and smaller emittance growth as well as reduced geometric aberrations. The peak dispersion is decreased, thus reducing the Touschek particles' amplitude across the IP. The crab sextupoles have also been included. The optical functions of half the IR ($\sqrt{\beta}$) are in Fig. 3: in each half IR two couples of non interleaved sextupoles (H,V), at –I phase, provide correction of first order horizontal and vertical chromaticity. Two more sextupoles (H, V) at low-β locations are used to have a larger bandwidth for off-energy particles, and a horizontal sextupole has been added to cancel residual geometric aberrations from off-phase sextupoles. Two octupoles on each side of the IP are used to correct third order aberrations.

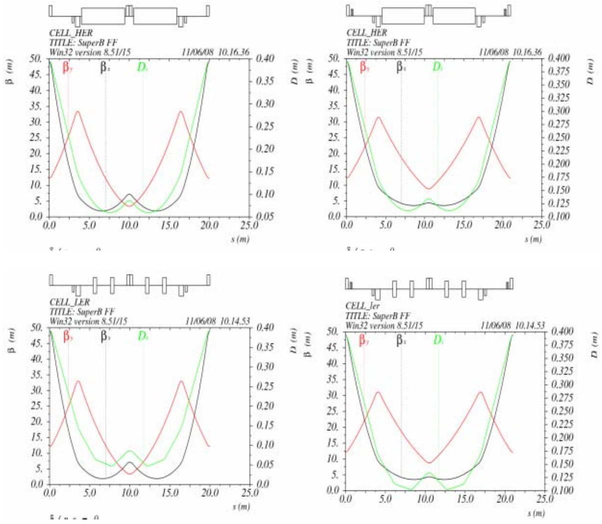

Figure 2: HER (top) and LER (bottom) arc cells: $\mu_x = 0.72$ (left), $\mu_x = 0.5$ (right).

The first drift length is L* = 0.4 m. The large crossing angle geometry allows then for having two separate QD0 for HER and LER. The horizontal separation of the beam lines at the QD0 entrance (2 cm ~ 180 σ_x) is enough to accommodate four layers of super-conducting windings and two cold beam pipe walls, still leaving a reasonable aperture. The mechanical constraints are too tight for a conventional septum magnet, a novel concept to compensate the cross-talk among the two QD0's core and fringe fields has then been studied [7], and 3D finite-elements simulations show field errors well under ten parts per million. This design strongly reduces the rate of off-energy particle losses near the IP, thus reducing the background rates seen in the detector with respect to a conventional design with a shared QD0. An additional small D-quadrupole will provide the necessary focusing to the HER beam.

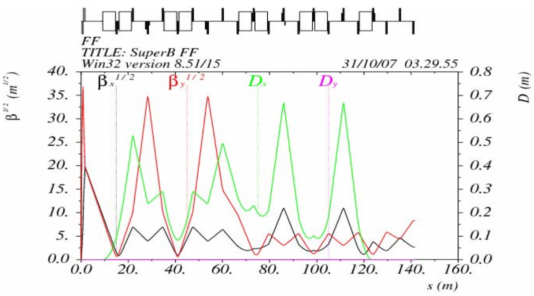

Figure 3: Optical functions in half IR, IP is at s=0, crab sextupole at s = 140.

DYNAMIC APERTURE

Dynamic aperture (DA) studies are presently carried out with the Acceleraticum code [8] which allows for optimization of DA and machine working point (WP) at the same time. The code uses the "best sextupole pair" method to find the optimal sextupoles configuration. Figs.

4 and 5 show preliminary calculations of LER and HER DA for on and off-energy particles (green curve is with synchrotron oscillations) with just two sextupole families. Units are number of $\sigma_{x,y}$ at the straight section opposite to the IP. DA reduction comes mainly from the strong FF, LER having higher chromaticity, however tuning the IR octupoles helps (black curve in the top plot). An example of sextupoles optimization and scan of the DA as a function of tunes for the HER is shown in Fig. 6, where in red are “good” DA regions, with a different WP (black dot) preferred to the nominal one (cross). A further DA reduction comes from the strong crab sextupoles, not included in these examples. Optimization of HER and LER DA is in progress, cross-checking good DA WP with good beam-beam WP.

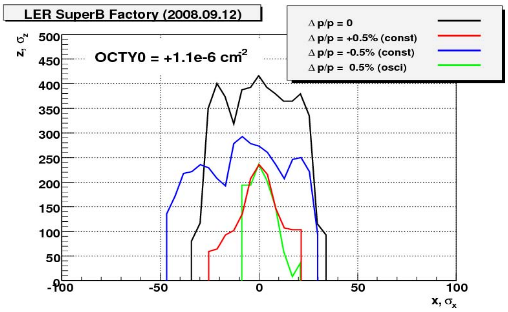

Figure 4: LER dynamic aperture (preliminary).

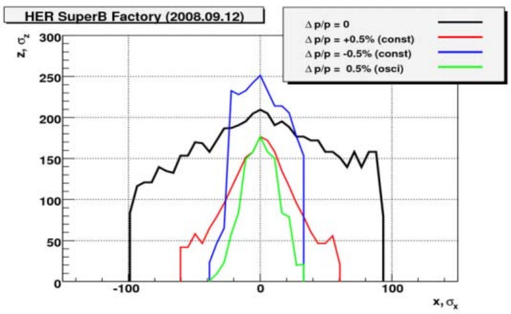

Figure 5: HER dynamic aperture (preliminary).

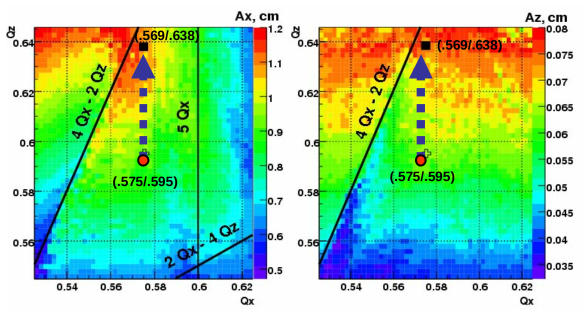

Figure 6: Example of HER DA vs tune scan.

SPIN ROTATOR

At SuperB energies, Sokolov-Ternov polarization takes too long and polarized electrons will be injected. The injector will have the necessary spin handling, and polarized sources with the required intensity exist (e.g. the SLC gun). At the IP, the desired polarization is longitudinal; this can be provided in principle either by 90° spin rotators up and downstream of the IP or by a Siberian Snake (180° rotator) diametrically opposite in the ring, thus avoiding the need for spin rotators matched to the critical IR optics. The rotators or Snake(s) can be designed either using solenoids or vertical dipoles together with horizontal dipoles. The overall spin matching in SuperB will be less critical than in facilities like HERA or LEP because of the short beam lifetime. This causes frequent injection of freshly polarized beam, thus reducing the effect of depolarization in the ring, so that maintaining above 90% of the injecting polarization is an achievable goal, provided rotators are spin-matched across the whole energy spread of the beam. It is still important to avoid integer spin tunes (and their synchrotron sidebands) as the spin orientation will move away from longitudinal at the IP for such values. Solenoid spin rotators tend to be more compact than pure dipole rotators, however for first-order spin matching they need to be anti-symmetric about the IP, leading to a horizontal "dog leg" in the IR layout causing a distortion of the ring geometry. The orbital coupling introduced by the solenoids is compensated by inserting a plane twister between two half-solenoids [9]. A pure dipole spin rotator has been designed that avoids this, i.e. its dipoles become part of the overall 360° bending, however, the vertical bends will raise the minimum vertical emittance achievable [10]. A novel scheme investigated would use 7 Siberian Snakes to maintain longitudinal polarization at the IP without local rotators, while at the same time maintaining sufficiently long (de-)polarization time to have good polarization at high luminosity [11].

CONCLUSIONS

The SuperB lattice, based on the reuse of PEP-II hardware, fits in the Tor Vergata University campus site near Frascati. The new cell layout is more flexible in terms of emittance, and wigglers are no longer needed for the nominal operation scenario, with a net gain in wall plug power and costs. The rings are shorter and less costly, since the total number of magnets has been reduced. The upgrade parameters are achievable with the installation of two, 40 m long, wigglers in each ring. Spin rotator sections are being studied and matched into the HER lattice. Dynamic aperture calculation is in progress.

REFERENCES

[1] J. Seeman et al, WEPP039, this conference.
[2] P. Raimondi, WEXG02, this conference.
[3] M.Zobov et al, WEPP045, this conference.
[4] C. Milardi et al, WEPP036, this conference.
[5] SuperB CDR, arXiv:0709.0451 (2007) 480 pp.
[6] M. Sullivan et al, WEPP042, this conference.
[7] E. Paoloni et al, WEPD002, this conference.
[8] P. Piminov, Master’s Thesis, BINP, Russia (2000).
[9] A. Zholents and P. Litvinenko, BINP Report 81-60, Novosibirsk, Russia
[10] I. Koop, Proc. ICFA 2008, BINP, Russia, 2008.
[11] I. Koop, private communication.

AN IMPROVED DESIGN FOR A SUPER-B INTERACTION REGION *

M. Sullivan†, J. Seeman, U. Wienands, SLAC, Menlo Park, CA 94025, S. Bettoni, CERN, Geneva, Switzerland, M. Biagini, P. Raimondi, INFN, Frascati, Italy, E. Paloni, INFN, Pisa, Italy.

Abstract

We present an improved design for a Super-B interaction region. The new design attempts to minimize the bending of the two colliding beams which results from shared magnetic elements near the Interaction Point (IP). The total crossing angle at the IP is increased from 34 mrad to 50 mrad and the distance from the IP to the first quadrupole is increased. Although the two beams still travel through this shared magnet, these changes allow for a new magnetic field design with a septum which gives the magnet two magnetic centers. This greatly reduces the beam bending from this shared quadrupole and thereby reduces the radiative bhabha background for the detector as well as any beam emittance growth from the bending. We describe the new design for the interaction region.

INTRODUCTION

The success of the two B-factories has encouraged the study of yet higher luminosity machines. The physics community has expressed the desire to have a B-factory with a hundred-fold increase in luminosity from present day B-factories (PEP-II and KEKB). With this increase in luminosity and the acquisition of at least 75 ab^{-1} (5 yrs of running at 1×10^{36} $cm^{-2}s^{-1}$) they argue that the sensitivity to very rare decays becomes high enough to enable the possible observation, in some cases, of new physics up to the 10 TeV mass scale [1-3]. With this incentive, some of us have started looking at ways to increase luminosity at the Upsilon 4S center-of-mass energy. KEK has studied the possibility of increasing the number of bunches and beam currents (up to 5000 bunches and 9.4A on 4.1A) while shortening the beam bunch length down to 3 mm and crabbing the beam bunches so they collide head-on. They have a plan to upgrade their present B-factory to obtain these parameters and obtain a luminosity of 5×10^{35} $cm^{-2}s^{-1}$.

A small PEP-II team has also considered this approach (short beam bunches and high beam currents) but found difficulties with the design. The experience of the present B-factories with damaged vacuum components due to increased beam currents and/or attempts to shorten the beam bunch as well as increased power usage argued that this was a difficult path for a luminosity upgrade [4-6]. A new accelerator design, pioneered by P. Raimondi, that uses very low emittance beams and very small β_y^* values in a large crossing angle scheme with a way of crabbing the magnetic waist, has design parameters that achieve a luminosity of over 1×10^{36} cm^2s^{-1} with beam currents and bunch lengths similar to those found in today's B-factories [2,7,8]. This interesting design is currently being tested at the DAFNE accelerator in Frascati, Italy [9]. A Conceptual Design Report for a new Super-B factory accelerator was written up in the fall of 2007 [2]. It describes the older Interaction Region (IR) design mentioned below.

*Supported by US DOE contract DE-AC02-76SF00515.
†sullivan@slac.stanford.edu

INTERACTION REGION DESIGN

In table 1, we list some of the machine parameters important for the IR design. The extremely low β^* values mean the final focusing elements need to be close to the IP.

Table 1: The most recent accelerator design values for a Super-B that are important for an interaction region design

	Nominal	Upgrade
Parameter	HER/LER	HER/LER
Luminosity ($\times10^{36}cm^{-2}s^{-1}$)	1	2
Beam Energy (GeV)	7/4	7/4
Beam Current (A)	1.85/1.85	1.85/1.85
β_x* (mm)	20/35	20/35
β_y* (mm)	0.39/0.22	0.27/0.16
Emittance x (nm-rad)	1.6/2.8	0.8/1.4
Emittance y (pm-rad)	4/7	2/3.5
Bunch spacing (m)	1.26	0.63
Crossing angle (mrad)	±25	±25

Previous IR Design

The previous IR design described in the CDR had the final vertically focusing quadrupole (called QD0) as a magnetic element shared by both beams. The magnet is located 0.3 m from the IP and is 0.45 m long. The quadrupole center is aligned with the detector magnetic field and is horizontally displaced so that, on average, the incoming beam is centered in this quad. The smaller opening angle of the CDR design (±17 mrad) then minimizes the beam separation in this quad thereby minimizing the horizontal bending of the outgoing beam while producing enough separation to get the beams into separate beam pipes just outboard of QD0. Figure 1 shows a layout of this design. Although the bending of the off-axis beam was minimized in this design, the bending is still significant and causes several concerns. The radiative bhabha beam particles which now have too low an energy are swept out of the beam by this off-axis bending in QD0 and cause a significant background in the detector. In addition, the bending creates high power synchrotron radiation (SR) fans that can be managed but do cause more exotic magnet designs for the outgoing beam magnets. The final concern was emittance growth from the high field bending in these shared quads. More information about this design can be found in the following references [2, 10].

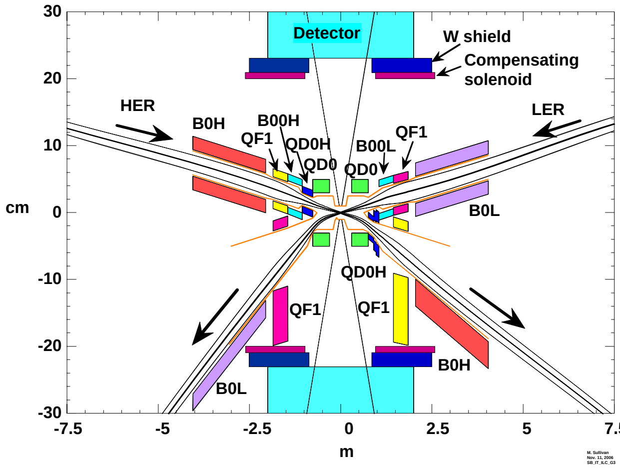

Figure 1. Layout of the IR design in the CDR. Note the large bending angles for the outgoing beams. The outgoing magnet apertures have to be quite large to accommodate the outgoing SR fans.

New IR Design

In order to eliminate some of these concerns and further improve the IR design, a new layout and a new kind of QD0 magnet is envisioned. The new QD0 is a double quadrupole in that it has two magnetic centers with a septum of super-conducting coils. The magnet bores are cold in order to minimize the material between the two beams thereby maximizing the beam-stay-clear (BSC). In addition, the crossing angle has increased to ±25 mrad and the QD0 magnet face has moved back from the IP. The magnet is now located 0.4 m from the IP and is 0.25 m long. The two coil windings of QD0 are assumed to be equally energized. In a like fashion to the CDR design, the High-Energy Beam (HEB) needs more vertical focusing and hence we add an additional small vertical focusing quadrupole to the HEB beam line just outboard of QD0 called QD0H. The following two magnets are, respectively, the horizontal final focusing magnets for the Low-Energy Beam (LEB) and for the HEB. Figure 3 shows a layout of the new IR design.

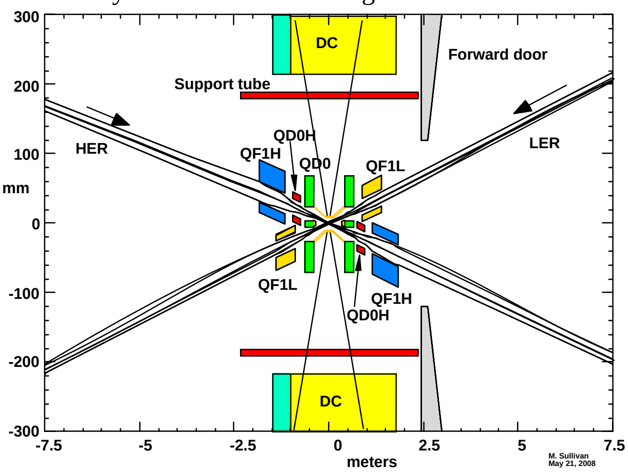

Figure 3. Layout of the new IR design. The QD0 is now a septum magnet with super-conducting windings in the septum.

RADIATIVE BHABHAS

One can see that the outgoing beams in the new design are essentially straight with very little bending. Figs 3 and 4 show the difference between the designs of the radiative bhabha energy spectrum. The energy of beam particles that can escape from the beam envelope is much lower in the new design. Clearly the detector backgrounds from this source are greatly reduced. The lack of bending also eliminates the concern of emittance growth.

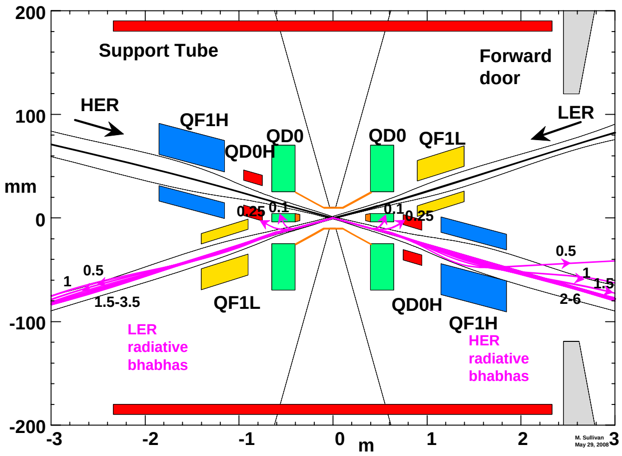

Figure 3. Plot of the trajectories of the off-energy beam particles for the radiative bhabha events for the new design. Figure 4 below is the same plot for the previous design. Only the lowest energy beam particles now have a chance of escaping from the beam envelope and hitting the beam pipe near the detector. The reason even these low energy beam particles escape is because there is still a little bending in the new QD0.

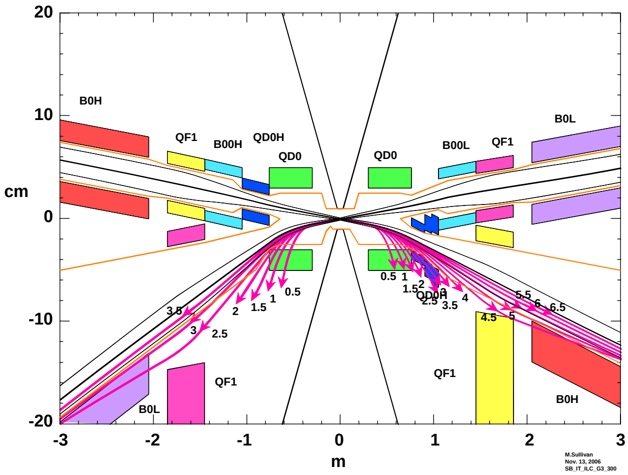

Figure 4. Plot of the radiative bhabha trajectories from the CDR design. Many more higher-energy particles are swept out of the beam envelope due to the strong bending in the shared QD0 magnet.

SYNCHROTRON RADIATION

Synchrotron radiation (SR) from the beam as it goes through the final bend magnet and through the final focus quadrupoles on its way to the IP can be a source of detector backgrounds. The final bend magnet is nearly 10 m from the IP so very little of the total bending power from this magnet reaches the area near the IP. The low emittance beams are a help in reducing backgrounds from SR. However, an added constraint is that very little power from SR is allowed to strike the cold bore surfaces of QD0. A careful first order study has been done for both of these designs and both designs do produce SR backgrounds in the detector but for both cases the level is acceptable. In both designs one of the upstream final focus magnets has been slightly displaced horizontally in order to steer the SR generated by the beam in the QF1 magnet away from the detector beam pipe. The detector beam pipe is a 20 cm long cylinder 1 cm in radius. The actual physics window is a cylinder that is about ±4 cm long for a detector aperture of ±300 mrad. Figure 5 shows the power in Watts from SR on various surfaces near the detector beam pipe.

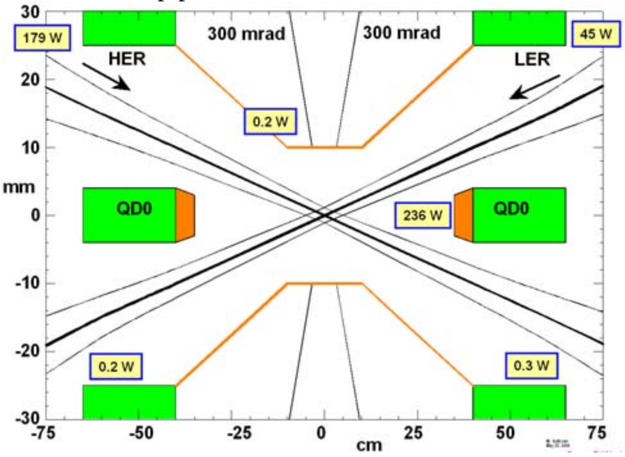

Figure 5. Diagram of the power incident on nearby surfaces from synchrotron radiation.

There are small amounts of power on the downstream cold bore surfaces of QD0. The amount of power (<1 W) is considered acceptable. There are no SR photons that strike the upstream cold bore surfaces and there are no photons that strike directly on the detector beam pipe. There is still a significant amount of SR power that strikes the mask in front of the downstream HER QD0 (236 W in this case). This is a high enough number to warrant further investigation, which we did, and a first order solid angle calculation reveals that the backscatter rate from this septum surface to the detector beam pipe is acceptably low.

SUMMARY

The success of the two B-factories has prompted interest in a Super-B factory design. An interaction region design is an important aspect of any collider design where detector background concerns and machine performance are interrelated. The present design is an improvement on the first design in that we have avoided bending the outgoing beams by using a more sophisticated design for the focusing magnet closest to the IP, QD0. Instead of sharing the quadrupole field with both beams we make QD0 into a septum quad with each beam being centered on a separate quadrupole field. This eliminates the strong bending of the outgoing beams that we had in the previous design. This reduces detector backgrounds from off-energy beam particles created by the radiative bhabha interaction at the IP and also eliminates the beam emittance growth seen in the older design. The new design has increased the distance of the first focusing element and the IP thereby increasing the beta function peaks. The new design also increases the crossing angle.

CONCLUSIONS AND OUTLOOK

We have come up with an improved IR design for a Super-B accelerator. There is still much to do. The new QD0 magnet is a challenging design in that we have presently only 8 mm of space in the septum between the two beams to make the super-conducting magnet. We are already exploring modifications to the design to improve the septum space. We are also looking at reducing the SR power from the upstream bending magnets in order to minimize the total amount of SR in the area around the IP. Many more iterations on the design are needed as well as more cross-checks, but it is beginning to look like a creditable design for a Super-B interaction region can be made.

REFERENCES

[1] “The Discovery Potential of a Super B Factory”, Proceedings of the 2003 SLAC workshops, SLAC-R-709, December 2004.

[2] “Super-B a High-Luminosity Heavy Flavour Factory”, Conceptual Design Report, INFN/AE-07/2, SLAC-R-856, LAL 07-15,March 2007.

[3] A. Stocchi, “The Super Flavour Factory Physics Case”, Presentation at Super-B meeting, La Biodola, Isola d'Elba, May 31st - June 3rd, 2008, http://www.pi.infn.it/bfactory/SuperB_elba2008/index.html

[4] U. Wienands, *et. al.*, “High-Intensity Effects in PEP-II”, These Proceedings, WEPP041.

[5] A. Novokhatski, *et. al.*, “A model of an Electrical Discharge in the Contacts with Omega Seals at High Currents in PEP-II”, These Proceedings, TUPP054.

[6] A. Novokhatski, *et. al.*, “Loss Factor of the PEP-II Rings”, These Proceedings, TUPP055.

[7] J. Seeman, *et. al.*, “Design of a 10^36/cm^2/s Super B-factory”, These Proceedings, WEPP039.

[8] M. E. Biagini, *et. al.*, “New Low Emittance Lattices for the Super-B Accelerator Project”, These proceedings, WEPP040.

[9] P. Raimondi, “Crabbed Waist Collisions in DAFNE and SuperB Design”, These proceedings, WEXG02.

[10] M. K. Sullivan, *et. al.*, “Interaction Region for a Super-B Factory”, Proceedings of PAC07, 2007, TUPAS066, pg. 1085.

SUPPRESSION OF BEAM-BEAM RESONANCES IN CRAB WAIST COLLISIONS

P. Raimondi, M. Zobov, LNF-INFN, Frascati, Italy;
D. Shatilov, BINP, Novosibirsk, Russia

Abstract

The recently proposed Crab Waist scheme of beam-beam collisions can substantially increase the collider luminosity since it combines several potentially advantageous ideas. One of the basic ingredients of the scheme is the use of dedicated sextupoles in the interaction region for the vertical beta function waist rotation at the interaction point. In this paper we show how this nonlinear focusing helps to suppress betatron and synchrobetatron resonances arising in beam-beam collisions due to particles' vertical motion modulation by their horizontal oscillations.

INTRODUCTION

In high luminosity colliders with standard collision schemes the key requirements to increase the luminosity are: very small vertical beta function β_y at the interaction point (IP), high beam intensity and large horizontal emittance ε_x and beam size σ_x. However, β_y can not be much smaller than the bunch length σ_z without incurring in the "hour-glass" effect. It is, unfortunately, very difficult to shorten the bunch in a high current ring without exciting instabilities. In turn, the beam current increase may result in high beam power losses, beam instabilities and a remarkable enhancement of the wall-plug power. These problems can be overcome with the recently proposed Crab Waist (CW) scheme of beam-beam collisions [1] where a substantial luminosity increase can be achieved without bunch length reduction and with moderate beam currents.

In the following we briefly describe the Crab Waist collision concept and discuss in detail one of the basic mechanizms that allows increasing the luminosity in crab waist collisions, namely, the suppression of beam-beam resonances induced due to modulation of particles' vertical motion by their horizontal oscillations. Numerical examples demonstrating the effect of crab waist sextupoles are also shown.

CRAB WAIST CONCEPT

The Crab Waist scheme of beam-beam collisions can substantially increase collider luminosity since it combines several potentially advantageous ideas. Let us consider two bunches colliding under a horizontal crossing angle θ (as shown in Fig. 1a). Then, the CW principle can be explained, somewhat artificially, in the three basic steps. The **first one** is large Piwinski angle. For collisions under a crossing angle θ the luminosity L

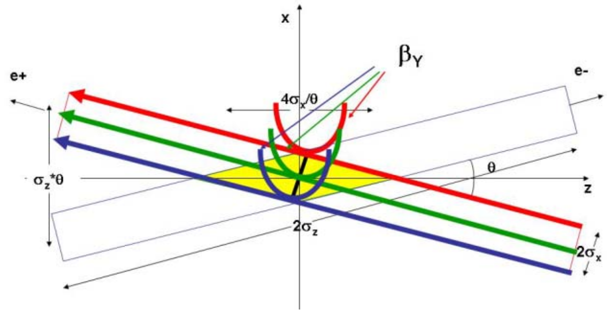

a) Crab sextupoles OFF.

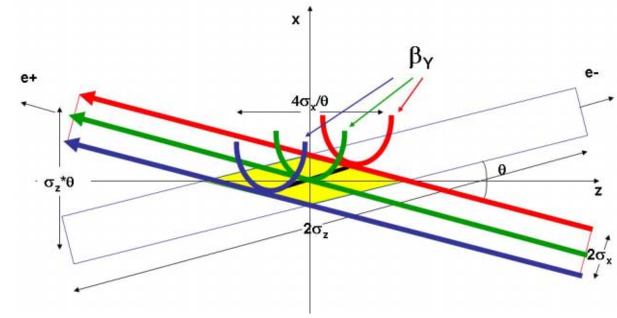

b) Crab sextupoles ON.

Figure 1: Crab Waist collision scheme.

and the beam-beam tune shifts scale as (see, for example, [2]):

$$L \propto \frac{N\xi_y}{\beta_y^*}; \quad \xi_y \propto \frac{N\sqrt{\beta_y^*/\varepsilon_y}}{\sigma_z\theta}; \quad \xi_x \propto \frac{N}{(\sigma_z\theta)^2} \tag{1}$$

with N being the number of particles per bunch. Here we consider the case of flat beams, small horizontal crossing angle $\theta << 1$ and large Piwinski angle $\phi >> 1$, where Piwinski angle is defined as:

$$\phi = \frac{\sigma_z}{\sigma_x} tg\left(\frac{\theta}{2}\right) \approx \frac{\sigma_z}{\sigma_x}\frac{\theta}{2} \tag{2}$$

The idea of colliding with a large Piwinski angle is not a new one (see, for example, [3]). It has been also proposed for hadron colliders [4, 5] to increase the bunch length and the crossing angle. In such a case, if it were possible to increase N proportionally to $\sigma_z\theta$, the vertical tune shift ξ_y would remain constant, while the luminosity would grow proportionally to $\sigma_z\theta$, see (1). Moreover, the horizontal tune shift ξ_x drops like $1/\sigma_z\theta$. However, differently from [4, 5], in the crab waist scheme described here the Piwinski angle is increased by decreasing the horizontal beam size and increasing the crossing angle. In this way we can gain in luminosity as well, and the horizontal tune shift decreases. Moreover, parasitic collisions (PC) become negligible since with higher crossing angle and smaller horizontal beam size the beam separation at the PC is large in terms of σ_x. But the most important effect is that the overlap area of the colliding bunches is reduced, since it is proportional to σ_x/θ (see Fig. 1).

Then, as the **second step**, the vertical beta function β_y can be made comparable to the overlap area size (i.e. much smaller than the bunch length):

$$\beta_y^* \approx \frac{\sigma_x}{\theta} << \sigma_z \tag{3}$$

It worth to note that usually it is assumed that ξ_y (see the expression for L in (1)) always reaches the maximum allowed value, so called "beam-beam limit". So, reducing β_y at the IP gives us several advantages:

- Luminosity increase with the same bunch current.
- Possibility of the bunch current increase (if it is limited by ξ_y), thus farther increasing the luminosity.
- Suppression of the vertical synchrobetatron resonances [6].
- Reduction of the vertical tune shift with the synchrotron oscillation amplitude [6].

Besides, there are additional advantages in such a collision scheme: there is no need in decreasing the bunch length to increase the luminosity as proposed in standard upgrade plans for B- and Φ-factories. This will certainly helps solving the problems of HOM heating, coherent synchrotron radiation of short bunches, excessive power consumption, etc.

However, large Piwinski angle itself introduces new beam-beam resonances which may strongly limit the maximum achievable tune shifts (see [7], for example). At this point the crab waist transformation enters the game boosting the luminosity. This is the **third step**. As it is seen in Fig. 1b, the beta function waist of one beam is oriented along the central trajectory of the other one. In practice the CW vertical beta function rotation is provided by sextupole magnets placed on both sides of the IP in phase with the IP in the horizontal plane and at π/2 in the vertical one (as shown in Fig. 2).

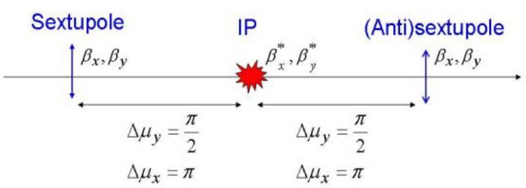

Figure 2: Crab sextupole locations.

The crab sextupole strength should satisfy the following condition depending on the crossing angle and the beta functions at the IP and the sextupole locations:

$$K = \frac{1}{\theta}\frac{1}{\beta_y^*\beta_y}\sqrt{\frac{\beta_x^*}{\beta_x}} \tag{4}$$

The crab waist transformation gives a small geometric luminosity gain due to the vertical beta function redistribution along the overlap area. It is estimated to be of the order of several percent [8]. However, the dominating effect comes from the suppression of betatron (and synchrobetatron) resonances arising (in collisions without CW) due to the vertical motion modulation by the horizontal betatron oscillations [9, 10].

In the following we explain the mechanism of beam-beam resonances suppression.

SUPPRESSION OF RESONANCES

First of all, for large Piwinski angles ϕ>>1 we need to change the concept of Collision Point (CP). Indeed, for large horizontal separations (in units of σ_x) the vertical beam-beam kick drops as $1/R^2$, while the horizontal one drops as 1/R. It means that for the vertical kick the center of the opposite bunch becomes not so important and can be not seen at all by the particles with large longitudinal displacements due to large horizontal separation. Thus CP has to be defined in a different way: it is *the point where a test particle crosses the longitudinal axis of the opposite beam*. In particular it means that the X-coordinate of CP in the "strong" frame is always zero, by the definition.

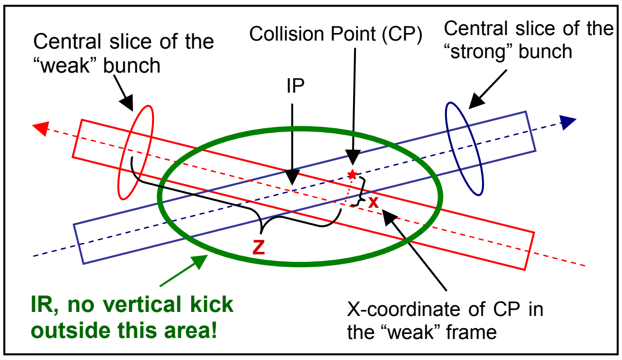

Figure 3: Collision with large Piwinski angle.

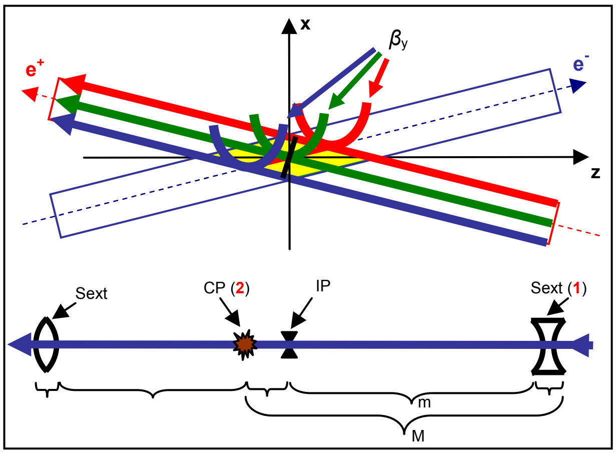

Figure 4: Crab Waist scheme.

Now let us show that the CW transformation kills the vertical betatron phase modulation. According to [9] the transport matrix ***M*** (see Fig. 4) from the entrance of the first sextupole (point 1) to the CP (point 2), vertical betatron motion only, can be written as:

$$M = \begin{pmatrix} 1 & L \\ 0 & 1 \end{pmatrix} \cdot \begin{pmatrix} m_{11} & m_{12} \\ m_{21} & m_{22} \end{pmatrix} \cdot \begin{pmatrix} 1 & 0 \\ V & 1 \end{pmatrix} \qquad (5)$$

where the first matrix corresponds to the drift space from IP to CP, L being the drift length, the last matrix corresponds to the sextupole, considered here as a thin linear lens, and in the middle we have the unperturbed matrix ***m*** from the sextupole location to the IP. For this unperturbed matrix we have $m_{22} = 0$, since $\alpha_y = 0$ at the IP and $\Delta\mu_y = \pi/2$. As a result we get $M_{22} = 0$ as well. On the other hand, considering the "new" lattice (sextupoles included) we can write the standard formula for M_{22}:

$$M_{22} = \sqrt{\beta_y / \beta_{1y}} \cdot \left(\cos(\Delta\mu_{1y}) - \alpha_{1y} \cdot \sin(\Delta\mu_{1y})\right) \qquad (6)$$

where β_{ly} and α_{ly} are the beta- and alpha-functions at the CP. Since it is the waist at the CP, α_{ly} must be equal to zero, so we get $\cos(\Delta\mu_{1y}) = 0$, resulting in $\Delta\mu_{1y} = \pi/2$, that is exactly what we wanted. In the other words, the vertical betatron phase advance from the first sextupole to CP and then from CP to the second sextupole remains to be $\pi/2$ for all the particles independently on their X-coordinate. This feature allows substantial increase of the beam-beam tune shift ξ_y.

We performed a number of beam-beam simulations which confirmed advantages of the Crab Waist scheme. In Fig. 6 one can see two luminosity tune scans performed for the SuperB set of parameters [11]. The "geographical map" colors were used: red corresponds to the maximum luminosity, blue – to the minimum. One can see a clear resonance suppression and "good" areas expansion when the Crab sextupoles are switched on. It worth to note that the bunch current in Fig. 5b is higher by a factor of 2.5! One more example is given in Fig. 6, where the beam tails and vertical blowup (r.m.s. beam size which affects the luminosity) for one of the good working points are shown versus the bunch current.

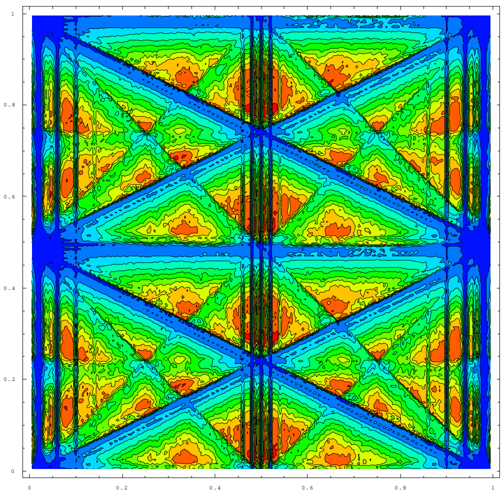

Figure 5a: Luminosity tune scan, CW=0.

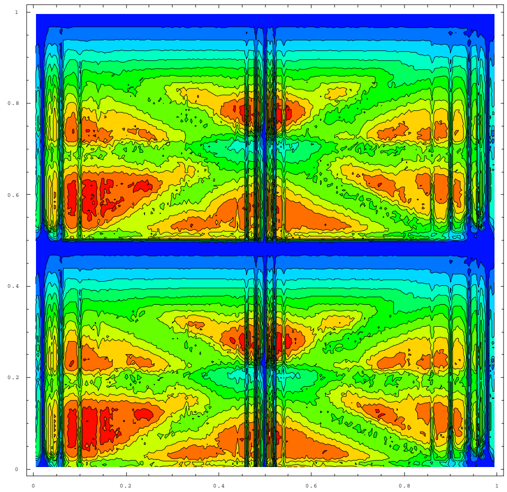

Figure 5b: Luminosity tune scan, CW=1.

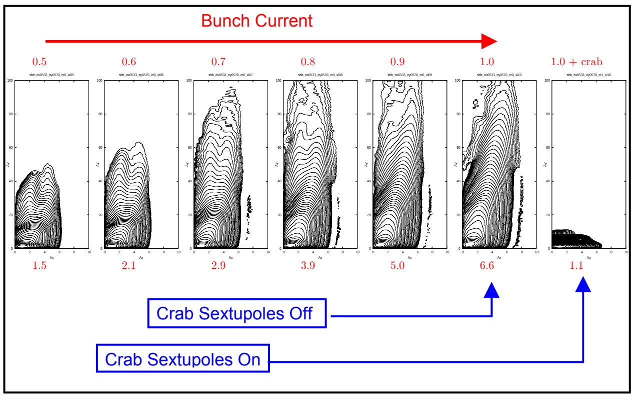

Figure 6: Beam tails and vertical blowup (numbers at the bottom) vs. bunch current and Crab Waist.

CONCLUSIONS

Collision scheme with large Piwinski angle and Crab Waist looks very attractive, since it strongly suppress the beam-beam resonances, thus allowing significant increase of the beam-beam tune shift ξ_y and the collider luminosity. This has been confirmed by the recent experimental results obtained on DAΦNE [12].

REFERENCES

[1] P. Raimondi, 2nd SuperB Workshop, Frascati, 2006.
[2] D. Shatilov and M. Zobov, ICFA BDN 37, 99 (2005).
[3] K. Hirata, Phys.Rev.Lett.74:2228-2231,1995.
[4] K.Takayama et al., Phys.Rev.Lett.88:144801,2002.
[5] F. Zimmermann, F. Ruggiero, PRSTAB5 :061001.
[6] D. Pestrikov, Nucl.Instrum.Meth. A336, 427 (1993).
[7] K. Ohmi et al., PRSTAB 7, 104401 (2004).
[8] I. Koop, private communications.
[9] P. Raimondi et al., e-Print:physics/0702033, 2007.
[10] K. Ohmi et al., PAC07, p.1493.
[11] "SuperB Conceptual Design Report", 2007, arXiv: 0709.0451.
[12] C. Milardi et al., WEPP036, this Conference.

COMMISSIONING OF THE IGP FEEDBACK SYSTEM AT DAΦNE

Alessandro Drago (INFN/LNF, Frascati, Italy), John Fox (SLAC, Menlo Park, USA),
Dmitry Teytelman (Dimtel, San Jose, USA), Makoto Tobiyama (KEK, Ibaraki, Japan).

Abstract

The iGp (Integrated Gigasample Processor) is an innovative digital bunch-by-bunch feedback system developed by a KEK / SLAC / INFN-LNF joint collaboration. The processing unit can sample at 500 MHz and compute the bunch-by-bunch output signal for up to ~5000 bunches. The feedback gateware code is implemented inside just one FPGA (Field Programmable Gate Array) chip, a Xilinx Virtex-II. The FPGA implements two banks of 16-tap FIR (Finite Impulse Response) filters. Each filter is realtime programmable through the operator interface. At DAΦNE, the Frascati Φ-Factory, two iGp units have been commissioned in the April 2007. The iGp systems have substituted the previous betatron feedback systems. This insertion has been very fast and has shown no problems involving just a substitution of the old, less flexible, digital systems, letting unchanged the baseband analog frontend and backend. The commissioning has been very simple, due to the complete and powerful EPICS operator interface, working well in local and remote operations. The software includes also tools for analyzing post processor data. A description of the commissioning with the operations done is reported.

INTRODUCTION

In lepton circular accelerators, nowadays digital bunch-by-bunch feedback systems are largely used to damp coupled bunch instabilities in both transverse and longitudinal plans. The need of this kind of systems and the continuous technology developments ask for always new powerful designs [1].

To avoid wasting efforts in term of manpower and budget, large international collaborations between high energy laboratories feedback teams have been carried on with very good results in several colliders and light sources [2][3]. Commissioning done on multiple machines makes much more simple and fast testing and debugging hardware and software of the systems.

The iGp feedback has been designed by joint efforts of feedback teams from high energy laboratories spread in three continents. At DAΦNE, the Frascati Φ-Factory, two iGp feedback units have been commissioned in the April 2007 and other two in this year. In the following, starting from a system overview, the commissioning operative procedures and results are described.

SYSTEM OVERVIEW

The iGp (Integrated Gigasample Processor) [4] [5] is an innovative digital bunch-by-bunch feedback system developed by a KEK / SLAC / INFN-LNF joint collaboration. The processing unit can sample at 500 MHz and compute the bunch-by-bunch output signal for up to ~5000 bunches. The feedback gateware code is implemented inside just one FPGA (Field Programmable Gate Array) chip, a Xilinx Virtex-II. The FPGA implements two banks of 16-tap FIR (Finite Impulse Response) filters. Each filter is realtime programmable through the operator interface. In the Fig. 1, the iGp block diagram is shown.

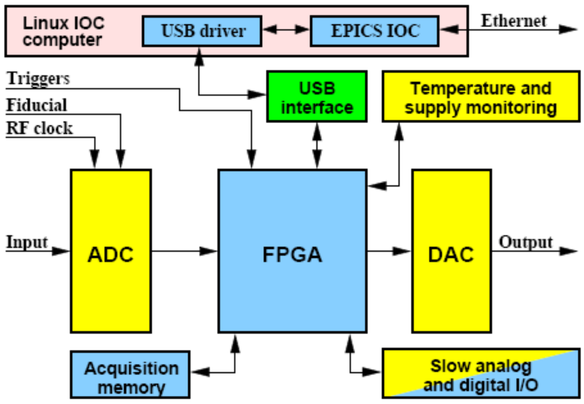

Figure 1: iGp block diagram.

The FPGA communicates by a USB interface with a commercial personal computer located in the iGp chassis. An EPICS IOC software package [6] is running in the internal PC Linux environment and by an Ethernet link can talk to the operator interface in the EPICS client PC.

In Fig. 2 the EPICS operator interface plotting two FIR filter coefficient sets is shown.

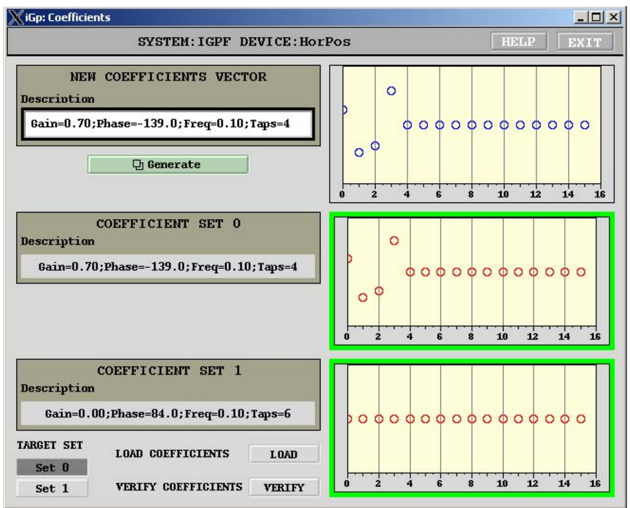

Figure 2: FIR filter coefficient set EPICS panel.

In order to produce a new coefficient set, the parameters to be chosen by the human operator are the following: gain (in the range from 0 to 1), phase (-180, 180 in degrees), filter center frequency, number of taps (from 1 to 16). Other important parameters can be set using the Control panel shown in Fig. 3.

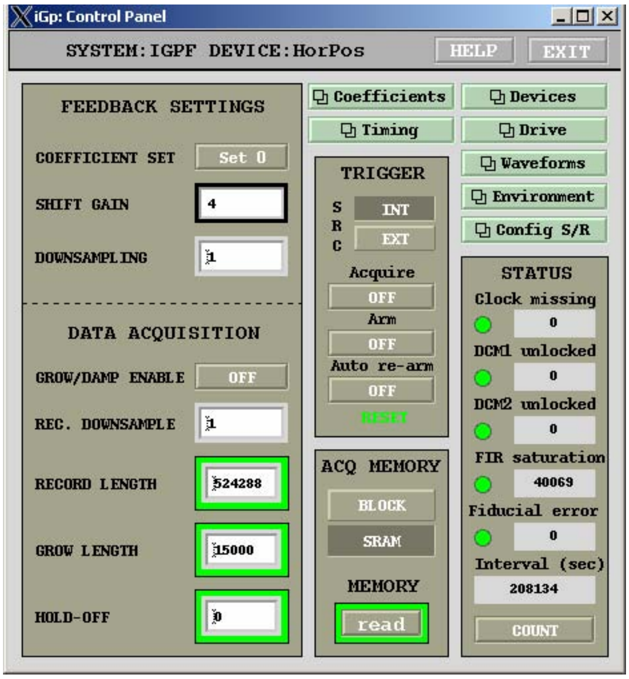

Figure 3: EPICS Control panel.

In order to operate on the feedback settings, the Control panel can allow choosing the coefficient set (1 or 2), the shift gain (0:7), meaning a binary shift by 0:7 position in the output signal, and the downsampling factor.

Other Fig. 3 command blocks manage data acquisition for offline analysis, internal or external trigger feature and internal memory size to be used for data acquisition. Diagnostics about feedback correct work is shown in the status block. Other important features can be called by seven subpanel pointers in the right top of the Fig. 3. In particular, the “Waveforms” panel shows the real time behaviour plot in time and frequency, the “Drive” panel can excite the beam or a specific bunch pattern by different waves generated by the system, the “Timing” module (see Fig. 4) can modify the front end or back end timing set, the “Environment” panel (see Fig. 5) shows internal temperatures for diagnostics purpose, the “Config s/r” panel is used to save or restore the feedback setup.

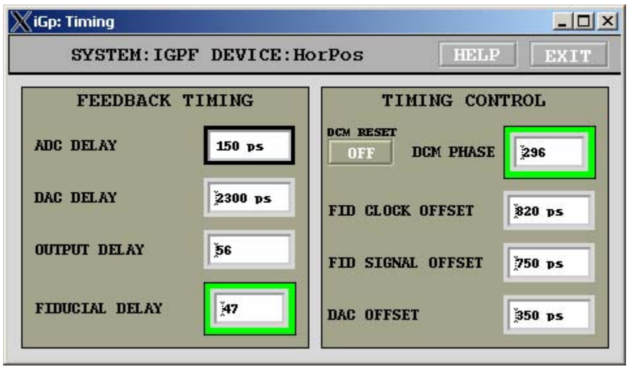

Figure 4: EPICS Timing panel.

COMMISSIONING AT DAΦNE

Two iGp units have been commissioned in the April 2007 at DAΦNE. The iGp systems have substituted the previous betatron feedback systems. The insertion has been very fast and has shown no problems involving just a substitution of the old, less flexible, digital systems [7], letting unchanged the baseband analog frontend and backend.

Commissioning, as it is well known, is the phase of installation and start-up of a technical supply, and of verification that it is complying with specifications.

The iGp commissioning has been very simple, using the powerful EPICS operator interface, working well both in local and remote operations. The software includes also tools for analyzing post processor data. A description of the operations done to find the best feedback setup and to complete the commissioning is reported below.

The iGp commissioning has been very fast and basically has been stepped in the following five operations:

1) front end timing (single bunch)
2) back end timing (single bunch)
3) best betatron phase response selection, with and without using white noise excitation (single bunch);
4) gain and shift gain selection (single bunch);
5) final tests with multibunch injected pattern.

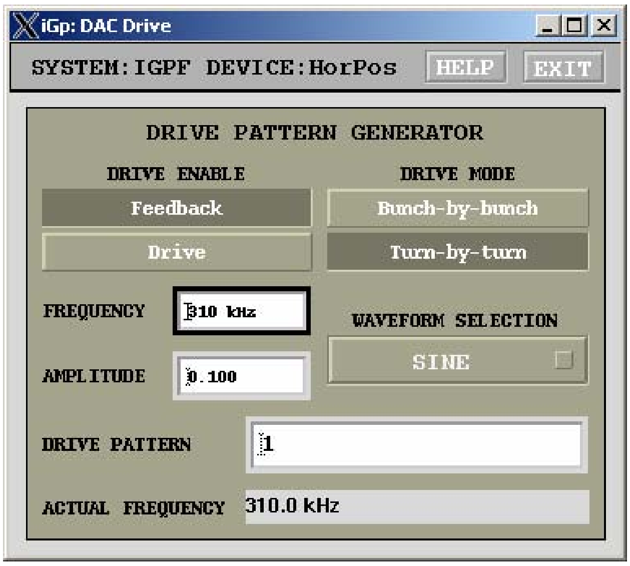

Figure 5: EPICS Drive panel.

The first point (frontend timing) has been accomplished storing a single bunch in the ring, sweeping the f.e. delay value and finding the peak of the response (in the “Waveforms” panel) for a single bunch. The use of an orbit bump at the feedback pickup can be helpful.

The second goal has been achieved in two equivalent ways: selecting a single tap filter or using an output pulse generated through the “Drive” panel. In both cases, looking at the two kicker downstream ports by an oscilloscope and sweeping the b.e. delay value, it has been possible to find a precise overlap between the excitation and the bunch signals. A check on the signal equalization in magnitude and skew between the two kicker ports is always very useful.

The third point, i.e. to find the best betatron phase advance, has been accomplished experimentally, storing in the ring a single bunch, exciting it by external white noise, then closing the feedback loop and sweeping the feedback betatron phase on 360 degrees to evaluate the best value looking at the betatron sidebands by using a spectrum analyzer or directly in the "Waveforms" panel.

Feedback gain and shift gain have been set for a single bunch pattern and, after this step, injecting multiple bunches with progressively increasing beam currents. At high currents it is possible to find better and more precise setups. This ways to proceed is necessarily iterative because beginning with a "rough" feedback setup makes possible to store multibunch patterns and to increase the beam current. At this point it is possible to try a new, more suitable setup, changing feedback parameters in real time, without loosing the beam, by small steps. In particular it may be interesting to note that often the best filter center frequency at high beam current can differ from the best single bunch value in a range of 5%.

The first commissioning of the iGp feedback, after a fast hardware and software installation including the necessary Ethernet connections, has requested only two hours of dedicated machine time for each system.

Analysis off line tools [8] have used to study beam dynamic in DAΦNE: in the e+ horizontal plane, an extremely fast mode -1 limits the beam stability and the storable beam current.

2008 UPGRADE

During the year 2008 other two iGp system have been installed at DAΦNE, completing the transverse planes in both rings. A new software and gateware revision has been implemented in the four iGp units and tested with the beams. The EPICS client package, for Fedora-8 Linux environment, has been installed in a powerful dual core personal computer used as dedicated interface for the operators in control room.

With the last revision, new features have been tested as, for example, an off-line tool to measure the betatron bunch-by-bunch tune spread, as shown in Fig. 6.

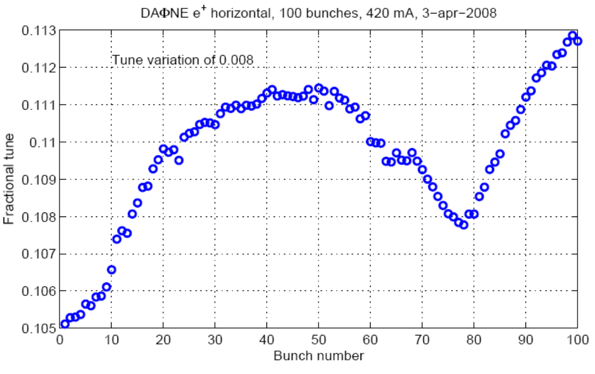

Figure 6: Bunch-by-bunch e+ horizontal tune.

CONCLUSION

Four iGp feedback systems have been commissioned in the transverse plane at DAΦNE. The insertion of these new systems has been done rapidly and has shown no problems requesting only a very little dedicated machine time. The commissioning has been very simple, due to the complete and powerful EPICS operator interface, working well both in local and in remote operations.

Powerful diagnostics inside the system help to understand beam current limits, to study beam dynamics and evaluate feedback performances. Analysis off line tools have shown an extremely fast mode -1 and a large tune spread in the e+ horizontal plane limiting the beam stability and the storable beam current.

REFERENCES

[1] A.Drago, "Trends in Fast Feedback R&D", arXiv:0806.1864 , Jun 12, 2008.

[2] J.D.Fox, H.Hindi, I.Linscott, J.Olsen, G.Oxoby, L.Sapozhnikov, D.Teytelman (SLAC), A. Drago, M. Serio (INFN-LNF), J.Byrd, J.Corlett (LBL), "Operation and Performance of a Longitudinal Damping System using Parallel Digital Signal Processing", EPAC 1994.

[3] J.Fox, S.Prabhakar, D.Teytelman, A.Young (SLAC), G.Stover (LBL, Berkeley), A.Drago, M.Serio (INFN-LNF), S.Khan, T.Knuth (Bessy, Berlin), Y.J.Kim, M.K.Park (Pohang U.Sci.Tech.), "Programmable DSP Based Multibunch Feedback: Operational Experience from Six Installations", SLAC-PUB-8410, May 2000. Published in *Cambridge 2000, Beam instrumentation* 226-233.

[4] D.Teytelman, C.Rivetta, D.Van Winkle, R.Akre, J.Fox, A.Krasnykh, (SLAC), A.Drago, (INFN/LNF), J.Flanagan, T.Naito, M.Tobiyama, (KEK), "Design and Testing of Gproto Bunch-by-Bunch Signal Processor", THPCH103, EPAC2006.

[5] D.Teytelman,"iGp-120F Signal Processor - Technical User Manual", Rev.1.4, Jan.5, 2008.

[6] EPICS documentation: http://www.aps.anl.gov/epics/

[7] A.Drago, A.Argan, M.Serio (Frascati), "Fast Electronics for the DAFNE Transverse Feedback Systems", ICALEPCS-2001-WEAP048, Nov 2001. Published in eConf C011127:WEAP048, 2001. Also in *San Jose 2001, Accelerator and large experimental physics control systems* 376-379. e-Print Archive: physics/0111209.

[8] Shyam Prabhakar, "New diagnostics and cures for coupled bunch instabilities". SLAC-R-554, SLAC-R-0554, SLAC-554, SLAC-0554, UC-410, UMI-99-86494-MC, Feb 2000. 188pp. Ph.D. Thesis.

A WIDE RANGE ELECTRONS, PHOTONS, NEUTRONS BEAM FACILITY

B. Buonomo, G. Mazzitelli, F. Murtas, L. Quintieri
INFN/LNF, Via E. Fermi 40, 00044, Frascati (Roma)
P. Valente
INFN Roma, P.le Aldo Moro 5, Roma

Abstract

The DAFNE Beam Test Facility (BTF) is in operation since the 2003 and has been continuously improved and upgraded in order to take into account the many different requests coming from the high energy and accelerator community. The facility was initially optimized to produce single electron and positron in the 25-750 MeV energy rage, manly for high energy detector calibration and testing; it can now provide beam in a wider range of intensity, up to 10^10 electrons/sec, typically needed for accelerator diagnostic tests. In the last two years the facility has also been modified in order to produce tagged photons, and the possibility to deliver tagged neutrons in the MeV energy range is under study. The main results obtained, the performance and the most significant characteristics of the facility diagnostics and operation are presented, as well as the users experience collected during these years of operation.

INTRODUCTION

The BTF is part of the DAFNE collider devoted to the production of very high rate Φ meson. It consist of a high current electron-positron LINAC and 510 MeV, a dumping ring and two 100 m Main Rings (MR).

The e+/e- beam from the LINAC is stacked and damped in the accumulator ring for being subsequently extracted and injected into the MR. When the injector is not delivering beam to the accumulator, the LINAC beam can be transported into the Beam Test area by a dedicated transfer line (BTF line). The main components of the line are described in the following [1].

The main parameters of the S-band LINAC (length 60 m) are listed in the table below:

Table 1: LINAC parameters

Particle	Electron	Positron
Energy	800 MeV	510 MeV
Max. Current	500 mA/pulse	100 mA /pulse
Transverse Emmittance	≤ 1 mm mrad at 510 MeV	≤ 10 mm mrad at 510 MeV
Energy spread	~1% at 510 MeV	~2.5 % at 510 MeV
Pulse duration	1 or 10 ns	
Repetition rate	1-50 Hz	

Electron (positron) beams in that energy range are suitable for many purposes: high energy detector calibration, low energy calorimetry, low energy electromagnetic interaction studies, detector efficiency and aging measurements, test of beam diagnostic devices etc. Since the end of 2005 a photon tagging system has been installed and started operation with the first users.

THE BTF TRANSFER LINE

The layout of the BTF transfer line is shown in Fig.1. The transfer line is about 21 m long, from the outlet of DHPTB101 (the pulsed dipole extracting the beam to the BTF line) to the bending magnet DHSTB002 in the BTF hall that is one of the two beam exits, and has an inner diameter of about 5 cm. All the line is kept under high vacuum (10-10 bar) with the exception of the final part (from the DHSTB002 inlet to the 2 beam exits in the experimental hall), that is working, at present time, at 10-4 bar. The part under high vacuum ends with a Be window of 0.5 mm thick. The 10 cm air gap between the Be window and the inlet of the DHSTB002 bending allows the insertion of the silicon micro-strip chambers needed for tagged photon production.

The injector system provides beam both to the DAFNE damping ring and to the test beam area. The DHPTB101 allows driving each of 49 pulses per second either to accumulator or to the BTF line, thus permitting a quasi-continuous operation, limited only by electron/positron LINAC switch (30-40 sec). Indeed, even when beams are injected into the DAFNE main rings, not all the bunches are needed for machine filling, so that beam can still be delivered to the BTF, but with a lower repetition rate [2]. Obviously, in this operation scheme the pulse duration and the primary beam energy must be the same of DAFNE (10 ns). This is not a strong limitation, since the facility is mainly operated in single particle mode (electrons/positrons), which is the ideal configuration for detectors calibration and testing.

The intensity and the spot of the beam at the begging of BTF line can be measured by a beam current monitor (BCM1 beam charge to charge output ratio 50:1) and a fluorescent screen of beryllium-oxide type (FLAG01).

The intensity of the beam can be tuned by means of a vertical collimator (SLTB01), located upstream respect to FLAG01 in the BTF transfer line. In the high multiplicity (107 up to 1010 particles/bunches) range, the diagnostic elements of the line are completed by another beam charge monitor BCM2 (high sensivity, beam charge to output charge ratio 5:1) and two fluorescent screens FLAG02 (beryllium oxide), FLAG03(YAG:CE) mounted at the two exits of the line. In the following, the number of particles per bunch is also referred as “multiplicity of the beam”.

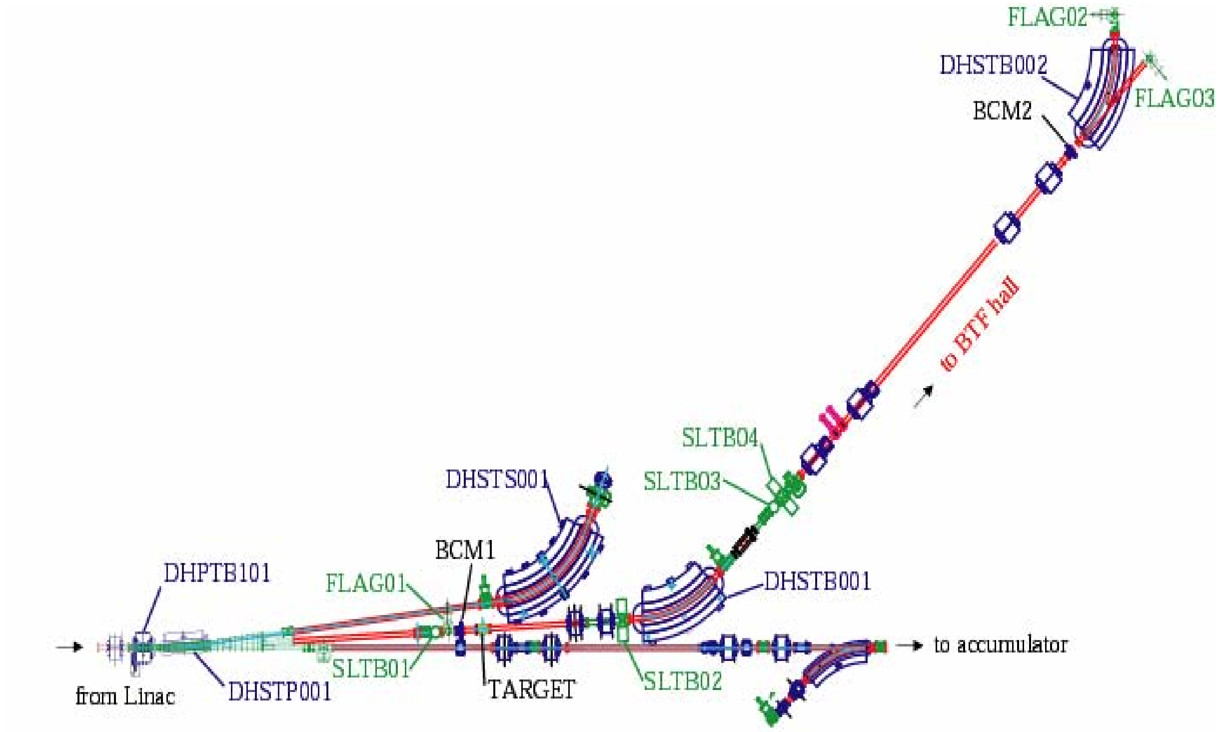

Figure 1: The BTF transfer line. In figure are shown the diagnostic elements mounting on the line, and the position of the target and the four collimator which is necessary to produce a beam with a variable number of particles.

When the facility operates in low multiplicity range, it is necessary to strongly reduce the primary beam of the LINAC. The minimum beam current that can be detected by the BCM2 current monitors is I≈1 mA, and the corresponding number of electrons (positrons) is 107/pulse. It is thus necessary to strongly reduce the number of particles to reach the few particles range. The reduction of the particle multiplicity can be achieved with different methods; the one chosen for the BTF operation is the following: first the LINAC beam is intercepted by a variable thickness TARGET, in order to strongly increase the energy spread of the primary beam; then the out coming particles are energy selected by means of a bending magnet DHSTB001 and two horizontal collimators (SLTB02 and SLTB04).

This energy selector accepts a small fraction of the resulting energy distribution of particles, thus reducing the number of electron/positron by a large and tunable factor. The TARGET is shaped in such way that three different values of radiation length can be selected (1.7, 2.0, 2.3 X0) by inserting it at different depths into the beam-pipe. The momentum of the selected particles has a resolution better than 1%.

After the energy selector, the beam is driven by a 12 m transfer line into the experimental hall by means of a focusing system of four quadrupoles. At the end of the BTF line a second bending magnet allows to use two separate beam-lines alternatively: a straight line is used when the magnet is off, while particles exit from a 45 degrees curved line when the magnetic field is properly set. In table 2 the beam parameters of the facility operated at different multiplicity are reported.

Table 2: BTF parameters for electron/positron beam; A) time-sharing with the DAFNE collider operation, B) continuous operation.

Operation mode	Time sharing	Dedicated
Energy range	25-500 MeV	25 – 750 MeV
Repetition rate	20-49 Hz	49 Hz
Pulse duration	10 ns	1 or 10 ns
Multiplicity	1 up to 10^5	1 up to 10^{10}
Duty cycle	80%	96 %
Spot size (σ_x*σ_y)	~ 2x2 mm (low multliplicity) ~ 10x10 mm (high multiplicity)	
Divergence	~2mrad- 10mrad	
Energy resolution	< 1%	

BTF PERFORMANCE.

Since November 2002, the facility has hosted many users that have worked in different conditions of beam parameters (wide range of energy and multiplicity) running typically more then 250 days/year.

Many different diagnostic devices for spot size, position, multiplicity measurements have been developed and are available for user in the wide rage of energy and multiplicity. Since 2005, the tagged photon source has been designed, built and tested. The photons are produced by bremsstrahlung of electrons, on a pair of x-y silicon micro-strip chambers, placed at the inlet of the last bending magnet DHSTB002. The photons are tagged in energy using the same bending dipole: the walls of the curved beam-pipe inside the magnet are covered by 10 modules of silicon micro-strip detectors [3].

An example of calorimeter spectrum acquired with charge ADC is shown in Fig2. The individual peaks corresponding to the number of electrons can be easily identified. The total number of events in each peak should represent the probability of producing n particles: by fitting the distribution of the number of events in each peak with the Poisson function, the average number of particles can be determinated.

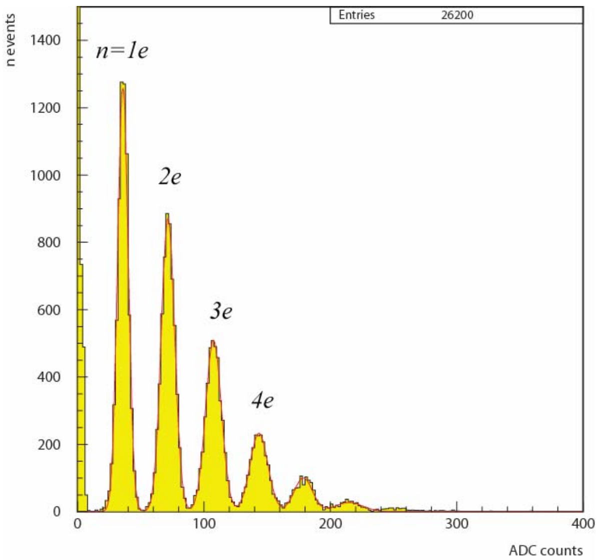

Figure 2: Calorimeter spectrum of BTF beam at low multiplicity.

The beam spot profile and position are measured by a x-y scintillating fiber system with millimetric resolution and multi-anode PMT readout, in the range from single particle up to 10^3 particles/pulse [4].

In the low multiplicity range a silicon micro-strip chamber (the active target of the photon tagged source) can be used to measure the beam spot profile and position with ≈ 200 micron resolution (Fig 3).

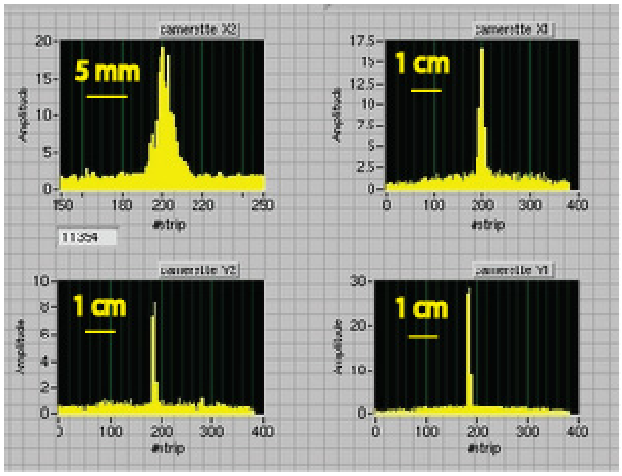

Figure 3: Beam spot profile acquisited with a silicon microstrip chamber.

CONCLUSIONS

The DAFNE Beam Test Facility showed very good performance, both from the point of view of operation reliability and the flexibility in order to cope with very different experimental needs. The diagnostic devices, data acquisition system and tools available for experiments are continuously improving.

In the last upgrade, the duty-factor of the facility has been greatly improved (up to 90%) thanks to the installation of a new dedicated pulsed dipole magnet (DHPTB101), capable of driving any of the 50 Linac pulses either to the accumulator ring or to the BTF transfer line.

First preliminary study has been done in order to develop a neutron source at the Beam Test Facility.

ACKNOWLEDGEMENTS

We deeply thank the DAFNE operators and the technical staff of the accelerator division for having continuously supported the upgrade of the Beam Test Facility

REFERENCES

[1] G. Mazzitelli, A. Ghigo, F. Sannibale, P. Valente and G. Vignola, “Commissioning of the DAFNE beam test facility” Nucl Instr. Meth A 515 (2003) 516.

[2] B. Buonomo, G. Mazzitelli and P. Valente, “Performance and upgrade of the DAFNE Beam Test Facility”, IEEE Nuclear Science symposium, Rome 2004.

[3] B. Buonomo et al, “A Tagged photon source at the Frascati Beam-Test Facility”, DIPAC 2007, Venice, Italy, May 20-23, 2007.

[4] M. Anelli, B. Buonomo, G. Mazzitelli, and P.Valente, *A scintillating-fiber beam profile monitor for the* DAFNE BTF, LNF 04/24P (2004).

SIMULATIONS OF THE EMITTANCE COMPENSATION IN PHOTOINJECTORS AND COMPARISON WITH SPARC MEASUREMENTS

C. Ronsivalle, L. Giannessi, M. Quattromini, ENEA, Frascati (Roma), Italy,
M. Ferrario, L. Ficcadenti, D. Filippetto, V. Fusco, B. Marchetti, M. Migliorati, A. Mostacci, L. Palumbo, C. Vaccarezza, INFN/LNF, Frascati (Roma), Italy
A. Cianchi, INFN-Roma II, Roma, Italy
A. Bacci, A.R. Rossi, L. Serafini, INFN-Milano, Milano, Italy

Abstract

FEL photoinjectors are based on the emittance compensation process, by which a high brightness beam can be accelerated without degradation. The experimental results obtained in the SPARC facility for which the beam dynamics has been extensively simulated confirm the theoretical predictions. The paper illustrates the most relevant beam dynamics results as well as a comparison between simulations and measurements.

SHORT REVIEW OF EMITTANCE COMPENSATION IN PHOTOINJECTORS

The new generation of linac photoinjectors employs the emittance compensation technique in order to get the high brightness electron beams required for the production of FEL radiation in the range from UV to X-rays.

A typical photoinjector scheme consists in a RF gun provided with a photocathode illuminated by a few picoseconds laser pulse followed by a linac accelerating the electron bunch emitted by the cathode to relativistic energies. As the space charge induced rms emittance growth in the RF gun is partially correlated, it is possible to achieve a decreasing evolution of the rms emittance from the gun exit to the output of the booster.

The emittance compensation is well described theoretically in literature [1, 2]: it is done by locating a solenoid at the exit of the gun followed by a drift space and then properly matching the beam to the following accelerating sections according to the so called "invariant envelope" condition, consisting in injecting the beam at a laminar waist (σ'=0) in a matched accelerating structure of a linac booster given by

$$\gamma' = \frac{2}{\sigma_w} \cdot \sqrt{\frac{\hat{I}}{2 I_o \gamma}} \qquad (1)$$

where I_o=17kA y is the Alfven current,γ'~2Eacc..

This condition, according to the theoretical description of ref. [1], guarantees the damping of the normalized emittance oscillations (also referred as plasma oscillations), that are caused by slice envelope oscillations produced by mismatches between the space charge correlated forces and the external focusing gradient. The process has been extensively simulated: figures 1 and 2 shows the emittance evolution in the region downstream the gun and from the gun to the booster exit in optimized matching conditions with the linac for a 1nC charge and different pulse shapes

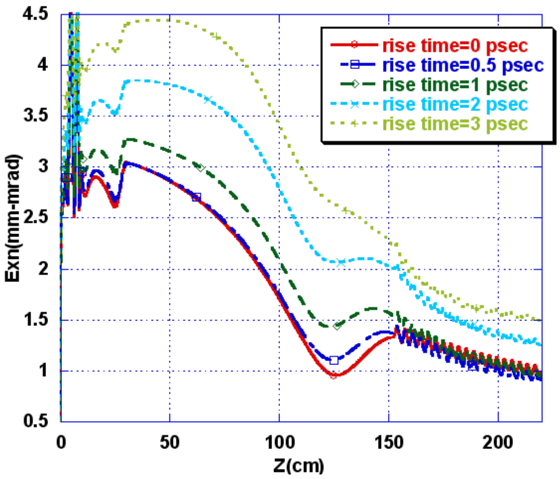

Figure 1: PARMELA simulation of emittance compensation for a 1nC-10ps FWHM pulse and different pulse rise time in the drift downstream the RF gun

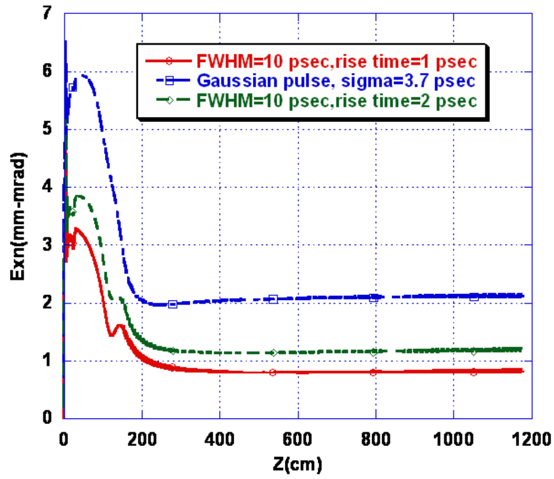

Figure 2: PARMELA simulation of emittance compensation for a 1nC beam and different pulse shapes from the RF gun to the booster exit

In the simulations the "invariant emnvelope" condition is fulfilled and the booster is placed in the position corresponding to the local maximum of the so called "double minimum" emittance oscillation (Ferrario working point [3]) in order to shift the second emittance minimum frozen at low level to the booster exit.

SPACE CHARGE MODELS

The emittance compensation process occours when the beam is in a regime dominated by the space charge, i.e. when the space charge collective force is largely dominant over the emittance pressure. Many numerical codes based on different models have been developed to simulate this regime.

Usually a first scan of initial parameters to identify possible operating points has done by using HOMDYN, a fast semi-analytical code that models the beam as a sequence of slices propagated by a set of envelope equations. It assumes a uniform transverse and longitudinal distribution and neglects the non-linearity in the electromagnetic electric fields. The further exploration of the working points is done by using multiparticle codes as PARMELA (SCHEFF-2D routine) [4] or ASTRA [5] using for the space charge fields the "static" approximation. It consists in calculating the self-fields by solving the Poisson equation for the electrostatic field in the reference frame where the beam may be considered at rest and then transforming the fields back to the laboratory frame where kicks to the particles are applied. In these calculations, assuming a cylindrical symmetry of the beam, a typical number of 20K macro-particles is used. The SCHEFF routine allows to treat also elliptical beams introducing a correction factor on the space charge fields if the ratio between the beam semiaxes doesn't exceed 1.2. If non-homogeneities in the beam spot generated by quantum efficiency variation on photocathode and non-uniformities of laser spot give a significative degradation of the emittance full 3D computations requiring more particles and mesh points than 2D are necessary. In order to evaluate in a quantitative way the beam quality a new parameter, referred as spatial autocorrelation, that is an index of how the uniformities are distributed has been recently introduced [6]: the knowledge of this parameter together with the standard deviation of the spot image allows to give an evaluation of the impact of non-uniformities on the emittance that results higher when the non-homogeneities are more localized. In this case the beam can be modelled by 3D codes such as PARMELA/SPCH3D or the parallel code IMPACT-T [7]. Both codes keep the "static" approximation, collecting and depositing the particles on a three-dimensional grid where the POISSON equation is solved in the beam rest frame. This approximation is good enough until the energy spread is not so high. However in order to handle high energy spreads the IMPACT-T code divides the beam in multiple energy-bins, for each one the space-charge forces are calculated and summed together before being interpolated to individual particles. Another peculiarity of IMPACT-T is the use of an integrated Green function to efficiently and accurately treat beams with large aspect ratio. Recently this last technique has been implemented also in the SPCH3D routine of an upgraded version of PARMELA named TStep [8] reducing the sensitivity to the aspect ratio of the cell dimensions that limited the applicability of the LANL version of PARMELA to aspect ratio not larger than 4.

The "static" approximation is completely disregarded in a different class of three-dimensional codes that are based on the use of retarded potential. Typical examples are TREDI [9] and RETAR [10] codes, that calculate the fields according to the Lienard-Wiechert formalism, taking into account the finite velocity propagation of the signals. This is accomplished by storing the histories of macro-particles and by tracking back in time the source coordinates until a retarded condition is fulfilled, that results in a much time consuming approach. Comparison with other codes [11] that don't take into account this effect show that the finite velocity propagation of the signals doesn't not affect the results in typical photoinjector and that the "retarded" mode is more suitable to describe other classes of problems such as CSR effects in bendings.

EMITTANCE COMPENSATION STUDIES IN SPARC

One of the aims of the SPARC R&D photoinjector facility [12] now under commissioning at INFN-Frascati laboratories is to study the emittance compensation process through accurate comparison between measurements and simulations.

The SPARC facility

The SPARC facility is devoted to the production of a high brightness electron beam driving SASE-FEL experiments at 530 nm and SASE@Seeding HHG tests at 266, 160, 114 nm. It is also the test prototype of the injector of the recently approved SPARX Project [4] for the generation of radiation in the range of 13.5-6 nm and 6-1.5 nm, at 1.5 and 2.4 GeV respectively both in SASE and seeded FEL configurations.The schematic layout is shown in Fig. 3. It consists of a UCLA/SLAC/BNL 1.6 cells S band RF gun with an incorporating metallic cathode operating at a maximum gradient of 120 MV/m followed by a solenoid lens composed of four independently powered coils and three SLAC-type travelling waves accelerating a 1nC-10ps beam with a projected emittance ≤ 2 mm-mrad and a slice emittance ≤ 1 mm-mrad. to 150-200 MeV.

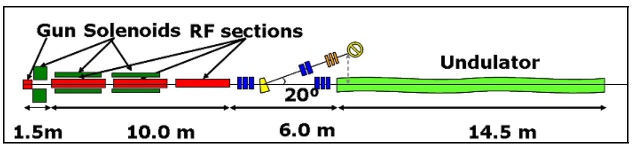

Figure 3: Schematic SPARC layout

The first two accelerating sections are embedded in a solenoid in order to match the beam envelope with the linac and to control the emittance during "velocity bunching" experiments in view of the use of this compression technique for the implementation in SPARX of the hybrid RF-magnetic compression scheme that is one of the peculiarities of the facility.

First SPARC commissioning phase

The first phase of the SPARC commissioning (fig. 4) consisted in characterizing the electron beam in the region downstream the gun by using the movable emittance-meter, a sophisticated diagnostic tool that allowed to measure the evolution of beam size, energy spread, rms transverse emittance and transverse phase space at different locations along the beamline in a range of 1-2.1 m from the cathode. The most relevant experimental results are reported in references [13,14].

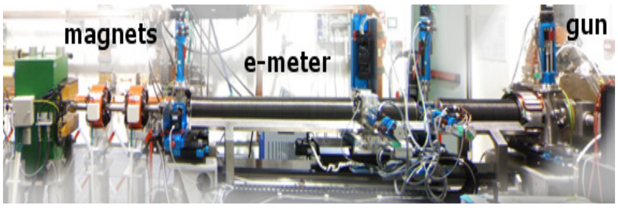

Figure 4: SPARC in the first commissioning phase

In this way it has been possible to study experimentally the emittance compensation process under different operating conditions (variation of pulse shape, charge, gun RF phase) and to perform accurate comparisons between measurements and PARMELA code simulations. The beam model was based for the longitudinal distribution on the cross-correlator measurement of the time profile and for the transverse distribution on the "virtual cathode" image obtained by splitting the laser beam before it enters in the vacuum system.

Some approximations are included in this model: as to the longitudinal distribution the modification of the pulse due to the Schottky effect is not taken into account that can be considered as a second-order effect and, as to the transverse distribution, it is assumed that the laser spot distribution is not strongly modified by disuniformities of the cathode emission. This last approximation was found very good expecially for rms spot sizes less than 400 µm.

The strategy of comparison between measurements and simulations has been done in two steps. The first one was based on the use of an equivalent uniform beam with σ_x and σ_y retrieved from the virtual cathode image and a longitudinal distribution equal to the measured pulse shape. Also due to the reduced level of ellipticity that usually was less than 1.1 it has been possible to use this equivalent beam in some fast 2D runs based on only 20K particles in which the consistency of the main operation parameters with the measured envelope has been checked, by moving the values within some small ranges of uncertainties around the measured value (±1° for the phase, ±5% for the charge and ±1% for the energy). Including these degrees of freedom in simulations is a way to take into account the systematic errors.

The second step of the comparison technique consists in the refinement of computations based on a full 3D model based on a number of particles up to 500K in order to take into account the local disuniformities of the laser spot to compare at the best the simulated and measured emittance. The number of mesh intervals used for these 3D calculations was 32 for the two transverse directions and 64 for the longitudinal direction. The mesh size is automatically adjusted by the code.

A short review of the most relevant results is shown in the plots of figure 5 with the corresponding initial laser spots and pulse shapes reported in figure 6. The emittance oscillations foreseen by the theory and simulations have been observed confirming the reliability of the theoretical and numerical model. In particular Figure 5c refers to the first experimental observation of the "double minimum" emittance oscillation" on which the SPARC working point is based [6]. Figure 7 shows a comparison between the phase spaces retrieved from the measurements and the computed ones in three different z-positions around the relative maximum of the emittance oscillation. A cross-shape is visible due to the fact that under laminar conditions different parts of the bunch reach the space charge dominated waist in different longitudinal positions.

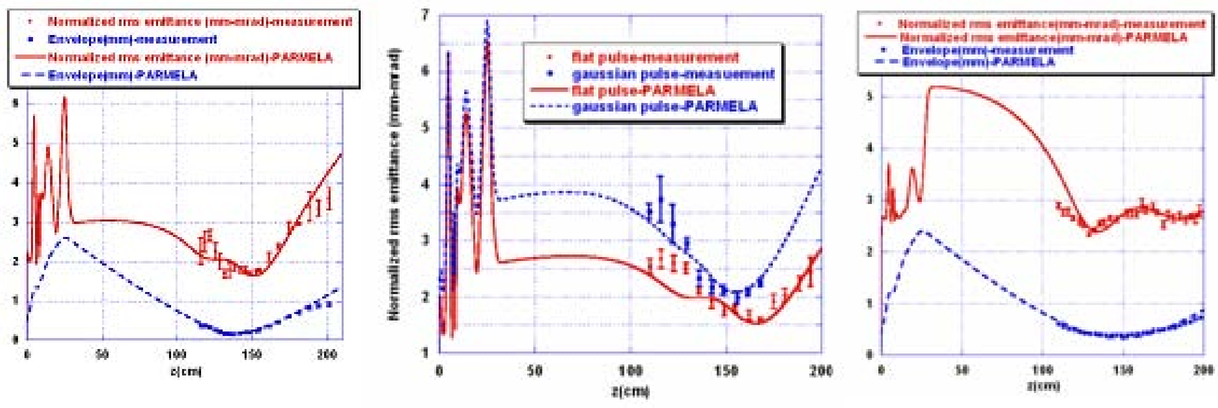

(a) (b) (c)

Figure 5: Emittance-meter measurements and simulation comparison: (a) Emittance and envelope vs z for the highest measured brightness beam (7 10^{13} A/m^2); (b) Emittance evolution comparison between a gaussian and a flat pulse with the same FWHM for a 740 pC beam (c) "Double minimum" emittance oscillation: emittance and envelope vs z.

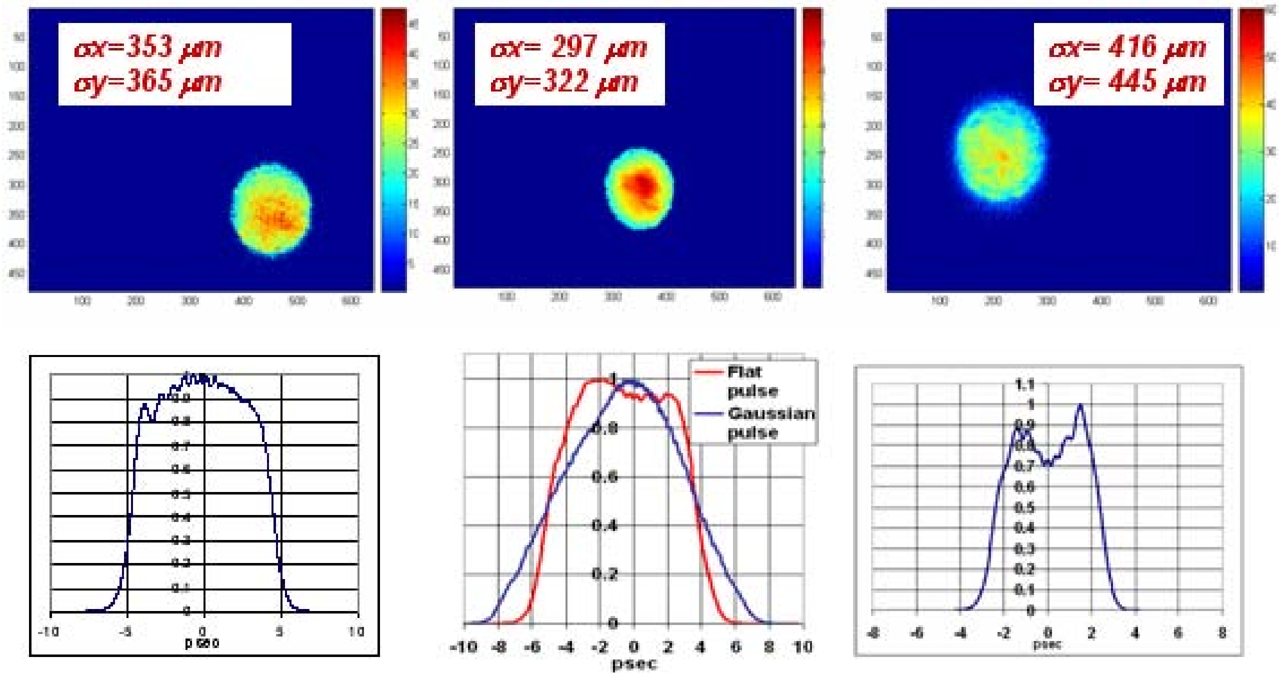

(a) (b) (c)

Figure 6: Virtual cathode spot and pulse shapes coresponding to the plots of figure 5

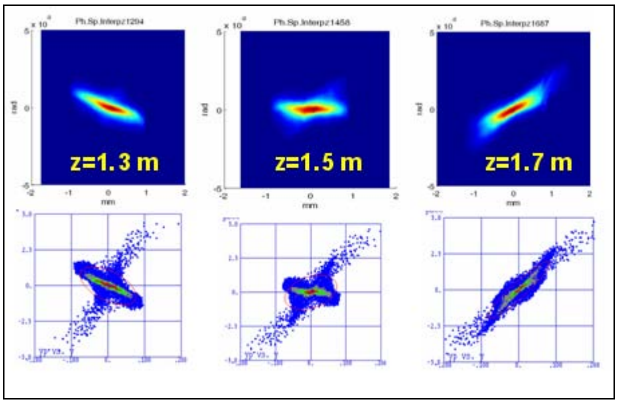

Figure 7: Measured and computed phase spaces in three different z positions in the region of the "double-minimum" emittance oscillation

Figure 8: SPARC in the second commissioning phase

Second SPARC commissioning phase

The second commissioning phase, concerning the beam characterization at full energy, is underway (fig.8). It foresees a detailed analysis of the beam matching with the linac based on the "invariant envelope" criterium and the demonstration of the emittance control in regime of "velocity bunching" in the linac. A poorer performance of the cathode in terms of efficiency, emission uniformity and stability respect to the first phase did not allow to work at the maximum charge and to perform systematic studies of beam optimization. However it has been possible to do some preliminary tests of beam transport up to the exit of the third accelerating structure for checking the diagnostic systems [16] and doing the first comparison with simulations.

Following the experience done in the first phase of the commissioning we firstly looked for the agreement between measurements and fast simulations based on an equivalent uniform beam respect to an envelope measurement. During the transport the spot rms size is measured on four YAG screens: each one of the three first screens is placed at the entrance of the RF structure and the fourth is located at the exit of the linac, where the rms emittance is measured by a quadrupole scan and the bunch length and slice emittance are measured with a high resolution RF deflector [17].

During the first tests an emittance slightly below 2 mm-mrad in the two planes has been obtained with 500pC and a pulse length of 8.5 psec. Figure 9 shows the envelope sampled along the linac compared with a PARMELA simulation. The agreement with simulations is very good, but shows that the transport in the linac is not optimized

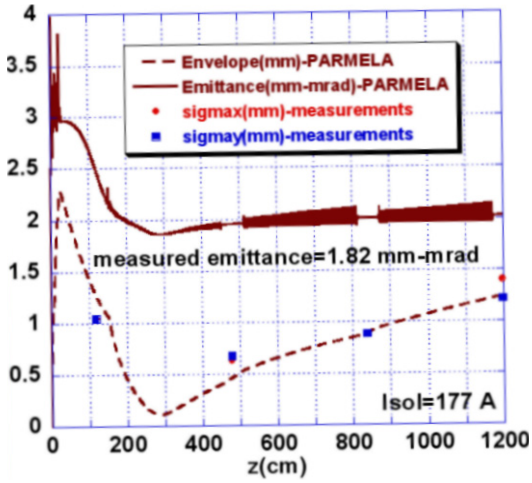

Figure 9: PARMELA simulation of envelope compared with the measured envelopes (red and blue rectangles) an emittance

In fact simulations of a fine magnetic field scan show that some additional improvement in the beam quality are possible as it shown in figures 10 and 11: the solenoid current minimizing the emittance is 185 A (against the value of 177 A used in the measurement) corresponding to a better matching of the beam envelope in the linac, able to decrease the emittance to 1.34 mm-mrad.

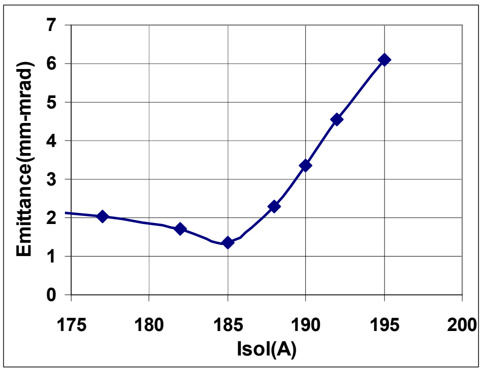

Figure 10: PARMELA simulation: scan of the magnetic field of the gun solenoid

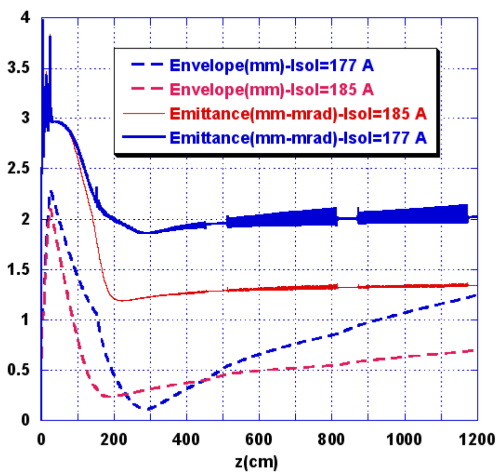

Figure 11: PARMELA simulations: emittance-envelope comparison between the measurement conditions (Isol=177 A) and the optimized maching (Isol=185 A)

Some preliminary tests of beam longitudinal dynamics in regime of "velocity bunching" have been also performed. Figure 12 shows the measured compression factor for a 250 pC beam vs the phase of the first travelling wave section measured by the RF deflector. The reduction of the bunch length from 5 psec to 2.5 psec for a phase range variation of 20 degs is in agreement with PARMELA simulations.

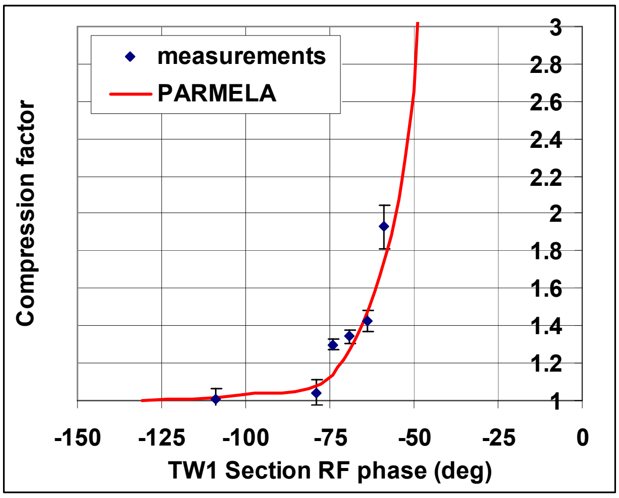

Figure 12: First test of velocity bunching: compression factor vs the phase of the first TW section. Comparison between measurements and simulations

REFERENCES

[1] B. E. Carlsten, NIM A 285, 311-319 (1989)

[2] L. Serafini, J. B. Rosenzweig, Phys. Rev. E 55, 7565-7590 (1997)

[3] M. Ferrario et al., SLAC-PUB-8400, (2000)

[4] L. M. Young, PARMELA, Los Alamos National Laboratory Report LA-UR-96-1835

[5] K. Floetmann, ASTRA http://www.desy.de/~mpyfloASTRA_dokumentation

[6] V. Fusco et al., "Spatial autocorrelation for transverse beam quality characterization", this conference

[7] J. Qiang et al., Phys. Rev. Special Topics – Accel. Beams 9, 044204, (2006)

[8] L. Young, private communication

[9] F. Ciocci et al., Nuclear Instruments & Methods A 393, 434 (1997)

[10] A. Bacci et al, Proceedings of PAC03, p. 3512

[11] C. Limborg et al., Proceedings of PAC03, p. 3548

[12] M. Ferrario et al., "Recent results and Future Perspectives of the SPARC Project", this conference.

[13] L. Palumbo "Status of the SPARX Project", this conference

[14] A. Cianchi et al., PRST-AB, 11, 032801 (2008)

[15] M. Ferrario et al., Phys. Rev. Let. 99, 234801 (2007)

[16] A. Cianchi et al., "Preliminary characterization of the beam properties of the SPARC Photoinjector", this conference

[17] C. Vaccarezza, "Slice emittance measurements at SPARC Photoinjector with a RF deflector", this conference

SINGLE SPIKE OPERATION IN SPARC SASE-FEL

I. Boscolo, F.Castelli, S. Cialdi, V. Petrillo, Università di Milano, Milano (Italy)
A.Bacci, L.Serafini, INFN, Milano (Italy)
R. Bonifacio, M. Boscolo, M. Ferrario, C. Vaccarezza, LNF, INFN, Frascati (Italy)
L. Giannessi,C. Ronsivalle, ENEA Frascati, (Italy)
L. Palumbo, M. Serluca, Università La Sapienza Roma (Italy)
J. Rosenzweig. S. Reiche, UCLA, LA (USA)LNF, INFN, Frascati (Italy)

Abstract

The single spike operation regime has been analysed in the case of the SPARC injector and free-electron-laser. Four different beams at 50 pC are studied, with different production condition and performance.

INTRODUCTION

In the FEL emission two different regimes occur depending on the length L_b of the beam.

If the L_b is larger than 2π times the cooperation length L_c, the radiation presents a longitudinal structure constituted by several chaotic peaks, while, if the length of the beam is shorter than $2\pi L_c$, the emission produces a radiation pulse shaped in one single spike [1]. This regime occurs because the radiation emitted by the electrons, travelling from the tail towards the head of the beam, covers all the distance inside the bunch in a time shorter than few gain times, correlating all the particles. The properties of this regime are well-known in 1d: however, the study of single-spike ultra-short radiation in the X rays range [2], as well as in the visible light [3], by means of start-to-end simulations from the photocathode to the end of the undulator, has shown that transverse and non-homogeneity effects due to radiation diffraction and to non–ideal characteristics of the electron beam such as emittance and energy spread change considerably the properties of the emission process. A fundamental problem is also how to produce a suitable beam. In the second part of this paper, the analysis of the 3d scaling law is presented. Then we present some numerical start-to-end FEL simulations made in the case of the SPARC FEL, for some different beam regimes at 50 pC. The performance of the various bunches are compared and the most interesting of them are discussed.

SCALING LAW

The single spike operation requires that the beam length L_b satisfies the following requirement:

$$L_b \leq 2\pi L_c \qquad (1)$$

with $L_c=L_{c1d}(1+\eta)$

where: $L_{c1d}=\lambda/(\sqrt{3}\,4\pi\rho)$ and η is defined as in [4] :

$$\eta = 0.45\eta_d^{0.57} + 0.55\eta_\varepsilon^{1.6} + 3\eta_\gamma^{2} + 0.35\eta_\varepsilon^{2.9}\eta_\gamma^{2.4} + 51\eta_d^{0.95}\eta_\gamma^{3} + 5.4\eta_d^{0.7}\eta_\varepsilon^{1.9} + 1140\eta_d^{2.2}\eta_\varepsilon^{2.9}\eta_\gamma^{3.2}, \qquad (2)$$

with $\eta_d = L_{g1d}\lambda/(4\pi\sigma_x^2)$ term that accounts for radiation diffraction, $\eta_\varepsilon = \dfrac{4\pi L_{g1d}\varepsilon_{n,x}^2}{\sigma_x^2\gamma^2\lambda}$ for the emittance and $\eta_\gamma = 4\pi\dfrac{L_{g1d}}{\lambda_u}\dfrac{\delta\gamma}{\gamma}$ for the energy spread effects. In these last expressions $L_{g1d}=\lambda_u/(\sqrt{3}\,4\pi\rho)$ is the 1d gain length, $\varepsilon_{n,x}$ the normalized transverse emittance, $\delta\gamma/\gamma$ the energy spread and λ is the radiation wavelength given by the resonance condition $\lambda = \dfrac{\lambda_u(1+a_w^2)}{2\gamma^2}$.

The FEL parameter ρ, in terms of the beam average current I, of the radial r.m.s dimension σ_x of the beam, of the undulator parameter $K_0=\sqrt{2}\,a_w$ and period number $k_u=2\pi/\lambda_u$, of the Lorentz factor of the beam γ can be written as:

$$\rho = \left[\frac{1}{16}\frac{I}{I_A}\frac{K_0^2[JJ]^2}{\gamma^3\sigma_x^2 k_u^2}\right]^{1/3} \qquad (3)$$

where I_A=17 KA is the Alfven current and $JJ = (J_0(\xi)-J_1(\xi))$, J's are Bessel function of argument $\xi = \dfrac{a_w^2}{2(1+a_w^2)}$.

In (4) the current I is defined as $I=cQ/L_b$ with L_b the whole beam length if the beam current is flat top, or $L_b=\sqrt{2\pi}\sigma_z$ with σ_z the FWHM length, if the longitudinal beam profile is Gaussian.

The single spike condition is:

$$L_b=2\pi L_{c1d}(1+\eta) \qquad (4)$$

and the Q vs L_b scaling law becomes

$$Q = \left(\frac{\pi^2 I_A}{3\sqrt{3}c}\right)\left(\frac{\lambda_u(1+a_w^2)^3}{K_0{}^2[JJ]^2}\right)\left(\frac{\sigma_x^2}{L_b^2\gamma^3}\right)(1+\eta)^3 \qquad (5)$$

where in the factor η a further irrational dependence on Q and L_b is contained.

The solution of (5) for four different beams obtained with four different beam lines at 50 pC is presented in Fig 1. The beams present different values of emittance, energy spread, current profile, longitudinal width and transverse dimension. Their position in the Q vs σ_z plane is represented by green stars in Fig 1, together with single spike operation curves at different σ_x.

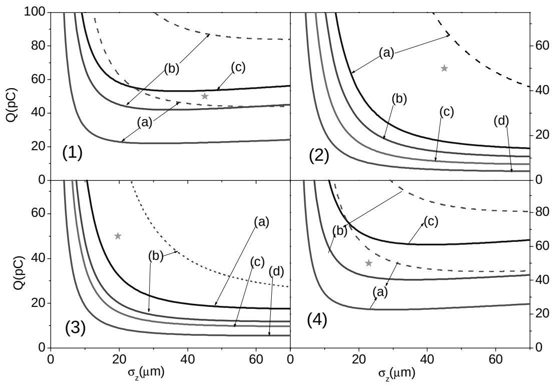

Figure 1:single spike scaling law: solid: 1 spike, dashed: 2 spikes for: (1) beam 1 (a) σ_x=50 μm, (b) σ_x=100 μm (c) σ_x=126 μm. (2) beam 2 (a) σ_x=200 μm (b) σ_x=150 μm (c) σ_x=104 μm, (d) σ_x=50 μm. (3) beam 3: (a) σ_x=150 μm,(b) σ_x=100 μm (c) σ_x=80 μm (d) σ_x=50 μm. (4): beam 4 (a) σ_x=150 μm, (b) σ_x=100 μm, (c) σ_x=50 μm.

Table 1

beam	ϕ(°)	ε_n μm	ΔE/E %	σ_z μm	I_{peak} A
1	-84.5	0.47	2.35	45	120
2	-95	0.45	0.69	45	120
3	-89.9	0.63	0.97	20	300
4	-91.4	2.	2.1	22.8	430

OPERATION AT 50 pC

Four different beams generated and driven in the SPARC line [5] have been analysed, characterized substantially by different values of the injection angle ϕ in the first accelerating structure . The RF compression method has been used. The phase spaces together with the current profile are presented in Fig 2. The first beam (fig. 2, window (1)) has been obtained in the standard SPARC operation regime, scaling the parameters from the 1 nC working point by means of the scaling law at the cathode $\sigma_{xyz} \sim Q^{1/3}$ [6], and using therefore a laser pulse length of σ_t=1 psec, illuminating a region of R=0.4 mm. The injection angle ϕ was -84.5°. The beam was compressed at σ_z =45 μm, with a peak current of 120 A.The simulations of the beams 1, 2 and 4 was done with Parmela [7], while case 3 was simulated by ASTRA [8].
was obtained in the blow out regime with a laser pulse of 0.2 psec and an injection angle of -95° in the over-compression condition. The final beam length is again 45 μm and the peak current 120 A, but the energy spread and the transverse dimension are smaller and the current has a different shape.
The last two beams (3, shown in Fig. 2 , window (3) and 4, Fig. 2, window (4)) have been injected around the maximum compression phase (respectively -89.9° and -91.4°), obtaining more peaked currents. The difference between them is that beam (3) has been optimized with the genetic algorithm [9], leaving free the intensities of the 12 magnetic coils of the first structure and the injection angles in the last two structures (respectively -34.9° and -2.8). These adjunctive degrees of freedom have permitted to obtain a current very much larger than the first two cases, only a bit smaller than case (4), but with a better control of emittance and of energy spread. The last beam 4 belongs to the high current operation regime, widely explained in Ref [3].

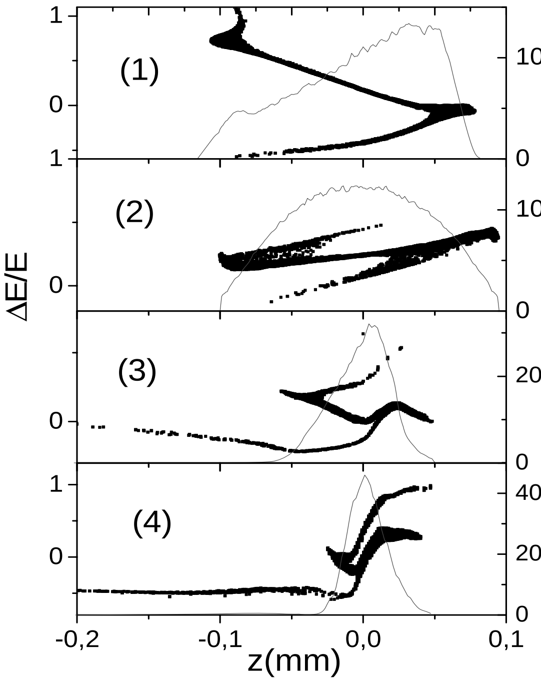

Figure 2: Left axis: Phase space ΔE/E in % vs z (mm) . Right axis: current (a) vs z (mm) for (1): beam 1, (2) beam 2, (3) beam 3 and (4) beam 4.

In table 1 the different characteristics of the beams are summarized. In the last two cases the effect of the large longitudinal space charge forces is that of prevent the complete overcompression, the particles being pushed forward by the electric repulsive forces applied by the slices behind. The result is a folding in the phase space in correspondence of the maximum density with inversion of the energy phase correlation.

FEL SIMULATIONS

The optimum focusing condition for the four beams has been deduced by the scaling law shown in Fig. 1. Values of σ_x and σ_x leading to the single spike operation with the maximum focalization (corresponding to the maximum energy extraction) have been used. For the beam (1) the condition of single spike occurs for σ_x=100 μm. In fact in

Fig 1 (1) the green star is positioned near curve (b) solid line (1 spike, and (b) σ_x=100 µm) and well above curve (b) dashed line (2 spikes, σ_x=100 µm). As the beam at 12 meter has σ_x=126 µm, it has been transversally matched to the undulator entrance by means of the SPARC transfer line constituted by two triplets far 3.8 m. The second beam has σ_x=104 µm, so it can be not focused. Beam 3 presents σ_x=79 µm at 12 m, so it has to be matched, as well as beam 4 that exits from the linac with σ_x=208 µm.

The undulator and lattice characteristics are: 6 undulator section of 2.15 m, λ_u=2.8 cm, a_w=1.51, dB/dz=8. T/m. Radiation with wavelength of 500 nm is produced.

In table 2 the most significant radiation characteristics are presented for various values of σ_x. The FEL simulations have been done with GENESIS 1.3 [10] .

Table 2: radiation properties: N_{sp}: number of radiation spikes, E: total energy of the pulse, div: radiation divergence, $\sigma^{z,}_{rad}$:radiation length, bw: normalized bandwidth

beam	**σ_x µm**	**N_{sp}**	**P_{max} GW**	**E µJ**	**div mrad**	**$\sigma^{z,}_{rad}$ µm**	**bw %**
1	104	1-2	0.13	23	1.7	30	1
	50	1-3	0.095	30	1	70	1
2	104	1-2	0.037	10	0.7	50	0.8
	50	3	0.09	30	0.6	250	1
3	104	1	0.16	16.7	1	20	1
	79	1-2	0.32	44	1	40	1
	50	3	0.37	56	0.9	60	0.8
4	125	1	0.41	39.6	1.2	15	1.1
	100	1-2	0.7	50.8	2	20	1.2
	70	1-2	0.8	68.4	1.6	25	1.3

In figures 3 and 4 the radiation evolution is presented in the plane z(m) vs s (µm), together with the pulse shape P (W) vs s at 11 meter in the undulator. The cases presented are: beam 1, σ_x =104 mm, and beam 4 , σ_x =125 mm.As shown, the predictions of the scaling law are respected. The analysis shows that there is large margin of choice in the single spike operation. The maximum compression regime leads to minima pulse lengths, large peak power and total energy. However, the operation in this regime requires a tight control of the beam line elements (as for instance the magnetic field intensity in the coils of the first structure) and of the injection angles for avoiding the formation of tails that degrade the beam quality and for controlling emittance and energy spread. These last quantities are not demanding for the single spike occurrence, but determine some of the pulse characteristics as, for instance, the divergence and the spectrum.

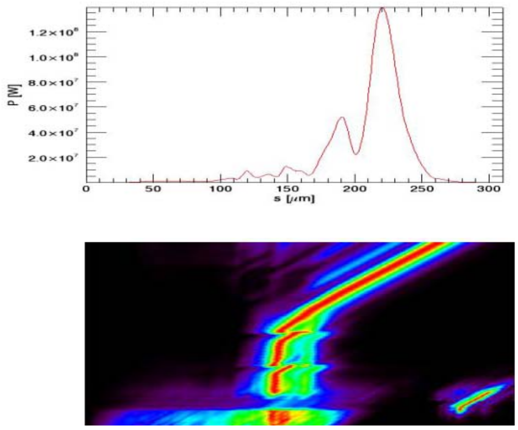

Figure 3: beam 1, σ_x =104 µm: pulse shape P (W) vs s(µm) at 11m. Normalized level curves in the plane z(m) vs s (µm).

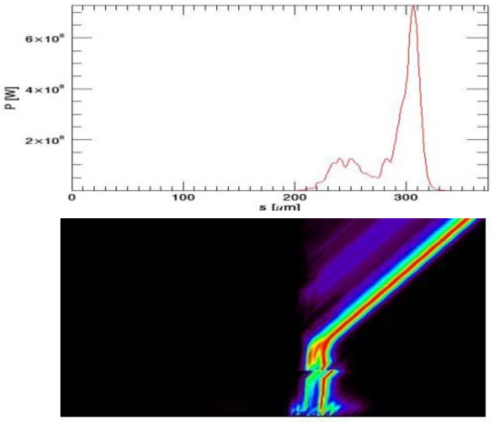

Figure 4: beam 4, σ_x =100 µm: pulse shape P (W) vs s(µm) at 11 meterr. Normalized level curves in the plane z(m) vs s (µm).

REFERENCES

[1] R. Bonifacio et al. PRL 73 (1994) 70
[2] J. Rosenzweig et al. NIMA (2008) in press
[3] M.Boscolo et al, NIMA (2008) doi:10.1016/j.nima.2008.04.074
[4] M. Xie in Proc. of the 1995 PAC, IEEE, Piscataway, NJ,1995, p.183
[5] M. Ferrario et al. PRL 99 (2007) 234801
[6] M. Boscolo et al.: SPARC BD-note BD-07-006
[7] L.M. Young, LANL Report No.LA-UR-96-1835
[8] K. Floetmann, ASTRA: http://desy.de/~mpyflo/Astra_dokumentation/
[9] A. Bacci et al., NIMB 263 (2007) 488
[10] S. Reiche: NIM A 429 (1999) 243

PRELIMINARY CHARACTERIZATION OF THE BEAM PROPERTIES OF THE SPARC PHOTOINJECTOR

A. Cianchi*, INFN-Roma Tor Vergata
D. Alesini, M. Castellano, E. Chiadroni, L. Cultrera, G. Di Pirro, M. Ferrario, L. Ficcadenti,
D. Filippetto, V. Fusco, G. Gatti, B. Marchetti, E. Pace, C. Vaccarezza,
C. Vicario, INFN/LNF, Frascati (Roma)
C. Ronsivalle, ENEA C.R. Frascati, Frascati (Roma)
A. Mostacci, University La Sapienza, Roma

Abstract

The SPARC photoinjector is the test prototype of the recently approved SPARX project. It is used as R&D facility to perform accurate beam dynamics studies, comparing measurements and simulations. The first results of beam characterization at full energy are presented.

INTRODUCTION

The SPARX project consists in an X-ray-FEL facility jointly supported by MIUR (Research Department of Italian Government), Regione Lazio, CNR, ENEA, INFN and Rome University Tor Vergata. The aim is the generation of electron beams characterized by ultra-high peak brightness at the energy of 1 and 2 GeV, for the first and the second phase respectively. The beam is expected to drive a single pass FEL experiment in the range of 13.5÷6 nm and 6÷1.5 nm, at 1 GeV and 2 GeV respectively, both in SASE and SEEDED FEL configurations. SPARX is the natural extension of the ongoing activities of the SPARC collaboration mainly focused on the SPARC photoinjector. It is a normal conducting linear accelerator hosted by INFN Frascati Laboratories that drives a FEL-SASE in the visible wavelength. The installation of the undulator modules is in progress and it will be finished for July this year. The commissioning of the Linac has been started delivering the beam at full energy of 150 MeV. Several and systematic studies are needed in order to achieve the design parameters. The preliminary results of the beam characterization are here reported as well as a description of the machine diagnostic.

SPARC LAYOUT

SPARC is a normal conducting accelerator. The RF gun is one of the most recent generation 1.6 cell S-band BNL/UCLA/SLAC type follow by 3 S-band travelling wave accelerator constant gradient structures. The power sources are the 45 MW peak, 2856 MHz klystron TH2128C. The Klystron n.1 feeds the the RF gun and the third accelerating structure with 4.5 μs RF pulses. Klystron n.2 feeds two high gradient accelerating sections through an energy compressor that allows to obtain 60 MW - 0.8 μs RF pulses. Around the first and the second accelerating structure several solenoids are placed to provide additional focusing both for velocity bunching [1] and to match the beam envelope with the linac according with the invariant envelope scheme [2]. The undulator [3] is composed by 6 sections of permanent magnet undulator, separated by 0.36 m gaps, and featuring single quadrupoles which focus the electron beam in the horizontal plane. Every module contains 75 periods each one 2.8 cm length, with an undulator parameter kw = 1.4. The FEL will operate in self amplified spontaneous emission (SASE) mode at a wavelength of about 500 nm with an expected saturation length of about 10-12 m. For this stage of commissioning we have operated with a laser pulse with gaussian longitudinal profile of FWHM in the order of 6-8 ps. The bunch charge was between 200 pC up to 700 pC, mainly limited by the low (in the lower order of 10^{-5}) and not constant quantum efficiency of the cathode.

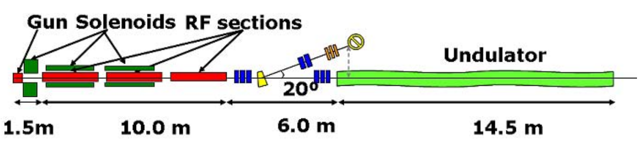

Figure 1: SPARC layout.

DIAGNOSTIC HARDWARE

The measurements of the beam transverse parameters is mainly a measurement of the beam rms size. So far we used mainly Ce:YAG radiator, while OTR metallic foils are installed and they will be used for high charge run (about 1 nC). The doping level of Cerium in the crystal is 0.18%. The response is linear up to 0.01 pC/μm^2 [4]. The radiation emitted in the forward direction from the Ce:YAG crystal is collected by a 45 degrees mirror downstream the radiator, on the same screen holder. We observe the back side of the transparent crystal radiator, thus minimizing the degradation of the spatial resolution due of the optics field depth. The small thickness of the crystal (100 μm) prevents appreciable blurring effects due to the crystal bulk emission, as well as significant multiple scattering.

Images are acquired using 8 bit digital CCD cameras (Basler 311f) equipped with 105 mm “macro” type objectives from SIGMA.

The beam envelope is measured in four different positions: one before the first accelerating module, 1181 mm

* cianchi@roma2.infn.it

far away from the cathode, two others positions are between the accelerating module, and the last at the exit of the third module.

Downstream the last section several diagnostic tools for a full characterization of the beam parameters are installed. A triplet of quadrupoles are installed, followed by the SPARC RF deflector [5], the dipole for the high energy measurement and the flags to evaluate the beam parameters (see Fig. 2). The quadrupoles are used both for quadrupole scan measurements and for the slice emittance measurements with the RF deflector on. The drift between the last quadrupole and the measuring flag is 3.9 m. Also the longitudinal phase space can be investigated using the RF deflector together with the spectrometer dipole.

The energy in the gun area is evaluated monitoring the displacement of the beam center changing the current in a steering coil. This coil has a high field quality and a field flatten for about 2 cm as reported in [6]. The lunch phase is set referring to the phase where the energy is maximum.

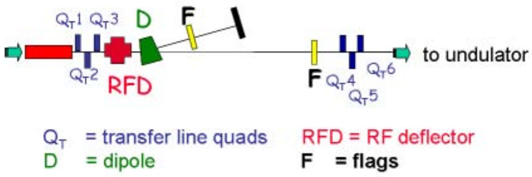

Figure 2: Layout of the experimental area at 150 MeV.

ENVELOPE MEASUREMENTS

To match the beam size into the linac and to control the emittance compensation process the envelope is measured in all the available flags. An example of a series of measurement is shown in Fig. 3 where are reported the rms transverse size in different position for several values of the gun solenoid.

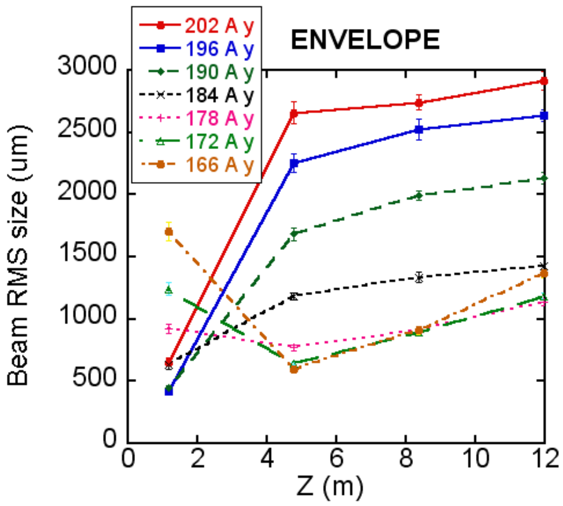

Figure 3: Envelope measurement along the linac.

The bunch length was 6.5 ps, with 340 pC of charge and a rms size on the virtual cathode of about 340 μm.

EMITTANCE MEASUREMENTS

Several measurements of emittance has been performed with the standard technique of quadrupole scan. The resolution of the optics is set in the order of 30 μm per pixel to have both large field of view and a reasonable number of samples for an accurate measurement of the beam size in the waist. A typical result of the quad scan is shown in Fig. 4.

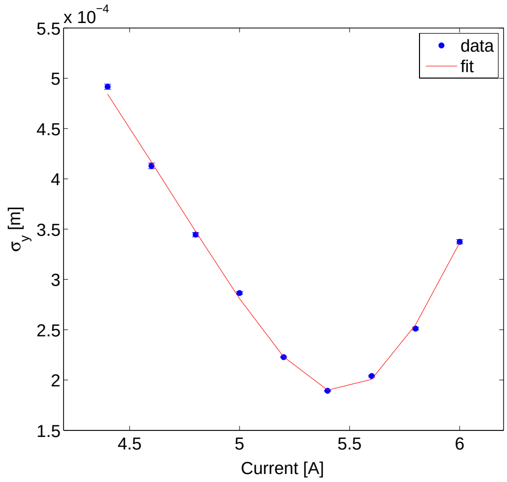

Figure 4: Fit of the data of the quadrupole scan.

In order to study the emittance compensation process and in particular the influence of the focusing solenoids on the traveling wave structures, a systematic analysis of the transverse emittance is important. In the Fig. 5 are reported the results of the first measurement. The charge was 500 pC with bunch length of 6.5 ps and a laser beam spot size of around 400 μm on the cathode.

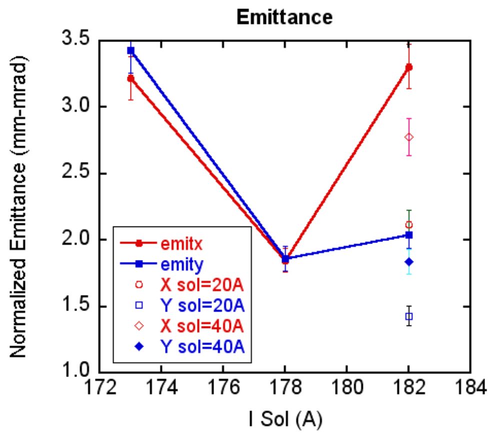

Figure 5: Emittance measurement for different configuration of the gun solenoid and the additional coils around the accelerating structures.

Cross checks of the data with the simulation are ongoing and are reported in [7]. Anyway the effect of the focusing solenoid on the value of the emittance is already visible in the Fig. 5.

Slice Emittance

A preliminary measurement of slice emittance has been performed. The bunch charge was 300 pC, 5.3 FHWM bunch length, with a beam energy of 145 MeV. The result is consistent with a measurement of the projected emittance that gives (2.8±0.1) mm-mrad.

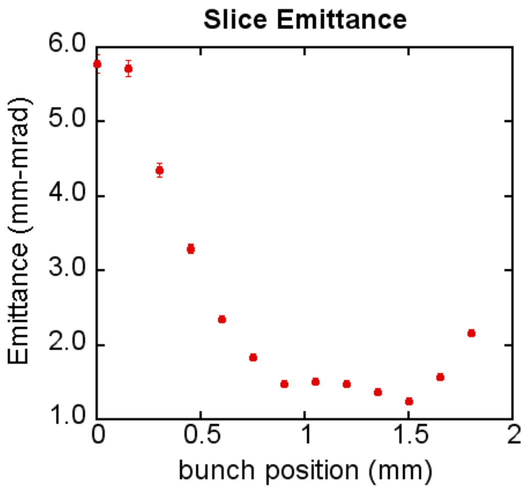

Figure 6: Slice emittance measurement.

Referring to Fig. 2 only the quadrupoles named QT2 and QT3 have been used together in order to maintain the vertical dimension (i.e. the longitudinal resolution) constant during the scan. The slice length has been set to 150 μ i.e. about 0.5 ps. More details can be found in [8].

BUNCH LENGTH MEASUREMENTS

The evaluation of the bunch length is mandatory especially in the foreseen studies of the velocity bunching. The RF deflector is used for this task. The ultimate temporal resolution is affected not only from the deflecting voltage but also from the intrinsic vertical dimension of the beam size at the flag when the deflector is off. In the actual condition the temporal resolution is estimated to be around 1 ps.

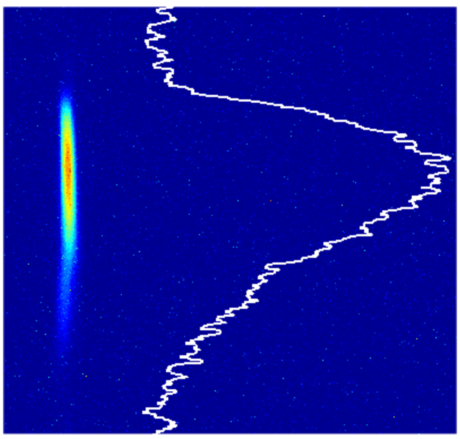

Figure 7: Bunch length measurement.

In Fig. 7 a measurement with 300 pC charge is reported, giving a length of 7.7 ps FWHM equal to 5.5 mm on the flag.

Longitudinal Phase Space

Using the RF deflector and the spectrometer dipole is possible to study the longitudinal phase space.

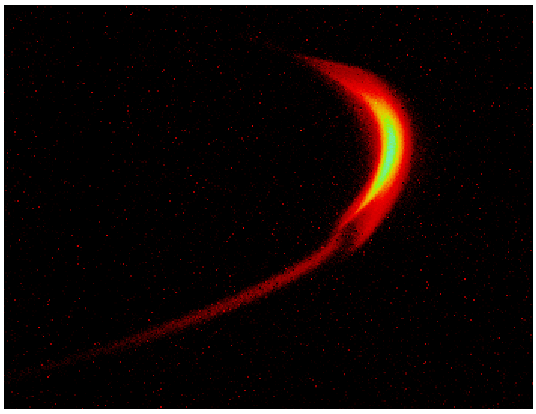

Figure 8: An example of the longitudinal phase space.

An example of non perfect optimized beam is shown in Fig. 8.

CONCLUSION

The SPARC commissioning has begun. In this early stage the beam has been delivered to the end of the linac at the nominal energy of 150 MeV. All the diagnostic and the analysis tools have been tested and commissioned. Preliminary beam characterization has been done with a lower charge, due to reduced and variable cathode emissivity.

REFERENCES

[1] L. Serafini and M. Ferrario, in Physics of, and Science with, the X-Ray Free-Electron Laser, edited by S. Chattopadhyay, M. Cornacchia, I. Lindau, and C. Pellegrini, AIP Conf. Proc. No. 581 (AIP, New York, 2001).

[2] Luca Serafini and J. B. Rosenzweig, Phys. Rev. E 55, 7565 (1997).

[3] A. Renieri et al. Status report on SPARC project, in Proc. of the 26th FEL conference, Trieste 2004

[4] D. Filippetto, Ph.D. thesis, University of Rome La Sapienza,2007, to be published at http://padis.uniroma1.it/

[5] D. Alesini, et al., RF deflector design and measurements for the longitudinal and transverse phase space characterization at SPARC, Nucl. Instrum. Meth. A 568, 488-502, 2006

[6] B.Bolli et al., SPARC NOTE SPARC-MM-06/001

[7] C. Ronsivalle et al. Simulations Of The Emittance Compensation In Photoinjectors And Comparison With Sparc Measurements, these proceedings

[8] C. Vaccarezza et al., “Slice Emittance Measurements at SPARC Photoinjector with a RF Deflector”, these proceedings

SPATIAL AUTOCORRELATION FOR TRANSVERSE BEAM QUALITY CHARACTERIZATION*

V. Fusco#, M. Ferrario, LNF-INFN, Frascati, ITALY
C. Ronsivalle, ENEA, Frascati, ITALY.

Abstract

Low emittance beams are required for high brightness beams applications. Contributions to emittance degradations come from electromagnetic fields' non-linearities which can be reduced using a transversally and longitudinally uniform beam. For these reasons the evaluation of the beam quality is a very important task. Concerning the transverse analysis the spatial autocorrelation parameter has been introduced: it gives an evaluation of how beam non-uniformity is distributed. The paper describes the spatial autocorrelation concept and applies it to the evaluation of a laser beam for high brightness beam applications. Moreover the paper shows the spatial autocorrelation evolution along a photo-injector as an additional tool for beam dynamics studies.

INTRODUCTION

Concepts such as mean, variance and standard deviation can be used to evaluate uniformity of a set of data distributed on a surface, as in the case of the transverse spot of an electron beam or of the laser itself.

The mean describes the central value of the data. In the case of a laser or of a beam cross section analysis, a matrix of pixel of certain intensity is given (each pixel representing the electrons or photons charge). For a matrix of elements the mean is obviously calculated as:

$$< a >= \frac{1}{T}\sum_{i=1}^{N}\sum_{j=1}^{M} a_{ij} \tag{1}$$

where N and M are the matrix dimensions, $T=NM$ is the number of pixel involved, and a_{ij} the matrix element representing the generic sample, that is the pixel intensity.

The variance represents the distance from the central value, that is the spread, and for a *2D* matrix it is calculated as follows:

$$\mathrm{var}(a) = \frac{1}{T}\sum_{i=1}^{N}\sum_{j=1}^{M}(a_{ij} - < a >)^2 \tag{2}$$

The obtained quantity is always positive so that the standard deviation can be defined as:

$$\sigma_a = \sqrt{\mathrm{var}(a)} \tag{3}$$

which is a quantity whose dimensions are comparable to the mean. The argument $(a_{ij}-<a>)$ defines a new matrix where every element represents the distance from the mean and $(a_{ij}-<a>)^2$ is the variance matrix. It is obtained as a distance squared so that bigger differences are emphasized respect to the smaller ones.

For a perfectly uniformly charged beam cross section, normalized to the higher sample, $<a>=1$ and $\sigma_a=0$. Of course more the cross section is non-uniform more the standard deviation will be far from the ideal values. The above parameters, describe non-uniformity without describing the way non-uniformity is distributed. It has been shown [2] the importance of the distribution of the non-uniformity because it can give different results concerning the emittance degradation.

Spatial correlation describes such a property [1]. It is necessary to introduce the covariance for a matrix point to define the spatial correlation. The quantity covariance answers the question whether a sample and its neighbour are at the same time different or not from the mean and it's defined as:

$$\mathrm{cov}(a,h) = \frac{1}{T}\sum_{i=1}^{N}\sum_{j=1}^{M}(a_{ij} - < a >)\cdot(a_{ijh} - < a >) \tag{4}$$

where a_{ijh} is the mean of the samples localized around the main sample a_{ij}. The argument $(a_{ij}-<a>)(a_{ijh}-<a>)$ is called the covariance matrix.

The samples can be taken in different ways depending also from the distance h from a_{ij} as represented in Figure 1:

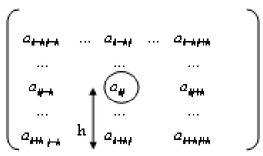

Figure 1: The a_{ij} is the generic sample whose variance is compared with the other samples' variance at a certain distance h..

As can be easly seen it results:

$$a_{ijh} = \frac{1}{(2h+1)^2 - 1}\left[\sum_{l=-h}^{h}\sum_{m=-h}^{h} a_{i+l\,j+m} - a_{ij}\right] \tag{5}$$

#valeria.fusco@lnf.infn.it

which is the mean of the samples around a_{ij}.

The distance h and the matrix dimensions N, M define the resolution of the spatial autocorrelation investigation. The index Λ, which describes the spatial correlation, can be defined as the the covariance normalized to the standard deviation σ_a squared:

$$\Lambda(a,h) = \frac{\mathrm{cov}(a,h)}{\sigma_a^2} \tag{6}$$

which is a quantity whose value is between *-1* and *1*. The minus sign simply means most samples are lower than the mean.

Meaning of the spatial autocorrelation index

The spatial autocorrelation meaning is shown in the following examples.

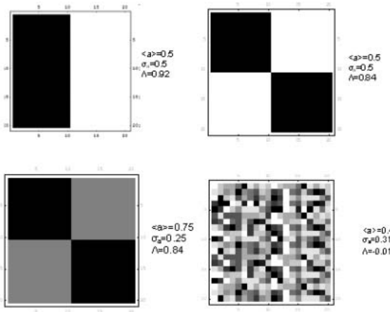

Figure 2: Examples of the spatial autocorrelation and standard deviation calculation.

The results underline that, given the same mean and the same standard deviation, the spatial correlation maybe different: the matrix on the left hand side has a unique big spot whilst the matrix on the right hand side has two distributed spots of intensity, resulting in more distributed spots; in the first case it gives $\Lambda=0.92$ whilst in the second case, as expected, the spatial correlation is smaller ($\Lambda=0.84$).

It's worth noting that, as represented on the left hand side (bottom) of Figure 2, the mean can be enhanced keeping the same spots distribution: in this case spatial correlation remains unchanged no matter of the intensity of the distribution.

Finally spatial correlation decreases as the spots of intensity become more random. This is shown in Figure 2 where on the right hand side (bottom) is depicted a completely random distribution of samples.

A plot of the spatial autocorrelation as a function of the distance h is called correlogram of a given spot. The spot and its correlogram are represented in Figure 3.

Two points P_1 and P_2 are correlated if they are placed at a certain distance. This distance can be evaluated arbitrarily fixing the Λ to be less than a certain value and it coincides with the mean distance of the non homogeneity.

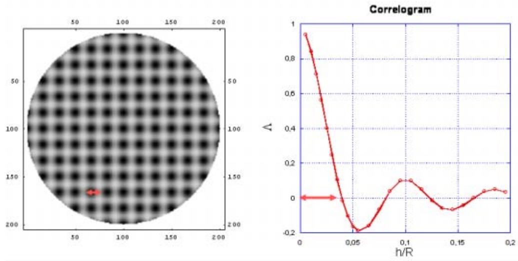

Figure 3: A theoretical laser spot with distributed non-uniformities and the corresponding correlogram.

SPATIAL AUTOCORRELATION AND BEAM DYNAMICS STUDIES

Theoretical laser spot analysis

Concerning the evaluation of the beam quality, it is clear from the previous examples that a well-behaving beam has a low standard deviation and spatial correlation. This property has been verified studying the effects of beam charge in-homogeneities on the emittance[2].

The charge distribution extracted from the cathode has been modelled as a sine and cosine function having a frequency n and a charge intensity δ. The latter will be presented in details here. Figure 4 shows the matrix representing a non-uniform beam as the frequency n increases. The generic matrix element is represented by the following function:

$$\rho(i,j) = \rho_0(1+\delta\cos k_n i)(1+\delta\cos k_n j) \tag{7}$$

where $k_n=2\pi n/r_p$ and r_p is the beam radius.

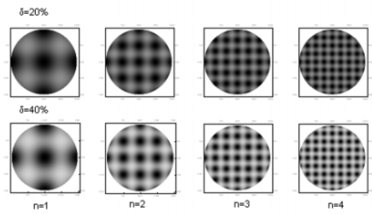

Figure 4: Matrix representation of Eq.7 showing non-uniform distribution versus n and for different δ ($\delta=40\%$ and $\delta=20\%$). In this case $\rho_0=1$, $r_p=100$..

Table 1 and Table 2 show the obtained spatial correlation for different frequency n and the standard deviation for different intensity of non uniformity δ.

Table 1: Λ for different frequency n of Eq. (7)

n	1	2	3	4
Λ	0.92	0.71	0.45	0.18

Table 2: σ for different charge intensity δ of Eq. (7)

δ	10%	20%	30%	40%
σ	0.08	0.14	0.18	0.21

Such distributions have been analyzed, concerning the emittance degradation with the Parmela code where the accelerator machine set up is the one used for the SPARC project [3]. The results are depicted in the Figure 5 where the emittance growth is represented as a function of the spatial autocorrelation Λ for different value of the standard deviation.

Real laser spot analysis

A program devoted to the calculation of spatial correlation has been built using the Mathematica software. Briefly the algorithm reads the image, coming directly from a camera acquisition, and it changes it in a matrix whose elements represent the intensity of the pixels. The bias is eliminated and the threshold is chosen making the mean of the pixels around the barycentre of the filtered distribution and lowering it of a percentage: in this way the beam boundary are established. Note that the spatial autocorrelation depends very little from the threshold.

Thus a good laser image, medium and bad obtained at SPARC have been analyzed and are shown in the ε-Λ plot of Figure 5.

It's worth noting the brilliance measured at SPARC with the good laser spot is better than that obtained with the bad laser spot [4].

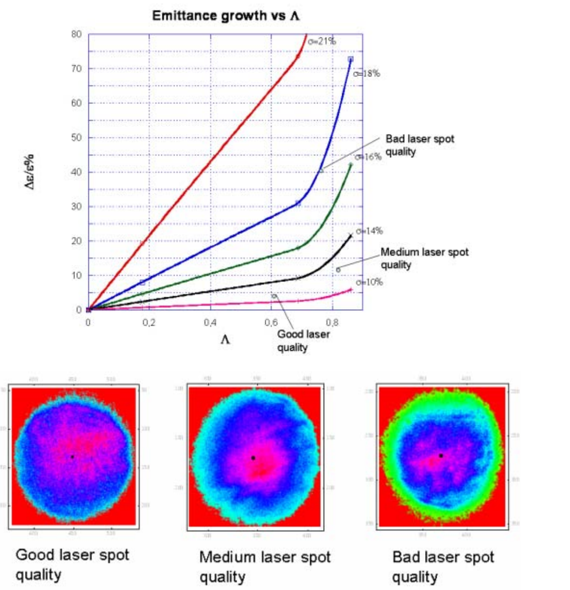

Figure 5: ε-Λ curve: emittance growth percent versus the spatial autocorrelation for different values of the standard deviation σ. In the plot the position of a good, medium, bad laser spot are reported..

Autocorrelation evolution along a photoinjector

As a conclusion it is reported in Figure 6 the evolution of the autocorrelation Λ along the SPARC photo-injector. A uniform beam evolution is first considered, transported with the Parmela code. In the waist the beam shows a wave breaking due to space charge non-linearities enhanced by the solenoid focusing force; thus the autocorrelation increases.

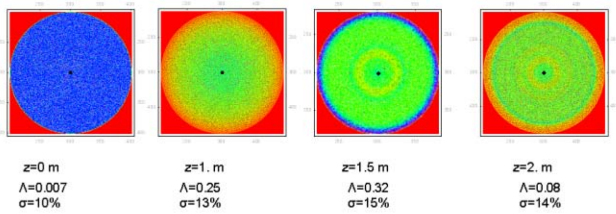

Figure 6: Evolution of a uniform laser beam along the photoinjector (z=1.5 m) is the waist.

Figure 7 shows a real beam behaviour along the photo-injector: the autocorrelation index demonstrates that non homogeneities don't spread along the photo-injector, on the contrary they appear again in the waist of the beam (solenoid focusing force) modified by space charge non linearities.

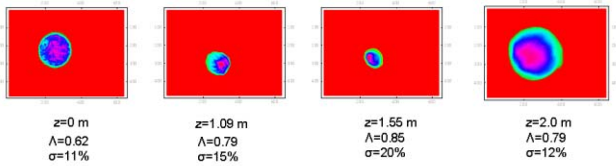

Figure 7: Evolution of a real laser beam along the photoinjector (z=1.5 m) is the waist.

CONCLUSIONS

The spatial autocorrelation index and the standard deviation describe the transverse quality of a laser beam. The latter describe the uniformity and the former how non uniformity is distributed. The knowledge of both allows to place the laser spot on the ε-Λ curve thus giving an idea of the corresponding emittance growth.

As a conclusion the evolution of the autocorrelation of a uniform laser spot and a real laser spot along the photo-injector demonstrates that non homogeneities don't spread along the photo-injector. On the contrary non homogeneities, modified by space charge, appear again in the waist of the beam due to solenoid focusing force.

ACKNOWLEDGEMENT

We would like to thank A. Cianchi, A. Mostacci, F. Pompili, A. R. Rossi for their help and precious advices.

REFERENCES

[1] V. Fusco, M. Ferrario, C. Ronsivalle, http://www.lnf.infn.it/acceleratori/sparc/TECHNOTES/EBD/SPARC_EBD_07_007.pdf
[2] M. Quattromini et al., "Emittance Dilution due to 3D Perturbations in RF Photo-injector, Proceedings of EPAC 2004, Lucerne, Switzerland
[3] A. Cianchi et al., Phys. Rev. Accel. Beams 11, 032801 (2008)
[4] C. Ronsivalle, MOZAG01, these proceedings

DESIGN AND FABRICATION OF AN X-BAND TRAVELING WAVE DEFLECTION MODE CAVITY FOR LONGITUDINAL CHARACTERIZATION OF ULTRA-SHORT ELECTRON BEAM PULSES*

A. Murokh**, R. Agustsson, S. Boucher, P. Frigola – *RadiaBeam Technologies LLC, 13428 Beach Ave, Marina Del Rey, CA 90292, USA*

J. Rosenzweig, J. England, G. Travish – *UCLA Department of Physics and Astronomy, 405 Hilgard Ave, Los Angeles, CA 90095, USA*

D. Alesini – *INFN/LNF, Frascati, Italy*

V. Yakimenko – *Brookhaven National Laboratory, Building 820 M, Upton, NY 11973, USA*

Abstract

An X-band Traveling wave Deflector mode cavity (XTD) has been developed at Radiabeam Technologies to perform longitudinal characterization of the sub-picosecond ultra-relativistic electron beams. The device is optimized for the 100 MeV electron beam parameters at the Accelerator Test Facility (ATF) at Brookhaven National Laboratory, and is scalable to higher energies. An XTD is designed to operate at 11.424 GHz, and features short filling time, femtosecond resolution, and a small footprint. RF design, fabrication procedure, and commissioning plans are presented. An experimental program at ATF to utilize the deflector for compressed beam characterization is discussed, including proposed measurements of the phase space filamentation due to non-linear processes in a chicane compressor.

INTRODUCTION

Some of the most compelling and demanding applications in high-energy electron beam-based physics, such as linear colliders, X-ray free-electron lasers, inverse Compton scattering (ICS) sources, and excitation of wakefields in plasma for future high energy physics accelerators now require sub-picosecond pulses. The creation of ultra-short pulses presently relies on the use of RF photocathode electron guns. To achieve sub picosecond pulses, advanced photoinjector facilities employ compression techniques such as magnetic chicane bunch compressors [1] or velocity bunching [2] schemes. These methods require intricate transverse and longitudinal diagnostics in order to successfully compress the beams without degrading their quality. Hence, a better experimental utilization of fast beams relies on improving resolution and capabilities of fast longitudinal diagnostics.

RF deflecting cavity is being recognized as a robust solution for diagnosing the characteristics of 10's of femtosecond-class electron beams, that is drawing increasing attention in the ultra-fast beam community. An S-band deflector, termed LOLA IV and built in the late 1960's [3] has been recently resurrected for use on the SPPS beamline at SLAC [4]. More compact standing wave deflecting mode cavities have been developed by the INFN-UCLA collaboration for the SPARC project [5] and the UCLA Neptune Lab [6]. Based on this experience, RadiaBeam is developing an X-band Traveling wave Deflecting mode cavity (XTD) to be utilized for direct longitudinal phase space measurements of compressed electron beams. The XTD surpasses the state-of-the-art in deflecting cavities by taking advantage of the greater efficiency and compactness of X-band RF structures; which naturally allows extension of the technique to very high energies, necessary for next generation light sources and linear colliders.

Deflecting cavity operates in a dipole mode: an ultra-short beam (ps duration or less) traverses a device near the zero-crossing phase of the RF wave, thus deflecting the front (earlier time) components of the beam differentially with respect to the trailing components, with an approximately linear time-slew. As a result, a certain temporal slice of the beam can be imaged if the differential kick over the relevant time period must give, after drifting the beam to a detector plane, a differential beam displacement that exceeds the betatron beam size at this point. Of course, the beam transport between deflection and detection may be more complex than a simple drift, and may include, for example, bending in the non-deflection plane.

The transverse pattern of the TM_{11} deflecting magnetic fields in the cavity are also shown in Figure 1. This pattern in which the transverse magnetic field is approximately constant near the axis, corresponds to a longitudinal electric field that vanishes on-axis. In a pill-box cavity, these are the only components of the electromagnetic field that exist; in the presence of irises that allow the beam passage, there is also a transverse electric field which has the effect of adding in phase to the total deflecting kick.

The capabilities of this type of measurement system can be straightforwardly extended to the measurement of longitudinal phase space, when a bend dipole is placed

* work supported by the U.S. DOE SBIR grant DE-FG02-05ER84370

** murokh@radiabeam.com

downstream of the deflector to disperse the momenta of the beam along the non-deflecting axis. Thus, one may expect that the longitudinal phase space will be displayed, subject to uncertainty introduced by the finite betatron beam size, at the post-dipole detector. The implementation of this type of measurement at ATF-BNL photoinjector is discussed in the experimental plans section.

DESIGN CONSIDERATIONS

The overall design philosophy of the X-band RF deflector is set by the need to maximize the RF deflection of a particle with a given arrival time Δt different from the design particle. As the deflection observed at the detector screen is given by,

$$\Delta x_d = \omega_{RF} \Delta t \sqrt{\beta_d \beta_f} \left(\frac{eV_0}{E} \right) \sin\left(\Delta \psi_\beta \right), \quad (1)$$

where β_d, β_f are the beta-functions at the deflector and screen, respectively, ω_{RF} is the RF frequency, V_0 is the RF voltage, E is the beam energy, and $\Delta\psi_\beta$ is the phase advance between deflector and detector (naturally chosen to be near $\pi/2$). For a clear measurement, a meaningful deflection value must exceed the betatron beam size of $\sigma_\beta = \sqrt{\beta_f \varepsilon}$, where ε is the geometric emittance. To satisfy this condition, even when, as in some applications under consideration, Δt is of the order of 10 fsec, large β_d is desired. The upper limit of β_d is defined by the aperture acceptance of the X-band cavity.

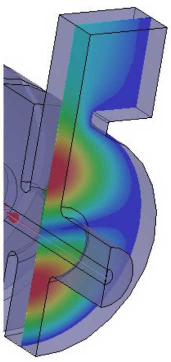

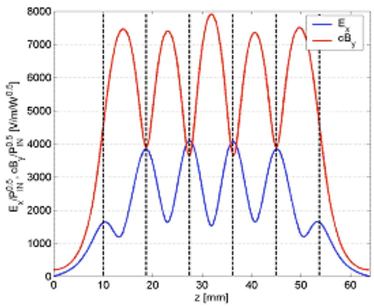

Figure 1: An HFSS model of the deflecting mode excitation (left), and transverse electric and magnetic fields amplitudes for 3-cell numerical XTD model (right).

Additionally, Eq. 1 explicitly shows the advantages of high frequency (ω_{RF}), and a high RF voltage (V_0) values. To achieve a higher voltage, it is natural to increase the length of the deflector, which can only be accomplished straightforwardly by use of a traveling wave device. As in a traveling wave RF linac, an optimum length of a deflector structure is just over one RF attenuation length. Finally, we note the explicit energy dependence in Eq. 1 favours low beam-energy operation, even with the natural damping of beam size (through emittance) as $E^{-1/2}$.

The RF design of the XTD was initially specified by examining the single cell and a short structure behaviour using the commercial 3D electromagnetic modelling code HFSS v10.0. The results of the short structure analysis were extrapolated to the behaviour of the whole device, and the final design parameters are shown in Table 1. The field balance for a model structure comprised of three full cells and two coupling cells is displayed in Figure 1. The transverse electric field is, as expected, lower in the coupling cells, and nearly balanced in the interior cells. The transverse magnetic field is more balanced due to the mode profile: it does not notably penetrate into the beam tubes.

Table 1: XTD design performance

Parameter	Value
Field amplitude, $\sqrt{E/P^{1/2}}$	8.48 kV/mW$^{1/2}$
Group velocity, v_g	0.0267c
Attenuation factor, α	0.66 m^{-1}
Cavity length, L_T	0.46 m
Number of cells, N	53
Power ratio, P_{out}/P_{in}	0.55

FABRICATION AND TUNING

The XTD is currently in the final stages of fabrication with one last prototype scheduled for brazing prior to completion of the final XTD structure. The entire device is fabricated from OFE 101 F68 Class1 Cu, with the exception of the SS tuning pins, water fittings, SLAC crush seal style RF flanges and vacuum flanges.

Proper handling and cleaning procedures are critical to the successful operation of any RF cavity and detailed travelers have been utilized to document the fabrication of the device, from raw material to final leak testing. Each copper component is also subjected to a modified version of the SLAC C01 cleaning procedure prior to braze. All fabrication will be performed with CNC lathes and mills, with a revised asymmetric waveguide taper eliminating the need for EDM processing. Non-sulfur containing cutting fluids will be employed to ensure UHV compatibility.

The mechanical design and fabrication of the XTD structure was informed and guided by tolerancing studies performed in HFSS. All dimensional deviations encountered in the manufacturing of the device will be overcome by the incorporation of tuning pins (Figure 2). These pins allow for a total of 15 MHz of resonant frequency modification per cell by means of dimple tuning. Each cell includes 'mode separation' geometries whose alignment is accomplished with the incorporation of a clocking grove on the outer diameter of each cell. Axial alignment of each cell is also built into the cell geometry.

The main structure of the XTD device is composed of 50 identical cells. Thus, to verify cell geometries by conventional metrological means such as with a CMM, would be expensive and time consuming. Therefore a more cost effective, time effective and informative QA process of measuring each cell frequency has been developed. This single cell RF test stand is precisely measured only once by a CMM and simulated with HFSS. All of the repeating 'main' cells in the structure will then be measured to verify its resonant frequency and overall conformance to fabrication tolerances.

All brazing of the XTD structure will take place in a Hydrogen furnace, using preformed braze filler when possible. All graphite and SS fixturing for the final prototype is currently in fabrication. Cu Coupons will travel with the assembly during furnace braze for future metallographic analysis.

Verification of the tuning procedure and algorithm will be performed on the final prototype under the contract with SLAC, utilizing the experience and infrastructure developed for the NLC X-band accelerating structures R&D program. This procedure will then be repeated on the final assembly prior to crating and delivery to the Accelerator Test Facility at Brookhaven National Laboratories.

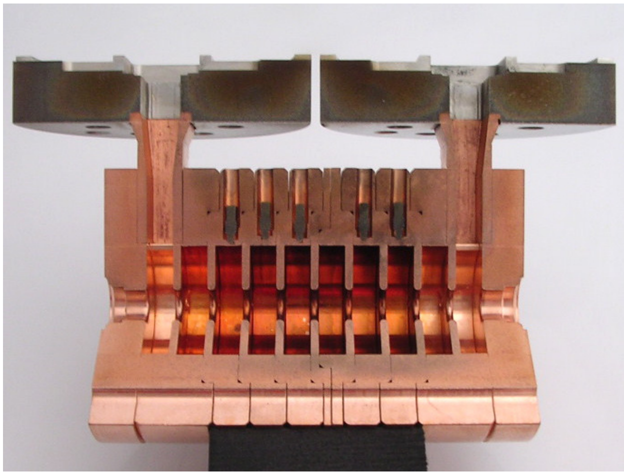

Figure 2: A cross-section of deflecting cavity prototype.

EXPERIMENTAL PLANS

XTD commissioning and initial experiments will be performed at Accelerator Test Facility at BNL in Fall of 2008. A numerical simulations of the XTD performance with ELEGANT [7] indicate the device longitudinal resolution less than 10 fs for ATF beam parameters. The beam experiments will be performed in collaboration with UCLA, and will include a direct phase space mapping experiment (Figure 3), when the beam is imaged behind the horizontal bending magnet, while deflected vertically in the XTD. As a result a detailed map of the longitudinal phase space will be available. The experiment will be performed after the ATF-UCLA chicane beam compressor [8], to study a longitudinal phase space fragmentation due to non-linear effects in the strongly compressed beam.

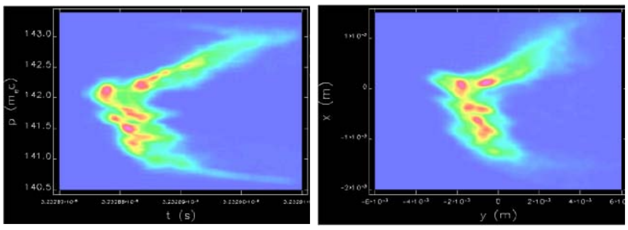

Figure 3: Numerical (ELEGANT) model of ATF XTD experiment: a post-compressor beam longitudinal phase space in (p,t)-coordinates (left); and a corresponding (x,y) map after the XTD and a bending dipole (right).

CONCLUSION

The X-band travelling wave deflection cavity is a promising tool for high resolution longitudinal diagnostic of ultra-fast beams, and is currently in the final stage of development at RadiaBeam Technologies. The device use can be extended to very high energies due to compactness and efficiency of the X-band approach. In the experimental stage of the project XTD will be used to perform a study of the physics of compressed beam with the unprecedented level of details.

This work has been performed under U.S. DOE SBIR contract No. DE-FG02-05ER84370. The authors thank Valery Dolgashev for his help with this project.

REFERENCES

1. B.E. Carlsten and S.J. Russell, "Subpicosecond compression of 0.1-1 nC electron bunches with a magnetic chicane at 8 MeV", *Phys. Rev. E* **53**, R2072 (1996).
2. S.G. Anderson *et al.*, "Velocity bunching of high-brightness electron beams", *Phys. Rev. ST AB* **8**, 014401 (2005).
3. R.H. Miller, R.F. Koontz, D.D. Tsang, "The SLAC Injector", IEEE Trans. Nucl. Sci., 804 (1965).
4. P. Krejcik. private communication.
5. D. Alesini, "RF deflector-based sub-ps beam diagnostics: application to FELs and advanced accelerators", in *Physics and Applications of High Brightness Electron Beams* (World Scientific, 2006) Erice, Sicily, 2005.
6. J. England et al., "X-Band Dipole Mode Deflecting Cavity for the UCLA Neptune Beamline", in *PAC 2005 Proc*. (IEEE, 2005).
7. M. Borland, "ELEGANT: A Flexible SDDS-Compliant Code for Accelerator Simulation", APS LS-287, (2000).
8. R. Agustsson, "Design, Construction, Simulation and Implementation of a Magnetic Electron Bunch Compressor", *Master thesis*, University of California, Los Angeles, (2004).

FERMI LOW-ENERGY TRANSVERSE RF DEFLECTOR CAVITY

P. Craievich*, S. Biedron, C. Bonţoiu, S. Di Mitri, M. Ferianis, M. Veronese (ELETTRA, Trieste, Italy)
M. Petronio (DEEI, Università degli Studi di Trieste, Trieste, Italy)
D. Alesini, L. Palumbo (Laboratori Nazionali di Frascati, INFN/LNF, Roma, Italy)
L. Ficcadenti (Università La Sapienza, Roma, Italy)

Abstract

FERMI@Elettra is a soft X-ray fourth generation light source under development at the ELETTRA laboratory. The single bunch beam is produced by a photo-injector, then accelerated up to 1.2 GeV by a linear accelerator, and finally transported to the undulators, where the free electron lasing occurs. In order to completely characterize the beam phase space by means of measurements of the bunch length and of the transverse slice emittance two deflecting cavities will be positioned at two points in the linac. One will be placed at 1.2 GeV (high energy), just before the FEL process starts; the second at 250 MeV (low energy), after the first bunch compressor (BC1). In this note we describe the low-energy bunch deflection, which allows the efficiency of the first bunch compressor to be measured. Furthermore the RF design and electromagnetic simulations are presented, with a complete evaluation of the wakefields inside the structure.

INTRODUCTION

Complete characterization of the beam phase space by means of measurements of the bunch length and of the transverse slice emittance are important tasks for the FERMI FEL project [1]. Deflecting cavities, such as iris loaded wave guide or multi cell standing wave structures, are a powerful tool to reach this aim. Two deflecting cavities will be positioned at two points in the linac: one at 1.2 GeV (high energy), just before the FEL process starts; the second at 250 MeV (low energy), after the first bunch compressor (BC1). Figure 1 shows the linac layout where the transverse deflecting structures are indicated with RF DEFL1 and RF DEFL2. In this note we describe the low-energy bunch deflection following the work done for the high-energy RF deflector [2]. The deflector following BC1 will operate in a vertical deflecting mode to allow measurements of the horizontal slice emittance and bunch length. This will allow the efficiency of the first compression to be estimated. The deflector will be followed by a multi screen emittance measurement station and the quadrupole magnets in-between the OTR screens will be separated by $\pi/4$ phase advance. The screen at a phase advance of $117deg$ with respect to the RF deflector will be used for the bunch length measurements. The worst phase advance on the screens is at $200deg$ downstream of the deflector. The vertical β-functions at the deflector and screens positions are $12m$ and $5m$, respectively. Deflecting cavities, such as iris loaded wave guide or multi cell standing wave structures, are a powerful tool to reach this aim. In particular the deflector at low energy will work at a maximum beam energy of 250 MeV and with an S-band RF frequency of $2998MHz$ (the operating frequency of the linac). Table 1 contains the beam parameters for the Medium Length Bunch option (MLB) [1]. These have been used for the calculations in the following sections.

* paolo.craievich@elettra.trieste.it

Table 1: Beam parameters for Medium Length Bunch (MLB) option.

Beam Parameter		**Unit**
Total Charge	0.8	nC
Bunch Length (RMS)	210	μm
Total Normalized Emittance	2.0	μm
Max Beam Energy	250	MeV

BUNCH LENGTH MEASUREMENTS

If the finite transverse emittance of the bunch is taken into account, then the RMS beam size at the screen after the deflection can be estimated by the quadratic summation of the RMS non-deflected particle transverse size distribution and of the RMS beam size in the pencil beam approximation estimated by following [3] and references therein:

$$\sigma_{y,S,\epsilon} = \sqrt{\sigma_{y,0}^2 + \sigma_{y,s}^2}$$
$$= \sqrt{\frac{\epsilon_N \beta_S}{\gamma} + \left[\frac{eV_\perp}{E}\sigma_z \left(\frac{\omega_{RF}}{c}\cos\varphi_{RF}\right) R_{34})\right]^2} \qquad (1)$$

Figure 2 shows the calculated beam size as a function of $V_\perp$ according to eq. 1. The observations at the OTR screens satisfy the requirements for both the worse beam optics ($200deg$) and the better beam optics ($117deg$). Finite emittance contribute to the increase of the beam size measured at the screen and Eq. 1 shows that if $V_\perp$ is sufficiently large the relative error due to finite emittance can be reduce, i.e. a relative error less than 3% requires a deflecting voltage $V_\perp \geq 1.6MV$.

Maximum Peak Voltage Specification

The measurement of the transverse slice emittance requires short portions of the bunch length to be resolved at the screen after the bunch is deflected. Assuming a uniform longitudinal charge distribution, the slice length at the

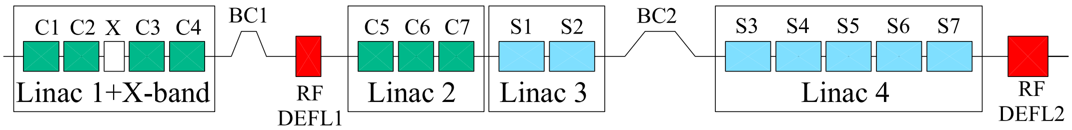

Figure 1: Sketch of the FERMI linac layout with the positions of the RF deflectors.

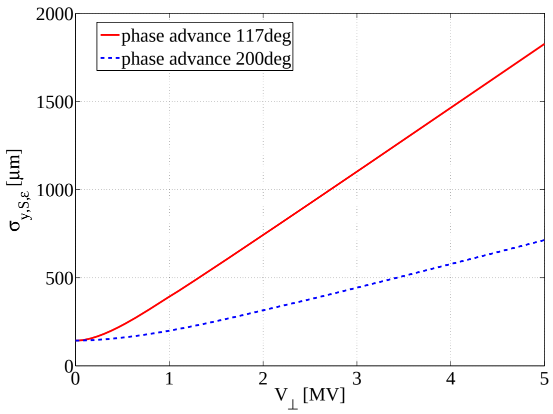

Figure 2: The calculated beam size at the OTR screens as a function of the deflector peak voltage $V_{\perp}$. Solid and dashed lines represent the beam size as calculated at the best and least effective screen locations.

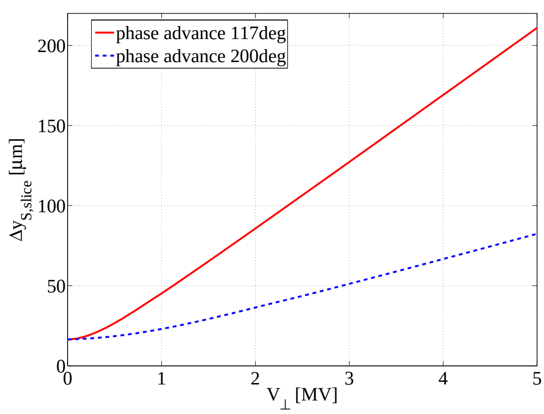

Figure 3: Slice length at the OTR screens as a function of the deflecting voltage $V_{\perp}$ considering a division of the bunch into 30 longitudinal slices.

screen is given by:

$$\Delta y_{S,slice} = \frac{\sqrt{12}\sigma_{y,S,\epsilon}}{30} \tag{2}$$

Figure 3 shows the slice length at the OTR screens as a function of deflecting voltage $V_{\perp}$ considering a division into 30 slices of the whole bunch. As seen in [3] assuming $10\mu m$ RMS resolution of the screen then a contrast of 70% allows the detection of the $40\mu m$ slice length. Going back to figure 3, in the approximation of the uniform bunch current distribution, a minimum peak voltage of $2.3MV$ is required in the worse optical condition for the bunch vertical deflection.

RF DEFLECTOR SPECIFICATIONS

The RF design and the choice between different options was done taking into account the following constraints:

- the minimum peak voltage $V_{\perp} \geq 2.3MV$;
- the working RF frequency $f_{RF} = 2998MHz$;
- RF pulse length $t_{RF} \leq 3\mu s$;
- the maximum available RF power $P_{RF} = 5MW$;

The minimum peak voltage $V_{\perp} = 2.3MV$ can be achieved by both traveling wave (TW) or standing wave (SW) structure. We have chosen to scale the deflecting SW structure developed for the SPARC project [4] to the FERMI operating frequency. Such a choice allows us reaching better resolution and flexibility. This could become important if one contemplates use of an even shorter bunch as in the single bunch compressor scheme which was proposed as a possible option for FERMI@Elettra [5].

RF DEFLECTOR DESIGN

The deflector is a SW structure composed of 5-cells operating on the π-mode. Table 2 lists the main RF parameters of the deflector such as the quality factor Q, the transverse shunt impedance $R_{\perp} = V_{\perp}^2/2P_{RF}$, the filling factor t_f when the coupling coefficient $\beta = 1$, and the nearest mode frequency separation Δf. L is the total length of the RF structure. The deflector geometric parameters are plotted in figure 4. They are the iris radius a, the iris thickness t, period L_{cell}, the coupling cell radius R_1 and the side radius R_2, R_3, the rectangular coupling window dimension x_w, y_w.

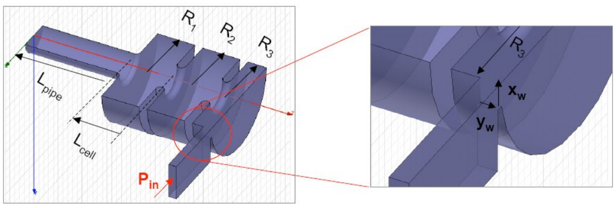

Figure 4: Schematic view of the standing wave deflector [6].

The proposed RF structure is about $0.5m$ long and satisfies all the RF constraints.

Table 2: Main RF and structure parameters of the transverse deflector.

L_{cell}	50.00 $[mm]$
R_1	58.25 $[mm]$
R_2	57.60 $[mm]$
R_3	57.45 $[mm]$
a	18 $[mm]$
y_w	8 $[mm]$
x_w	19.5 $[mm]$
t	9.5$[mm]$

f_{RF}	2.998 $[GHz]$
Q	15600
$R_\perp$	2.4 $[M\Omega]$
P_{diss}	150 $[W]$
τ	0.8 $[\mu s]$
$V_\perp@5[MW]$	4.9 $[MV]$

WAKEFIELDS EVALUATION

A special procedure has been used in order to find the longitudinal and transverse wake functions, as reported in [7]. Numerical results obtained with the ABCI code [8] have been fitted with exponential functions taken as perturbations to the well-know diffraction regime wake functions [9], namely ($0 < z \leq 3.5mm$):

$$w_{||}(z) = 0.36[e^{-21.03z^{0.499}} + e^{21.03z^{0.56}}]\frac{Z_0 c}{\sqrt{2}\pi^2 a}\sqrt{\frac{1}{z}} \quad (3)$$

and

$$w_\perp(z) = 0.37[0.85e^{-66\,z} + e^z]\frac{2^{3/2} Z_0 c}{\pi^2 a^3}\sqrt{z} \quad (4)$$

Figure 5 shows the longitudinal (top) and transverse (bottom) wake potentials as obtained using the parametrized wake functions in eqs. 3, 4 and as computed with ABCI. There is a very good agreement between the "analytical" and numerical results.

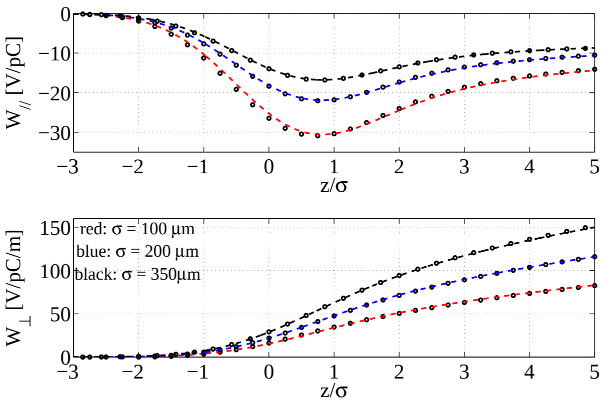

Figure 5: Longitudinal (top) and transverse (bottom) wake potentials for Gaussian bunches as obtained using the parameterized wake functions (eqs. 3, 4) (dashed lines)and as computed with ABCI (black circles).

In order to estimate the effects due to the wakefields on the electron beam we have considered a bunch with $\sigma = 200\mu m$ and calculated the loss factor $k_{||}$ and the kick factor $k_\perp$. The results are the following: $k_{||} = 15.5keV/nC$ and $k_\perp \approx 0.1\mu rad/nC/mm$ at $250MeV$. Thus, the passive influence of the low-energy deflector on the electron beam can be neglected.

CONCLUSION

In this paper the study of the electron bunch deflection at around $250MeV$ for the measurement of the bunch length and of the transverse slice emittance is performed. As a conclusion, a peak voltage of $2.3MV$ for the RF deflector is completely satisfactory for the bunch length measurement. The same specification allows for a resolution of 30 slices over the MLB with an intensity contrast of about 70%. A complete RF design has also been performed, taking also in account of the wakefields effects. The wakefield estimations have shown that the passive influence of the low-energy deflector on the electron beam can be neglected.

ACKNOWLEDGMENT

This work was supported in part by the Italian Ministry of University and Research under grants FIRB-RBAP045JF2 and FIRB-RBAP06AWK3.

REFERENCES

[1] FERMI@Elettra Conceptual Design Report, Trieste, Italy, 2007.

[2] P. Craievich et al., "A transverse RF deflecting cavity for the FERMI@Elettra project", Proceeding of the 8^{th} DIPAC, Venice, Italy, 2007.

[3] P. Craievich et al., "RF deflection of the electron bunch at high energy in FERMI@Elettra", Fermi technical note ST/F-TN-07/09, 2007.

[4] D. Alesini et al., *RF deflector design and measurements for the longitudinal and transverse phase space characterization at SPARC*, NIM A 568 (2000) 488-502.

[5] M. Cornacchia et al., *Running FERMI with One-Stage Compressor: Advantages, Layout, Performance*, ST/F-TN-07/08, 2007.

[6] L. Ficcadenti et al., *Electromagnetic design of the low energy RF Deflector for the FERMI@ELETTRA Project*, talk held at Frascati, October 2007.

[7] C. Bonţoiu and P. Craievich, The short-range wake functions of the low-energy RF beam deflector of FERMI, ST/F-TN-08/06, 2008.

[8] Y. H. Chin, `http://abci.kek.jp/abci.htm`.

[9] K. Bane and M. Sands, Wakefields of very short bunches in an accelerating cavity, SLAC-PUB-4441, Nov. 1987.

SLICE EMITTANCE MEASUREMENTS AT SPARC PHOTOINJECTOR WITH A RF DEFLECTOR

C. Vaccarezza, D. Alesini, E. Chiadroni, G. Di Pirro, M. Ferrario, L. Ficcadenti, D. Filippetto, G. Gatti, B. Marchetti, E. Pace, INFN-LNF, Frascati (Roma), Italy
A. Cianchi, INFN-Roma Tor Vergata, Roma, Italy
A. Mostacci, University La Sapienza, Roma, Italy.

Abstract

The SPARC photoinjector is a R&D facility performing beam dynamics studies and driving a SASE-FEL. The RF deflector, completely designed and built by the SPARC team, allows measurements of the longitudinal properties of the beam bunch. Using it and the well know technique of the quadrupoles scan, the slice emittance has been measured. We report the experimental setup description together with the first measurement results.

INTRODUCTION

The goal of the SPARC R&D facility [1] is to produce a high brightness electron beam able to drive a SASE-FEL in the visible light and exploring all the most critical issues of the future X-ray source subsystems. The stringent FEL experiment requirements on the normalized emittance, both projected and "slice", put a strong relevance on the experimental measurement of this beam feature. For this purpose a diagnostic beamline has been equipped at SPARC between the photoinjector and the undulators where a combined setup of a RF deflector cavity and a bending dipole is provided to fully characterize the six-dimension phase space of the photoinjector output beam. In this paper the slice emittance measurement with the RF deflector is described together with the preliminary results.

EXPERIMENTAL SETUP

The SPARC photoinjector consists of a 1.6-cell RF gun of the BNL/UCLA/SLAC type [2] operating at S band (2856 MHz), with a Cu incorporated metallic photocathode; it generates a 5 MeV electron beam. Three accelerating sections follow, S-band TW, raising the energy up to ≈150MeV. The M. Ferrario working point [3] is adopted for the beam transverse emittance compensation at the end of the SPARC linac. Downstream the third accelerating section a diagnostic beamline is located: a layout of the magnets and measurement flags used for the longitudinal and transverse phase space characterization is reported in Fig. 1. The longitudinal beam profile is measured powering the RF deflector and directly analyzing the image produced by the beam on the flag F1 while the complete longitudinal phase space is reconstructed using the RF deflector in combination with the dipole magnet, and analyzing the image produced by the beam on the flag FD1. Using the RF beam deflection in the vertical plane the horizontal slice emittance can be measured either on the transfer lines or on the dogleg, at the flags F1 or FD3,

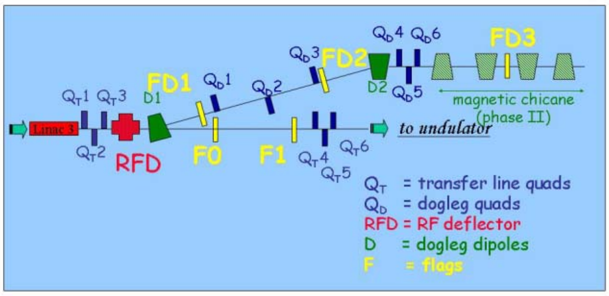

Figure 1: SPARC diagnostic beamline schematic layout

respectively. The last two quadrupoles after the linac sections, QT2 and QT3, are used for the quadrupole scan. In Fig. 1 the schematic layout of the beamline is reported.

RF Deflector

The SPARC RF deflector developed at SPARC is a 5-cell SW reaching a maximum transverse deflecting voltage of more than 3*MW* with an input power of nearly 2*MW* [4]. The main parameters and dimensions are reported in Table 1, while in Fig. 2 a picture of the deflector installed in the diagnostic beamline is shown besides a 3D sketch of a quarter of the structure.

The transverse distribution of the bunch at the screen position is the superposition between the deflected beam size and the vertical dimension of the bunch slices at the flag position (σ_y), as illustrated in Fig. 3. The rms resolution length (L_{res}) can be defined as the bunch length that gives, on the flag, a vertical spot exactly equal to σ_y. When a simple drift space is provided between the RF

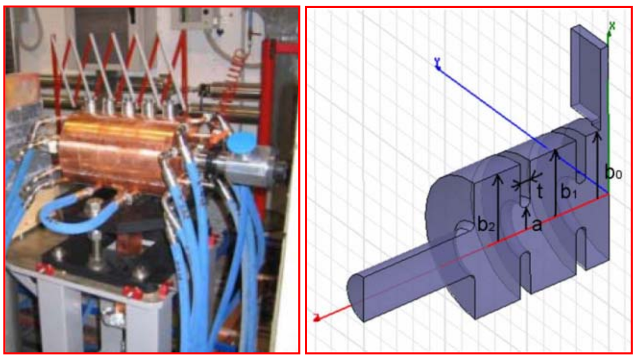

Figure 2 picture of the deflector as installed in the SPARC beamline and a 3D sketch of a quarter of the structure.

deflector and the considered screen, the achievable measurement resolution follows from (our case L=3.90m):

$$L_{res} \cong \frac{\sigma_y \, cE/e}{\omega_{RF} L V_\perp} = \frac{cE/e\sqrt{\varepsilon_y \beta_{y\_defl}}}{\omega_{RF} L V_\perp} \qquad (1)$$

Table 1: SPARC RF deflector dimensions and parameters.

Dimensions (mm)	Parameters	Dimensions (mm)	Parameters
b_2	60.92	b_2	60.92
b_1	59.93	b_1	59.93
b_0	60.04	b_0	60.04
a	20	a	20

MEASUREMENT PROCEDURE

RF Deflector Calibration

In order to better evaluate the scaling factor between the bunch longitudinal length and its vertical dimension on the screen, the RF-deflector deviation is calibrated by measuring the beam centre position vs. the varying RF-deflector phase: from the curve slope the scaling factor between the longitudinal and the vertical dimension is obtained. Applying $V_\perp = 1.8kV$, i.e. $P_{RF} = 700kW$, we obtain the scaling factor $f = 0.38(longmm)/mm$. The zero-crossing phase is provided by the centroid position previously determined with the RF deflector switched off, and the bunch length can be measured.

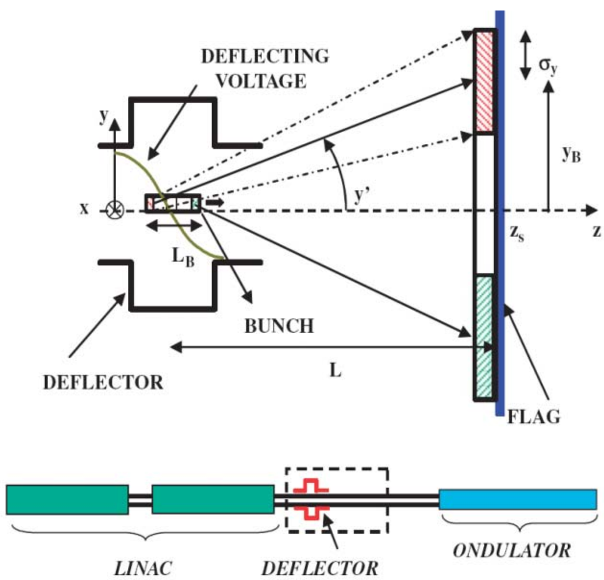

Figure 3: Bunch length measurement schematic setup using an RF deflector.

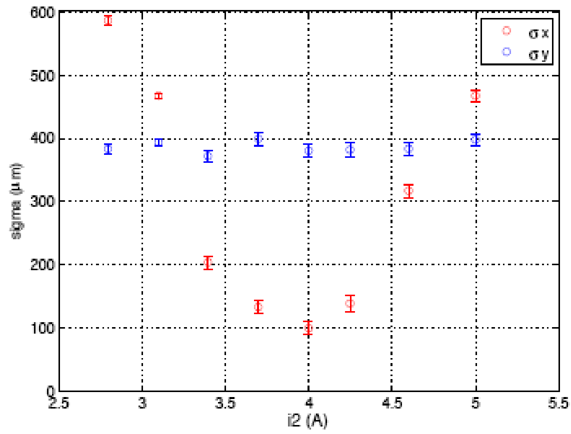

Figure 4 : Transverse beam dimensions as function of the second quad power supply applied current.

Quadrupole Scan

The quadrupole scan is performed with the two quadrupoles placed upstream the RF- deflector in order to keep constant the vertical dimension of the beam, with a typical value of $\sigma_y \approx 400\ \mu m$ and a stability of ≈0.07% as can be seen in Fig. 4 where the beam transverse dimensions are plotted as recorded during a q-scan with the RF-deflector switched off. Twenty images are averaged for each current step.

DATA ANALYSIS

The twenty images group is off-line analyzed performing for each one the region of interest, (ROI) selection. This is illustrated in Fig. 5 where from left to right the YAG screen contour is excluded from the analysis. The background in this case is not filtered due to negligible contribution of the dark current.

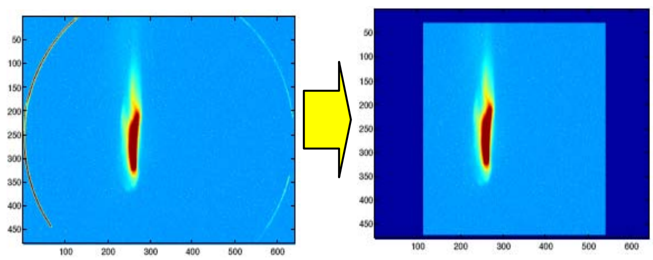

Figure 5: From each one of the recorded pictures the region of interest is selected using the maximum/3 threshold criterion.

For each quad-current step the beam vertical profile is obtained averaging over the twenty image group; the signal baseline is selected above the maximum/3 threshold, see Fig. 6.

The horizontal profile signal cleaning is performed with the same algorithm employed for the emittance-meter data analysis [5]: the initial value for the baseline and rms width is estimated at first, defining the ROI window, centered on the maximum of the distribution. The baseline is then calculated by averaging the portion of distribution out of the window, while the initial value for the rms width is calculated over the portion of distribution inside it. The fit results are then used to adjust the original

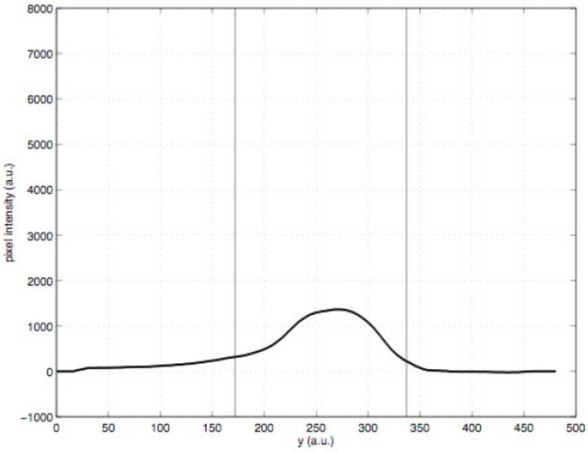

Figure 6: Vertical profile selection of the image and its footprint on the particle distribution

profile by subtracting the baseline and limiting the ROI to ± 5 times the rms width around the mean. Noise suppression of the profile curve is obtained by an iterative procedure which computes the rms value, then shrinks the region of interest down to ±3 times the rms and so on. The procedure stops when the new values match the result of the previous iteration. The algorithm converges typically after 4–5 iterations.

EXPERIMENTAL RESULTS

First slice emittance measurements have been performed on a 300pC beam, with E=145 MeV The vertical rms dimension was σ_y=400 µm, that with the measured calibration factor, corresponds to L_{res}= 150 µm for a measured total bunch length $L_b \approx 2.22$ mm. For the first analysis the considered slice length is ≈ 300 µm corresponding to a total of six slices, and then 13 slices for a slice length of ≈ 150 µm. The charge distribution is reconstructed to check the beam portion excluded from the analysis taking into account the signal threshold of maximum/3: the 78% of the beam results selected. The reconstructed slice emittance is shown in Fig. 7 for the six slices analysis, and in Fig. 8 for the thirteen slices The lowest value obtained are ε_{nx}=1.4 ± 0.1 and ε_{nx}=1.3 ± 0.1 for six and thirteen slices respectively, in reasonable agreement the one with each other.

CONCLUSIONS

The first slice emittance measurement results obtained at SPARC have been reported together with a brief description of the whole measurement data taking and analysis process. Even though not so relevant concerning the photoinjector optimization, nevertheless they represent a good test for the whole high energy diagnostic setup provided at the SPARC R&D facility, after the first experience with the emittance-meter [5]

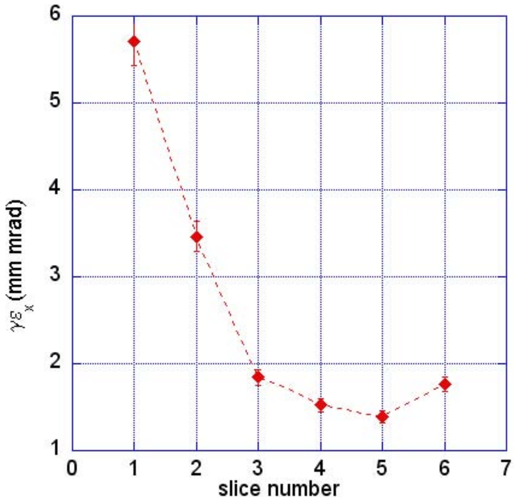

Figure 7: Horizontal slice emittance reconstruction with six slices considered, L_{slice}≈300 µm

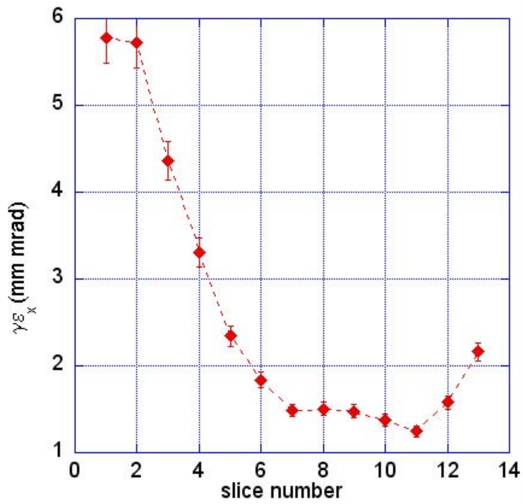

REFERENCES

Figure 8: Horizontal slice emittance reconstruction with thirteen slices considere, L_{slice}≈150 µm.

[1] http://www.lnf.infn.it/acceleratori/sparc/
[2] D.T. Palmer, The next generation photoinjector, Ph.D. Thesis, Stanford University, 1998.
[3] M. Ferrario et al., "HOMDYN study for the LCLS RF photoinjector", SLAC-PUB-8400, (2000
[4] D. Alesini et al., Science Direct, Nucl. Jnstr. Meth. Jn Phys. R. A 568 (2006), 488-502
[5] A. Cianchi et al., Phys. Rev. ST Accel. Beams **11,** 032801 (2008)

A POSSIBLE THz RADIATION SOURCE WITH A TRAIN OF SHORT PULSES IN THE SPARC HIGH BRIGHTNESS PHOTOINJECTOR

M. Boscolo[a,*], M. Castellano[a], E. Chiadroni[a], M. Ferrario[a], V. Petrillo[b], A. Stella[a], C. Vaccarezza[a]
[a] INFN/LNF, Via Enrico Fermi 40, 00044 Frascati (Roma), Italy
[b] University and INFN/MI, Via Celoria 16, 20133 Milano, Italy

Abstract

A radiofrequency electron gun followed by a compressor can generate trains of terahertz sub-picosecond electron pulses by illuminating the photocathode with a comb laser pulse. Any radiation process which does not change the electron distribution can be used to study the coherent spectrum of radiation emitted by a comb electron bunch. The coherent part of the spectrum is strongly enhanced by its N^2 dependence, where N is the number of particles in the bunch, being interesting both as possible source of Far-Infrared Radiation (FIR) and as diagnostic tool of the bunch structure.

A feasibility study for a possible experiment at SPARC to be realized with the addition of a dedicated magnetic chicane is discussed. An optimization study of a magnetic chicane with a negative and variable R_{56} is studied, together with a set of parameters relative to the SPARC machine with the intent of demonstrating the feasibility of this experiment. The dynamics is studied within the SPARC system with the PARMELA code.

INTRODUCTION

Electron pulse trains of some hundreds pC charge, sub-picosecond (sub-ps) length and repetition frequency of some terahertz can be useful to drive FEL experiments, plasma accelerators and efficient generation of terahertz (THz) radiation [1]. A radio-frequency (rf) electron gun whose photocathode is illuminated by a comb-like laser pulse generates at the cathode sub-ps high charge disk trains. The work done by the space charge force produces a negative linear energy chirp that can be exploited to restore the initial density profile either by means of an rf accelerating structure operating in the velocity bunching mode [2] or by a magnetic compressor with negative R_{56} [3,4,5].

The intent of the work is to study both the electron beam dynamics and THz radiation generated by a train of micro-bunches, produced by the comb beam feature through a magnetic compressor. The obtainable radiation power is compared to the one emitted by a single bunch. We present the feasibility study of a THz generation source at the high brightness SPARC [6] photoinjector that could be situated downstream the dogleg and magnetic compressor, as in the layout of Fig. 1.

The dogleg consists of two bending magnets with bend angles of equal magnitude but opposite sign separated by a straight section hosting three quadrupoles. After a straight line with three more quadrupoles necessary for matching conditions there is a magnetic compressor, consisting of four bending magnets and five quadrupoles, necessary for reaching highly negative R_{56} values. Downstream the magnetic compressor THz radiation could be generated as coherent transition radiation (CTR) emitted by the beam crossing a metal foil oriented at 45º incidence and autocorrelated using a Martin-Puplett-type interferometer.

The beam dynamics inside the rf-gun, accelerating cavities and downstream inside a magnetic compressor is studied by simulations with the PARMELA [7] code. We first discuss the results obtained with one short electron bunch and its coherent spectrum of radiation, then a train of two, three and five micro-pulses with an analysis of their coherent radiation spectrum.

SINGLE BUNCH SIMULATIONS

The intensity distribution of the radiation emitted by a bunch with longitudinal profile g(x) is the one emitted by a single electron multiplied by $[N+N(N-1)f(\omega)]$, where N is the number of particles in the bunch and $f(\omega)$ is the form factor, that is a number between 0 and 1 related to the bunch geometry, being defined by

$$f(\omega)=\left|\int_{-\infty}^{\infty} g(x)\cdot e^{-j\frac{\omega}{c}x}dx\right|^2$$

In our case $N\sim10^9$ and the coherent part of the spectrum is strongly enhanced by its N^2 dependence, interesting both as possible source of FIR radiation and as diagnostic tool of the bunch structure. We can assume that the radiation process does not modify the bunch

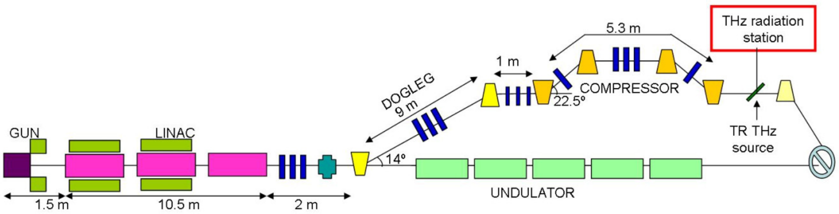

Fig. 1. Cartoon of the SPARC photoinjector with a THz radiation station downstream a dogleg and compressor, where bending and quadrupole magnets are marked by yellow wedges and blue lenses, respectively.

Table 1. Parameters for the rf-gun (first column), and three accelerating cavities (second, third and fourth column) used for comb beam simulation in the SPARC accelerator compressed in a magnetic chicane to be installed after the dogleg.

	Rf-gun	I TW section	II TW section	III TW section
Gradient [MV/m[	120	10	10	6
Energy [MeV]	5.6	35.5	65.6	83.7
Phase ϕ [deg]	32	0 (on crest)	0 (on crest)	0 (on crest)
Solenoid field [Gauss]	2730	400	0	0

case for the chosen process for THz radiation generation, i.e. CTR. The goal was to find an optimized parameter set first for a single bunch and afterwards for a bunch train suitable to produce THz radiation, that is with a spectral content in this range.

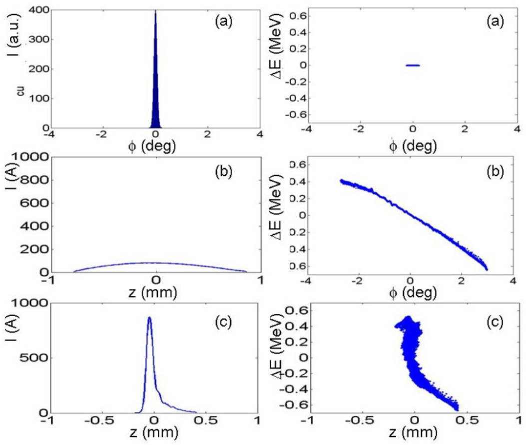

Fig. 2. Bunch (a) at cathode, (b) at exit of linac and (c). at the exit of the compressor. Left and right frames, respectively: longitudinal profile and ΔE(MeV) vs length.

To produce the theoretical curve of the spectrum content of the electron bunch at the TR foil, the creation and transport of the beam in the accelerating sections were first simulated using the tracking code PARMELA. This detailed simulation employed 50000 macroparticles. The beam obtained from PARMELA at the end of the linac was matched with MAD through the transfer line and dogleg up to the compressor entrance. With MAD we also found the right quadrupoles strength values in the chicane for the desired R_{56}, and used these values for tracking the electron beam with PARMELA from the linac exit up to the THz radiation source (see layout of Fig. 1). The longitudinal profile at this position is then used to calculate with a dedicated algorithm its form factor, for the prediction of the expected spectral content of its emitted radiation.

Dedicated simulations have shown that the chosen area of parameters corresponds to a non space charge dominated beam. 3-D space charge effects in the magnetic chicane can therefore be neglected.

The single bunch optimized for our purpose has Q=300 pC, full length at cathode L=200 fs and 1 mm of transverse radius (left (a) plot of Fig. 2). The beam enters the three accelerating sections on crest and beam energy at the end of beamline is about 83.7 MeV. The parameter set for the case under discussion is reported in Table 1.

The results of PARMELA simulation are shown in Fig. 2: (b) plots show the beam at the end of the linac with a negative linear chirp of about ΔE~1 MeV induced by the space charge force and (c) plots show the compressed beam at the exit of chicane. The maximum compression, about a factor 7, is obtained with R_{56}=-70 mm and the final bunch has σ_z=55 μm and peak current I_p=800 A. The full evolution of the beam emittance and envelope in the two transverse planes is shown from the cathode to the exit of the compressor in the left and right plots of Fig. 3, respectively. Such short pulse is suitable for THz radiation generation, as appears from the corresponding form factor shown in Fig. 7. However, being the form factor sensitive to the bunch length and charge, the optimal radiated power can be tuned experimentally with careful pulse shaping studies at cathode.

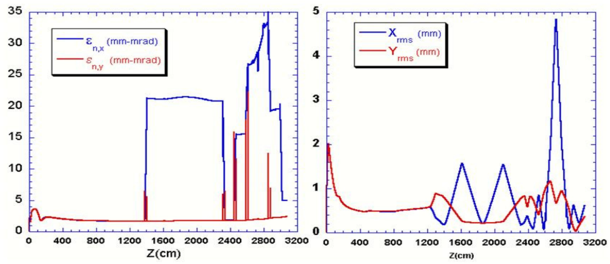

Fig. 3 Left and right frames, respectively show the beam emittance and envelope evolution for the single pulse case from cathode to the magnetic compressor exit

BUNCH TRAIN SIMULATIONS

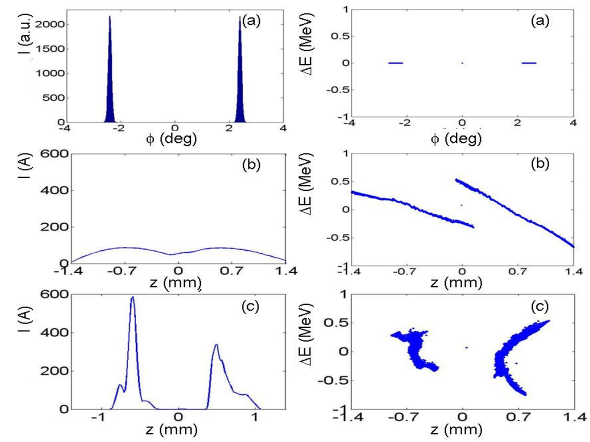

Fig. 4. Two pulses comb beam (a) at cathode; (b) at exit of linac and (c) at the exit of the magnetic compressor (R_{56}=-100 mm). Left and right frames: longitudinal profile and ΔE(MeV) versus length, respectively.

With a train of micro-pulses with a separation of the order of λ or some multiples the form factor approaches 1 at that wavelength. The form factor provides a useful description of the micro-bunches inter-distance, being very sensitive to this parameter. So, in our case, in order to enhance the emitted power of THz radiation, the micro-pulses inter-distance must be a multiple of 300 μm. Unfortunately, the initial micro-bunches inter-distance at cathode is slightly distorted both during acceleration and compression. Consequently, using the comb technique it is not trivial to obtain perfectly equally spaced micro-bunches, parameter that is crucial for the application under discussion. However, the solution can be overcome both experimentally and with simulation by finely tuning the inter-distance of bunches at cathode in order to obtain a form factor as close to 1 as possible at a desired THz frequency. Moreover, also the capability of the magnetic chicane to compress the micro-bunches by the same factor is important to produce a clean spectrum. This parameter could be adjusted at cathode, experimentally, as well.

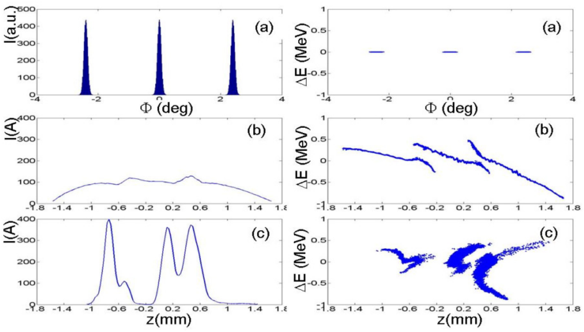

Fig. 5 Three pulses comb beam (a) at cathode; (b) at exit of linac and (c) at the exit of the magnetic compressor (R_{56}=-120 mm). Left and right frames: longitudinal profile and ΔE(MeV) versus length, respectively.

Examples of our studies are shown in Figs. 4, 5 and 6, for the two, three and five micro-bunches train, respectively. The charge for two and three pulses is 300pC/peak and is 120/peak for the five micro-pulses train.

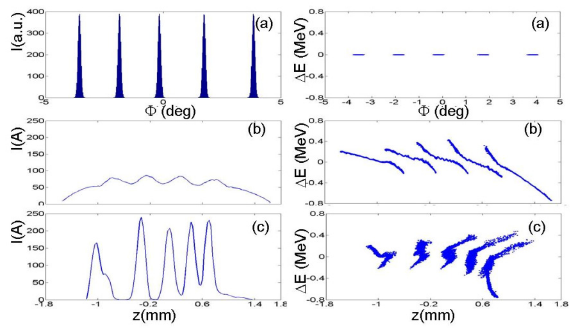

Fig. 6 Five micro-pulses comb beam (a) at cathode; (b) at exit of linac and (c) at the exit of the magnetic compressor (R_{56}=-120 mm). Left and right frames: longitudinal profile and ΔE(MeV) versus length, respectively.

The corresponding form factors are plotted in upper plot of Fig. 7. A realistic comparison of the different structures can be done only taking into account the total number of electrons involved in the process together with the single particle white frequency distribution of Transition Radiation. Lower plot of Fig 7 shows the form factor multiplied by the number of particles N^2 for the different cases of comb beams.

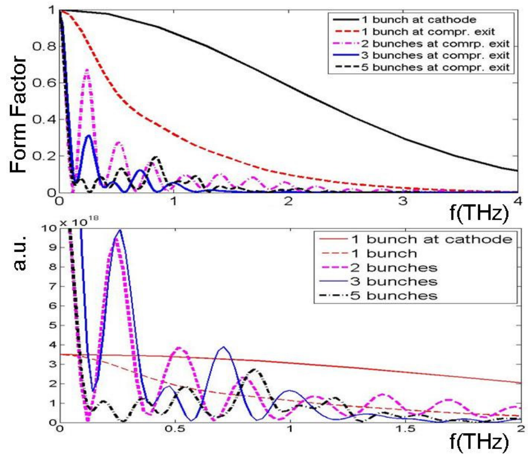

Fig.7 Form factor and (N^2·form factor) by for two (pink), three (blue) and five (black) micro-bunches compared to one bunch.

CONCLUSIONS

Simulations show that an rf-gun driven by a laser sub-ps pulse train in connection with a magnetic compressor can transform that laser pulse train into a sub-ps electron beam pulse train. The beam features in terms of peak current, energy spread and emittance are very sensitive to the charge of the macro-pulse, to the compensating solenoidal fields and to the R_{56} value of the magnetic chicane. In fact, R_{56} has to be around -100 mm to compress the beam using the negative linear chirp induced by the space-charge force.

The exploitation of the presented technique for the generation of THz radiation in SPARC machine has shown the feasibility of this experiment. We showed that the quality of the coherent spectrum emitted by a comb beam is tightly connected to the electron micro-bunches lengths and to micro-pulses inter-distance. To this regard, we think there is still margin of improvement and work is in progress to further optimize all the electron beam parameters to maximize the THz emitted power.

REFERENCES

[1] P.O.Shea et al., in: Proc. of 2001 Part. Acc. Conf., Chicago, IEEE, NJ, p.704 (2001).
[2] L. Serafini, M. Ferrario, AIP Conf. Proc. **581,** p.87 (2001).
[3] M. Boscolo et al., in: Proc. of EPAC06, p. 98 (2006).
[4] M. Boscolo, M. Ferrario, C. Vaccarezza, I. Boscolo, S. Cialdi, F. Castelli, , Int. J. Mod. Phys. B 21, p.415 (2007).
[5] M. Boscolo, M. Ferrario, I. Boscolo, F. Castelli and S. Cialdi, Nucl. Instr. and Meth. A, (2007)
[6] M. Ferrario, these Proceedings.
[7] J.Billen, PARMELA, LA-UR-96-1835 (1996).

RECENT RESULTS AND FUTURE PERSPECTIVES OF THE SPARC PROJECT

M. Ferrario, D. Alesini, M. Bellaveglia, R. Boni, M. Boscolo, M. Castellano, E. Chiadroni, A. Clozza, L. Cultrera, G. Di Pirro, A. Drago, A. Esposito, L. Ficcadenti, D. Filippetto, V. Fusco, A. Gallo, G. Gatti, A. Ghigo, B. Marchetti, A. Marinelli, C. Marrelli, M. Migliorati, A. Mostacci, E. Pace, L. Palumbo, L. Pellegrino, R. Ricci, U. Rotundo, C. Sanelli, F. Sgamma, B. Spataro, F. Tazzioli, S. Tomassini, C. Vaccarezza, M. Vescovi, C. Vicario, INFN-LNF, Frascati, RM, Italy
F. Ciocci, G. Dattoli, A. Dipace, a. Doria, G. P. Gallerano, L. Giannessi, E. Giovenale, G. Orlandi, S. Pagnutti, A. Petraia, M. Quattromini, C. Ronsivalle, E. Sabia, I. Spassovsky, V. Surrenti, ENEA C.R. Frascati, RM, Italy
L. Catani, A. Cianchi, INFN-Roma II, RM, Italy
M. Mattioli, M. Petrarca, M. Serluca, INFN-Roma I, Roma, Italy
A. Bacci, I. Boscolo, F.Broggi, F. Castelli, S. Cialdi, C. De Martinis, D. Giove, C. Maroli, V. Petrillo, A.R. Rossi, L. Serafini, INFN-Mi, Milano, Italy
J. Rosenzweig, UCLA, Los Angeles, CA, USA
M. E. Couprie, SOLEIL, Gif-sur-Yvette, France
M. Bougeard, B. Carré, D. Garzella, M. Labat, G. Lambert, H. Merdji, P. Salières, O. Tchebakoff, CEA Saclay, DSM/DRECAM, France

Abstract

The SPARC project foresees the realization of a high brightness photo-injector to produce a 150-200 MeV electron beam to drive 500 nm FEL experiments in various configurations, a Thomson backscattering source and a plasma accelerator experiment (these last two ones jointly with the project PLASMONX). The SPARC photoinjector is also the test facility for the recently approved VUV FEL project named SPARX. As a first stage of the commissioning, a complete characterization of the photoinjector has been accomplished with a detailed study of the emittance compensation process downstream the gun-solenoid system: this lead to the first direct experimental demonstration of emittance oscillations in a drift. The second stage of the commissioning, that is currently underway, foresees a detailed analysis of the beam matching with the linac in order to confirm the theoretically prediction of emittance compensation based on the “invariant envelope” matching and the demonstration of the “velocity bunching” technique in the linac. SASE and SEEDING experiments are foreseen by the end of the current year. In this paper we report the experimental results obtained so far and the scientific program for the near future.

INTRODUCTION

The SPARC project comprises an R&D photo-injector facility devoted to the production of high brightness electron beams to drive a SASE and SEEDED FEL experiments in the visible and UV light. The high beam quality produced by SPARC will also allow investigations into the physics of ultra-short beams, plasma wave-based acceleration, and production of advanced X-ray beams via Compton back-scattering. Moreover SPARC is the injector prototype of the recently approved SPARX project [1], that foresees the construction in the Frascati area of a new high brightness electron linac for producing SASE-FEL radiation in the 10-1 nm wavelength range. The first phase of the SPARC project, that is now concluded, consisted in characterizing the electron beam out of the photoinjector, a 1.6 cell S-band RF gun, at low energy (5.6 MeV with 120 MV/m peak field on the cathode), before the installation of the 3 S-band accelerating sections, which boost the beam energy up to 150-200 MeV. The results obtained during the first commissioning phase are reported in [2,3,4].

The second stage of the beam commissioning, that is currently underway, foresees a detailed analysis of the beam matching with the linac in order to confirm the theoretically prediction of emittance compensation based on the “invariant envelope” matching [5,6,7] and the demonstration of the emittance compensation during the “velocity bunching” experiment [8]. SASE and SEEDING experiments are foreseen by the end of the current year.

SPARC COMMISSIONING

Soon after disassembling the emittance-meter in January 2007, the installation of the whole machine took place, starting from the accelerating sections. Then the transport line to the undulators was completed, and the undulators themselves aligned on the reference beam line. The bypass and diagnostics channel was installed as last element. The present layout of the machine is shown in Fig 1. The 3 travelling wave accelerating structures have been conditioned and are now operating at a maximum gradient of 20-20-10 MV/m respectively, providing a final beam energy of 150 MeV. The low level RF control electronics to monitor and synchronize the RF phase of the accelerating structures along the linac and the laser shot on the photocathode has been also commissioned and it is now fully operative resulting in an energy stability less than 0.1 % [9]. Around the first and the second accelerating structure two long solenoids are placed to provide additional focusing (with a maximum field of 0.18 T) for matching the beam envelope with the linac, according to the invariant envelope conditions [5,6].

Figure 1: Picture of the SPARC photoinjector showing t3 accelerating structures with 2 long solenoids.

The undulator, realized by *ACCEL Gmbh* [10], is made by 6 permanent magnet sections with 2.8 cm period, 25 to 6 mm variable gap and undulator parameter k = 1.4, see Fig. 2. In between each module a 0.36 m long gap hosts quadrupoles for horizontal focusing and radiation diagnostic boxes.

Figure 2: Picture of the SPARC undulator chain during installation.

FIRST BEAM MEASUREMETS

The first beam measurement, concerning the beam characterization at full energy, started on May 2008. Unfortunately the cathode was performing at quite lower level of quantum efficiency, emission uniformity and stability with respect to the first phase: this prevented us to work at the maximum charge of 1 nC and to perform systematic studies of beam optimization in the laminar space charge dominated regime. Nevertheless, some preliminary tests of beam transport up to the exit of the third accelerating structure, checking the diagnostic systems and doing the first comparison with simulations [11], were performed. In this stage of commissioning we have been operating with a laser pulse with gaussian longitudinal profile 6-8 ps FWHM long. The bunch charge was in the range of 200 pC - 700 pC (quantum efficency in the lower order of 10^{-5}). The beam has been accelerated up to 150 MeV with an energy spread of 0.1%. During the beam transport tests the rms spot size has been measured on four YAG screens: three screens are located at the entrance of each RF structure while the fourth one is located at the exit of the linac, where the rms emittance is measured by a quadrupole scan [12] and the bunch length and slice emittance are measured with a high resolution RF deflector [13].

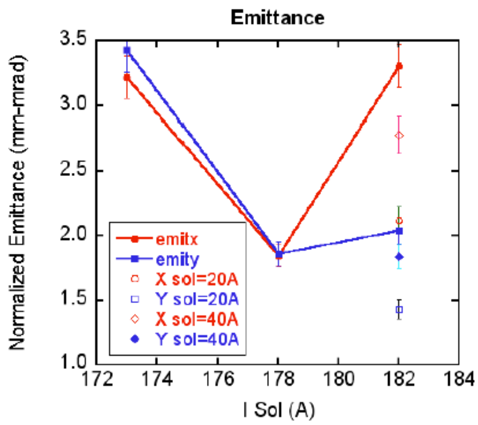

Figure 3: Emittance measurement for different configuration of the gun solenoid and the coils around the accelerating structures.

The measurements shown in Fig. 3 have been done at 500 pC and a Gaussian pulse of 8.5 ps FWHM. The best projected emittance obtained so far is slightly below 2 mm-mrad in both planes, in good agreement with PARMELA simulations (see Fig. 4). Optimal envelope matching conditions have not yet been achieved, but additional improvements in beam quality are expected [11].

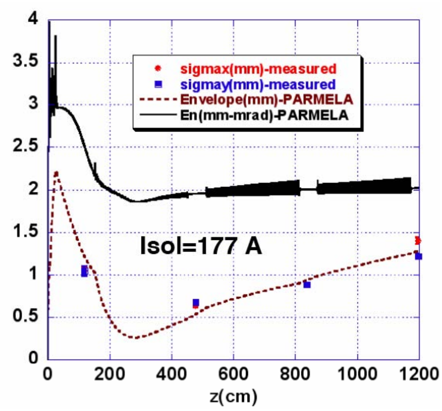

Figure 4: PARMELA simulation of the envelope and emittance corresponding to the best measurement shown in Fig. 3. The measured enevelopes (blue rectangle) are also shown.

FUTURE FEL EXPERIMENTS

One of the future experiments at SPARC, is to study and test the amplification and the FEL harmonic generation process of an input seed signal obtained as higher order harmonics generated in gases [14] and compare it with the single spike operation described in [15]. The main components of the seed source consist in the implementation of a second laser amplification chain operating in parallel to the photo-injector laser system, in the installation of a chamber devoted to the generation of high harmonics in gas, which has been realized at CEA [16], and finally in the implementation of the hardware required for injecting, in the electron transfer line connecting the SPARC linac with the SPARC undulator, the radiation generated in the chamber. A chicane deflecting the e-beam from the linac axis and a periscope allowing the injection of the harmonic beam have been realized for this purpose.

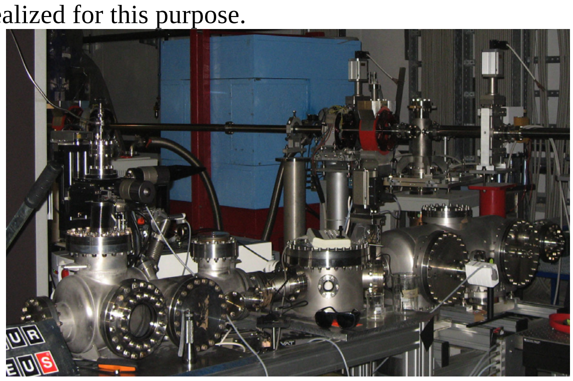

Figure 5: Harmonic generation chamber in the SPARC Hall.

The chamber was delivered to LNF in the beginning of 2007, see Fig. 5, and the laser system for the seeding experiment has been completed in November of the same year. In December the chambers have been aligned with the laser and the injection periscope, and have been commissioned. A preliminary test was concluded with the observation of the third harmonic of the Ti:Sa beam, see Fig. 6. The spatial profile of the radiation has been collected by projecting the beam on a reflecting screen. The image has been detected with an high sensitivity CCD camera (Canon IXUS 800 IS). The setup for the production of the harmonics in gas is composed by three chambers. The laser is focussed in the first chamber where harmonic generation occurs. In this chamber a cell is filled by Argon gas and is illuminated by the laser source. A second chamber is used to increase the vacuum gradient between the first chamber and the SPARC transfer line. Then the third chamber, 1.5 meters downwards, is used to match the harmonic beam with a waist located in the middle of the first undulator for a correct overlap with the e-beam. The optical mode shaping is performed using two spherical mirrors reflecting nearly at normal incidence, both equipped with motorized mounts, and an additional translation stage under the second mirror, for the adaptation of the focusing point in the undulator. The distance between the gas jet and the middle of the first undulator is about 8 m.

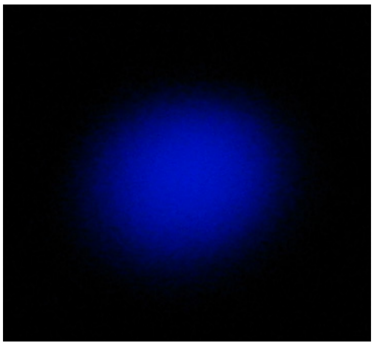

Figure 6: Spot of the UV radiation at the detection screen

REFERENCES

[1] L. Palumbo et al., “Status of SPARX Project”, these proceedings.
[2] A. Cianchi et al., Phys. Rev. ST-AB 11, 032801 (2008).
[3] M. Ferrario et al., Phys. Rev. Letters, 99, 234801 (2007).
[4] A. Mostacci et al., Review of Scientific Instruments 79, 013303 (2008)
[5] L. Serafini, J. B. Rosenzweig, Phys. Rev. E 55 (1997) 7565.
[6] M. Ferrario et al., SLAC-PUB-8400.
[7] C.-x. Wang et al., Phys. Rev. ST-AB 10, 104201 (2007)
[8] L. Serafini and M. Ferrario, AIP Conference Proceedings, 581, 87, (2001)
[9] A. Gallo et al., these proceedings.
[10] F. Ciocci et al. “SPARC undulator parameter set”, SPARC-FEL-03/003.
[11] C. Ronsivalle et al., these proceedings.
[12] A. Cianchi et al., these proceedings.
[13] C. Vaccarezza et al., these proceedings.
[14] L. Poletto et al., EUROFEL-Report-2005-DS4-008.
[15] V. Petrillo, “Single spike operation in the SPARC SASE-FEL”, these proceedings.
[16] O. Tcherbakoff, et al., Proc. of FEL 2006 conference, BESSY, Berlin, Germany.

PERFORMANCES OF THE SPARC LASER AND RF SYNCHRONIZATION SYSTEMS

Alessandro Gallo, David Alesini, Marco Bellaveglia, Giancarlo Gatti, Carlo Vicario
INFN/LNF, Frascati (Roma), Italy

Abstract

The SPARC project consists in a 150 MeV S-band, high-brilliance linac followed by 6 undulators for FEL radiation production at 530 nm. The linac assembly has been completed and the SPARC scientific program is presently in progress.

The low level RF control electronics to monitor and synchronize the RF phase of the accelerating structures along the linac and the laser shot on the photocathode has been commissioned and it is now fully operative. The laser synchronization is routinely monitored by measuring the phase of the free oscillation of an RF cavity impulsively excited by the signal of a fast photodiode illuminated by the laser shot, and slow drifts are automatically corrected by a dedicated shot-to-shot feedback system. A similar slow automatic regulation is implemented on each linac accelerating section acting either on low level or high power sliding lines. The phase noise in the 2 RF power stations is counteracted by fast intra-pulse phase feedback systems that have been developed and put in operation. Phase stability measurements taken over the whole synchronization system are reported, and performances of different synchronization architectures, μ-wave based or laser based, are compared.

INTRODUCTION

All the various projects of FEL radiation facilities [1] presently in operation, commissioning, construction or proposal phases share a common technical issue since they require an unprecedented level of synchronization [2] among RF systems, laser systems and beam diagnostics. The required beam quality in terms of emittance, energy spread, peak current and shot-to-shot reproducibility can only be met provided that a global synchronization at level of 50÷500 fs (depending on the application) can be maintained over long time scales (hours or days).

The SPARC project [3], situated at the INFN Frascati National Labs, is a test facility consisting in a 150 MeV injector followed by 6 permanent magnet ondulators to produce 530 nm SASE FEL radiation in saturation regime. The linac RF is the standard SLAC S-band (f_{RF} =2856 MHz) and the beam generated in an RF gun is accelerated up to the final energy by three travelling wave (TW) accelerating sections (constant gradient, 3 m long each). Two klystrons (45 MW peak, 4.5 μs pulse duration, 10 Hz rep rate) are used. The first one powers the RF gun, the 3rd TW section and an RF deflector located between the linac and the undulators for beam diagnostic, while the second one, equipped with a pulse compressor (SLED), drives the 1st and 2nd TW sections.

The basic architecture and the performances of the SPARC RF reference distribution and synchronization system are reported in [4,5]. In this paper we report the operational experience with the SPARC synchronization system and recent results of experimental measurements aimed at improving its performances. We also describe the system upgrades proposed to cope with the synchronization requirements of the whole SPARC scientific program of beam experiments.

SPARC SYNCHRONIZATION: OPERATIONAL EXPERIENCE

The SPARC operation has started in 2006, with the characterization of the beam emittance at the RF gun exit, and has continued in 2007 and 2008 with the whole linac installed. During this period the laser synchronization and low-level RF systems have been operated and upgraded, showing good performances and reliability.

Photoinjector Laser Synchronization

The frequency of the optical cavity of the SPARC photoinjector laser oscillator is locked to the RF reference in a PLL configuration (Synchrolock™) [4,5]. Motorized and piezo-controlled mirrors are used to tune the optical cavity and close the loop.

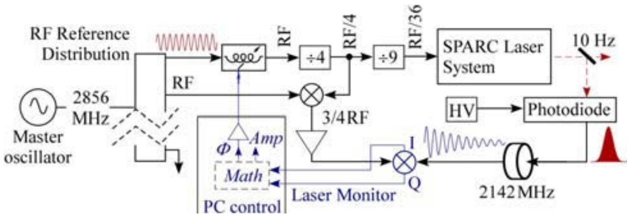

Figure 1: Laser synchronization monitoring and feedback.

The repetition rate of the laser pulses is reduced along the amplification chain from 79.33 MHz (RF/36, the frequency of the oscillator optical cavity) down to 10 Hz. The time of arrival of the laser shots after amplification is monitored using a resonant pulse stretching method, as sketched in Fig. 1. This technique, developed and implemented at SPARC, is based on a HV photodiode generating a narrow electric pulse synchronous with the laser which excites free oscillations of a resonant cavity tuned exactly at the frequency of the reference. The time of arrival is encoded in the phase of the free oscillations with respect to the reference, and is recovered by mixing the two signals. At SPARC we use the 3/4 RF = 2142 MHz signal as the reference for this measurement to reject the large environmental noise at the linac frequency appearing when the high power klystrons are in operation. The laser time of arrival is measured and acquired every shot, and the information is available in the SPARC computer control system for statistical analysis and slow feedback implementation.

The slow feedback keeps the phase of the laser arrival at a constant selectable value correcting the fluctuations by moving a motorized sliding delay line placed along the path of the laser reference signal. The phase jitter, i.e. the random shot-to-shot fluctuations, can not be corrected by the slow feedback loop but can be monitored in real time to qualify and tag the beam measurements. A typical sample of a short term acquisition is shown in Fig. 2, corresponding to a laser jitter of ≈ 400 fs.

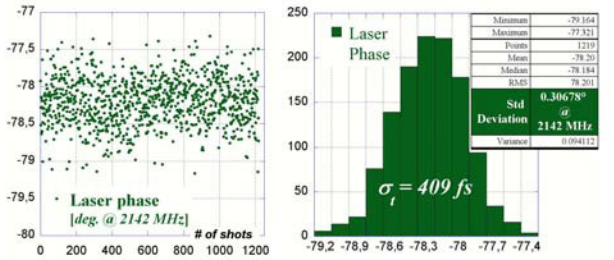

Figure 2: SPARC Laser measured phase jitter.

This is essentially the value already measured at the oscillator level [5], which means that laser amplification do not relevantly contribute to the jitter budget.

RF synchronization

The signal driving the two high power klystrons operating at SPARC is directly derived from the main RF distribution. The phase control implemented around each SPARC RF stations is sketched in Fig. 3 and consists of two main blocks: the fast intra-pulse phase lock, which encompasses the klystron and its driver amplifier, and the slow pulse-to-pulse feedback loops which includes the long coaxial and waveguide connections between the machine hall and the klystron tunnel.

The fast intra-pulse phase lock is a system developed and implemented at SPARC to reduce the contribution of the RF power stations to the total phase jitter of the RF fields interacting with the beam. To overcome the Nyquist limit associated to the 10 Hz pulse-to-pulse feedback loops, we have developed an analog system to measure the klystron output phase deviation with respect to the drive signal, and correct it along a fraction of the time duration of a single pulse. The required bandwidth of such a system is ≈ 1 MHz, which is obtained by using fast electronic phase shifters, while the loop error signal is processed by current-feedback operational amplifiers. The group delay of the klystron and the physical length of the signal path contribute with ≈ 100 ns and ≈ 50 ns to the total group delay of the loop, which has to be little enough to preserve the loop bandwidth. As a consequence the path length of the loop can not exceed ≈ 10 m. Under these conditions the transient regime of the loop error and correction signals lasts ≈ 1 µs over the ≈ 3 µs of the RF pulse duration, as shown in Fig. 3. The phase noise is thus reduced from ≈ 600 fs to < 80 fs.

Most of the coaxial and waveguide connections carrying the reference signal from the RF distribution rack (in the linac hall) to the klystrons (in the klystron tunnel) and the RF klystron power back to the linac cavities and accelerating sections are out of the fast intra-pulse loop. A slower feedback loop monitors the RF input power or directly the fields inside the RF devices connected to the klystron and acts on either low-level or high-power variable phase shifters to compensate the drifts that are mainly induced by thermal elongations. In this way the good phase stability of the stations equipped with the intra-pulse feedback loop is maintained across the RF devices over long time scales.

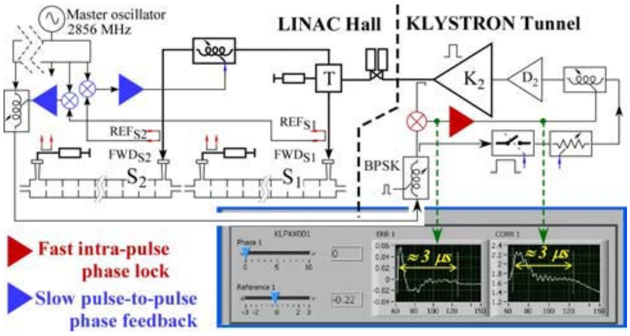

Figure 3: SPARC RF synchronization.

SPARC SYNCHRONIZATION DEVELOPMENTS

Tests of a laser-driven synchronization system

The previous presented data shows that presently the RF is a factor of ≈ 5 more accurately synchronized than the photoinjector laser. This is because the RF synchronization is a pure electronic process, and also because the RF pulse duration is long enough to allow for real time corrections. A possible way to increase the global synchronization of the machine is to eliminate the µ-wave master oscillator and use the signal coming from the laser oscillator as the machine reference.

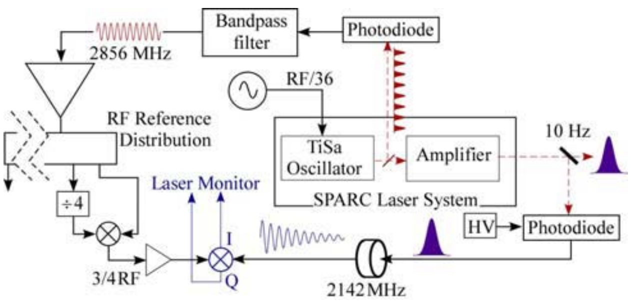

Figure 4: Laser driven synchronization set-up.

This will in principle make the laser high-power pulses intrinsically synchronous, while the conformity of the RF signals to the new reference should remain at the sub 100 fs level.

This alternative configuration has been preliminary tested only on the laser system as sketched in Fig. 4. A standalone 79.33 MHz RF reference has been provided to the laser oscillator to ensure long term stability of the optical cavity. A portion of the IR radiation leaving the optical cavity is converted in a sequence of narrow electric pulses by a fast, high rep-rate photodiode, and the 36^{th} harmonic of the signal (the 2856 MHz) is extracted by a tuned bandpass filter and used as the reference tone to drive all the RF distribution network.

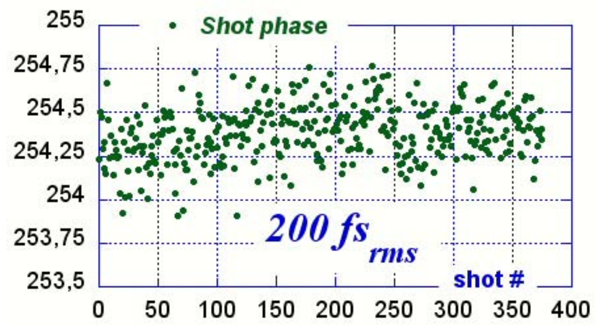

Figure 5: Jitter in the laser driven synchronization.

A measurement of the time of arrival stability of the laser pulses after amplification is reported in the Fig. 5 plot, showing a reduction of a factor ≈ 2 with respect to Fig. 2. We believe that most of the measured residual jitter (≈ 200 fs) can be attributed to the presence of the divider-by-4 prescaler board in the test set up, which could be in principle substitute by inserting a tuned 2142 MHz filter on a portion of the photodiode signal. We estimate that following this way a global synchronization at level of ≈ 100 fs is attainable.

Improvements of the time-of-arrival monitors

As an interesting by-product, the Fig. 5 measurement also shows that the resolution of our laser time of arrival monitor is < 200 fs. A more precise evaluation of the ultimate achievable resolution of arrival monitors based on resonant pulse stretching is of great interest for a comparison of this pure μ-wave method with high sensitivity, optical techniques based on cross correlation. Since no calibration sources with high stability (< 100 fs) and low repetition rate (< 100 kHz) are available for bench measurements, the resolution will be evaluated by duplicating the laser phase monitor of Fig. 1 to take the differential jitter between the two channels. A pair of equal HV photodiodes has been purchased for this task, while two resonant cavities have been designed and are going to be built. This part of the program is supported by the FAST (Femtosecond Active Synchronization and Timing) collaboration. FAST is an experiment approved by the INFN Committee for technological research to endorse the efforts aimed at improving the state-of-the-art in laser-to-RF and laser-to-laser synchronization.

The new photodiodes are rated for high saturation currents and are expected to deliver high peak voltages in the linear regime, where the photodiode AM-to-PM conversion is tolerable and do not significantly affect the phase jitter measurements. Large pulse voltages require less RF amplification after being filtered by the cavity, thus reducing the electronic noise.

Bunch arrival monitors based on the same principle are expected to be effective and much simpler with respect to laser ones, since a resonant idle cavity can be placed directly along the linac beam trajectory, and a decaying voltage oscillation synchronous with the bunch passage can be coupled out of the cavity and demodulated, with no need of photodiodes and RF amplifications. Two bunch arrival monitor cavities have been designed and will be installed after the 1^{st} and the 3^{rd} TW accelerating sections to study the bunch synchronization dependence on the laser arrival and on the amplitudes and phases of the RF fields for various working points and regimes (FEL seeding, bunch compression, ...). CAD 3D views of the SPARC bunch arrival monitor cavity equipped with two tuning plungers is shown in Fig. 6. A manual tuner will be used for coarse frequency regulation, while a motorized fine tuner will be remotely controlled to maintain the coherency between the cavity free oscillations and the reference frequency.

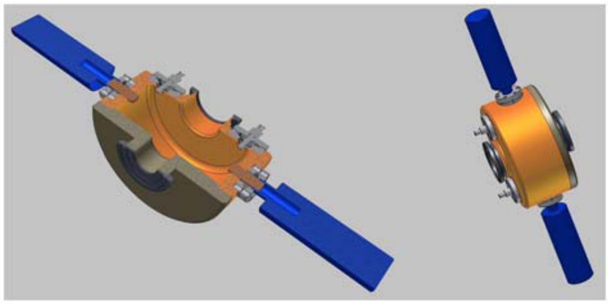

Figure 6: 3D views of the SPARC bunch arrival monitor.

CONCLUSIONS

Presently, the level of the synchronization obtained at SPARC (≈ 400 fs for the photoinjector laser and < 100 fs for the RF fields interacting with the beam) fully meets the machine requirements to have stable and reproducible beam conditions for SASE-FEL radiation production. It is also adequate for experiments of RF bunch compression and FEL seeding. Global synchronization at < 100 fs level requires improvements in the laser stabilization and/or implementation of different timing architecture. Laser and electron beams arrival monitors based on resonant pulse stretching are in operation and in preparation, respectively.

REFERENCES

[1] T. Shintake, “Review of the worldwide SASE FEL development”, Proc. of PAC07, Albuquerque, p. 89.
[2] J. Kim et al., “Femtosecond synchronization and stabilization tecniques”, Proc. FEL06, Berlin, p. 287
[3] M. Ferrario et al., “Recent results and future perspectives of the SPARC project”, WEPC075, this conf.
[4] A. Gallo, et al., “The SPARC RF synchronization system”, Proc. of PAC05, Knoxville, p. 1024
[5] A. Gallo, et al., “Laser and RF synchronization measurements at SPARC”, Proc. of PAC07, Albuquerque, p. 994

A COMPACT AND VERSATILE DIAGNOSTIC TOOL FOR CNAO INJECTION LINE

J. Bosser, G. Balbinot, S. Bini, M. Caldara, V. Chimenti, L. Lanzavecchia, A. Parravicini, Fondazione CNAO, Milano, Italy
A.Clozza, V. Lollo, INFN/LNF, Frascati (Rome), Italy

Abstract

CNAO, the first Italian center for deep hadrontherapy, is presently in its final step of construction. It will provide treatments with active scanning both with proton and carbon ion beams. Commissioning of the injection lines will be started by the time of the presentation of this report. CNAO beams are generated by two ECR sources, which are both able to produce both particle species. The beam energy in the Low Energy Beam Transfer (LEBT) line is 8 keV/u. A compact and versatile tank has been designed that contains a complete set of diagnostic tools. It is only 390mm long; it houses two horizontal and two vertical plates to suppress beam halo, measure emittance and eventually to limit beam size. It also comprises two wire scanners, for vertical and horizontal beam transverse profile, as well as a Faraday Cup for current measurement. Synchronous profile and intensity measurements and phase space distribution reconstruction can be performed with one tank monitors. Five identical tanks are installed in the LEBT, as consequence of a standardization strategy to facilitate monitoring and make maintenance easier. Expected performances and preliminary beam measurements are presented.

INTRODUCTION

CNAO accelerator is able to deliver carbon ions up to 400 MeV/u kinetic energy and protons up to 250 MeV/u, energies needed to treat deep seated tumours. Four treatment lines, in three treatment rooms, are foreseen in the first stage. For further technical details about CNAO cf. Ref [1] and [2].

The injection chain of the CNAO accelerator, placed inside the ring, is composed by a 8keV/u Low Energy Beam Transfer line (LEBT), followed by an RFQ accelerating the beam up to 400keV/u, a LINAC to reach synchrotron injection energy of 7MeV/u [3] and a Medium Energy Beam Transfer line (MEBT) to transport the beam to the synchrotron entrance.

LEBT

Description

Two ion sources are foreseen: one for carbon ions and one for protons. A first section (O1 and O2) is dedicated to each ion specie; a second section (L1 and L2), common to both lines, includes a beam chopper and a special Faraday cup (CFC) for beam current intensity monitoring. Figure 1 shows the schematic layout of LEBT line, with emphasis on the Beam Diagnostics (BD) elements.

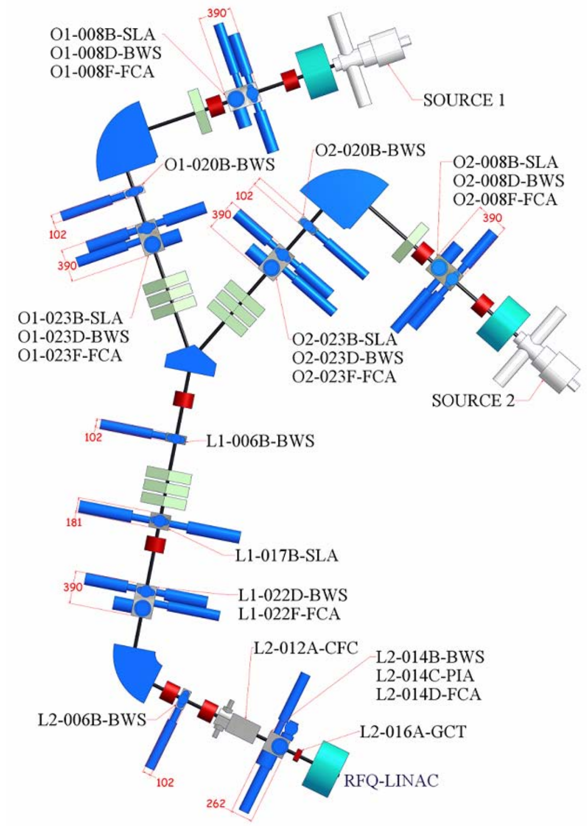

Figure 1: LEBT BD Instrumentation Layout with official elements names. SLA are Slits, BWS are Wire Scanner in both planes, FCA is Faraday Cup, CFC is the Chopper FC, PIA is Profile Grid and GCT is an AC beam current transformer.

In order to deliver 10^{10} protons and $4{\cdot}10^{8}$ carbon ions per extraction spill, with the assumed losses along the accelerator chain, the required minimum currents are 200 μA of C^{4+} and 450 μA of H_3^+.

The expected beam normalised total emittances are assumed to be less than 1 π mm mrad (240 π mm mrad geometrical). LEBT geometry allows measurement of one source while the other is in use. O1 and O2 sectors include a 90 degree dipole “spectrometer”, slits and profile and current monitors, before the switching magnet. When the Faraday cup upstream the quadrupoles triplet is inserted, the source can be monitored without disturbing the operation of the other source. Beam parameters can be measured also before the spectrometer dipole. The sources produce many different ion species at the same time; all together the total source current sums up to approximately 10 mA, depending on gas type used and source settings (Ref. [4]). Assuming a maximum total current of 20 mA, the very maximum total beam power is 480 W. Most of this power is lost into either the spectrometer vacuum chamber or in the Slits or Faraday Cup, if inserted into the beam path. In the final L1-L2 sectors the nominal intensity is 0.7 mA for H_3^+ and 0.2 mA for C^{4+}.

LEBT Beam Diagnostics instrumentation is designed in order to be small in terms of space occupancy, tolerant to high beam power deposit, in particular in the first sections, to cope with wide intensity range and to be standard. The main goals of the LEBT beam diagnostic are to select the ion specie, allow the sources fine tuning, monitor the beam profile, measure emittance up to the RFQ (LINAC) entrance.

A set of two slits (horizontal and vertical), two wire scanners (horizontal and vertical) and a Faraday Cup, are grouped in one common vacuum tank. The total longitudinal space occupancy of the tank is only 390mm. Five of these fully equipped tanks are permanently installed along the LEBT line; two additional tanks will be temporarely installed in place of the RFQ in order to measure emittance at its entrance. Each of them is able to measure beam profile, intensity and emittance. Additional four shorter tanks with a subset of the same BD instrumentation are also installed along the LEBT line.

Mechanical Issues

Each tank is machined from a unique Aluminium (Alloy AL6082T6) block; all the apertures are obtained removing material with a milling cutter; in order to minimize longitudinal space occupancy all the radial apertures are rectangular, except for the Faraday Cup. Each tank houses also a turbo molecular pump, two vacuum-meters and an injection gas dose valve; the LEBT working pressure is between $5{\cdot}10^{-6}$ and $5{\cdot}10^{-7}$ mbar, that can be worsened for beam neutralization studies by gas injection. Four pins are machined at the tank upper corners for alignment on the beam axis; a mechanically and optically qualified tank guarantee an absolute accuracy of the BD devices with respect to the tank external reference pins of 0.3mm. LEBT beam pipe internal diameter is 108.3mm, while tank one is 150mm; this latter value fixes BD monitors strokes and dimensions.

Slits

Four independent motorized copper plates compose the Slits. The four plates can create a vertical and a horizontal slit or can be positioned at the beam border, so to cut beam halo or to select ions species. A slit can also scan the beam keeping constant aperture in order to perform beam emittance measurements together with the wire scanner. A plate positioning precision is 30um. Due to the large power released by the beam, the plates are water-cooled. Secondary electrons emitted as a result of interaction between the beam and the plates could be suppressed by polarizing the plates up to 1kV. Slits plates are 1mm shifted longitudinally, so they can overlap. A special plate, with a precise cut inside, is used in the places where emittance has to be measured with high precision.

Wire Scanner (WS)

A profile measurement with a WS is performed by a synchronous acquisition of the current collected by the wire crossing the beam spot area (horizontally or vertically) and the wire instantaneous position. In the standard LEBT tank two wire scanners mounted at 90 degrees each other compose a beam profiler in H and V planes. An advantage with respect to multi-wire detectors is that only two electronics channels are needed for each plane. The wire is made by tungsten, 0.1mm diameter, and it’s able to scan the beam path with a constant (±0.1%) velocity settable up to 250mm/s; such high velocity ensures the wire integrity as concerns heating. WS is also able to work in “watch dog” mode. The wire positioning precision is the same of the Slit plates, since the same motion hardware is used. Due to beam collimation by Slits, the beam intensity can be reduced by orders of magnitude; thanks to a multi-gain electronics, profiles can be retrieved with a maximum resolution of 1nA.

Faraday Cup (FC)

FCs are used as beam stoppers for the source beam not in use, to monitor beam current stability and ripple, to measure beam profile associated with the slits.
In order to withstand the large beam power for long time, they are water cooled; the cup integrity is guaranteed by an interlocked system on the water cooling.
A repeller ring electrode, in front of the cup, pushes back secondary electrons. Measurements with beam showed that a correct intensity measurement is made by setting the repeller voltage at -350V (or above). An extra grounded metallic ring between the repeller and the cup insulating spacers avoids that leakage currents deteriorate the beam intensity measurement.

Electronics Issues

For the sake of standardization the same brushless motion system was chosen for Slits and WS displacement.

Both FC and WS collect particles beam current; such signals enter a custom transconductance amplifier (Gain = Vout/Iin [V/A]). The front end amplifier allows checking the WS wire continuity by connecting its free end to a precise current source. In the case of the Faraday cup, such test current is injected into the amplifier input in place of the cup signal. FC and WS amplifier exhibit a linearity of 2% and an output voltage of ±10V on high impedance for each gain. WS version has gains from 10^4 up to 10^8 [V/A] and a bandwidth (@ -3dB) of 400Hz, that can be reduced remotely to 200Hz. The FC, intercepting more beam with respect to WS, needs amplifier gains from 10^2 up to 10^8 [V/A] and bandwidth of 15kHz up to gain 10^4, 1kHz for higher gains.

High Voltages (HV) power supplies, containing compact commercial HV components (Ref. [5] and [6]), were developed for both Slits plates and FC repellers; the Slits HV power supply is sized to withstand 30mA, while the FC version provides a maximum current of 1mA.

All the Control System hardware interface, including data acquisition and motion control, was chosen to be made using NI PXI products, running under Labview RT (Ref. [7]).

BEAM MEASUREMENTS

Ion Species Spectrum

The ion specie spectrum measurement is performed setting horizontal slits before and after the 90 degrees dipole spectrometer and acquiring the FC current downstream the magnet, at different feeding currents or during a linear ramp. A measurement is presented in Figure 2.

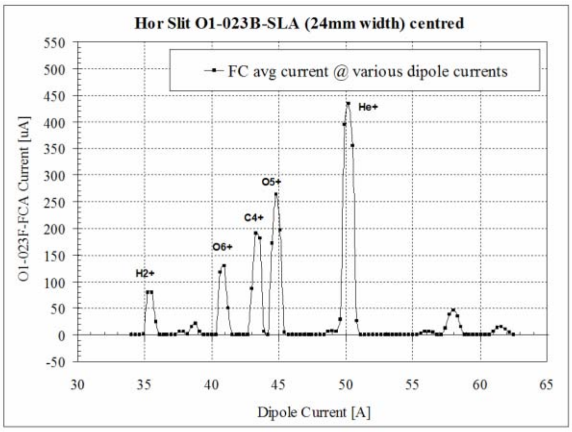

Figure 2 – Ion species spectrum of sector O1.

Profile

Beam profile can be measured in two different ways with different resolutions: using the WS, or acquiring the FC at different positions of the upstream Slit. The latter measurement is time-consuming, it has a lower-resolution with respect to the WS and needs for stable source current. Profiles obtained with WS and FC with Slits in the same tank are shown in Figure 3.

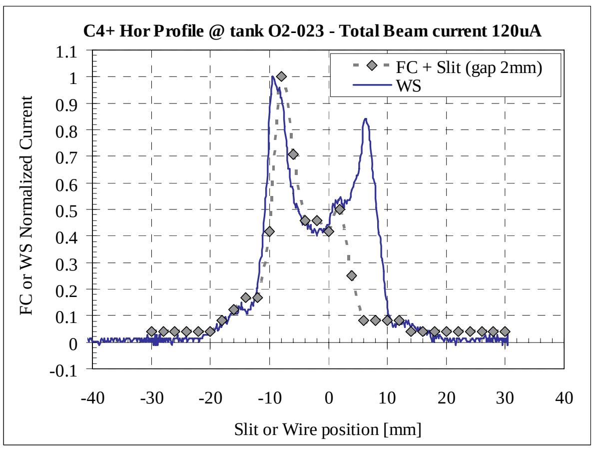

Figure 3 – Horizontal normalized profiles obtained with WS and with FC and 2mm Slit scanned across the beam.

Emittance

Beam emittance is computed from the phase space distribution measurement, obtained recording a sequence of particle beam divergences, using a WS, downstream a narrow Slit, positioned across all the beam spot area. That is made possible using every couple of Slit and Wire Scanner installed in the LEBT "compact" diagnostic tanks. A measurement is shown in Figure 4.

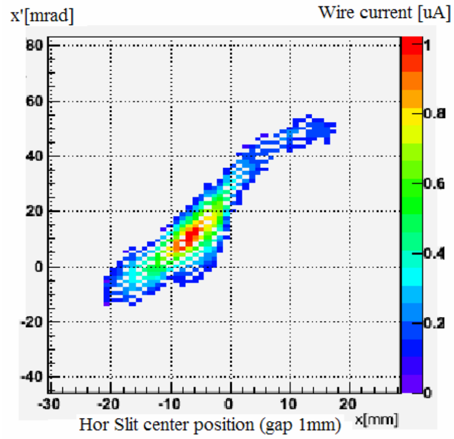

Figure 4 – Beam Horizontal phase space distribution at O2-023D-BWS. The total current on the FC was 700uA of H_3^+.

CONCLUSIONS

A total of ten compact beam diagnostic tanks, comprising five identical tanks with Slits, Wire Scanners and a Faraday Cup are presently in operation along the CNAO LEBT line during the commissioning. Mechanical and electronics issues, performances and first beam measurements of such Diagnostic tool were presented.

ACKNOWLEDGEMENTS

The effort of Comeb and Eurosystem companies has been very much appreciated by the authors.

REFERENCES

[1] S. Rossi, "Developments in proton and light-ion therapy", EPAC 2006.
[2] M.Pullia, "Status Report on the Centro Nazionale di Adroterapia Oncologica (CNAO)", EPAC 2008.
[3] H. Vormann, B. Schlitt (GSI, Darmstadt), G. Clemente, U. Ratzinger (IAP, Frankfurt am Main), S. Minaev (ITEP, Moscow), "RF Tuning of the IH-DTL for the CNAO Linac", EPAC 2008.
[4] S. Gammino, L. Celona, G. Ciavola, F. Maimone (INFN/LNS, Catania), R. Monferrato, M. Pullia, E. Vacchieri (CNAO Foundation, Milan), C. Bieth, W. Bougy, O. Tasset (PANTECHNIK, BAYEUX), "Commissioning of the ECR Ion Sources at CNAO Facility", EPAC 2008.
[5] http://www.emcohighvoltage.com/
[6] http://www.matsusada.com/
[7] http://www.ni.com

MEASUREMENTS ON AN A/D INTERFACE USED IN THE POWER SUPPLY CONTROL SYSTEM OF THE MAIN DIPOLES OF CNAO

G. Franzini, D. Pellegrini, M. Serio, A. Stella, INFN-LNF, Frascati, Italy
M. Donetti, M. Pezzetta, M. Pullia, CNAO Foundation, Pavia, Italy

Abstract

CNAO, the Italian Centre of Oncological Hadrontherapy located in Pavia, is in its final step of construction and is about to be fully operative. It is based on a synchrotron that can accelerate protons up to 250 MeV and carbon ions up to 400 MeV/u for the treatment of patients. In this paper we describe an A/D interface, used in the power supply control system of the synchrotron main dipoles, called B-Train. The field is measured in a dedicated dipole connected in series with the sixteen ones of the synchrotron and is then fed back to the power supply. The field is obtained integrating and digitizing the voltage induced on a pickup coil inserted in the gap of the seventeenth dipole. The A/D interface under study is based on a 64-channel current to frequency converter ASIC, in CMOS 0.35 µm technology, followed by a counter and uses a recycling integrator technique. The digital signal obtained is then used to generate a feedback signal for control system of the dipoles power supply. We present the electronic structure, the lab measurements and the behaviour for various setups of the A/D interface described.

INTRODUCTION

CNAO is an advanced research and hospital centre which is under construction in Pavia and is expected to be fully operative within 2009. The main goal of this project is to introduce hadrontherapy in Italy to treat patients affected by cancer. The hadrontherapy [1] involves the use of hadron beams instead of X rays (used in the most common radiotherapy techniques) in order to ionize DNA molecules and kill the diseased cells. The Hadron beam's energy release curve through the matter is affected by Bragg peak phenomenon resulting in a concentration of ionizing power in a volume of the order of 1mm^3, allowing to damage diseased cells while preserving the healthy cells which are near the treatment area.

ACCELERATOR LAYOUT

The CNAO accelerator is designed to employ proton beams up to 250 MeV and carbon ion beams up to 400 MeV/u [1]. Protons or carbon ions are collected from the sources, accelerated up to 7 MeV/u and injected into a circular synchrotron of about 25 m of diameter. They are collimated and accelerated and then directed to the extraction lines. Four independent extraction lines lead to three different treatment rooms, which allow to parallelize treatments. The typical magnetic cycle designed for the synchrotron is reported in Fig. 1. It lasts about 2 second, which is the duration of a single treatment cycle.

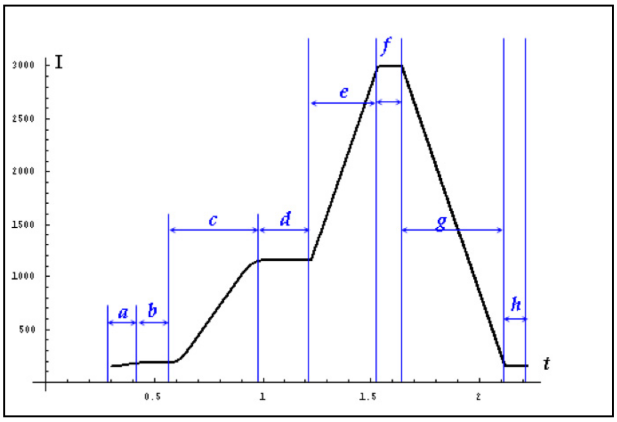

Figure 1: CNAO synchrotron magnetic cycle.

The first plateau (*b*) represents the injection phase, the following ramp (*c*) is used during the acceleration phase and the second plateau (*d*) is the beam extraction phase.

The following phases are needed to cycle the magnets for the next treatment cycle.

THE B-TRAIN SYSTEM

The 16 dipoles of the CNAO synchrotron are connected in series to a single power supply. Measurements of the magnetic field vs. magnet current characteristic showed, for the typical magnetic cycle, that the field lags the current by few ‰ with a characteristic time of the order of several hundred msec, impacting the treatment efficiency.

For this reason a dedicated system, similar to the field control system of PS at CERN and nicknamed B-train [2], has been developed to control the dipole power supply using a magnetic field reference signal instead of the usual current signal.

The B-train system provides a real time accurate measurement of the magnetic field in the synchrotron dipole magnets (Tab.1), which is used to generate a feedback signal for the power supply.

Table 1: Dipole Specifications

Parameter	Value
Maximum magnetic field	1.6 T
Maximum Dipole Current	3000 A
Magnetic Length	1677.2 mm
Slew Rate	3 T/s

It is used also to control the frequency of the accelerating cavity of the synchrotron, although, in this paper, we mainly focus on the bending magnets application.

The CNAO B-train system [3] block diagram is shown in Fig. 2. A digital measurement of the magnetic field is obtained by integrating and digitizing the voltage induced on the pickup coil inserted in the gap of a spare 17th dipole, connected in series with the synchrotron dipoles.

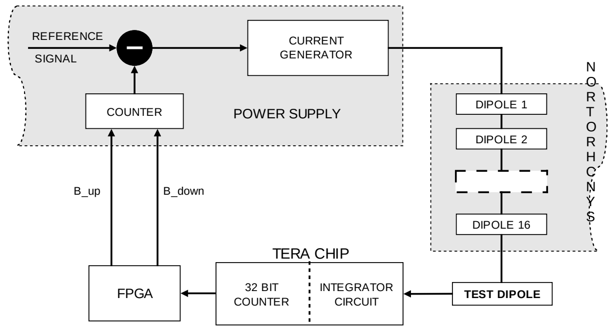

Figure 2: B-train block diagram.

The control system is driven by an FPGA which generates the control signals for the power supply and manages the digital magnetic fields readings, provided by an A/D interface. The digitized readings are translated by the FPGA into two digital single bit signals, *B_up* and *B_down*, which correspond respectively to an increment and decrement of the magnetic field of a given step. This information is then used by the power supply to manage the output current.

Since the magnetic field readings obtained through the pickup coil are differential measurements, the B-Train system is equipped with a nuclear magnetic resonance (NMR) probe, which is used to obtain the absolute value of the magnetic field at the beginning of every magnetic cycle and in the plateau (*f*) of Fig. 1, in order to calibrate the system.

To fulfil the role of the A/D interface discussed above, an ASIC chip in CMOS 0.35µm technology has been selected. The chip, called TERA, has been designed by INFN-Torino [4].

It is currently used for another application inside the beam diagnostics system of the CNAO project. Basically it is a 64-channel current to frequency converter followed by a 32 bit counter.

Each channel is independent and uses a charge balancing technique in order to nullify any deadtime during his working state. As can be seen from the diagram in Fig. 3, the input current which flows through an external impedance is integrated by a capacity C_{int} in parallel with an Operational Tranconductance Amplifier.

Two comparators with fixed thresholds are then used to drive a pulse generator which is connected to the output counter. The pulse generator drives also the charge balancing circuit: for every pulse generated, this circuit subtracts a fixed amount of charge from C_{int}, avoiding overloads and restoring the charge balance.

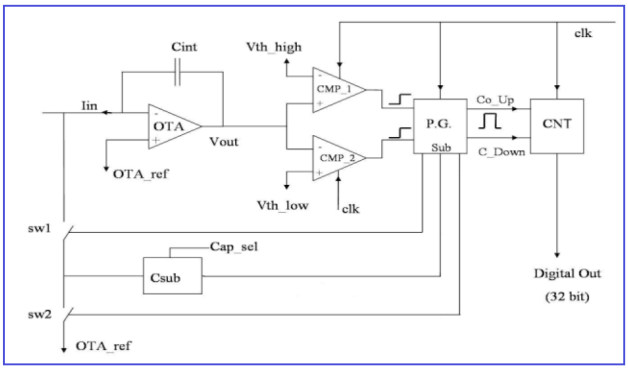

Figure 3: TERA chip block diagram.

The input-output relation is given by:

$$f = \frac{I_{in}}{Q_c} \qquad (1)$$

where *f* is the numbers of counts per second of the output counter, I_{in} is the input current and Q_c is the charge subtracted every cycle from C_{int}, via the balancing circuit.

The latter, which represents the quantization step, can be selected between 50 fC and 350 fC, with 50 fC steps.

MEASUREMENTS

The pickup coil used for magnetic readings provides a voltage output given by:

$$V(t) = -\frac{dB(t)}{dt} \cdot N \cdot S \qquad (2)$$

where NS=1.6 m^2, so that the maximum voltage for the given magnet slew rate is ~|4.8| Volt.

Bench measurements have been performed to evaluate the compatibility of the chip TERA with B-Train requirements reported in Tab. 2.

Table 2: B-train requirements

Parameter	Value
B-field measurements resolution	0.1 G
A/D conversion frequency	300 ks/s
Minimum System Bandwidth	10 kHz

The experimental setup is reported in Fig. 4: an FPGA module installed in a PXI system with an embedded controller is connected to the TERA chip via an optoisolator interface, in order to guarantee the electric isolation of the chip.

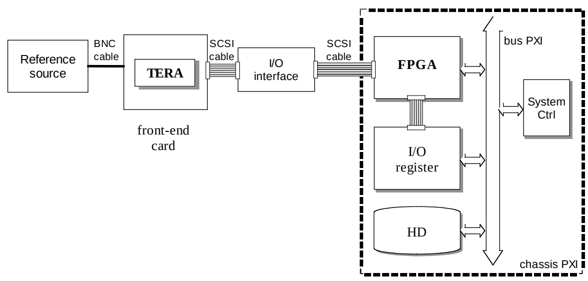

Figure 4: Measurement setup.

The FPGA receives output data from the chip via a 16 bit dedicated line and send them to an I/O interface (NI6534) for data storage and analysis. The entire measurement system has been controlled with dedicated LabView routines. The output of the pickup coil has been simulated with a HP3245A reference source connected to the input of the chip via an input resistance R_{in}.

The choice of a proper experimental setup involves considerations about:

- maximum input current
- resolution of the A/D conversion
- resistance of the pickup coil
- system bandwidth

These points put limits on the choice of R_{in} and Q_c.

The maximum input current can be derived from equation (1) and is of the order of few μA, considering that the maximum counter frequency is 20 MHz, which yields to R_{in} in the order of few megaohm.

An input resistance of order of magnitudes larger than the pickup coil resistence (r=1.6KΩ) also helps to minimize the effects due to thermal variation in the coil and if needed can be easily kept at a constant temperature.

Quantization error in the analog to digital conversion can be estimated by integrating eq. (2), which leads to:

$$\pm \Delta B = \mp \frac{R_{in}}{N \cdot S} \cdot Q_c$$

The B-Train system is aimed at realizing a closed loop controller for the dipoles power supply. An evaluation of errors due to the finite bandwidth of the controller device has been estimated, assuming a single pole low pass transfer function for the TERA chip. It led to an accettable minimum bandwidth of 10 KHz to reproduce the typical ramp current with an error smaller than 5ppm.

System bandwidth measurements for different input resistances ranging from 100 kΩ to 80 MΩ are reported in Fig. 5. As a result, values of R_{in}=10 MΩ and a Q_c=200 fC have been selected as compatible with requirements. This leads to a value of 0.0125G for a single output count.

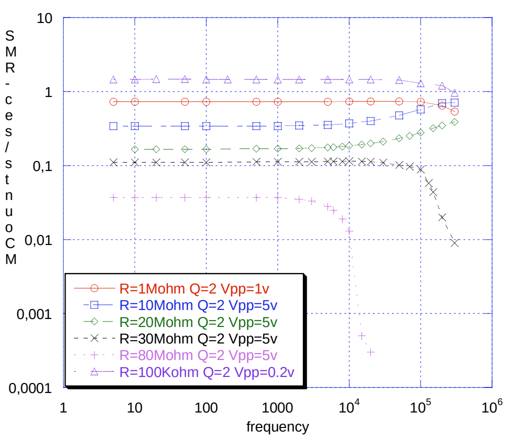

Figure 5: Bandwidth measurements.

Measurements on I/O dynamics show that the chip has a linear behavior over four decades,, working from few hundreds pA to few μA inputs. The maximum limit is due to the chip maximum frequency (f_{max}=20MHz), while the minimum is related to the noise, as it will discussed below. Measurements show differences between positive and negative current dynamics. Using our setup, the rate of counts for negative inputs are roughly 6% less than for positive inputs. This can be due to different behaviors in the charge subtraction circuit for positive and negative currents, but can be calibrated and corrected by software.

In Fig. 6 is reported the noise power spectrum obtained for a small input current. The 1/*f* trend given by *flicker noise* is dominant up to ~0.1Hz while white noise is dominant at higher frequencies. On top there are some noise peaks, which appear at frequencies in a binary sequence. Such signature can be due to a cross-talk between the digital output of the chip counter and the analog integrating front-end. It may compromise the conversion precision for our application, bringing it to a relative magnitude value of roughly 10^{-4}.

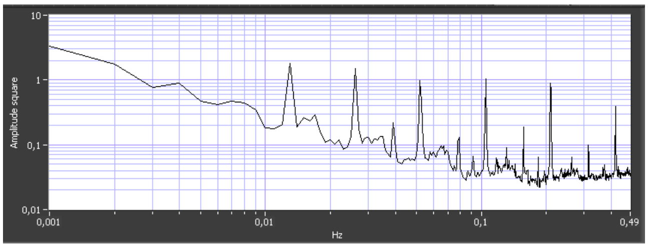

Figure 6: Noise power spectral density.

CONCLUSION

The chip TERA should be implemented in the B-Train system for integration and digital conversion of the voltage signal provided by a pickup coil inserted in one of the CNAO synchrotron dipoles. It has been characterized and tested with various setups to compare its performance with system requirements. While the frequency response and the A/D conversion frequency are adequate, its conversion resolution is up to two order of magnitude higher then the acceptable value.

This is due to cross-talk noise in the chip between the analog and digital sections.

A new TERA version is currently under test to verify its compatibility with the B-Train requirements also with respect to the cross-talk noise. With the new version of the chip, it is possible to read the single incremental counts and accumulate them at the FPGA level, bypassing the digital counter, to avoid the cross-talk noise.

REFERENCES

[1] U.Amaldi, Workshop on Space Rad. Research, 2000.
[2] P. Dreesen, I. Garcia-Alfonso, “A New B-Train System for The PS Accelerator”, CERN PS/PO Note.
[3] M.Pezzetta, CNAO Internal Note, 2007.
[4] G. Mazza et al, IEEE Trans. on nuclear science, Vol. 52, No. 4, (Aug 2005) p.847.

FAST HIGH-POWER POWER SUPPLY FOR SCANNING MAGNETS OF CNAO MEDICAL ACCELERATOR

M. Incurvati#, F. Burini, M. Farioli, G. Taddia, OCEM SpA, San Giorgio di Piano (BO), Italy
M. Donetti, S. Toncelli, CNAO Foundation, Milan, Italy
G. Venchi, University of Pavia Electrical Engineering, Pavia, Italy
I. De Cesaris, C. Sanelli, F. Voelker, INFN Laboratori Nazionali di Frascati, Frascati (RM), Italy
S. Giordanengo, F. Marchetto, INFN Sezione di Torino, Torino, Italy

Abstract

The paper presents the design aspects and performance measurements of the CNAO Scanning Magnets' power supply (PS) rated ±550A/±660V and developed in collaboration between OCEM SpA and INFN-CNAO. CNAO is a medical synchrotron producing carbon ions and protons for the cure of deep tumours. The Scanning Magnets are dipole magnets used to move the beam in an x-y plane at the very end of the beam extraction line. The PS current will be set in order to cover the targeted tumour area. To accomplish such a task the specifications of the PS are very stringent: current ramp speed is required to be as fast as 100 kA/s with an overall precision class of 100 ppm. Moreover the wide (20x20 cm^2) area to be covered by the beam requires a wide current range. High voltage peaks are required during transients whereas low voltage is needed during steady state. The above characteristics are challenging design issues both with respect to topology and control optimization.

INTRODUCTION

The CNAO medical synchrotron is finishing the installation and has just started the sources and LEBT commissioning and the PSs for the scanning magnets [1] complete the long list of topologies built in the past years by OCEM [2-3]. They will be used to feed dipole magnets to move the beam as a paintbrush on the targeted tumour area. The treatment plan is controlled by the Beam Delivery System (BDS) group optimizing the movements of the beam as a function of tumour shape. The BDS drives the PSs current through a 4 Mbaud optical link, sending a new current setting every 25 µs to precisely adjusting the beam position. The PSs send back to the BDS some useful information (actual current, set current, errors,…) This communication system allows for fast current control and safe operation. One of the main issues the treatment plan addresses is the maximization of the delivered dose in ill zones while minimizing it in healthful areas. To accomplish such tasks high precision and fast transient behaviour are required. The PSs also communicate with a Central Control System (CS) and a Timing System (TS) through Ethernet interfaces. The CS can thus collect information on the actual state of the PS and the TS synchronizes it with the main synchrotron events (injection, acceleration, extraction, energy,…)

#maurizio.incurvati@ocem.com

POWER SUPPLY CHARACTERISTICS

The PS principle diagram and a picture of it are shown in Fig.1 while its main characteristics and requirements are listed in Tab.1. The PS is composed of three main modules: a Booster (BO), and two Active Filters (AFs). The BO is a high-voltage high current IGBT H-Bridge whereas the AFs are IGBT H-Bridges used in interleaved modulation.

The BO, which is in series with the filtered output of the AFs stage, provides high voltage when the larger current steps are commanded by the BDS. The AFs provide both for maximum output voltage during transients and fast regulation for steady state current.

Table 1: Power Supply Specifications

Electrical Characteristics		
$R_{load}=R_{cable}+R_{magnet}$	40 mΩ	Load Resistance
L_{load}	4.4 mH	Load Inductance
$I_{load,nom}$	±540 A	Nominal Current
$V_{load,max}$	±660 V	Output Voltage
Dynamical Characteristics		
$T_{step}+T_{transient}$	200 us	Time to precision band
ΔI_{step}	<15 A	Current step amplitude
$T_{between}$	300 us	Min time between steps
Slope	>100 kA/s	Current slope for ΔI_{step} and $T_{step}+T_{transient}$
Precision Requirements		
CSCR	0 to ±100% f.s.	Current setting control range
CSRR	60 ppm	Current setting and readout resolution
CP	±100 ppm	Current precision after transient
CS8H	±200 ppm	Current stability over 8 hour
CRPP	<100 ppm	Residual peak-to-peak current ripple
COUS	<100 ppm	Current over/under shoot during transient

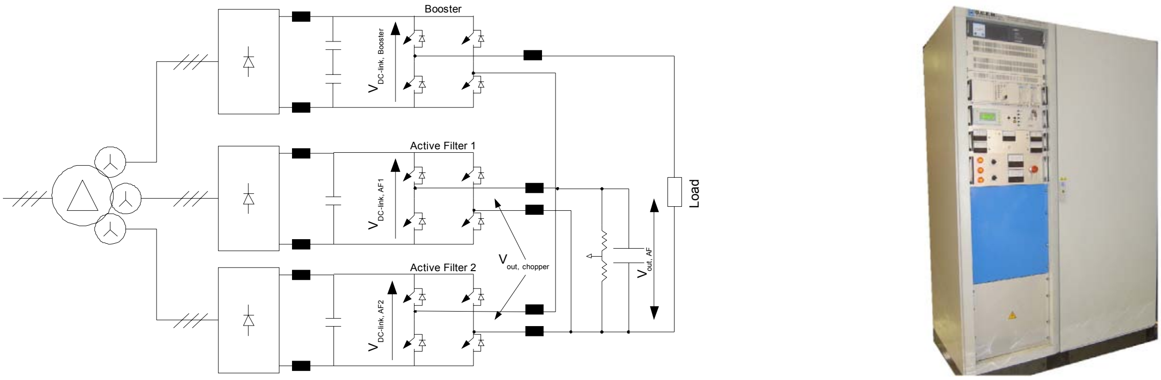

Figure 1: Scanning Magnets' Power Supply principle diagram and a picture

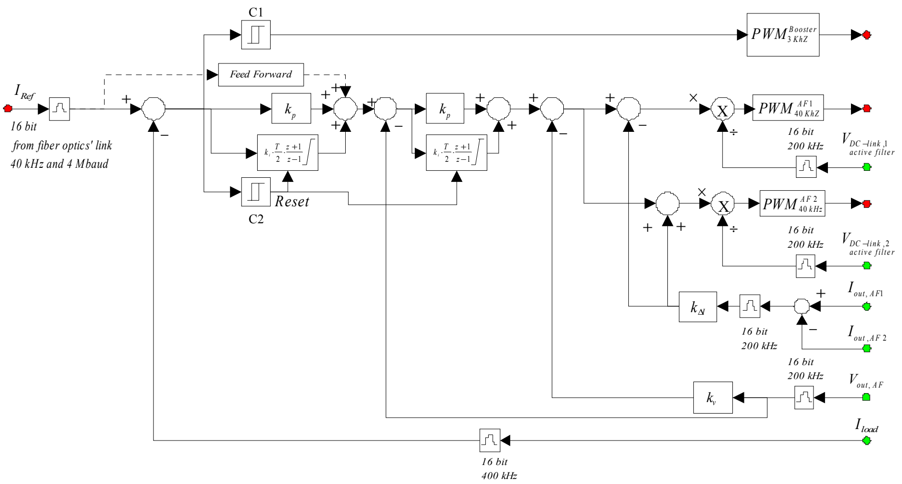

Figure 2: Control loops of the PS

Each leg of the AFs is switched at 20 kHz reaching at the output, with interleaving, an overall switching frequency of 80 kHz. Output filter design plays an important role in the overall performance of the PS.

CONTROL STRATEGY

As can be seen in Tab.1 the PS requirements are very stringent as the combination of dynamics and precision concern. After an in-depth analysis of the required performances and load characteristics, the following general principles were adopted:

- For current steps up to 2.5 A only the AFs are used while the BO is short circuited;
- For current steps larger than 2.5 A the BO is switched-on increasing ramp speed. The BO is switched-off by a comparator set at I_{set}±0.6 A. The current is then driven to the set level by the control loops of the AFs.

The detailed control loops' diagram is shown in Fig.2. The main issues faced during the design and tuning phases where:

- Selection of suitable ADCs precision and sample frequency to track current variation as fast as 100 kA/s; the sample frequency is important to minimize the BO comparator uncertainty.
- Tuning of the current loop integrator optimizing anti wind-up and reset thresholds to avoid overshoots as much as possible;
- Tuning of the inner voltage loop parameters to linearize the chopper behaviour on the full range even at very low duty-cycles;
- Tuning of the BO comparator thresholds to take into account the delays of the drivers and IGBTs as well as their variation with current level;
- Evaluation of actual magnet load non ideality under fast current transients.

The additional loops contribute to the overall performances of the PS (current sharing of AFs bridges and DC-link voltage variation).

The control algorithm has been implemented on a National Instruments PXI system that allows both for fault and status monitoring and communication facilities under Real Time environment and FPGA programming for fast and flexible regulation. The FPGA board NI-7833R is equipped with 8+8 16 bit ADCs/DACs and several digital outputs. The ADCs have a sample frequency of 200 kS/s. Two phase shifted ADCs are used for the current acquisition to reach 400 kS/s. The control loops run on the FPGA at 2.5 µs while the PWM has a quantization of 25 ns. To drive the 12 IGBTs a custom electronics has been developed by OCEM that fully

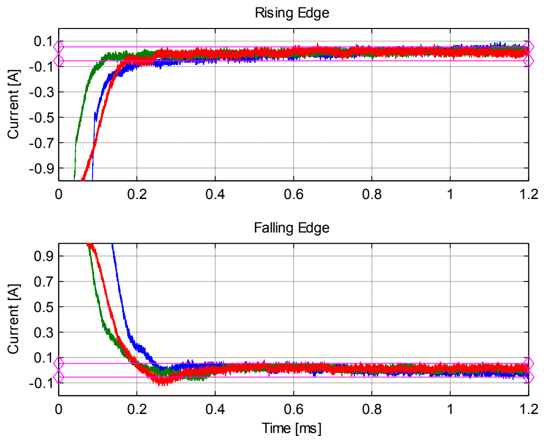

Figure 3: Current steps (0-15A,0-7A,0-2A)

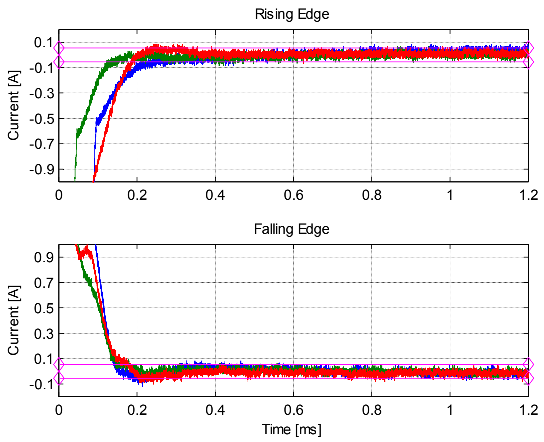

Figure 4: Current steps (525-540A,533-540A,538-540A)

integrates with PXI Bus generating optical signals directly from FPGA outputs.

EXPERIMENTAL RESULTS

A set of experimental results is presented. Figs. 3 and 4 show the typical current waveforms at the end of several steps. The figures' legend is as follows:

- Blue line: current step amplitude 15 A.
- Green line: current step amplitude 7 A.
- Red line: current step amplitude 2 A.

Each figure shows the rising and falling edge of the required step and the reached current level is represented by the zero on the vertical axis. Fig.3 shows the behaviour around 0 A dc level while Fig.4 is around the 540 A dc level. The start time of the current step is the origin of the horizontal axis; the steady state precision band of ±55 mA is shown by purple lines and the time to enter in precision band is 200 us as from Tab.1. The 7 A and 15 A current steps include the BO+AF operation whereas the 2 A includes only the AF.

As can be seen the PS behaviour is quite homogeneous with respect to step amplitude and dc current level. Moreover the stringent transient time and steady state precision is met without any appreciable overshoot. The PS has shown uniform behaviour on the whole current range even around the zero current level that represents the central position of the beam.

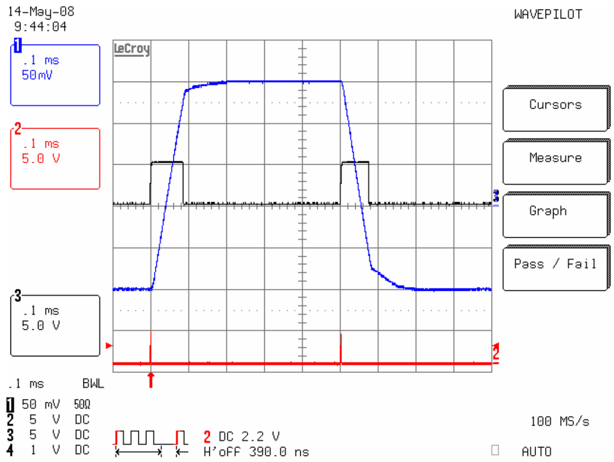

Figure 5: Typical current waveform

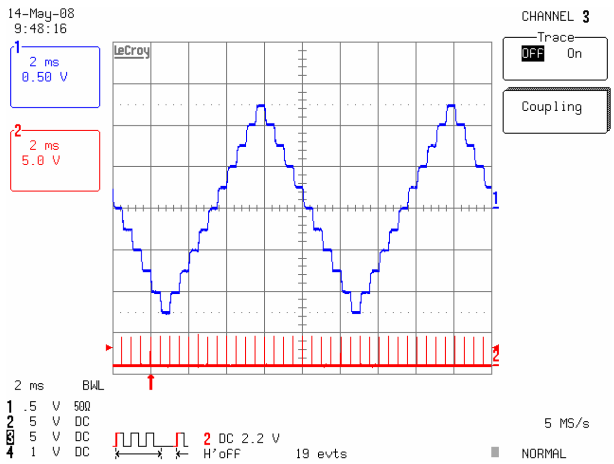

Figure 6: Example of current waveform for raster scanning

Fig.5 shows a typical current shape (blue line) of the PS for a 15 A step. It is clearly visible the current slope change as the BO switches-off and the smooth connection of the AF. Start trigger pulses are shown in red and BO on-off state is shown in black.A typical raster scanning current shape is shown in Fig. 6 where each step is of 15 A with 500 us between pulses; the number of steps is 10 and the current varies between –75 A and +75 A.

REFERENCES

[1] C. Sanelli, F. Voelker, et Alt., "Specification of Power Supplies for eight scanning dipole magnets of the CNAO project", CNAO internal Spec. CNA-SPDF-007WXX-03018

[2] M. Incurvati, C. Sanelli, G. Taddia, et Alt., "The Italian Hadrontherapy centre (CNAO): a review of the power supplies system for conventional magnets", EPAC06, Edinburgh.

[3] M. Farioli, M. Incurvati, C. Sanelli, et Alt., "CNAO Resonance Sextupole Magnet Power Converter", EPAC06 Edinburgh.

EXPERIMENTAL STUDIES ON DRIVE BEAM GENERATION IN CTF3

R. Corsini, S. Bettoni, S. Doebert, P. K. Skowronski, F. Tecker, CERN, Geneva, Switzerland
C. Biscari, A. Ghigo, INFN/LNF, Frascati, Italy
Y. Chao, Jefferson Lab, Newport News, Virginia, USA

Abstract

The objective of the CLIC Test Facility CTF3, built at CERN by an international collaboration, is to demonstrate the main feasibility issues of the CLIC two-beam technology by 2010. CTF3 consists of a 150 MeV electron linac followed by a 42 m long delay loop, an 84 m combiner ring and a two-beam test area. One key-issue studied in CTF3 is the efficient generation of a very high current drive beam, used in CLIC as the power source for the acceleration of the main beam to multi-TeV energies. The beam current is first doubled in the delay loop and then multiplied again by a factor four in the combiner ring by interleaving bunches using transverse deflecting RF cavities. The combiner ring and the connecting transfer line have been installed and put into operation in 2007. In this paper we give the status of the commissioning, illustrate the beam optics measurements, discuss the main issues and present the results of the combination tests.

THE CTF3 COMPLEX

It is generally accepted that the CLIC technology [1] is the only possible path to multi-TeV colliders. However, several critical issues still need to be addressed. The experimental program of the present CLIC Test Facility, CTF3 [2], tackles most of them and in particular the generation and use of the high-current drive beam [3]. CTF3 is presently being built and commissioned at CERN by an international collaboration which at present includes 24 institutes from 14 countries [4].

The facility is placed in the buildings of the former LEP Pre-Injector, LPI (see Fig. 1), the hardware of which is partly re-used. It includes a 70 m long drive-beam linac followed by two rings, where the beam current is multiplied by a factor eight: a 42 m delay loop and an 84 m combiner ring. The drive beam is then transported to the CLic EXperimental area (CLEX) to produce 12 GHz RF power for structure tests. In the same area, the CALIFES linac will provide a probe beam for a Two-Beam Test Stand (TBTS) and a decelerator (Test Beam Line – TBL) will be used for drive beam stability studies.

The drive beam injector includes a thermionic gun, three 1.5 GHz sub-harmonic bunchers (SHB), a 3 GHz bunching system and two 3 GHz accelerating structures. Solenoidal focusing is used all along. A three-bends chicane with collimators is then used to eliminate off-energy particles and to perform bunch compression. A beam current of 3 to 4 A with a momentum of about 25 MeV/c is typically achieved at the end of the injector.

The linac is composed of 11 modules, 8 of which are equipped with two travelling-wave structures each. A module is 4.5 m long and contains a quadrupole triplet.

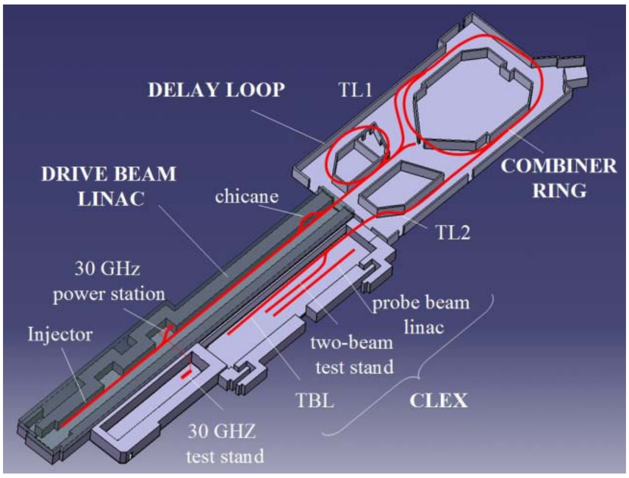

Figure 1: Schematic layout of the CTF3 complex.

The structures have a length of 1.22 m and operate at a full-loaded gradient of 6.5 MV/m. They use radial damping slots plus cell-to-cell detuning in order to control transverse wake-fields. Each module is powered by a klystron with peak power in the 35 MW to 45 MW range, doubled by RF compression to provide more then 30 MW at each structure input. The pulse compression system uses a programmed phase ramp to obtain a 1.5 μs flat top. A beam line branches off halfway along the linac. The beam can be sent there to be decelerated in a Power Extraction and Transfer Structure (PETS) and produce 30 GHz power, brought via a low-loss waveguide to a test stand in the former CTF II hall.

A four-bend magnetic chicane with variable momentum compaction factor is located at the end of the linac and is used to optimize the bunch length. Simulations have in fact shown that bunches with nominal bunch charge (2.5 nC) and less than 1 mm rms length would suffer from coherent synchrotron radiation effects in the delay loop and in the combiner ring. The delay loop has a two-fold symmetry, with double injection/extraction septa and 10 bending magnets. It includes an RF deflector used for injection/extraction and a wiggler for path length tuning. The design optics is achromatic and isochronous. A four dipole transfer line (TL1) with tuneable momentum compaction connects the delay loop to the combiner ring. The combiner ring has four achromatic and isochronous arcs, with three dipoles each. Injection and extraction regions are located in the long straight sections. For injection, two horizontal RF deflectors separated by a π betatron phase advance and located at each side of the injection septa are used. On the opposite side, a fast kicker is used for extraction. The ring has also a path-length tuning wiggler in one of the two short straights.

NEW INSTALLATIONS

A transfer line (TL2) with variable momentum compaction [55] will join the ring to the beam lines in CLEX, a hall of 42 m length and 8 m width, partly covered by a gallery for klystrons, power supplies and other equipment. Most of TL2 is already in place, and the line will be completed before the end of July 2008, during a dedicated shut down. The installation of the CALIFES probe beam injector [5] and of the TBTS [6] is also close to completion, and the last components will be installed in the same period. CALIFES will produce a low current electron beam in a photo injector and accelerate it to 170 MeV in three structures re-used from the former LPI. Both single-bunch and bunch-train operation will be possible. The probe beam will then be further accelerated by 12 GHz structures in the TBTS, which will also allow high-power testing of a PETS prototype with a drive beam of up to 30 A of beam current. The PETS has the same cross section as in CLIC, being only longer in order to produce the same peak power. It has a power recirculation circuit which can be used to enhance power extraction and will eventually be equipped with an on/off mechanism. Different structures could be tested in the TBTS, which is well instrumented to analyse their behaviour as well as the effect of RF breakdowns on the probe beam. In addition, in the TBL [7] final configuration the drive beam will be decelerated to about half its initial energy by up to 16 PETS. The aim is to demonstrate beam stability under significant deceleration, which will produce a momentum difference of up to a factor two between the first and the last bunches. The TBL is composed of modules, each one including a PETS, a beam position monitor (BPM) and a quadrupole on a movable support, in order to test beam-based alignment procedures. A total of about 2 GW of 12 GHz RF power can be extracted from the beam. Only one module of the TBL will be installed this year. The whole decelerator should come online in 2009.

COMMISSIONING STATUS

In 2003-2004 the injector, the linac, the mid-linac power station and the end-of-linac magnetic chicane were installed and commissioned. Full beam-loading operation was established [8] and the beam resulted remarkably stable, with no sign of beam break-up. An rf-to-beam efficiency of 94 % has been experimentally verified later on [9]. The first part of the linac is routinely used since 2005 as a source of 30 GHz RF power. Up to 100 MW can be produced in the PETS, and transported to the test stand with ~ 70 % efficiency. The delay loop was installed during 2005 and commissioned in 2006. Five 140 ns long bunch-trains were injected into the delay loop and combined with the following train, thus doubling the beam current [10]. In 2006 a short period was dedicated to the commissioning of the newly installed TL1. Short pulses of 200 ns were used. The beam was rapidly transported to the end of the line and a current of 3 A could be injected in the ring first straight section.

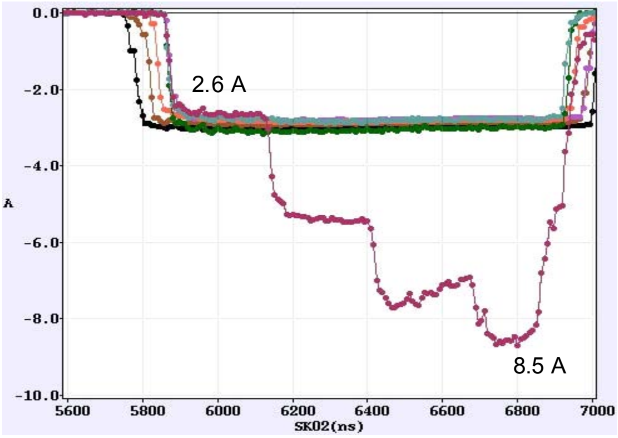

Figure 2: Beam current multiplication in the combiner ring. The traces show the beam current measured in several BPMs in the linac and TL1, and in one ring BPM. The incoming pulse has four times the ring length (4 × 280 ns). Losses from instability in the last two turns don't allow to reach a full factor four in current gain.

The combiner ring installation was completed at the beginning of 2007. Commissioning of the transfer line TL1 and of the combiner ring to the nominal beam performance continued in 2007, with several interruptions for repairs and installation work [11], and is presently under way. Several problems in the hardware and in the optics model were identified, mainly through beam measurements, and eventually fixed, including wrong BPM calibration and connections, quadrupole cabling errors, switched polarities and wrong current calibrations. The alignment of magnets and vacuum chamber elements was also re-checked and corrected when necessary. During 2007 we could finally obtain a beam circulating for several turns in the ring, albeit with non-negligible losses. A fast beam instability in the vertical plane was indeed discovered [12], which gives rise to growing vertical beam oscillations and eventually to beam loss.

The instability is believed to be caused by the vertical deflecting mode in the RF deflectors, excited by the beam. This mode is shifted in frequency by 48 MHz with respect to the horizontal deflecting mode by polarising rods in the deflector cells, but it is not damped. New RF deflectors are being built, to be installed in October 2008 [13]. At the end of the 2007 run, a recombination test over four turns was performed anyway, bypassing the delay loop (see Fig. 2). In 2008 the ring commissioning restarted. Waiting for the installation of the new deflectors in October, the aim is to clarify the last minor inconsistencies between the model and the machine and to explore the possibility to control the vertical instability by a proper choice of the vertical tune in the ring and of the β-function in the RF deflectors [12].

MEASUREMENTS

Several beam optics measurements were performed in CTF3 during the 2007 and 2008 runs. Among others:

1. Standard quadrupole scans, used to check the optics and perform re-matching of the different beam lines.

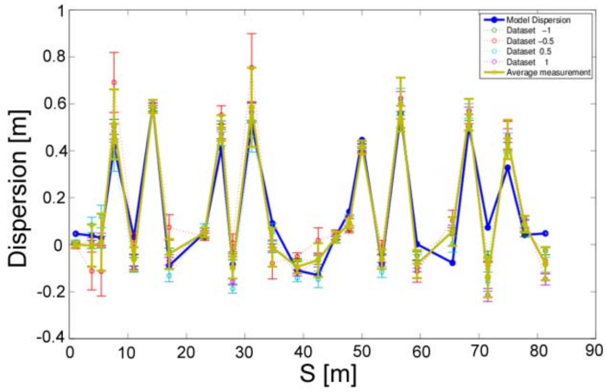

Figure 3: Results of dispersion measurements in the combiner ring (yellow line) compared with predictions from the MAD model (blue line).

2. Determination of transverse response matrix elements by orbit measurements with kick excitation. The data obtained were paramount in order to identify and correct errors in the quadrupole families.
3. Dispersion, typically measured by varying the strength of all magnetic elements over a 1% range and taking the orbit difference. Such technique is simpler then a beam energy change and has the additional advantage that dispersion can be measured locally, not being sensitive to incoming residual dispersion. A good agreement was found in all machine areas. See an example in Fig. 3.
4. Tune measurements, by FFT of horizontal and vertical signals of the ring BPMs. The measurements have shown, like kick-orbit studies, a disagreement with the MAD model. After the last corrections to the model and the calibration adjustments, a new measurement campaign is still required for verification.
5. Determination of the closed orbit. A first estimate is

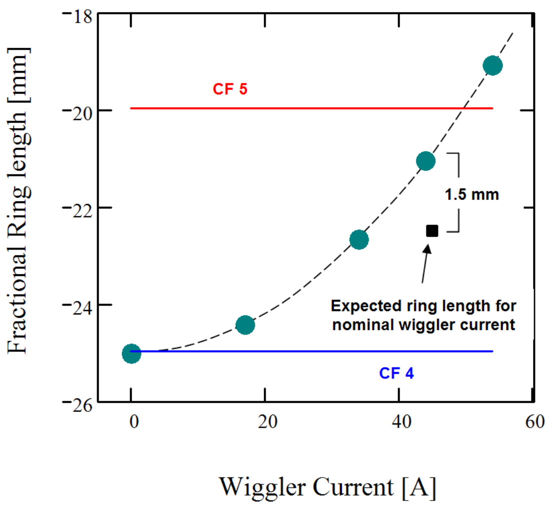

Figure 4: Ring length as a function of the tuning wiggler current. The actual length is an integer number of 3 GHz wavelengths, plus the fractional part shown here. The circles are measured values and the dashed line the expected variation. The black square is the nominal value and the horizontal lines mark the operational range.

done by averaging the first few turns. The injection is then optimized to minimize the turn-to-turn difference. An automatic closed orbit correction program is at present under test.

6. Measurement of the ring length, fundamental since the recombination process relies on a precise control of the revolution time, to the 10^{-5} level. The measurement was done using a 3 GHz RF phase monitor. An FFT of the signal gives the ring length modulo the RF wavelength (see Fig.4). The ring was found to be 1.5 mm longer than the nominal. A good closed orbit correction (not applied then) may in principle reduce the discrepancy, which is however within the limits of the needed operational range (corresponding to 4-turn to 5-turn recombination). The path length variation as a function of the tuning wiggler current behaved exactly as expected.

CONCLUSIONS

The CTF3 project is the main tool to demonstrate the feasibility of the CLIC scheme, in particular the generation of the high-current drive beam. A number of issues have already been addressed, such as full beam loading operation and the bunch phase coding and interleaving scheme. Commissioning of the combiner ring is in progress and a full combination test is expected after installation of the new RF deflectors, needed to damp the fast vertical instability which is the present limiting factor.

REFERENCES

[1] G. Guignard (Ed.), “A 3 TeV e+e- linear collider based on CLIC technology”, CERN 2000-008, 2000.
[2] G. Geschonke and A. Ghigo Eds, “CTF3 Design Report”, CERN/PS 2002-008 (RF).
[3] R. Corsini (Ed.), “The CLIC RF power source”, CERN 99-06, 1999.
[4] http://clic-meeting.web.cern.ch/clic-meeting/CTF3_Coordination_Mtg/Table_MoU.htm
[5] A. Sharma et al., “Design of the transfer line-2 for the CTF3 at CERN”, Proc. APAC’07.
[5] A. Mosnier et al., “The probe beam linac in CTF3”, Proc. EPAC’06.
[6] T. Ekelöf et al., “The Two-Beam Test-Stand in CTF3”, Proc. EPAC’06.
[7] S. Döbert et al., “Progress on the CTF3 Test Beam Line”, Proc. EPAC’06 and CLIC note 690.
[8] R. Corsini et al., “First full beam loading operation with the CTF3 Linac”, Proc. EPAC’04 and CLIC note 604.
[9] P. Urschütz et al., “Efficient long-pulse fully-loaded CTF3 linac operation,” Proc. LINAC’06 and CLIC note 697.
[10] D. Alesini et al., “Commissioning status of the CTF3 delay loop”, Proc. EPAC’06 and CLIC note 675.
[11] F. Tecker et al., “CTF3 combiner ring commissioning”, Proc. PAC’07 and CLIC note 718.
[12] R. Corsini et al., “Fast Vertical Beam Instability in the CTF3 Combiner Ring”, these Proceedings.
[13] D. Alesini et al., “Analysis of the Vertical Beam Instability in CTF3 Combiner Ring and New RF Deflector Design”, these Proceedings.

FAST VERTICAL BEAM INSTABILITY IN THE CTF3 COMBINER RING

R. Corsini, D. Schulte, P. K. Skowronski, F. Tecker, CERN, Geneva, Switzerland
D. Alesini, C. Biscari, A. Ghigo, INFN/LNF, Frascati, Italy

Abstract

The CLIC Test Facility CTF3 is being built at CERN by an international collaboration, in order to demonstrate the main feasibility issues of the CLIC two-beam technology by 2010. The facility includes an 84 m combiner ring, which was installed and put into operation in 2007. High-current operation has shown a vertical beam break-up instability, leading to high beam losses over the four turns required for nominal operation of the CTF3 ring. Such instability is most likely due to the vertically polarized transverse mode in the RF deflectors used for beam injection and combination. In this paper we report the experimental data and compare them with simulations. Possible methods to eliminate the instability are also outlined.

INTRODUCTION

The experimental program of the present CLIC Test Facility, CTF3 [1], addresses most of the main issues of the CLIC study in order to get an answer on the feasibility of the scheme before 2010. In particular, one of the critical issues is the validation of the drive beam generation scheme with a fully-loaded linac and bunch train combination by transverse RF deflectors [2].

CTF3 is being built and commissioned by an international collaboration formed at present by 24 institutes from 14 countries [3]. The facility, located at CERN in the area of the former LEP Pre-Injector (LPI), includes a 70 m long linac followed by two rings, where the bunch train combination is obtained: a 42 m delay loop and an 84 m combiner ring. The drive beam thus produced can then be used for RF power production, deceleration and two-beam operation tests in a close-by experimental area (CLEX).

The 4 A, 1.2 μs long beam-pulse from the electron gun is bunched by the three sub-harmonic buncher (SHB) cavities such that only every second 3 GHz RF bucket is populated. The SHB is a wide-band system and allows a very fast (5-6 ns) switch of the RF phase by 180°. The drive beam can thus be easily “phase coded” into eight 140 ns long sub-pulses, in which the main bunches occupy either even or odd buckets. The bunched beam is then accelerated to about 120 MeV/c in the linac, operated in full beam-loading mode [4].

The role of the delay loop that follows the linac is to rearrange the 1.2 μs beam-pulse from the drive-beam linac into four 140 ns pulses, separated by 140 ns gaps, increasing at the same time by a factor 2 both the current and the bunch repetition frequency. A transverse RF deflector working at 1.5 GHz sends the first phase-coded sub-pulse into the delay loop. The loop length of 42 m corresponds to the sub-pulse length of 140 ns, thus the first sub-pulse is back at the deflector at the same time as the next sub-pulse from the linac. The delay loop length is precisely tuned to an integer number of RF wavelength, therefore phase-coded bunches from different sub-pulses are interleaved. They then receive opposite kicks and are thus combined into the same orbit. The bunch spacing is halved to 10 cm and the beam current is doubled. The process also naturally produces the 140 ns gap needed for clean extraction from the combiner ring.

The combiner ring (see Fig. 1) has four achromatic and isochronous arcs, with three dipoles each. Injection and extraction regions are located in the long straight sections. For injection, two 3 GHz RF deflectors separated by a π betatron phase advance and located at each side of the injection septa are used. On the opposite side, a fast kicker is used for extraction. The ring has also a path-length tuning wiggler in one of the two short straights.

The four 140 ns pulses from the delay loop are combined in the ring using a principle similar to the one described above. The ring length is equal to the distance between pulses and it is precisely tuned to $(n + ¼)\ \lambda$, where n is a (large) integer. The RF deflector after the injection septa kicks each incoming pulse into the closed orbit. The deflector located before the septa is synchronized with the first one to generate a closed bump, such that the injected pulses are kept on the closed orbit when they come round and are interleaved with the incoming ones. After four turns, before the circulating beam can hit the septum, the combined pulses are extracted by the kicker on the other side of the ring to be sent to the CLEX area. The final beam current is eight times the initial one and the bunch distance is 2.5 cm.

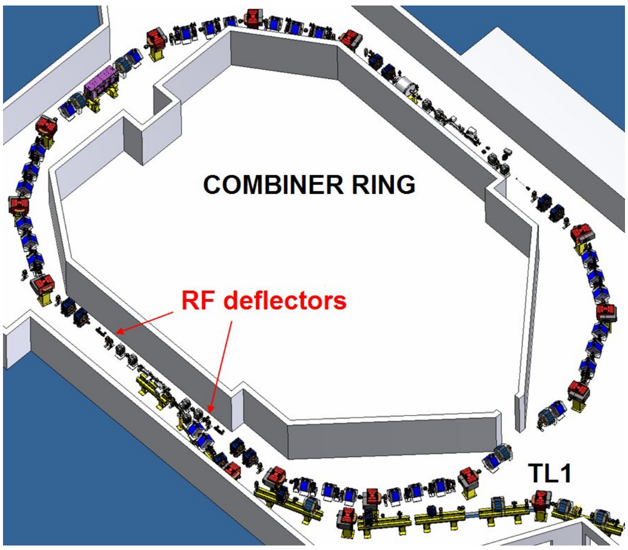

Figure 1: Combiner ring layout. On the bottom the transfer line from the delay loop to the ring (TL1). The position of the RF deflectors is also indicated.

OBSERVATION OF THE INSTABILITY

Beam commissioning of the transfer line TL1 and of the combiner ring to the nominal beam performance took place in 2007. The setting-up procedure requires to establish injection using the RF deflector located after the septa, timing the RF pulse such that both travelling-wave deflectors would be empty of RF power during the second turn. Such a procedure (RF injection) permits to store the beam pulse for a large number of turns, making it possible to perform a number of beam studies, such as tune measurement and precise determination and correction of the closed orbit. The number of circulating turns is in principle limited only by synchrotron radiation losses (no accelerating cavity is installed in the combiner ring).

After having solved several hardware and modeling problems [5] it was possible to get a beam circulating for many turns with the nominal isochronous optics. However, only a small fraction of the beam current survived to up to 180 μs, corresponding to more than 600 turns, while most of it was lost in the first few turns.

Further observations showed how the beam loss was much faster for longer pulses (see Fig. 3) and for higher beam current, a clear indication of a collective effect taking place. A closer look at the analog BPM signals with a fast scope revealed a strong vertical oscillation along the pulse, barely visible in the bandwidth-limited digitized signals. The oscillation started from the 2nd or 3rd turn for the nominal beam parameters, and caused rapidly heavy losses (see Fig. 4). It should be noted that the amplitude and phase of the oscillations were remarkably stable, every pulse showing almost exactly the same trace on the scope.

The oscillation frequency was determined by an FFT of the vertical signal, and was find to be equal to 48 MHz. This was the first strong hint that the instability was due to the vertically polarized mode of the RF deflectors used for injection.

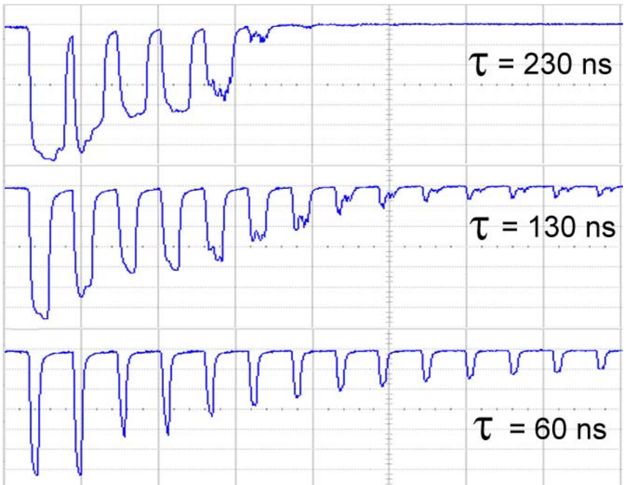

Figure 2: Scope traces showing the beam current at a ring BPM as a function of time, for different injected pulse lengths. Shorter pulses, with less charge, survive for longer times, indicating a collective instability.

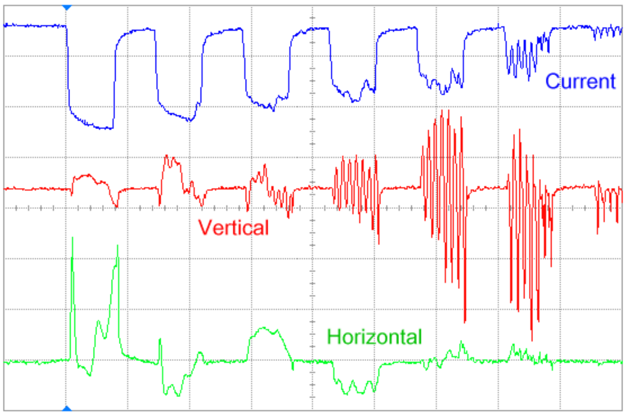

Figure 3: Scope traces from a ring BPM showing, from top to bottom, the circulating beam current and the vertical and horizontal signal. The fast growing oscillation in the vertical plane is obvious and well correlated with beam losses. No such behaviour is visible in the horizontal plane.

Such mode had been in fact decoupled in frequency from the main horizontal mode by inserting metallic rods in the deflector cells, in order to avoid mode conversion of the injected power. The resulting frequency for the vertical mode is 3.0443 GHz, while the main mode has the same frequency of the bunch train, 2.9985 GHz. The frequency difference is therefore equal to the measured beam oscillation frequency, within the experimental uncertainties. In order to exclude the possibility of a fast beam ion instability, which could cover a similar frequency range, the vertical oscillation frequency was measured for different beam currents. Contrary to the predictions of the theory of fast beam ion instability [6], the oscillation frequency remained stable. We also tried to change the operating temperature of the deflectors. A temperature variation of 8°C essentially did not change the scenario. Changing the orbit in the vertical plane seemed to have some effect. However, no systematic study was done and the instability was always present, constituting a limiting factor in the recombination test [7].

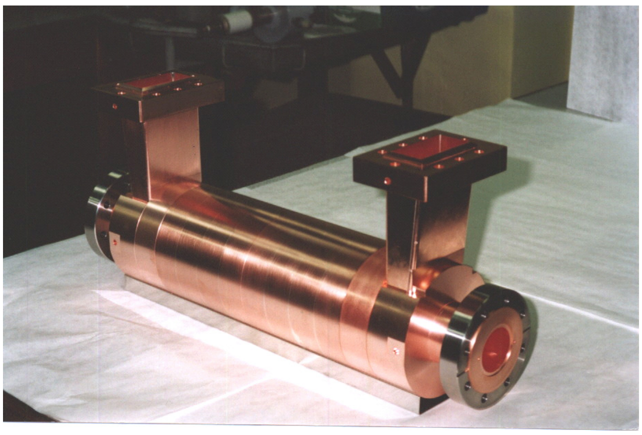

Figure 4: CTF3 Travelling wave RF deflector. The horizontally polarized mode is coupled in and out through the waveguide couplers. The vertically polarized mode, excited by the beam, is trapped in the cavity.

SIMULATIONS AND OUTLOOK

The possibility of an instability arising from the deflector had been indeed considered in the design phase of CTF3. But while a thorough analysis [8] had been made for the effect of the horizontal polarization (resonant with the bunch frequency) the vertical mode had been considered less relevant, since the bunch train spectrum have a very small component at its excitation frequency. However, while the horizontally polarized mode is rapidly extracted by the output coupler the vertical mode can be trapped over subsequent turns. In order to confirm the suspicion and to determine the possible remedies, a dedicated tracking code has been written to study the multi-bunch multi-turn effects [9].

The resonant frequencies, quality factors and transverse shunt impedances of the vertical modes have been calculated by HFSS and used in the code.

The simulation results confirmed the presence of a strong instability, driven by a few mm off-axis beam, and showed a good agreement with the experimental observations. In particular:

1. The profile of the vertical oscillation as a function of the bunch positions is the same shot by shot.
2. The oscillation spectrum show side-bands at Δf = 40/50 MHz with respect to the fundamental.
3. The instability is stronger for an increased bunch charge.
4. The instability is stronger for longer bunch trains, at fixed bunch current.
5. Dependence on the temperature of the deflectors: no large effect for a frequency change of ~ 3 MHz, corresponding to 8°C.
6. The instability occurs both in the case of a single train doing different turns than in the case of recombination.
7. A better vertical steering inside the deflectors minimize the oscillations.

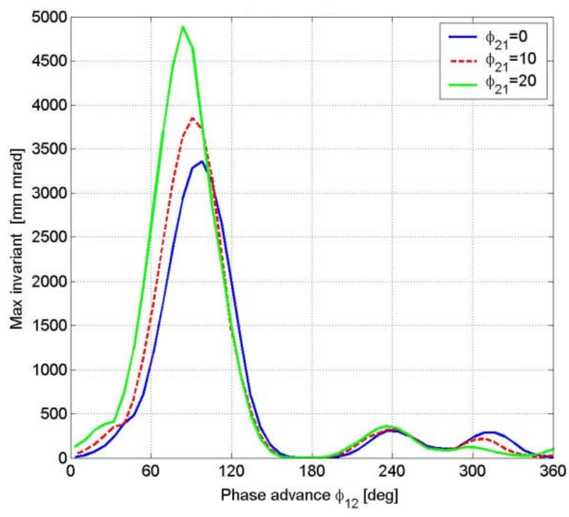

Figure 5: Emittance increase after four turns for 2 mm initial offset; ϕ_{21} is the vertical phase advance between the deflectors across the septa, ϕ_{12} the phase advance in the rest of the ring (the tune is the sum of both).

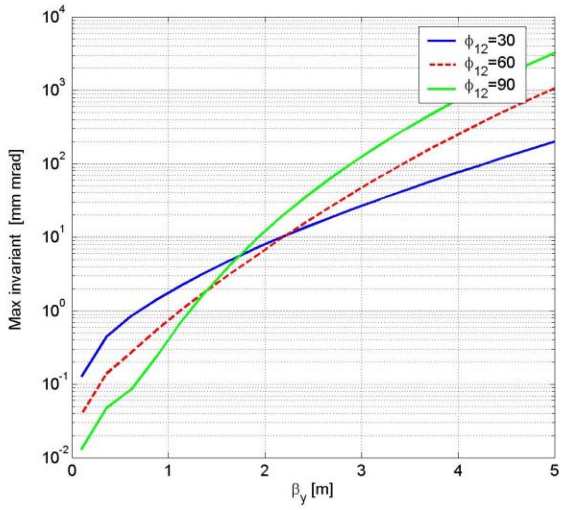

Figure 6: Emittance increase as a function of the local β-function, for different phase advances ϕ_{21}.

A study on the dependence on the ring tune show that a tune near the half integer can reduce the effect by a large factor (see Fig.5). The reduction of the vertical β-function at the deflector can also help in the control of the instability (Fig. 6). Similar conclusions were obtained in the past for the horizontal instability [8], and the combiner ring horizontal β-function and tune was indeed chosen following this requirement. A new working point for the ring had now been calculated, and beam tests are presently ongoing. However, the best method to avoid the instability is to damp the vertical deflector mode.

Several possibilities had been studied, and it has been decided to build new RF deflectors with polarising rods as well as loop antenna in each cell, to efficiently extract the vertical mode [9]. They should be installed in October 2008 and are expected to definitively solve the problem.

REFERENCES

[1] G. Geschonke and A. Ghigo Eds, “CTF3 Design Report”, CERN/PS 2002-008 (RF).

[2] R. Corsini (Ed.), “The CLIC RF power source”, CERN 99-06, 1999.

[3] http://clic-meeting.web.cern.ch/clic-meeting/CTF3_Coordination_Mtg/Table_MoU.htm

[4] P. Urschütz et al., “Efficient long-pulse fully-loaded CTF3 linac operation,” Proc. LINAC’06 and CLIC note 697.

[5] F. Tecker et al., “CTF3 combiner ring commissioning”, Proc. PAC’07 and CLIC note 718.

[6] T. O. Raubenheimer and F. Zimmermann, “Fast beam-ion instability. I. Linear theory and simulations”, Phys. Rev. E 52, 5487 - 5498 (1995).

[7] R. Corsini et al., “Experimental studies on drive beam generation in CTF3”, these Proceedings.

[8] A. Gallo et al., “Studies on the RF deflectors for CTF3”, Proc. EPAC 2000 and CLIC note 472.

[9] D. Alesini et al., “Analysis of the vertical beam instability in CTF3 combiner ring and new RF deflector design”, these Proceedings.

DETAILED DESIGN, MANUFACTURING AND TESTING OF A STRIP-LINE EXTRACTION KICKER FOR CTF3 COMBINER RING *

I. Rodríguez#, E. Rodríguez, F. Toral, L. García-Tabarés, CIEMAT, Madrid, Spain
T. Fowler, I. Syratchev, CERN, Geneva, Switzerland
D. Alesini, A. Ghigo, F. Marcellini, M. Zobov, INFN, Frascati, Italy

Abstract

The first calculations to design the CTF3 Combiner Ring extraction kicker are reported elsewhere. The last computing step before fabrication is the wakefield analysis, to determine if the bunch disturbance is acceptable. Two different codes have been used for cross-checking: CST Particle Studio and GDFidl. The computation is challenging because of the long structure (2.4 m) with a short bunch (3 mm). Besides, both transitions are not equal, as a result of different straight sections of the input and output beam pipe, and then the solution method is more complex. On the other hand, the main challenges for manufacturing are the long electrodes support by ceramic stand-offs and the flexible electrical connections to allow for electrodes thermal differential displacement. Special tooling has also been developed for assembly within the required tolerances. The device has been successfully leak tested. High frequency transmission coefficients and dielectric strength were also measured.

IMPEDANCE ANALYSIS

The first kicker calculations are reported in [1]. The last stage related with those calculations is the wakefield analysis [2]. This device will be installed in the CTF3 combiner ring (CR), to extract the recombined beam after four turns. This kicker is a very long device with internal discontinuities and, therefore, the impedance analysis constitutes a necessary calculation to avoid beam instabilities. Nevertheless, long range wakefield effects are not expected to be dangerous as they do not have enough time to resonate. Moreover, the structure is fully done in stainless steel and the quality factor of the resonant modes is very low. So that, even matched high order modes should quickly decay [3].

Simulations in GDFidl and CST Particle Studio were developed using several models. Since the device is very long (about 2.4 m, flange to flange) compared to the bunch size (sigma = 3 mm), the finite difference method commonly used in time-domain simulation must use plenty of elements in the sake of a good accuracy. Indeed, at least twenty elements per wavelength are needed to get good time-domain simulation. That yields an enormous memory requirement, not affordable by standard computers. That is why the problem was divided into smaller parts which were first studied independently: the input section (Fig. 1), the output section, and a full model using a higher sigma bunch, all of them using CST Particle Studio. The end cross section of partial simulations was modelled with an absorbing port to simulate an infinitely long structure, without wake reflection. All the models were configured with absorbing ports in the coaxials, which damps the wakefields for the coupled frequencies up to first hundred coax. modes.

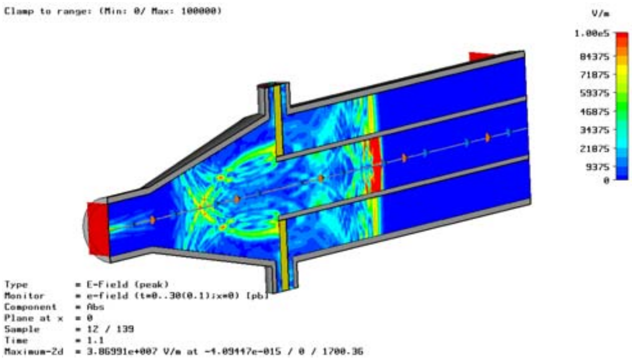

Fig. 1: Old input section simulation in CST Particle Studio

First Transition Calculations

Originally, the transitions between the beam pipe and the kicker chamber were done by two identical conical transitions (Fig. 1). The results of the wakefield simulations for this geometry were obtained in CST Particle Studio for longitudinal wakes (Fig. 2) and GDFidl for transverse wakes (Fig. 3).

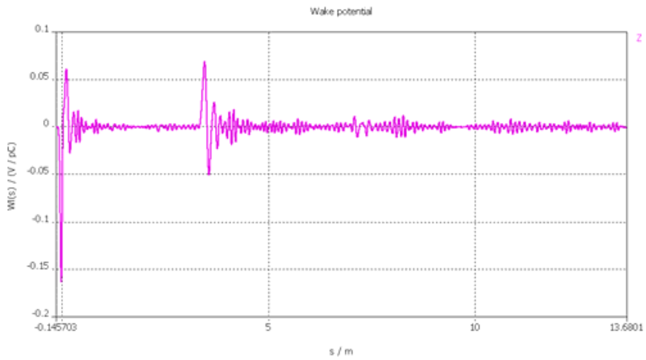

Fig. 2: Long range longitudinal wake in CST software

The absorbing effect of the simulation coaxial ports in the second reflection of the wake is clearly shown in Fig.2. The distance between the first two peaks is about twice the device length.

*Work supported by Spanish Ministry of Education and Science under project FPA2004-20954-E

#iker.rodriguez@ciemat.es

No major problems are expected after analyzing wake impedances around resonating frequencies and, therefore, no high order mode damping seems necessary.

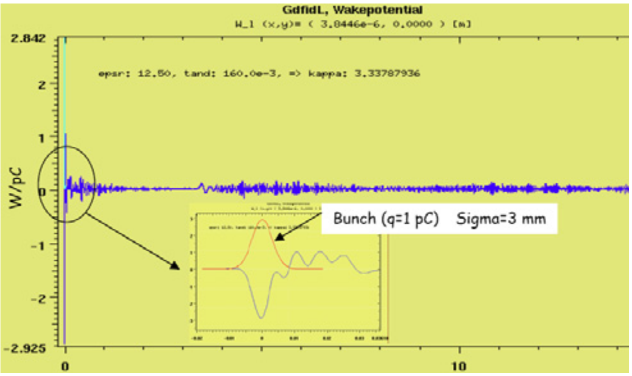

Fig. 3: Long range transverse wake in GDFidl

Definitive Transition Calculations

Due to some modifications on the ring layout, the definitive transitions are not symmetric. One half meter long conical transition was designed to fit inside a steering quadrupole aperture while improving the beam impedance. The other end was made with a short circular to racetrack transition.

Calculations using new transitions were only developed with GDFidl (Fig. 4) at CERN because of their complexity. Indeed, the required memory is even higher due to the new length of the device using the new transitions. Moreover, the CPU processing time is also higher because of the different input and output transitions, which makes the Shobuda-Napoly integration applied to 3-D [4] necessary for good precision.

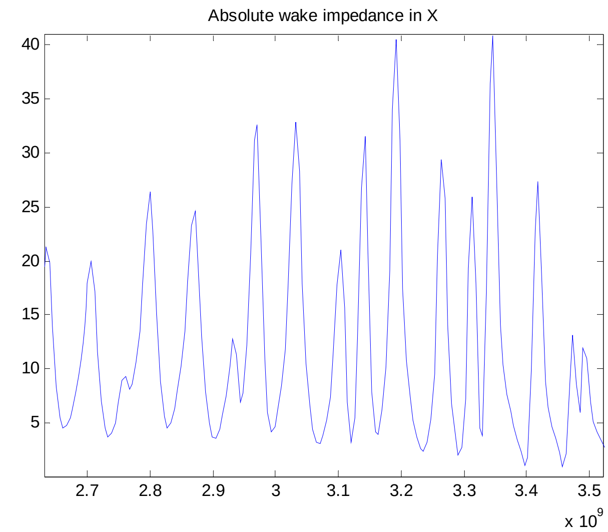

Fig. 4: Transverse wake impedance around 3 GHz

Analyzing these results, it can be concluded again that no major problems are expected in frequencies close to the beam frequency spectrum (3GHz and multiples).

MAIN FABRICATION CHALLENGES

It was necessary to address several problems during the manufacturing of the kicker, mainly related with mechanical aspects of the ceramic supports, electrode connections and welds. The manufacturing of the kicker was made by a Spanish company, named G&P Vacuum Projects.

Ceramic Supports

Five supports per electrode have been used for the kicker. Only the central one is fixed, the others are sliding to allow electrode thermal displacement. The insulating ceramic stand-offs are made of a ceramic material named steatite and they have low precision threaded holes. In order to achieve better binding to the kicker tube and improve support stiffness, a thermal interference fit method was used for the ceramics. The steatite was supported by an interference fit case screwed to a steel cap which is welded to the kicker tube (Fig. 5). The sliding supports have been provided with a copper washer between the ceramic and the electrode to reduce friction.

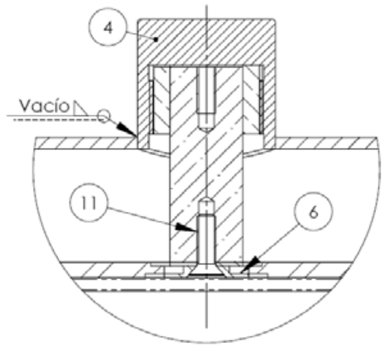

Fig. 5: Interference fit method for ceramics

Electrode Connections

A flexible connection between the feedthrough and the electrode is needed for possible mild bake out. Differential thermal displacement is not expected to be higher than 1.5 mm at each electrode edge (ΔT=100 ºC). The preferred connection method is a small piece of highly flexible copper cable fixed to a Ceramaseal set screw contact (Fig. 6).

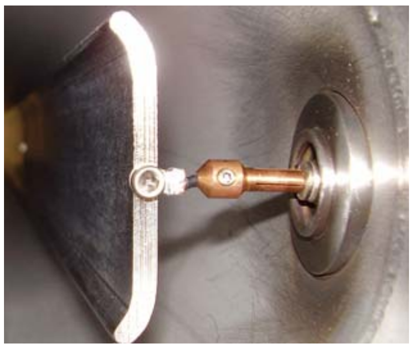

Fig. 6: Electrical connection of electrodes

Welding and Assembly

The kicker full assembly (Fig. 7) has a lot of vacuum welds, some of them not easy to do because of their dimension and/or precision. The vacuum welds between the kicker tube and the stand-off caps are quite challenging because of the steel contraction after welding, which can affect to the position of the electrodes. In the same way, the welds between the feedthrough and the kicker tube are also demanding. A dummy tube was used to test the weld contraction before actual welding and assembling the device.

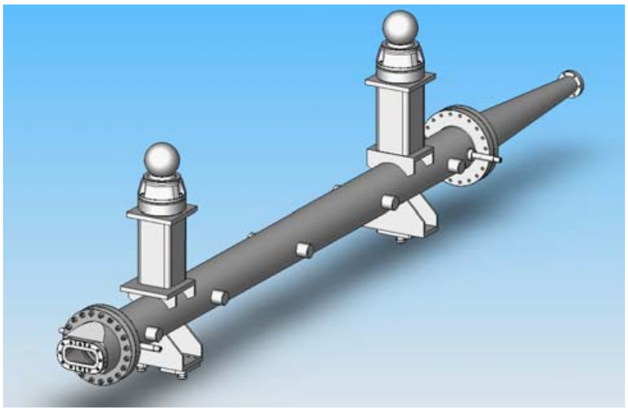

Fig. 7: 3D model of the final kicker

The assembly of the electrodes is not a straightforward process. A long special tool has been developed to hold the electrodes at the correct position before screwing the caps and final welding.

DEVICE TESTS

The tests include leak detection, RF measurements and High Voltage dielectric tests. The first test was done at the company, while the rest were done at INFN/Frascati.

Vacuum Tests

The leak detection was successfully done down to a value of 1.2×10^{-10} mbar.l/s. Concerning the vacuum limit, 2×10^{-7} mbar were achieved after 3 days pumping with a turbo pump prior to bake out.

The vacuum test was repeated at CERN when installing the kicker in the CR. A mild bake-out was needed in order to achieve the required level (10^{-8} mbar). The bake-out was done very slowly up to 100 ºC to avoid dangerous stresses in ceramics and electrode connections.

RF Tests

Both S-parameters measurements and high voltage pulser tests were carried out. The network analyzer RF tests returned low frequency S parameters as expected, with very low reflection up to 35 MHz (less than 0.2% of input power). This frequency range represents the pulse frequency content, which means good transmission of the pulser power. High frequency testing was a bit more challenging over 1 GHz because of problems with RF cables and hybrids specifications. However, results up to 1 GHz agreed HFSS simulations [1].

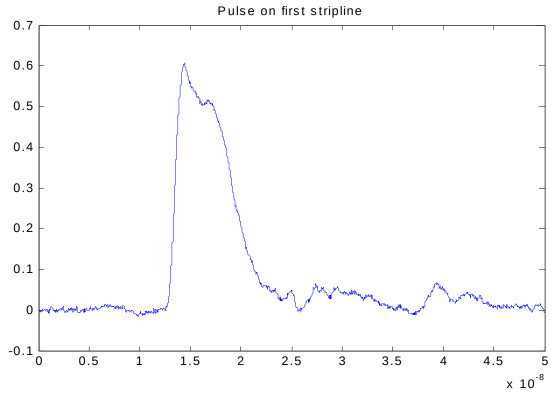

Fig. 8: Fast pulse after passing through the kicker

Fast high voltage pulser tests were also successful. The very fast pulse (~5 ns, 16 kV) that passed through the kicker was barely modified by the own kicker (Fig. 8), arriving at the 50 Ohm load loosing only frequencies over 2 GHz.

High Voltage DC Tests

Each kicker plate was tested up to 18 kV DC voltage (no current) in 2×10^{-7} mbar vacuum. No major problems were found in both strip-lines, only some sparks at the beginning of the test probably because of small impurities on the electrodes.

CONCLUSION

- Successful wakefield simulations have been presented. No major problems are expected.
- All the fabrication challenges have been solved and the know-how will be used in future devices.
- Kicker tests have reported good behaviour in vacuum, RF and high voltage subjects. The device has already been installed at the CTF3 Combiner Ring and it will soon be operating.

REFERENCES

[1] I. Rodríguez, "Design of a strip-line extraction kicker for CTF3 Combiner Ring", EPAC'06, Edinburgh, June 2006, MOPLS090.

[2] A. Gallo, A. Ghigo, F. Marcellini, M. Serio, B. Spataro, M. Zobov, "The Transverse Feedback Kicker", DAFNE Technical Note, INFN-LNF Accelerator Division (1995).

[3] L. Palumbo, V.G. Vaccaro, M. Zobov, "Wake fields and impedance", CAS Advanced School on Accelerator Physics, Rhodes - Greece, September 1994.

[4] H. Henke, W. Bruns, "Calculation of wake potentials in general 3D structures", EPAC'06, Edinburgh, June 2006, WEPCH110.

ANALYSIS OF THE VERTICAL BEAM INSTABILITY IN CTF3 COMBINER RING AND NEW RF DEFLECTOR DESIGN

D. Alesini, C. Biscari, A. Ghigo and F. Marcellini, LNF-INFN, Frascati (Rome), Italy.

Abstract

In the last CTF3 run (November 2007) a vertical beam instability has been found in the Combiner Ring during operation. Possible sources of the instability are the vertical deflecting modes excited by the beam in the RF deflectors. In the first part of the paper we illustrate the results of the beam dynamics analysis obtained by a dedicated tracking code that allows including the induced transverse wake field and the multi-bunch multi-passage effects. To reduce the effects of such vertical trapped modes, two new deflectors have been designed. In the new devices special antennas absorb the power released by the beam to the modes. The structures will be made in aluminium to reduce the costs and delivery time.

INTRODUCTION

The second stage of the bunch train compression in CTF3 [1] is realized in the 84 m circumference Combiner Ring (CR). This is achieved by means of two travelling wave (TW) RF deflectors (RFDs) working at f_{RF}=2.99855 GHz already built [2] and successfully tested in the CTF3 Preliminary Phase [3]. In the last run a vertical beam instability has been observed during operation [4]. The phenomenology of such instability (described in detail in [4]) can be summarized as follows:

a) the profile of the vertical oscillation as a function of the bunch positions was the same shot by shot;
b) the measured Δ-frequency of the oscillation with respect to f_{RF} was ~48 MHz;
c) the instability is stronger if we increase the train length or the bunch charges;
d) changing the temperature of the deflectors by $8\,°C$ did not change the scenario;
e) the instability occurred both in the case of a single train and of recombined trains;
f) probably a better steering inside the deflectors yielded a weaker instability (no systematic study done).

A possible source of this instability has been identified in the vertical deflecting modes (VDMs) trapped in the RFDs and excited by the beam. A detailed study of the wakefields induced by these modes and their effect on beam dynamics is presented in the second and third paragraph. In the last paragraph we illustrate the design of the new RFDs with damped vertical modes.

VERTICAL MODES IN THE RFDS AND WAKEFIELD ANALYSIS

The RFDs intalled in the CR are TW devices that deflect the beam in the horizontal plane (Fig. 1a). The main parameters of the structures are reported in Table 1. Two metallic rods have been inserted into each cell to separate in frequency the deflecting mode with vertical polarity. The dimensions and position of the rods have been chosen to fix the polarity of the horizontal mode, avoiding tilt of the working polarity through the deflector and avoiding the excitation of the vertical mode by the beam power spectrum line at 2.99855 GHz. These vertical modes are not coupled to the input and output couplers, as shown in Fig. 1b where their typical H field lines are plotted.

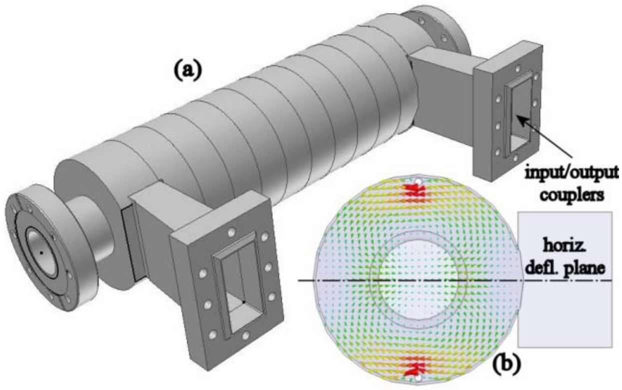

Figure 1: (a) RFD of the CR; (b) typical H field of the vertical modes.

Table 1: Main RFD Parameters

RFD frequency	2.99855 GHz
TW mode of operation	$2\pi/3$
Number of cells	12
Deflector length	~40 [cm]
Filling time	~47 [ns]
Deflection angle	5 [mrad]
Max input power	2 MW

To evaluate the effect on beam dynamics due to the transverse wakefields induced by VDMs, the resonant frequencies (f_{res}), quality factors (Q) and transverse shunt impedances (R_T)(*) of each VDM have been calculated by HFSS [5]. The results are plotted in Fig. 2. It is easy to note that there is a "dominant" mode (in term of R_T) corresponding to the mode with a ~2π/3 phase advance per cell. In the following calculations we have considered the contribution of this dominant mode only (whose parameters are reported in Table 2). It is straightforward to extend all the obtained results to the more general case of multi-modes.

* We defin the transverse shunt impedance by the formula:

$$R_T = \frac{\left|\int_{cavity} \left(cB_x + E_y\right) e^{j\omega_{RF} z/c} dz\right|^2}{2P_{diss}}$$

where Bx and Ey are the magnetic and electric transverse field components, z is the beam traveling direction, , P_{diss} is the total dissipated power in the cavity.

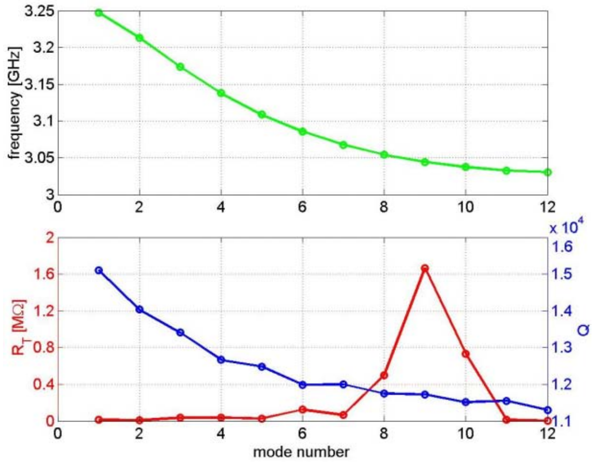

Fig. 2: Vertical trapped modes parameters.

The general expression of the transverse voltage (as a function of time) induced by a point-like charge (q) passing into the deflector with a vertical offset (y) with respect to the deflector axis is given by [6]:

$$V_T(\tau) \cong q \frac{\omega_{res}^2}{c} \frac{R_T}{Q} y e^{-\frac{\omega_{RF}}{2Q}\tau} \sin(\omega_{res}\tau)$$

The induced wakefield has a sine-dependence (it is so-called 90 deg. out of phase wake). It is straightforward to note than, since the separation between bunches is an integer multiple of f_{RF} this mode is not excited perfectly on resonance by the beam train. This may results in a net deflecting kick on the bunches of the same train. Moreover, for the same reason, the filling time can become much shorter than the nominal resonant mode filling time ($2Q/\omega_{res}$). Both aspects are important to intuitively understand the mechanism of such strong and fast instability.

Table 2: Parameters of the Dominant Vertical Mode

Q	11500
f_{res}	3.0443 GHz
R_T	1.6 MΩ

TRACKING CODE RESULTS

A dedicated tracking code has been written to study the multi-bunch multi-passage effects. In the code each bunch, represented as a macro-particle, enters the 1st deflector with a given vertical orbit (Y_{in1}), interacts with the wake left by the bunches ahead, contributes to the wake and exits from the deflector. The bunch is then transported to the other deflector by the CR transport matrix, enters the 2nd RFD with a given vertical orbit (Y_{in2}) plus the perturbation given by the residual oscillation induced by the wakes in the 1st RFD, interacts with the RF field and wakes of this second device and so on. At the end of the merging process each macroparticle ends up with vertical Δ-positions with respect to the original orbit (y_{out}, y'_{out}) given by the corresponding values of the Courant-Snyder invariant (I_{out}). The tracking allows studying the distribution of I_{out} for all bunches and its dependence on the resonant mode properties and ring optical functions. Since all the results scale with the charge per bunch (q) and beam energy (E_0) we fixed q=2.33 nC (nominal CTF3 charge) and E_0=100 MeV (beam energy during the last run). As an example the output vertical positions, angles and I_{out} normalized to the nominal CR emittance (ε=0.4 mm mrad) of one train of bunches after 4 turns are reported in Fig. 3 assuming the parameters shown in the same figure (β, α and ϕ are the usual optical functions at the RFDs). The FFT of the vertical oscillations have frequency components centered around 45-50 MHz (†) very similar to the measured ones.

The maximum I_{out}/ε as a function of the CR vertical phase advance (ϕ_{12}) and vertical β-function at the RFDs are given in Fig. 4 for different vertical phase advances between the two RFDs (ϕ_{21}).

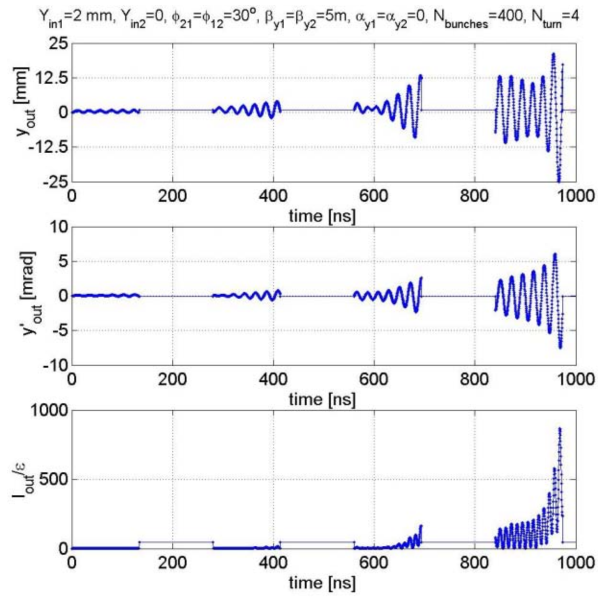

Figure 3: Output vertical positions, angles and I_{out}/ε of a circulating train after 4 turns.

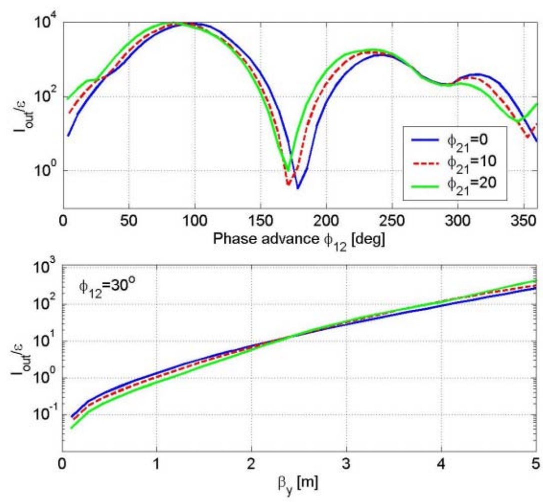

Figure 4: Maximum I_{out}/ε as a function of the CR vertical phase advance (ϕ_{12}) and vertical β-function at the RFDs.

† Equal to the difference between f_{RF} and f_{res}.

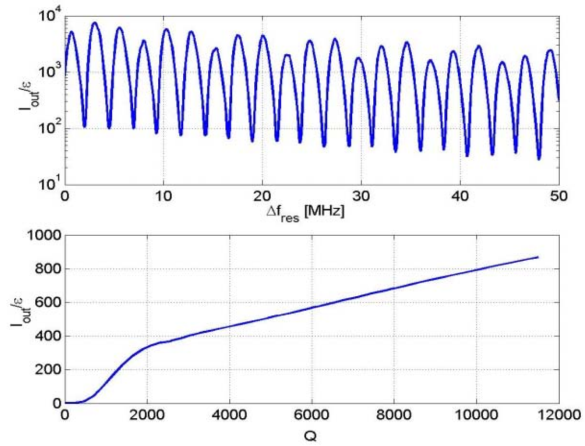

Figure 5: Maximum I_{out}/ε as a function of the mode resonant frequency and quality factor.

Fig. 5 shows the maximum I_{out}/ε as a function of the mode resonant frequency and quality factor (‡). In the first case the maximum I_{out}/ε has a periodic behaviour due to the interaction between the finite bandwidth resonance and the periodic spectrum of the circulating beam. Similar results can be obtained considering different train lengths or recombination.

From the previous plots it is possible to conclude that this strong instability is caused by a few mm off-axis beam passage into the deflectors (1-2 mm was the order of magnitude of the orbit inside this devices in the last run) and that a better orbit control inside these structures can reduce the instability. A vertical tune near half integer can reduce the instability effects also (§) as well as the reduction of the vertical β-functions at the RFDs. For this reason a new optics with half integer vertical tune has been implemented and is now under test in the new run [4]. Changing the mode resonant frequencies by few hundred kHz (for example, by changing the temperature of the RFD by few degree) does not help much because we need few MHz of detuning to measure some relevant effects. A strong reduction of the Q-factors of the modes can instead strongly reduce the instability.

NEW RF DEFLECTORS DESIGN

The new RFDs have been designed to increase the vertical modes frequency separation (by few hundred MHz) and to strongly reduce the quality factor of the vertical modes (**). The mechanical drawing is shown in Fig 6. In the new RFD the vertical mode in each cell is damped through an antenna/loop directly connected to the rods. Moreover the rods themselves have been moved towards the deflector axis in order to increase the vertical modes frequency separation of more than 300 MHz. The quality factors of the vertical modes in this new RFDs are so low that they cannot be well calculated. The power flowing through the antennas in the external loads is given by the power transferred from the main RF source at f_{RF} that is slightly coupled to the antennas because the structure is not perfectly symmetric and by the contribution of the power transferred from the beam to the accelerating mode which is coupled to the antennas themselves. The two contributions do not exceed few watts rms at least from HFSS simulations. To reduce the cost and the delivery time of the device we decided to built the new RFDs in aluminium. The cells will be clamped together and soldered. RF power tests before the installation in the CTF3 CR will be done to investigate if multi-pacting phenomena occur. If this is the case we intend to provide Ti-coating to reduce the secondary emission yield.

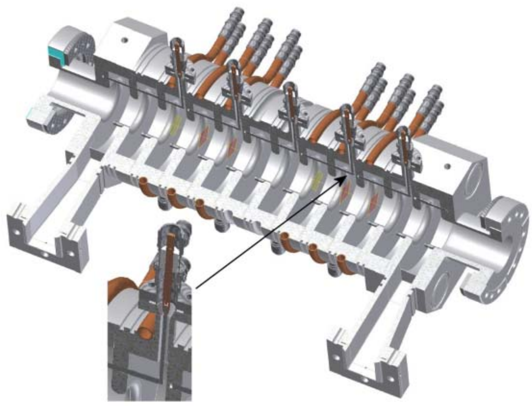

Figure 6: New RFDs mechanical drawing.

CONCLUSIONS

Vertical trapped modes in the RFDs of the CR are probably responsible for the vertical beam instability found in the last CTF3 run. To study the beam dynamics a dedicated tracking code has been implemented. The results show that the instability can be mitigated by a more accurate control of the orbit inside the RFDs, by adopting a half integer vertical tune or by reducing the vertical β-function at the RFDs. The instability can be completely cancelled with a strong reduction of the Q factors of the modes. For this reason new RFDs have been designed and are now under construction. In the new devices special antennas absorb the power released by the beam to the modes. The structures will be made in aluminum to reduce the cost and delivery time.

‡ In both cases we suppose that the two VDMs of the two RFDs have exactly the same frequency and Q.

§ This can be intuitively understood because, in the case of an half integer tune, the vertical kicks given by the wakefields do not change the vertical beam offset at the RFD after one turn. On the contrary the maximum instability occurs when the vertical kick is completely transformed into vertical displacements (tune near 0.25 or 0.75).

** The design has been done using HFSS.

REFERENCES

[1] "CTF3 Design Report", CERN PS 2002-008 (RF), Geneve, (2002).
[2] D. Alesini, et al., EPAC 2002, p.2115.
[3] F. Tecker, et al., PAC03, p. 684.
[4] R. Corsini, MOPP011, This conference.
[5] www.ansoft.com
[6] for example, D. Alesini, et al., EPAC04, p. 2077.

NEW EXPERIMENTAL RESULTS WITH OPTICAL DIFFRACTION RADIATION DIAGNOSTICS*

E. Chiadroni†, M. Castellano, LNF-INFN, Frascati, Italy
A. Cianchi, INFN Roma "Tor Vergata", Roma, Italy
K. Honkavaara, G. Kube, DESY, Hamburg, Germany

Abstract

The characterization of the transverse phase space for high charge density and high energy electron beams is demanding for the successful development of the next generation light sources and linear colliders.

The interest in a non-invasive and non-intercepting beam diagnostics is increasingly high due to the stringent features of such beams. Optical Diffraction Radiation (ODR) is considered as one of the most promising candidates to measure the transverse beam size and angular divergence, i.e. the transverse emittance.

An experiment, based on the detection of the ODR angular distribution, has been set up at DESY FLASH Facility to measure the electron beam transverse parameters. In this paper we report the preliminary analysis on the incoherent diffraction radiation produced by a 900 MeV energy electron beam going through a 0.5 mm rectangular slit.

INTRODUCTION

The final goal of our experiment is measuring the transverse beam size and divergence. A dedicate analysis of the Optical Diffraction Radiation (ODR) angular distribution [1] allows then to separate the two effects. If the beam is in a waist on the DR screen, the transverse emittance can be derived with a single non-intercepting measurement.
Some modifications have been done on the hardware in order to let synchrotron radiation (SR) contribute as less as possible. At this regard, a thin metallic screen (Fig. 2) has been installed to stop SR, but during measurements it has shown interesting peculiarities which need to be further investigated, both analytically and experimentally.

DR THEORY

DR is produced when a charged particle goes through a slit or passes by the edge of a metallic screen, due to the interaction between the EM field of the traveling charge and the target surface [2]. The intensity of the radiation increases linearly with charge and is proportional to $e^{-\frac{2\pi a}{\gamma\lambda}}$, where a is the slit aperture, γ the Lorentz factor and λ the emitted wavelength. The factor $\frac{\gamma\lambda}{2\pi}$, called as DR impact parameter, is the natural size of the radial extension of the EM field, thus when $a \cong \frac{\gamma\lambda}{2\pi}$ DR is emitted.

The DR angular distribution is produced by the interference of radiation from both edges of the slit. The visibility of the interference fringes is mainly affected by beam parameters in the plane orthogonal to the slit aperture: when the transverse beam size is increased, both the peak intensity and the central minimum increase, resulting in the reduction of their ratio. The effect is also affected, in a slightly different way, by the angular divergence of the beam: the ODR angular distribution becomes wider and the intensity of the minimum higher, when the beam divergence increases.

EXPERIMENTAL APPARATUS

Our experiment is carried out at FLASH, Free electron LASer in Hamburg, at DESY. FLASH is an excellent facility for this experiment, since it can drive long bunch trains, up to 800 bunches per macropulse allowing a high charge operation, and it has a good long term stability, a small transverse emittance ($\sim$ 2 mm mrad), and a high electron beam energy, approaching 1 GeV.

Our experimental set-up is placed in the by-pass beam line (Fig. 1) very far (about 40 m) from the dipole magnets in order to minimize the contribution coming from the synchrotron light.

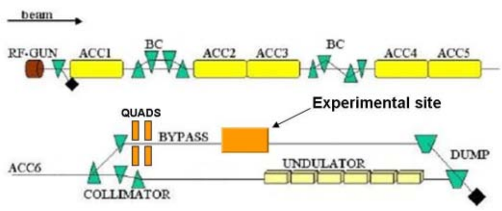

Figure 1: FLASH layout and experimental site.

The experimental apparatus has an aluminized silicon nitride screen (DR screen) mounted at 45^o angle with respect to the beam direction. The DR screen is constructed by lithographic technique starting from a silicon nitride wafer and opening two slits, one of 0.5 mm and the other of 1 mm aperture, by means of chemical etching. The slits are spaced by 2 cm and the space between the slits is used as a standard OTR screen. The main advantage of the silicon nitride with respect to SiO_2 [3] is a much less etching rate which preserves the silicon substrate from damages and makes the surface much more uniform. An aluminum layer is deposited by sputtering on the target to enhance the reflectivity.

* Work supported by the European Community Infra-structure Activity under the FP6 "Structuring the European Research Area" program (CARE, contract number RII3-CT-2003-506395)

† enrica.chiadroni@lnf.infn.it

A thin shielding mask (Fig. 2) is mounted at 45^o with respect to the DR target and normally to the direction of beam propagation. Two slits, 1 mm and 2 mm aperture, are machined in order to let both the beam and the radiation field go through without interacting with the screen. Furthermore the screen surface is machined such that reflections should be suppressed. The great advantage of this screen is the strong minimization of the SR background. On the other end, interference effects between the ODR emitted on the shielding mask in the forward direction and the radiation from the DR target are observed in the ODR angular distribution pattern (see next section).

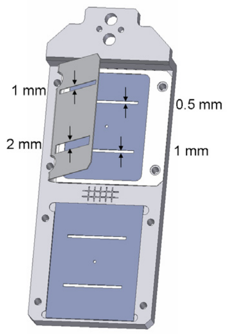

Figure 2: Sketch of the shielding mask. The DR radiator is visible behind.

Radiation from the target is reflected by a mirror and sent through an optical system to the camera. Two lenses, one to image the beam, the other one to produce the DR angular distribution, can be selected. They have different focal length in order to have the focus on the same plane. Two interferential filters, at 800 nm and 450 nm, and a polarizer may be inserted on the optical axis. Due to the very low radiation intensity, a high sensitivity CCD camera (Hamamatsu Model C4742-98-LGLAG2) is used. The optical system layout is shown in Fig. 3.

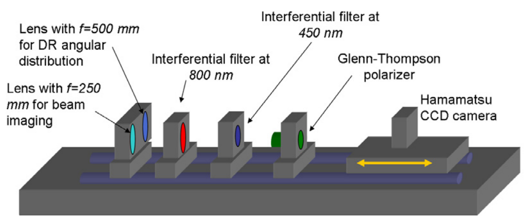

Figure 3: Sketch of the optical system.

PRELIMINARY RESULTS

To reduce the impact of SR background two big improvements have been done, on one side on the hardware with the installation of the shield screen and, on the other side, on the electron beam optics with runtime entirely dedicated to optimize the beam transport on the by-pass. Moreover the higher energy and the better quality of the beam allowed to get promising results. Unfortunately a severe contribution of the dark current (Fig. 4) from the cathode was a big drawback, being from time to time a source of transition radiation (see Fig. 7c).

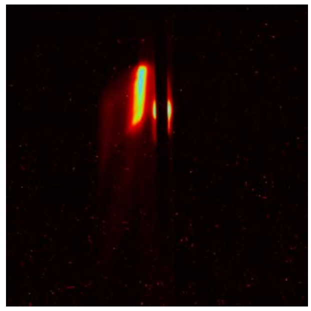

Figure 4: Beam in the 0.5 mm slit. On the left edge side the severe contribution of the dark current is visible.

In this section we report the preliminary results obtained with a 900 MeV electron beam energy going through a 0.5 mm slit. During measurements reported in this paper, FLASH was operated with up to 11 electron bunches (1 nC per bunch) per macropulse with 1 MHz bunch spacing. The macropulse repetition rate was 5 Hz.

The image of the beam and its intensity projection are shown in Fig. 5a and Fig. 5b, respectively. The rms beam transverse size, evaluated from a Gaussian fit, is about 80 μm.

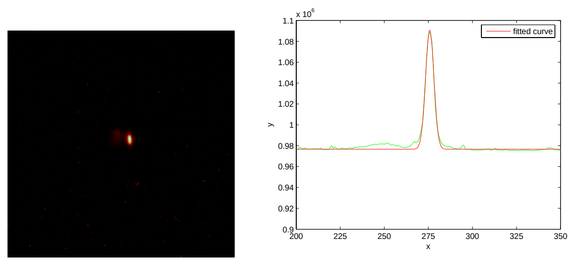

(a) Beam image (b) Beam projection

Figure 5: Image of the beam on the OTR screen (a) and the projection fit (b).

The analysis of the Optical Transition Radiation (OTR) angular distribution (Fig. 6) allowed an estimation of the beam energy of about 820 MeV.

Measurements

The first part of our shifts has been dedicated to the optimization of the beam transport, in terms of both small rms transverse size and low gradient in the quadrupoles in order to avoid any contribution of synchrotron light coming from them. The strong contribution of the dark current (Fig. 7c) could not be avoided, but easily subtracted because it does not depend on the beam.

In this conditions several scans have been done moving the

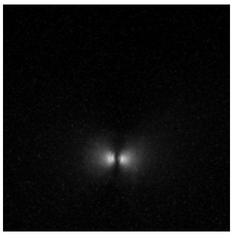

(a) OTR angular distribution

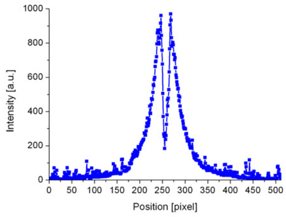

(b) OTR profile

Figure 6: OTR angular distribution with polarizer and 800 nm filter: a) image and b) projection of central line.

beam transversely in the slit and looking at the ODR angular distribution. Figure 7a) shows the ODR angular distribution in the case the beam goes through the 0.5 mm slit with an impact parameter of 150 μm. It is worth noting

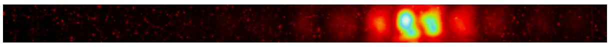

(a) ODR angular distribution

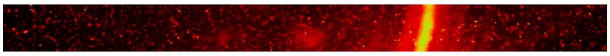

(b) SR background

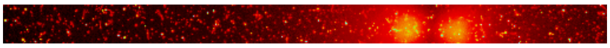

(c) Dark current background

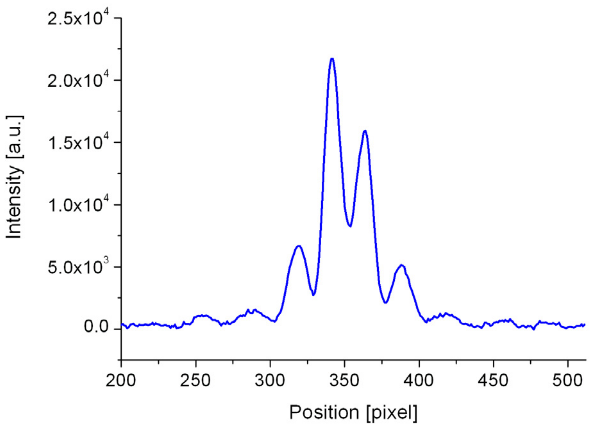

(d) ODR projection

Figure 7: ODR angular distribution (a), SR background, dark current-generated background (c) and vertical projection (d). Both 800 nm interference filter and polarizer are inserted.

the clear evidence of the higher orders of oscillation, highlighted by the interference effects between the two ODR sources, the one produced on the shielding mask in the forward direction (FDR), and the one generated by the DR screen in the backward direction (BDR). Since the amplitude of the two sources are opposite in sign, the interference results in the supression of the central peaks and the enhancement of the side maxima. Figure 8 shows the ODR angular distribution for a complete scan done moving the slit edge transversely in order to change the impact parameter. The asymmetry with respect to the central minimum must be addicted to the fact that the two slits (the one on the shielding mask and the one on the DR target) are not perfectly aligned, resulting in a different impact parameter.

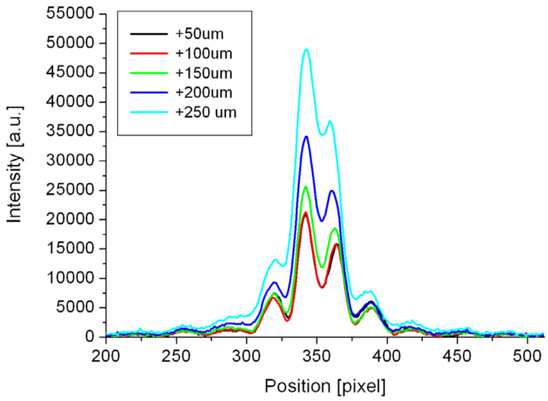

Figure 8: Angular distributions for different positions of the beam with respect to the center of the slit. Both the polarizer and the 800 nm filter are inserted.

CONCLUSIONS

The installation of a shielding mask produced interesting results. On one side it has helped in the reduction of the background signal coming from SR, on the other side it has highlighted the lateral peaks of the ODR angular distribution. A detailed and quantitative study of these effects is ongoing.

ACKNOWLEDGEMENT

Special thanks are to FLASH shift crews, in particular, the authors are grateful for Nina Golubeva and Vladimir Balandin for beam optics calculations and tuning the linac in order to get optimum beam conditions required for the experiment. We thank also R. Sorchetti and L. Cacciotti (INFN-LNF) for their fundamental technical assitance.

REFERENCES

[1] M. Castellano, Nucl. Instr. and Meth. in Phys. Res. A **394**, 275 (1997)

[2] M.L. Ter-Mikaelian, “High-Energy Electromagnetic Processes in Condensed Media”, Wiley-Interscience

[3] E. Cianci et al., “Micromachined silicon slit for beam diagnostic in particle accelerator”, Proc. SPIE, 4557, pp.242-249 (2001)

[4] E. Chiadroni et al., Proceedings of PAC07, Albuquerque, New Mexico, USA

CERN SPS IMPEDANCE IN 2007

E. Métral, G. Arduini, T. Bohl, H. Burkhardt, F. Caspers, H. Damerau, T. Kroyer, H. Medina, G. Rumolo, M. Schokker, E. Shaposhnikova, J. Tuckmantel (CERN, Geneva, Switzerland), B. Salvant (EPFL, Lausanne, Switzerland), R. Calaga (BNL, Upton, NY, USA) and B. Spataro (INFN, Frascati, Italy)

Abstract

Each year several measurements of the beam coupling impedance are performed in both longitudinal and transverse planes of the CERN Super Proton Synchrotron to keep track of its evolution. In parallel, after the extensive and successful campaign of identification, classification and cure of the possible sources of (mainly longitudinal) impedance between 1998 and 2001, a new campaign (essentially for the transverse impedance this time) has started few years ago, in view of the operation of the SPS with higher intensity for the LHC luminosity upgrade. The present paper summarizes the results obtained from the measurements performed over the last few years and compares them to our predictions. In particular, it reveals that the longitudinal impedance is reasonably well understood and the main contributors have already been identified. However, the situation is quite different in the transverse plane: albeit the relative evolution of the transverse impedance over the last few years can be well explained by the introduction of the nine MKE kickers necessary for beam extraction towards the LHC, significant contributors to the SPS transverse impedance have not been identified yet.

INTRODUCTION

The impedance reduction program, which took place between 1999 and 2001, revealed an impedance reduction factor of ~ 2.5 in the longitudinal plane and ~ 0.4 in the vertical one (See [1] and references therein). Since then, in order to extract the beam towards the LHC, new extraction kickers (MKE) were installed: five in 2003 (leading to a total of 16 kickers), and four in 2006 (leading to a total of 20 kickers). Note that one of the MKE kicker was shielded on 2 cells. In 2007 one MKE kicker was removed and one MKE was "fully" shielded, leading to a total of 19 kickers.

To be able to follow the impedance increase and its impact on the beam dynamics, systematic beam-based impedance measurements were performed over the last few years. The aim of the present paper is to summarize the main results and to compare them to our predictions. The outline is the following: the first section deals with the vertical coherent tune shift vs. intensity. The second section is devoted to the study of the Transverse Mode-Coupling Instability (TMCI) at injection. In the third section, head-tail growth/decay rate measurements vs. chromaticity are discussed, while in the fourth section the results of the localization of the vertical impedances from measurements of the betatron phase-beating vs. intensity are analyzed. Finally the longitudinal impedance is addressed in the fifth section from measurements of the quadrupole synchrotron frequency shift with intensity.

VERTICAL COHERENT TUNE SHIFT

The measurements of the single-bunch vertical coherent tune shift vs. intensity are depicted in Fig. 1. It can be first seen that in 2001 the measured "total" (i.e. dipolar plus quadrupolar) effective impedance was reduced by 40% compared to the measured value in 2000. Secondly, one can observe that the measured "total" impedance increase from 2001 to 2006 (i.e. due to the installation of the 9 MKE kickers) is 4.5 MΩ/m, which has to be compared to 5.2 MΩ/m expected from theory (see Table 1). Furthermore, a slight reduction of the impedance was expected in 2007 (due to the removal of one MKE kicker and shielding of another one). This seems also to be reflected in Fig. 1, even though one might reach the precision limit for the measurements and the exact predicted "total" impedance of the shielded kicker could not be given as the quadrupolar impedance is missing (only the dipolar impedance was measured). This good agreement reveals that the impact of the hardware modifications can be reasonably well explained since 2001. Note that the imaginary part of the vertical effective dipolar impedance of the shielded kicker is $\mathrm{Im}[Z_{y,dip}]_{eff}$ = 0.24 MΩ/m, whereas it was 0.27 MΩ/m

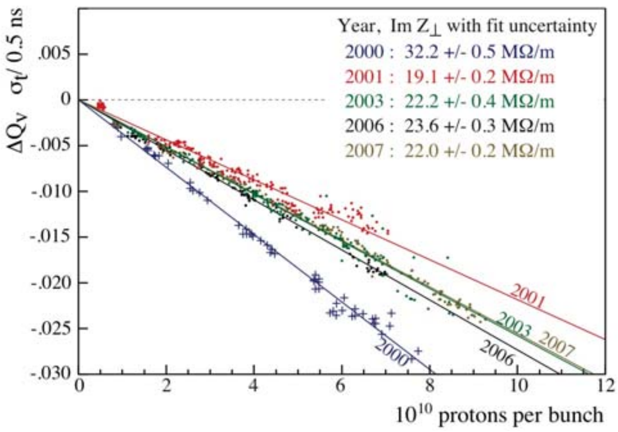

Figure 1: Measurements of the single-bunch vertical coherent tune shift vs. intensity over the last years.

before the shielding, revealing a small effect of the shielding in the vertical plane. Furthermore, the imaginary part of the vertical effective "total" impedance from space charge (which contributes to the coherent tune shift) is $\mathrm{Im}[Z_y]_{eff}$ = 2.6 MΩ/m.

The conclusions of these measurements are that (i) the contribution from all the kickers vs. time can be reasonably well explained, (ii) all the kickers in 2006 (and 2007) contribute to ~ 40 % of the total measured impedance and (iii) 13 MΩ/m are still missing.

Table 1: Summary and comparison between measurements (of the whole SPS) and theoretical predictions (using only the contribution of the kickers).

$\mathrm{Im}(Z_y)_{eff}$ [MΩ/m]	Meas	delta	Theory (kickers)	delta	Error delta [%]
2001	19.1		3.5		
2003	22.2	3.1	6.4	2.9	7
2006	23.6	1.4	8.7	2.3	-39
2007	22	-1.6			

TMCI AT INJECTION

This subject is discussed in detail in Ref. [2]. The main results are that a double instability threshold and a tune step were observed on both tracking simulations (using the impedance of the kickers) and on SPS experiments performed in 2007. These mechanisms can both be explained by a first regime of mode coupling-decoupling (leading a small instability) followed by the main mode-coupling (leading to the fast instability). The simulated (main) intensity threshold is ~ 9.3 10^{10} p/b, while ~ 7.6 10^{10} p/b were measured (see Fig. 2), which leads to an already quite good agreement (~ 20 %).

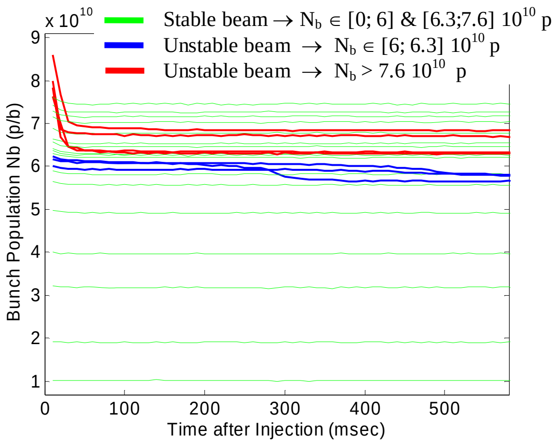

Figure 2: Bunch intensity vs. time for a bunch with low longitudinal emittance (ε_L = 0.16 eVs).

HEAD-TAIL GROWTH/DECAY RATE

Changing the (vertical) chromaticity the growth or decay rates of the single-bunch head-tail instability can be measured. This provides information about the real part of the vertical impedance (see Fig. 3). The conclusion from these measurements is that the real part of the effective vertical impedance from all the (20) kickers in 2006 contribute to ~ 50% of the total measured impedance. A more precise comparison will be performed with the improved impedance model used in Ref. [2].

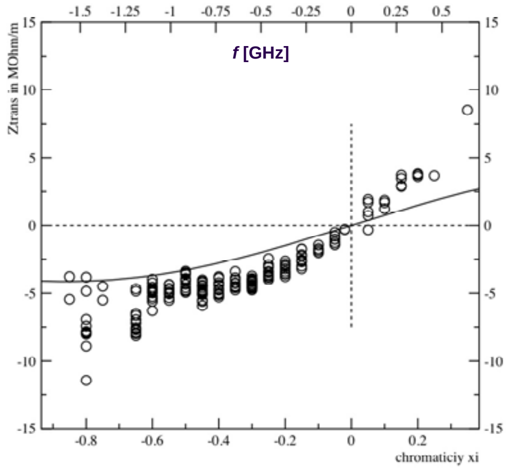

Figure 3: Comparison between the measured (dots) and computed (full black curve) real part of the effective vertical impedance vs. chromaticity.

IMPEDANCE LOCALIZATION

An effort to localize the vertical impedance sources in the SPS was carried out using beam based techniques as proposed in Ref. [3]. Simulations using the HEADTAIL code [4] were performed to understand the effectiveness of this technique and the imposed constraints. The analysis from HEADTAIL, using as source impedances only the SPS kickers, indicates that: (i) all focusing and defocuing quadrupoles when used as variables in response matrix correction are able to approximately reconstruct the source location without any constraints, (ii) the amplitude and transverse orientation of the impedance source cannot be easily inferred from a quadrupole response matrix. More advanced choice of the

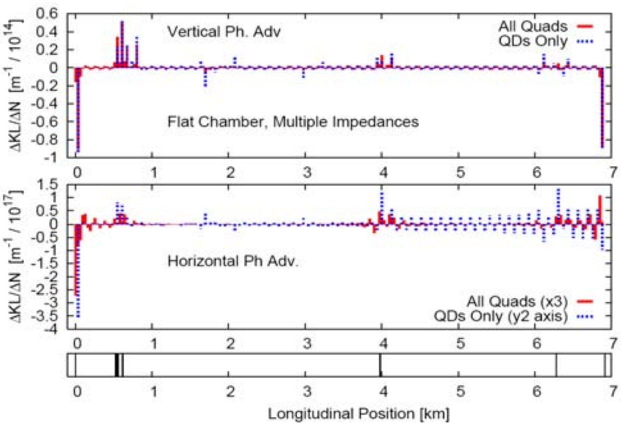

Figure 4: Local impedance distribution around the SPS ring from the simulated (with HEADTAIL) current-dependent phase beating at 26 GeV/c, considering all the kickers only (whose position is shown in the lower plot).

variable vector space and algorithms maybe help improve the solution, (iii) effects of noise and faulty BPMs are under investigation to define the confidence level of the localization with real data. Analysis of SPS data based on the developments from HEADTAIL simulation are underway.

QUADRUPOLE FREQUENCY SHIFT

The inductive part of the effective longitudinal impedance can be assessed by measuring the quadrupole oscillation synchrotron frequency shift vs. intensity. The results of these measurements over the last years can be found in Fig. 5. It can be first seen that in 2001 the measured effective impedance was reduced by a factor of ~ 2.5 compared to the measured value in 1999. Secondly, one can observe that the effective impedance increase from 2001 to 2006 (i.e. due to the installation of the 9 MKE kickers) is 3 Ω, which has to be compared to 4 Ω expected from theory (see Table 2). A slight reduction of the impedance was expected in 2007 (due to the removal of one MKE kicker and shielding of another one). Contrary to the expectations first measurements in 2007 revealed an increase of the impedance by ~ 40 %. More measurements were performed at the end of the 2007 run, where the result of 2006 was recovered. The conclusions from these measurements are that (i) the contribution from all the kickers vs. time can be reasonably well explained until 2006/2007, (ii) depending on the bunch length and longitudinal emittance, huge differences can be observed (as expected) [5].

Note that the longitudinal effective inductive impedance of the shielded kicker is $\mathrm{Im}[Z_l/n]_{eff} = 0.1\ \Omega$, whereas it was 0.4 Ω before the shielding, which reveals the important effect of the shielding. Furthermore, the longitudinal effective inductive impedance from space

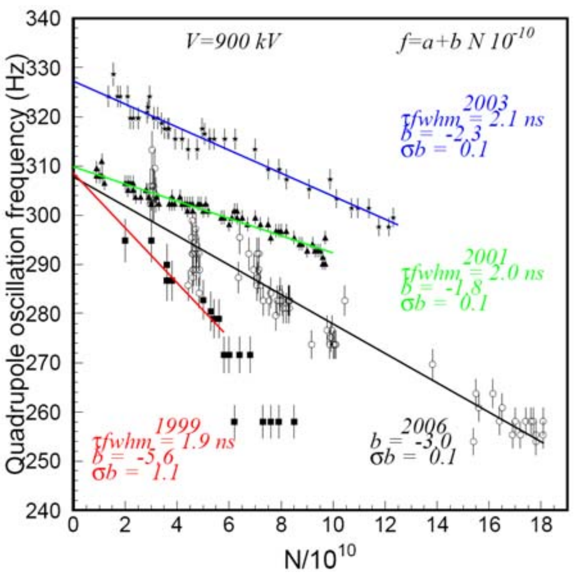

Figure 5: Quadrupole synchrotron frequency vs. intensity from 1999 to 2006.

charge is $\mathrm{Im}[Z_l/n]_{eff} \approx -1\ \Omega$, and it has already been subtracted from the above cited numbers.

Table 2: Summary and comparison between measurements (of the whole SPS) and theoretical predictions (using only the contribution of the kickers).

$\mathrm{Im}(Z_l/n)_{eff}$ [Ω]	Meas	delta	Theory (kickers)	delta	Error delta [%]
2001	4.4		1.2		
2003	6.2	1.8	3.4	2.2	-18
2006	7.4	1.2	5.2	1.8	-33
2007	10.2	2.8	4.4	-0.8	-450

CONCLUSION

Although a relatively good agreement is obtained when relative values are discussed, the kickers can only explain ~ 40% (9.4 MΩ/m deduced from simulations in Ref. [2]) of the vertical impedance measured from vertical coherent tune shift. Removing the contribution from space charge to the coherent tune shift, ~ 13 MΩ/m are still unexplained. The vertical impedance of several other equipments has been computed or simulated, but it is negligible compared to the missing impedance [1]. The next steps will consist in: (i) adding all the impedances of the simulated equipments into ZBASE [6] and (ii) continuing the identification of additional sources.

The head-tail growth/decay rate measurements also confirm that ~ 50% of the vertical impedance is still unexplained, whereas a better agreement (~ 20%) seems to be obtained from TMCI studies [2].

In the longitudinal plane, the agreement is relatively good (when both relative and absolute values are discussed) as the main remaining part, ~ 3.2 Ω (= 4.4 Ω – 1.2 Ω) in 2001, could be mainly explained by the RF cavities [1]. In the future more time should be devoted to study the HOMs responsible for the (quite low) longitudinal coupled-bunch instability threshold.

Finally, the fact that the quadrupole synchrotron frequency shift was not very well determined during first measurements in 2007 was attributed to the lack of reproducibility of bunch length and emittance at injection [5]. In the future more attention should be paid to make these parameters reproducible.

REFERENCES

[1] E. Métral et al., “SPS Impedance”, Proc. HHH-CARE BEAM’07, CERN, Geneva (2007).

[2] B. Salvant et al., “Transverse Mode-Coupling Instability in the CERN SPS: Comparing MOSES Analytical Calculations and HEADTAIL Simulations with Experiments in the SPS”, these proceedings.

[3] G. Arduini et al., “Localizing Impedance Sources from Betatron Phase Beating in the CERN SPS”, Proc. EPAC’04, Lucerne, Switzerland, 2004.

[4] G. Rumolo and F. Zimmermann, CERN-SL-Note-2002-036 AP.

[5] T. Bohl et al., AB-Note-2008-025-RF.

[6] O. Brüning, CERN-SL-96-069-AP (1996).